

Finite Volume/Immersed Boundary Solvers for Compressible Flows: Development and Applications

A thesis submitted
in partial fulfillment of the requirements
for the Degree of

DOCTOR OF PHILOSOPHY

in

Mechanical Engineering

by

Shuvayan Brahmachary



Department of Mechanical Engineering
Indian Institute of Technology Guwahati
Guwahati - 781 039

“The journey is the reward”

— The Pirates (Steve Jobs)

Dedicated to
Ma, Baba and Dada

CERTIFICATE

This is to certify that the work presented in the thesis entitled "**Finite Volume/Immersed Boundary Solvers for Compressible Flows: Development and Applications**" submitted by Shuvayan Brahmachary to Indian Institute of Technology Guwahati for the award of the degree of Doctor of Philosophy in Mechanical Engineering is a bona fide record of research work carried out by the student himself under our supervision and have not been submitted elsewhere for any degree or diploma.

Signature:

Date:

Supervisor: Dr. Ganesh Natarajan

Department of Mechanical Engineering,
Indian Institute of Technology Guwahati,
Guwahati-781039, Assam, India.

Signature:

Date:

Supervisor: Prof. Niranjan Sahoo

Department of Mechanical Engineering,
Indian Institute of Technology Guwahati,
Guwahati-781039, Assam, India.

ACKNOWLEDGEMENT

Seems just like yesterday when I had enrolled for Ph.D, not knowing what laid in front of me. After 6 long years in this journey, I couldn't possibly come up with the names of all those people who have directly or indirectly helped me. Here are few important people who did.

I owe a huge debt of gratitude to my supervisors Dr. *Ganesh Natarajan* and Prof. *Niranjan Sahoo* for their guidance. They are responsible for shaping the thesis in its present form and without their support, all of this would be a distant dream. They have always been kind enough to accept my inefficiencies, provide a conducive environment for research and make me see the better side of the things. I consider myself to be extremely fortunate to have worked under them.

Sincere acknowledgements is in order for Dr. *Vinayak Kulkarni*, who has been a constant source of motivation. I am thankful to him for providing me with the opportunity to work with him as a JRF, especially before I was even a Ph.D scholar. That transition from a graduate student to a JRF was a defining point in my career. I take this opportunity to thank ISRO to provide us the financial support which were helpful towards achieving some of the contents of this thesis. I would also like to sincerely thank my DC members Prof. *Anoop K. Dass*, Dr. *Deepak Sharma* and Dr. *Suresh Kartha*, who were equally insightful and constructive in their comments towards my work. I sincerely thank Dr. *Vibin Ramakrishnan* for being my meditation instructor.

I have been blessed with very good friends on and off campus. Specifically, I would like to thank 'The League' comprising of my very good friend(s) *Jay, Cookie and Abhi*. Your presence outside of academics has been such a wonderful treat, including the memorable 'Sikkim trip'. I thank you for understanding all those days when I had to cancel on you guys at the last moment. Special mention goes to my friends: *Sumit* for being the guy that he is (omnipresent), *Siddesh* for being an ever-positive source and *Snehasish* for those interesting conversations. I can write endlessly about the days we have spent together on the campus but some things are better left unsaid; atleast not in a Ph.D thesis. I am deeply thankful to *Mukesh Kumar* for always fixing my lab PC and being extremely patient with me whenever I pulled his leg. I fondly remember some of the best food that you cooked for me and for that I must thank *Vishnu* for inviting me to his place on more than one occasion. I would like to thank

Shatru & Soni for dragging me to play badminton with them and taking pride in beating me (just don't forget you had a better badminton racket). It is only fitting for me to thank Dr. *Simon Peter* and Dr. *Jitendra Patel* for introducing me to certain concepts in IB and various other valuable inputs including L^AT_EX. I hope to see you both some day in a conference, while IB is still a thing, atleast for incompressible flows. I deeply thank Dr. *Bhaskar Bora* for always guiding me and being like a big brother to me. I acknowledge the fact that you possessed such an endearing personality which encouraged everyone else to stay grounded. Special thanks goes to *Mandeep* for helping me understand MGG, being my PUBG partner and so much more. While I am still figuring out to use *xfig* properly, I am grateful to you for teaching me to draw quality images in *Teeplot*. I would also like to thank *Juan* for my first guitar lesson, the Shillong road trip and introducing me to 'SW's' music. I hope to see you pursue your Doctoral studies soon. I cannot sum up my appreciation for *Jubajyoti* in few lines and I will try not to. Kidding. I am very thankful indeed for your programming lectures (so many of them!). I have learned a lot from your passion towards programming and I wish I had more days to absorb even more. I would also like to convey my thanks to *Moni* for helping me correct glaring grammatical error in the thesis. While this thesis is not a finished article yet, I really appreciate your efforts. I am grateful to *Soumya & Saibal* for being so helpful in every aspect. Your assistance in last minute arrangements will always be remembered. I fondly appreciate *Ali* for his fresh perspective upon things and those games of Basketball. I would also like to thank *Narendra Nanal* for assisting me creating mesh in Gambit and *Josef Runsten*, a.k.a *jrunsten* from CFD online community in helping me generate three dimensional block structured mesh. My days in the campus have been specially memorable due to my juniors and I am extremely grateful to them for it. I acknowledge *Rahul & Joe* for some of the most brilliant discussions we had over the years, *Naman, Nayan, Rachit, Prashant, Yash* for exhibiting fun part of hostel life and *Jai, Shobhit and Piyush* for their witty remarks.

My family are the sole reason for my accomplishments, however small it may be. I feel a deep sense of gratitude towards my *Ma, Baba and Dada* who have been extremely patient, understanding and supportive throughout this journey and beyond. I deeply appreciate the sacrifices you have made for turning my dream to reality. I would also like to convey my gratitude to *Bhavi* for the moral support throughout.

Shuvayan

ABSTRACT

This thesis is devoted to the development of a robust and accurate Immersed Boundary/Finite Volume (IB-FV) framework for compressible flows and their applications to design and optimisation. The framework is devised by combining an unstructured data based finite volume flow solver with a sharp interface immersed boundary method. The finite volume flow solver employs limited linear reconstruction in conjunction with vanLeer and AUSM schemes for convective fluxes while central differencing is employed for viscous fluxes. A new approach to compute gradients, which are critical to the computation of inviscid and viscous fluxes, based on a variant of Gauss divergence theorem is proposed. The strategy referred to as Modified Green Gauss (MGG) reconstruction is a one-step approach but leads to marginally lesser dissipation and allows for the use of marginally higher Courant number than existing reconstruction techniques. A novel non-iterative variant of MGG reconstruction for non-orthogonal meshes is also described and its robustness in high-speed flows has been studied. A sharp-interface Immersed Boundary (IB) technique based on local reconstruction of the solution has been proposed for inviscid and viscous flows. The boundary conditions are imposed directly at the geometry interface and is employed to obtain the solution in the near vicinity of the solid(s). This reconstruction approach which also employs the finite volume solutions obtained away from the solid, is effectively an interpolation technique that does not strictly conserve the mass, momentum and energy. Two different strategies, based on inverse distance weighting (IDW) for inviscid flows and one-dimensional reconstruction (HCIB) for viscous flows are described and explained in this work. We show that the finite mass conservation errors diminish linearly with grid refinement and that the reconstruction approach does not degrade the nominal second-order accuracy of the flow solver. The IB-FV solver computes wall pressure and skin-friction distributions quite accurately, although the latter requires sufficient fine meshes in the vicinity of the body. However, finite levels of mesh refinement does not produce accurate heat flux estimates in laminar hypersonic flows past blunt geometries. We probe the possible causes of this under-prediction using an in-depth diagnostic analysis. The investigations indicate that errors due to temperature reconstruction which are linked to a loss in energy conservation are primarily responsible for the inaccurate estimation of wall heat-flux and stagnation point heat transfer. We prove using numerical experiments that the use of adaptive meshes and non-linear/non-polynomial interpolations do not improve the heat flux estimates

and that the errors are larger as Reynolds and Mach numbers become higher. The utility of the FV and IB-FV frameworks proposed in this work are highlighted by their application to three selected problems of design and optimisation. These frameworks are employed in conjunction with variable fidelity approaches for the design of minimum drag geometries, scramjet intakes and supersonic nozzle. The large spectrum of canonical problems in this thesis over a wide range of Mach and Reynolds number indicate the efficacy of the IB-FV solver while also highlighting some of its drawbacks. The IB-FV framework, despite its limitations, is also found to be a promising tool to evolve multi-fidelity optimisation frameworks that can accelerate the design and optimisation in hypersonic flows.

CONTENTS

1	Introduction	1
1.1	Gradient reconstruction strategy	4
1.2	Cartesian grid based methods	6
1.3	Multi-fidelity framework for optimisation/design problems	11
1.4	Objectives of the thesis	13
1.5	Outline of the thesis	14
2	Governing Equations and Mathematical Preliminaries	15
2.1	Navier-Stokes equations	15
2.2	Finite volume formulation	17
2.3	Inviscid and viscous flux computations	19
2.3.1	Inviscid flux discretisation	19
2.3.2	Viscous flux discretisation	21
2.4	Temporal discretisation	22
2.5	Implementation of boundary conditions	22
2.5.1	Supersonic inlet & outlet	23
2.5.2	No-slip walls	23
2.5.3	Inviscid wall or symmetry boundary	23
3	Modified Green-Gauss Reconstruction	25
3.1	Overview of Green–Gauss reconstruction	26
3.2	Modified Green Gauss reconstruction	29
3.3	Numerical studies	34
3.3.1	Supersonic vortex flow	35
3.3.2	Grashof vortex	38
3.3.3	Hypersonic flow past compression ramp	40

3.4	Summary	43
4	Sharp Interface Immersed Boundary for Inviscid Flows	44
4.1	Sharp interface immersed boundary method	45
4.1.1	Classification	46
4.1.2	Reconstruction	46
4.2	Discrete Conservation	51
4.2.1	Transonic flow past bump	51
4.2.2	Supersonic flow past wedge	54
4.3	Order of accuracy study	56
4.4	Numerical investigations	58
4.4.1	Supersonic flow past a cone	59
4.4.2	Hypersonic Flow past Sphere	61
4.4.3	Hypersonic flow past a double ellipse	62
4.4.4	Hypersonic flow in a scramjet intake	64
4.4.5	Supersonic flow with moving bodies: Cylinder lift-off	67
4.4.6	Shape optimisation: Minimum drag geometries in hypersonic flow	69
4.5	Summary	71
5	Sharp Interface Immersed Boundary for Viscous Flows	72
5.1	Hybrid Cartesian Immersed Boundary Method	73
5.1.1	Reconstruction for velocities	75
5.1.2	Reconstruction for pressure	76
5.1.3	Reconstruction for temperature	76
5.1.4	Reconstruction for density	77
5.1.5	Calculation of wall pressure, shear stress and heat flux	78
5.2	Numerical investigations	80
5.2.1	Inviscid hypersonic flow past a hemisphere	80
5.2.2	Subsonic flow past NACA0012 airfoil	81
5.2.3	Transonic flow past biplane NACA0012 airfoil	84
5.2.4	Low supersonic flow past a 4% thick bump	85
5.2.5	Supersonic flow past NACA0012 airfoil	87
5.2.6	Hypersonic flow past a flat plate	89
5.2.7	Hypersonic flow past a compression ramp	90
5.2.8	Hypersonic flow past a cylinder	92
5.2.9	Hypersonic flow past a sphere-cone model	95
5.3	Summary	97

6 Revisiting the Sharp Interface Immersed Boundary for Viscous Flows	98
6.1 Resolution and reconstruction errors	99
6.2 Studies with local grid refinement	103
6.3 Selective solution reconstruction	106
6.4 Alternate reconstruction approaches	108
6.5 Dependence on freestream and wall conditions	111
6.6 Discussions and remedial approaches	116
6.7 Summary	119
7 Applications Towards Design and Optimisation	120
7.1 Aerodynamic shape optimisation of nose cone	121
7.2 Design of scramjet inlets	131
7.3 Design of optimal nozzle for supersonic flows	136
7.4 Summary	140
8 Conclusions and Future Scope	142
8.1 Conclusions	142
8.2 Scope of future work	145
Appendix A	147
Publications	149
References	152

LIST OF FIGURES

1.1	(a) Overlapping grid approach (b) Cartesian cut-cell approach	6
1.2	(a) Diffused-interface IB approach (b) sharp-interface IB approach	8
1.3	(a) Interpolation scheme for ghost-cell (b) neighbouring points (NP)	9
2.1	Cell nomenclature	18
2.2	Linear reconstruction for the cell centered scheme	20
3.1	(a) Cell geometry (b) nomenclature for non-orthogonal grid	26
3.2	Schematic for the supersonic vortex flow computational domain	36
3.3	Computational grid adopted (a) uniform (b) stretched (c) triangulated	37
3.4	(a) Numerical dissipation for inviscid isentropic vortex (b) behaviour of numerical dissipation with limiter constant K	39
3.5	Computational grid adopted for flow past ramp	41
3.6	Steady-state convergence for flow past compression ramp at (a) $CFL = 0.1$ (b) $CFL = 0.175$	41
3.7	(a) C_f distribution for flow past compression ramp (b) P_w/q distribution for flow past compression ramp	42
4.1	Classifications of cells in the immersed boundary finite volume (IB-FV) solver	46
4.2	Schematic of reconstruction scheme where subscript j refers to the immersed cell	47
4.3	Computational stencil for inverse-distance weighting (IDW) reconstruction	48
4.4	Computational domain for transonic flow past bump along with boundary condition	52

4.5	Mach contours depicting normal standing shock for different grid (a) 150×50 (b) 225×75 (c) 300×100 (d) 450×150 (Min: 0, $\Delta : 0.117$, Max: 1.52) (Top:- IB-FV solver; Bottom:- FV solver on body fitted mesh)	53
4.6	Coefficient of pressure distribution along the surface of the body from (a) IB-FV solver on non-conformal grid (b) FV solver on conformal grid	53
4.7	(a) Coefficient of pressure distribution along the surface of the body on conformal and non-conformal mesh (b) Numerical entropy generation along immersed cells	54
4.8	Variation of mass defect Δm with grid refinement	56
4.9	Computational domain for supersonic vortex flow	57
4.10	Order of accuracy for IB-FV (non-conformal grid) and FV (conformal grid) using (a) L_2 norm (b) L_∞ norm	58
4.11	Shock wave angle β with grid refinement	59
4.12	(a) Comparison of coefficient of pressure distribution with theoretical correlation and body-fitted FV result (b) Coefficient of pressure dis- tribution using IB-FV solver on two different grid resolution (zoomed view)	60
4.13	Comparison of numerical Schlieren (below) and experimental Schlieren (top) [116] for supersonic flow over cone	60
4.14	Comparison of (a) coefficient of pressure distribution obtained using IB-FV solver with experimental data (b) shock shape obtained using IB-FV solver with theoretical correlation	61
4.15	Comparison of numerical Schlieren (below) and experimental Schlieren (top) [117] for hypersonic flow over sphere	62
4.16	(a) Uniform (b) non-uniform Cartesian grid employed in IB-FV solver for flow over double-ellipse	62
4.17	(a) Coefficient of pressure distribution (b) Mach contours for double ellipse (Min: 0, $\Delta : 0.5$, Max: 8.15)	63
4.18	Entropy distribution on uniform and non-uniform grid	63
4.19	Scramjet geometry	64
4.20	Curvilinear grid used with struts immersed in it (every fourth grid line shown)	65
4.21	Mach contours for scramjet simulations (Min: 0, $\Delta : 0.22$, Max: 5.4) . .	66
4.22	(a) Center-line Mach number variation (b) Pressure coefficient distri- bution along the surface of scramjet struts	66
4.23	Location of body and shock at time $t = 0$ s	67
4.24	Two numerical solutions	67
4.25	Two numerical solutions	67

4.26	Two numerical solutions	69
4.27	Optimal configuration of the axisymmetric forebody	70
5.1	Reconstruction for obtaining ϕ at immersed cells	75
5.2	(a) Comparison of shock shape with Billig correlation [118] (b) comparison of numerical (bottom) and experimental (top) Schlieren	80
5.3	Comparison of normalised pressure coefficient with experimental data [117]	81
5.4	(a) Computational domain (not to scale) (b) Non-uniform initial grid	82
5.5	Three levels of refinement across the NACA0012 airfoil at (a) leading-edge portion (b) trailing-edge region	82
5.6	Surface distribution of (a) pressure coefficient C_p (b) skin-friction C_f (c) C_f along region of separation	83
5.7	(a) Computational domain (not to scale) (b) Non-uniform initial grid	84
5.8	Streamlines for flow past NACA0012 staggered airfoil (a) Jawahar and Kamath [129] (b) Qiu et al. [130] (c) IB-FV	84
5.9	Comparison of surface distribution of (a) pressure coefficient C_p and (b) skin-friction coefficient C_f	85
5.10	(a) 4% thick bump in a channel configuration (b) non-uniform computational grid (c) enlarged portion of the bump with adapted grid	86
5.11	(a) Mach contour (Min: 0, Δ : 0.04, Max: 1.42)	87
5.12	Comparison of skin-friction coefficient C_f along the bump and wall with [131]	87
5.13	(a) Computational domain (not to scale) (b) non-uniform adapted grid	87
5.14	Mach contour (Min: 0.2, Δ : 0.11, Max: 2.18)	88
5.15	Comparison of surface distribution of (a) pressure coefficient C_p and (b) skin-friction coefficient C_f	88
5.16	Distribution along the surface of the wall for (a) wall pressure (b) Stanton number with experimental data of Lillard and Dries [133]	89
5.17	(a) Ramp geometry (b) locally adapted grid (c) pressure contour for flow past compression ramp (Min: 0, Δ : 51.66, Max: 620)	91
5.18	Comparison of (a) pressure coefficient C_p (b) skin-friction coefficient C_f (c) Stanton number St with experimental data [109]	92
5.19	(a) Cylinder geometry (b) pressure contour for flow past cylinder (Min: 0, Δ : 5087, Max: 71220)	93
5.20	Pressure distribution along the cylinder and its comparison with experimental data [134]	93

5.21 (a) Sphere-cone model (b) pressure contour for flow past the sphere-cone model (Min: 0, Δ : 5700, Max: 74930)	95
6.1 (a) Stair-step boundary (b) body conformal grid	100
6.2 Comparison of (a) pressure (b) skin-friction coefficient C_f	101
6.3 Distribution of near wall temperature	102
6.4 (a) Comparison of skin-friction coefficient C_f on adapted grid (b) enlarged view of adapted grid	103
6.5 Distribution of (a) near wall temperature (b) normalised wall heat flux q/q_o	104
6.6 Comparison of skin-friction coefficient C_f along the cylinder on the adapted grid	104
6.7 Comparison of (a) skin-friction coefficient C_f (b) wall heat-flux	106
6.8 Comparison of near wall temperature along the cylinder	107
6.9 Comparison of (a) pressure coefficient C_p (b) skin-friction coefficient C_f , along the cylinder	109
6.10 Comparison of skin-friction C_f along the cylinder for freestream Mach number (a) 2.0 (b) 3.5 (c) 5.0	111
6.11 Comparison of near wall temperature distribution for freestream Mach number (a) 2.0 (b) 3.5 (c) 5.0	112
6.12 Comparison of skin-friction C_f along the cylinder for freestream Reynolds number (a) 500 (b) 5000	113
6.13 Comparison of near wall temperature distribution for freestream Reynolds number (a) 500 (b) 5000	113
6.14 Comparison of (a) pressure (b) skin-friction coefficient C_f , along the cylinder	114
6.15 Distribution of skin temperature	114
7.1 Flowchart describing the proposed multi-fidelity optimisation framework	124
7.2 Optimal bodies at different l/d	124
7.3 Semi-vertex angle θ_{LE} of optimal bodies for different l/d	126
7.4 Convergence acceleration for maximum C_d body at $l/d=2$	127
7.5 Convergence acceleration for minimum β body at $l/d=6$	127
7.6 Min. C_d body at $l/d = 2$	127
7.7 Max. β body at $l/d = 6$	127
7.8 Cross-objective performance for different l/d	128
7.9 Heat flux distribution along the length of the maximum β body at $l/d=6$	129
7.10 Heat flux distribution for optimal bodies at $l/d=6$	129

7.11 Scramjet inlet schematic representation where β and θ represent the shock and flow-deflection angle respectively	132
7.12 Low-fidelity flowchart	132
7.13 Total pressure recovery obtained from LF framework	134
7.14 Flow non-uniformity in the isolator	134
7.15 Mach contour for the scramjet intake configuration (a) $n=3$, $m=1$ (bottom) (b) $n=3$, $m=2$ (top) (Min: 0, Δ : 0.888, Max: 8.0)	135
7.16 Variable area nozzle	137
7.17 Schematic of the nozzle configuration	138
7.18 Convergence history	138
7.19 Optimal nozzle configuration obtained from LFF	139
7.20 Mach contour obtained from IB-FV flow solver for the optimal nozzle configuration (Min: 0.05, Δ :0.0493, Max: 3.45)	139
7.21 Comparison of Mach number obtained from both flow solvers	140

LIST OF TABLES

3.1	The algorithm for MGG reconstruction	33
3.2	Numerical dissipation produced in terms of ΔS	38
3.3	Comparison of computational time to achieve steady-state solution using SGG and MGG reconstructions for hypersonic flow past compression ramp. The blanks indicate that the solution process did not converge .	41
4.1	Mass defect Δm on different grids	55
4.2	Position of centre of mass of cylinder (in m) at time $t = 0.30085\text{s}$. .	69
5.1	Comparative study showing point of separation and force coefficients .	82
5.2	Comparison of stagnation point heat flux q_o	94
5.3	Comparison of total force on the body	96
5.4	Comparison of stagnation point heat flux q_o	96
6.1	Comparison of stagnation point heat flux q_o	102
6.2	Comparison of stagnation point heat flux q_o in adapted grid	103
6.3	Comparison of stagnation point heat flux q_o on the adapted grid . . .	110
7.1	Flow conditions	125
7.2	Total computational time in hours for MFF and HFF frameworks. The number of optimisation cycles is indicated in parentheses	127
7.3	Stagnation point heat flux and heat load at $l/d = 2$ and 6	130
7.4	Comparison of LF and HF frameworks at $M_\infty=8$ for the $n=3$ and $m=2$ configuration	135
7.5	Low-fidelity flow solver	137
A	The flux formulas for the vanLeer and AUSM scheme are given in the Table below	147

CHAPTER 1

INTRODUCTION

“Heavier-than-air flying machines are impossible”

- Lord Kelvin, 1895, *On sustainable flight*

“Houston, Tranquility Base here. The Eagle has landed”

- Neil Armstrong, 1969, *On moon landing*

High speed flows has been a subject matter of great interest to various groups of researchers as well as commoners. The unwavering desire to mimic bird’s flight has propelled businessman turned inventors the Wright brothers, into discovering the “flying-machine” in 1903, which since then has seen tremendous alterations by scientist, in arriving at today’s interplanetary flight vehicles [1]. The remarkable leap of such structural design in the last century has foreseen many hurdles which were primarily caused by the highly complex flow features, one of which include the infamous crash of Ralph Virden P-38 aircraft in 1941. This incident was attributed to the “*compressibility effects*” which was later addressed by NACA Langley Memorial Laboratory and Ames Aeronautical Laboratory. What followed this unfortunate incident was the re-embarkment of humankind into a new flow regime of supersonic flow where the so-called “*Mach barrier*” was crossed by Chuck Yeager in 1947 in his Bell X-1. This was soon followed by the first hypersonic flight by Robert White at Mach number of 5.3 in his X-15.

This remarkable feat was made possible by countless hours of research carried out by scientist to generate highly precise experimental data and empirical correlations.

The enormous cost associated with experimental procedures meant that numerical methods like Computational Fluid Dynamics or CFD gained more prominence. While CFD finds its roots in some of the earliest work by Richardson [2], it was not until the late 1950s when CFD slowly started making its presence felt largely by the work of the Los Alamos National Lab, T3 group who were probably the first to simulate Navier-Stokes equations as well. With the advent of robust numerical algorithms and faster means of computation since late 1980s, CFD has established itself as a prominent means of computing flow features with greater accuracy at a situation where experimental procedures are not feasible. This is indeed the case with supersonic and hypersonic flow regimes which are encountered in a vast range of aeronautical and aerospace applications that include cruise fighter aircraft, cruise missiles, and launch vehicles. Numerical simulations of high speed flows have gained prominence over the last two decades owing to their ability to provide valuable inputs for the preliminary design of hypersonic vehicles.

The need for accurate simulations of fluid flow and heat transfer problems involving complex geometries requires a robust flow solver that is also fast and accurate. A key requirement to obtain accurate solutions in such problems, particularly in the high speed regime is the need to generate good quality meshes. The generation of block-structured grid over complex configurations is however quite cumbersome and requires significant user expertise. The use of unstructured meshes offers a possible solution since it alleviates the cumbersome task of generating block structured grids but requires the use of a discretisation approach for conservation laws that can work with unstructured data. Cell-centered (or collocated) FV approaches [3] are also amenable to unstructured data, have been employed in the compressible CFD community for long [4–6], but their accuracy depends upon discretisation of the conservation laws that are impacted by the accuracy of the gradient estimation. The need for gradient computation in FV solvers is two-fold. Firstly, the gradients are necessary for the implementation of high-resolution convective schemes which are nominally second-order accurate. Secondly, the viscous fluxes are obviously dependent on the velocity derivatives which necessitate their estimation. The gradients also play a role in slope limiting (employed routinely in compressible solvers) and are critical in error estimation for adaptive refinement strategies [7]. The requirements of a robust flow solver and the need of gradients in ancillary computations indicate that the methodology employed for gradient estimation is vital for successful numerical simulations of complex flows.

While unstructured finite volume solvers help to compute accurate numerical

solutions in compressible inviscid and viscous flows, a major bottleneck when using computational frameworks in the primary design cycle is that the grid generation process is still a time-consuming affair. In particular, the generation of hybrid conformal meshes in viscous simulations over three dimensional configurations requires significant user expertise and a considerable part of the solution process is essentially spent on the grid generation. Furthermore, analysing the effects of minor alterations to the geometric configuration(s) on the aerothermodynamic performance would also constitute a huge computational overhead primarily due to the need to regenerate these conformal meshes. It is therefore desirable to evolve a numerical framework that may be automated and yet remain accurate. This has led to the emergence of non-traditional approaches which include mesh-free methods [8] and Cartesian grid-based approaches [9, 10]. The latter class of methods has gained popularity over the past decade owing to the ease of Cartesian grid generation (uniform and non-uniform) and its automation thereby reducing its dependency on the user to generate good quality meshes.

The true utility of any numerical framework for compressible flows lies in its applicability to design aspects. Cartesian grid-based approaches do allow for an automated design cycle but it is also important to note that many practical designs tend to optimise the geometry for one or more objective functions. For instance, missile nose cone could be designed to minimise total drag so as to increase its total range, while re-entry aeroshells could be designed to maximise the ‘drag area’, to enable a quick deceleration while it enters into the environment. It is therefore imperative that the continuum CFD framework be combined with optimisation strategies to devise multi-fidelity frameworks that can assist in the quick design of optimal shapes encountered in the hypersonic flow regime. The total cost for such a framework, therefore, could be determined by the numerical approach inherent to it and a faster optimal shape may be arrived at by combining the high-fidelity frameworks with their low-fidelity counterparts. Such a low-fidelity framework typically do not employ CFD based solvers but rather incorporate one-dimensional gas dynamics relations or algebraic approaches to compute the cost functions of interest.

The present thesis is devoted to the development of a Cartesian grid-based numerical framework and its application to design and optimisation problems in compressible flows. To achieve this overall objective we begin by carrying out an extensive literature survey of previous numerical efforts in developing unstructured and Cartesian grid-based CFD frameworks and their use in design and optimisation.

1.1 Gradient reconstruction strategy

Gradient calculation strategies on unstructured collocated meshes may be broadly classified as least-squares based approaches and Green–Gauss based approaches [7]. The least-squares based approaches obtain the derivatives by minimising the sum of squares of errors between the true and estimated values in a suitably defined neighbourhood. These approaches involve the solution to a system of equations in each control volume depending on the order of derivatives needed in the calculations. The gradients on three-dimensional meshes necessitate the solution of a 3×3 system of equations in each cell and the neighbourhood needs to be defined with care, particularly on non-uniform and unstructured meshes to ensure non-singular matrices in the least-squares reconstruction. Diskin and Thomas [11] have extensively evaluated the least-squares approach on unstructured meshes for different grid topologies, with and without weights to assess the accuracy of estimated gradients and their impact on convective flux discretisation. Their work focuses on high aspect ratio meshes with curvature typical of viscous simulations and unweighted least-squares estimates are found to be erroneous on highly stretched meshes. Mavriplis [12] carried out investigations along similar lines and reported that both the unweighted and weighted least-squares constructions fail to provide accurate gradients on highly stretched curved meshes. Both these works, however, point out that poor gradient reconstruction accuracy must not be equated with poor solution accuracy and that low discretisation errors may be observed in regions where the mesh is aligned with the flow. Studies with compressible flow solvers in [12], however, indicate that large discretisation errors can be incurred with least-squares based approaches on curved meshes in highly viscous flows with and without the use of entropy fix. Shima and co-workers [13] also reached similar conclusions on the inaccuracy of the weighted least-squares approach on thin meshes and Katz and Sankaran [14] reported on the lack of robustness of this approach in their studies on prismatic high-aspect ratio meshes.

Green–Gauss based approaches, which are derived using a variant of the Gauss divergence theorem, typically involve a smaller compact stencil and give closed-form expressions for the solution gradients. These class of methods requires estimates of the solution at the face and this necessitates the use of cell-to-face interpolation strategies. The various interpolation strategies lead to different variants of Green–Gauss reconstruction and the accuracy of the estimated gradients is strongly dependent on the accuracy of the interpolation in these methods. Sozer et al. [15] have shown that Green–Gauss based approaches with volume (and inverse volume)-weighted interpolation leads to inconsistent gradients on arbitrary polygonal meshes. The only known

approaches of this class which give consistent gradients are those using a cell-to-node interpolation based on the linearity-preserving pseudo-Laplacian strategy [16, 17], the nodal projection scheme proposed by Katz and Sankaran [14], the auxiliary control volume approach [18] and the iterative GG reconstruction suggested by Karimian and Straatman [19]. While the first two approaches require the solution to a system of equations to obtain solution values at nodes which are then averaged to get the faces values, the approach in [19] uses a linear reconstruction involving the gradients themselves to obtain the face values necessitating an iterative approach. The auxiliary control volume approach constructs a virtual volume (for every cell) whose edges are the lines joining the centroids of its face-sharing neighbours. The practical implementation of these consistent reconstruction approaches is however not without issues. For instance, the weights computed for nodal interpolation in the linearity-preserving pseudo-Laplacian strategy have to be “clipped” for stability. This could, in turn, lead to inaccuracies in gradient calculations [11] and adversely affect the steady-state convergence for viscous flows. Similarly, while the gradients are calculated to first-order in the auxiliary control volume approach, it necessitates the generation of an auxiliary volume for each cell in the domain. There are difficulties in iterative convergence reported in the literature with the iterative GG reconstruction [20] and the nodal projection method, while promising, has not been applied to problems of engineering interest and is at a relatively nascent stage.

There are no definitive answers on which class of approaches is the “best” for gradient estimation and it is only possible to compare the advantages and limitations of various approaches based on the performance for canonical problems. In fact, while the least-squares approaches have been found to be inaccurate as compared to Green–Gauss based methods in [12], the findings of Correa [21] contradict these observations. This has led to attempts at devising alternate approaches for gradient estimation including strategies that harness the merits of least-squares and Green–Gauss based approaches. Shima and co-workers have proposed a hybrid approach referred to as GLSQ which blends the Green–Gauss and least-squares reconstruction using a geometry-dependent blending function [13]. A curvilinear gradient method, which maps the local gradient stencil of a cell to a uniform Cartesian mesh was discussed in [15]. Among variants of the least-squares approach, a modified least squares method was proposed by Mahesh et al. [22] for pressure gradients in the context of kinetic energy preserving schemes and an improved variant for skewed meshes was suggested by Ham and Iaccarino [23]. An alternate approach for gradient calculation applied to pressure derivatives in incompressible flows on Voronoi grids that do not belong to either Green–Gauss or least-squares based approaches was employed by Vascon-

cellos and Maliska [24]. A recent study by Syrakos and co-workers [20] presents a good overview of existing gradient reconstruction methods with a critical analysis of some popular reconstruction schemes with an equal emphasis on least-squares and Green–Gauss based approaches.

1.2 Cartesian grid based methods

The numerical simulations of flow past complex geometries particularly those in motion pose a stiff challenge to conventional approaches in CFD. While Arbitrary Lagrangian Eulerian (ALE) can handle moving body problems, it still requires the grid to conform to the shape of the body thereby, limiting its applicability to rigid bodies with small deformations only. Large deformations would, therefore, require re-meshing which again adds to the total computational cost and also requires interpolation between old and new meshes. The use of “overlapping grid” or “chimera” approaches [25] provides a possible solution but is also fraught with the additional complexity of interpolation whose accuracy in turn effects the accuracy of the computed numerical solution (Figure 1.1(a)). The use of non-conformal Cartesian grid-based methods, however, provides a simple means of handling moving body problems without mesh regeneration and can be broadly classified into two categories: Cartesian cut-cell and Immersed Boundary approach.

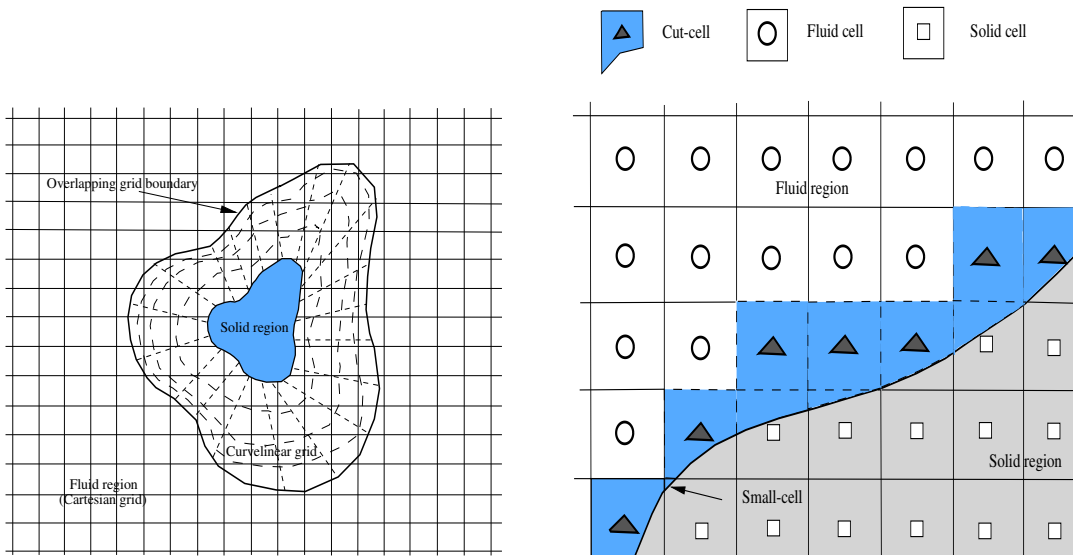


Figure 1.1: (a) Overlapping grid approach (b) Cartesian cut-cell approach

Cartesian cut-cell approach (Figure 1.1(b)) represents the body boundary as a sharp-interface by locally altering the cell-topology according to the intersection of the Cartesian grid with the Lagrangian body points. Several interpolation strategies can be implemented at those cut-cells near the body boundary to obtain solutions such

as a two-dimensional polynomial interpolation function [9] or bi-linear polynomial fit [26]. The complexity in implementing these strategies arises from the fact that the shape of the irregular cell depends upon the nature of the intersection. In certain situations, the irregular cell can be several order smaller in magnitude than regular cells and gives rise to “small-cell” problem (as highlighted in Figure 1.1(b)) and it results in additional stiffness related issues. Hence, those cells often require special treatment as suggested in literature [9, 27–30]. This method has since then been applied to complex three dimensional [31] and moving body problems [32]. It must also be pointed out that there have also been efforts to develop frameworks that employ “nearly” Cartesian meshes which are discretely conservative as well. Mondal and co-workers proposed the “grid-stitching” technique [33] where the cells near the boundary are locally modified so as to conform to the surface. The hybrid grid methodology proposed by Ashok et al. [34] is similar but “stitches” the Cartesian grid to a prismatic layer that is conforming to the geometry.

The Cartesian grid-based approach which has gained greater visibility among researchers is the immersed boundary (IB) method. IB methods were first introduced in the context of simulating flows in human hearts by Peskin [35] and have been employed over the last decade for a wide range of problems such as phonation[36], aquatic locomotion[37], cardiovascular dynamics[38], human walking [39] and multi-phase flows [40]. There are several variants of this method which involve non-conformal background grids into which the solid is ‘immersed’. The challenge in IB methods is, however, to “communicate” the presence of the bodies to the background mesh in an accurate and cost-efficient manner. This problem of enforcing the boundary conditions can be tackled in different ways and have led to the development of several IB algorithms in the literature. The IB methods can further be classified as continuous and discrete forcing methods or may be categorised as diffuse interface or sharp interface based methods.

Diffuse interface immersed boundary approach typically solves a “unified” form of the governing equations everywhere in the domain (including the solid) that reduce to the conservation laws outside of the solid while recovering the Dirichlet boundary conditions inside it (Figure 1.2(a)). One of the diffuse interface IB approaches that have gained prominence is the work by Pan [41]. The method has since then been applied to problems involving heat transfer [42] and multi-fluid flows [43]. The notable contributions in the use of diffuse interface IB methods are the Brinkman penalisation approaches [44–46]. While the implementation of the diffuse interface immersed boundary methods is relatively easy, it does suffer from a few important limitations.

For instance, while handling the Dirichlet boundary condition is quite straightforward, the implementation of Neumann and Robin boundary conditions in this class of IB method is certainly not easy. The diffused interface IB methods to high Reynolds number flows remains a challenge because the body boundary is smeared over few cell width and thin boundary layer may not be easily resolved. More importantly, the use of diffuse interface IB methods for compressible flows, which is the focal point of this thesis, is not widespread and to the best of our knowledge, the only notable contribution in use of diffuse interface IB methods for compressible flows are the Brinkman penalisation approach of Liu and Vasilyev [47] and Boiron et al. [48].

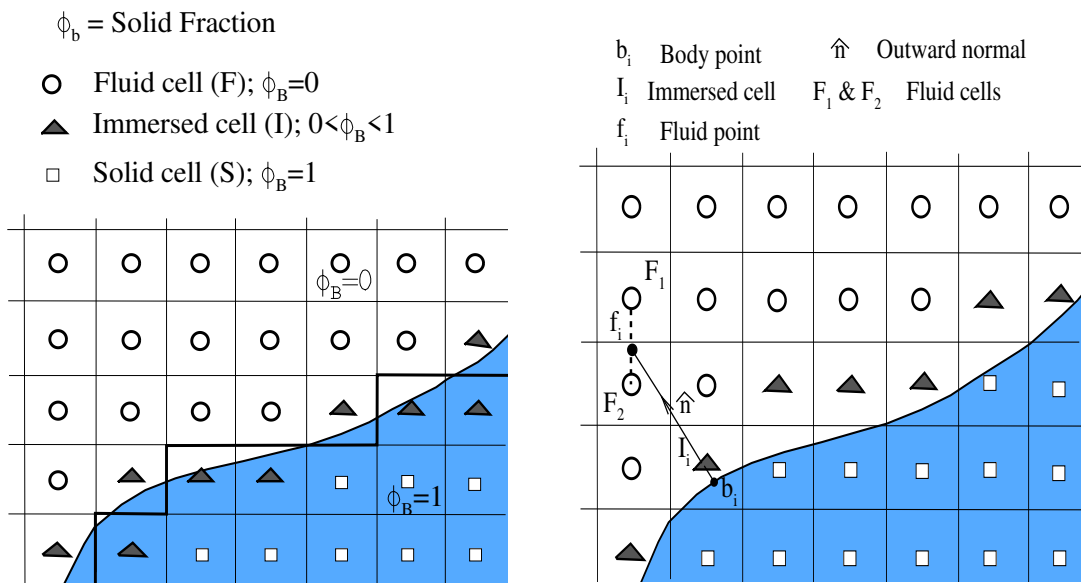


Figure 1.2: (a) Diffused-interface IB approach (b) sharp-interface IB approach

The difficulties associated with the diffuse interface immersed boundary method particularly in compressible flows may be overcome while devising sharp interface immersed boundary approaches. These approaches retain the sharp representation of the boundary by enforcing the boundary conditions accurately on the geometry interface. Immersed boundary approaches that belong to this category which have gained prominence over the last few years include the “ghost cell” immersed boundary method. This method was first proposed by Majumdar et al. [49] where they showed that different interpolation strategies can be used to evaluate the value of the flow properties at ‘interior point’ (IP) (Figure 1.3 (a)). Stiffness related difficulties arising from IP being too close to the boundary point can be overcome by using an “inverse-distance weighting” based approach, as shown by Gao et al. [50] and Chaudhuri et al. [51] (Figure 1.3 (b)). Other notable variants include the ghost-cell immersed boundary approach proposed in [52–54], where they have used this approach to study flow

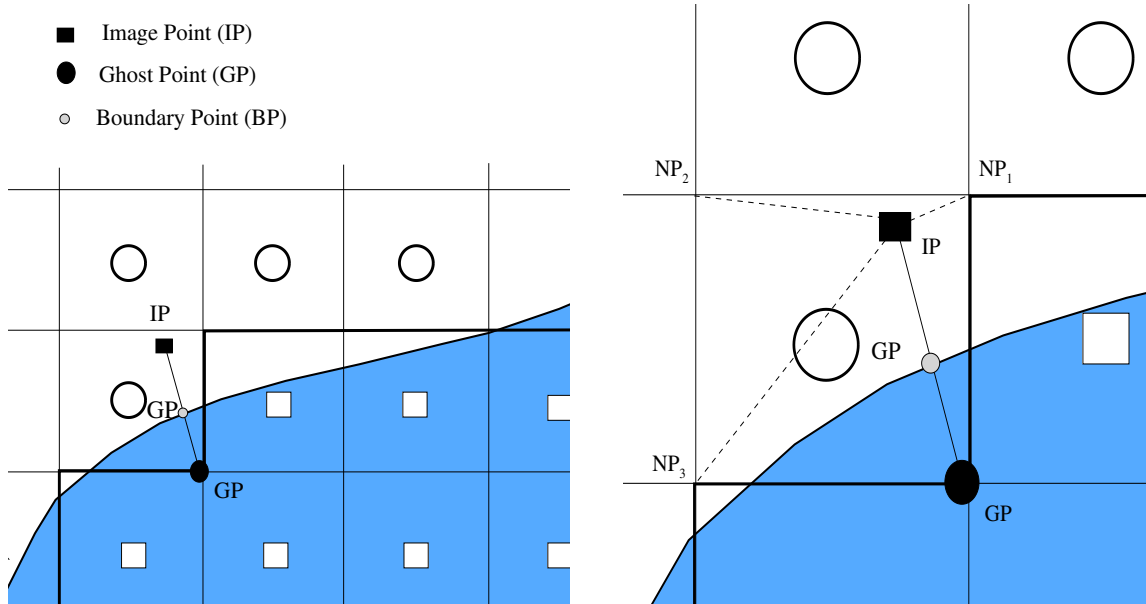


Figure 1.3: (a) Interpolation scheme for ghost-cell (b) neighbouring points (NP)

past complex bodies such as bluegill sunfish, dragonfly, geophysical flow over bump etc.

The other class of sharp interface methods is based on the philosophy of Modh. Yusuf [55] that was later adapted by Fadlun et al. [56] that computes the solution in the vicinity of the body by using the boundary condition at the body point and the solution obtained from the governing equation in the fluid region. This completely eliminates the need for any ghost point and the interpolation is locally performed using a one-dimensional stencil that comprises of the fluid point ‘f’ in Figure 1.2 (b). This method is referred to as Hybrid Cartesian Immersed Boundary approach (HCIB) and its applicability to a wide range of problems have been explored in the literature. Gilmanov et al. [57] employed the idea of one-dimensional local reconstruction to solve incompressible laminar flows over three-dimensional geometries. A similar technique was then applied by Balaras [58] who successfully performed Large Eddy Simulations (LES) on turbulent flows for a channel with wavy walls. Verziocco et al. [59] also demonstrated the use of a similar methodology for turbulent flows in internal combustion engines and three-dimensional turbulent simulations at sufficiently high Reynolds number were performed in [56, 60]. Sharp interface immersed boundary methods have also been used to simulate flows containing complex bodies such as the motion of an insect wing, fish-like body, planktonic copepod etc. [37], stationary and a moving human body [39], a fish and a dragonfly [53]. A useful review of IB related works towards fluid-structure interaction can be found in [61].

One can easily see from the survey of the literature that the vast majority of inves-

tigations discuss flow problems in the incompressible regime with emphasis on turbulent flows [62], heat transfer [63] and multi-phase flows [64] where accurate numerical solutions have been computed despite the grids not conforming to the geometry. In comparison, there is relatively less number of works employing the IB methodology for tackling compressible fluid flows. While our survey of literature on the use of IB techniques for the solution of compressible flow problems detailed below is by no means exhaustive, we attempt to highlight some of the salient efforts in the recent past in this field. Among the earliest works that have used the IB methodology for solving compressible viscous flows are the direct forcing approach of De Palma et al. [65] and the ghost cell immersed boundary approach (GCIB) proposed by Ghias and co-workers [66]. While these approaches differ in the manner by which the boundary condition on the immersed geometry is enforced in the solution procedure, they both belong to the category of sharp-interface IB methods. Sharp interface IB approaches have been largely favoured in the compressible CFD community and there have been recent studies that have employed variants of this technique for Euler flows. Zhang and Zhou [67] devised a Hybrid Cartesian Immersed Boundary method based flow-solver for three-dimensional Euler flows while a Ghost-Cell Immersed Boundary method with bi/tri-linear interpolation was proposed in [68] for two and three-dimensional compressible inviscid flows. The importance of adaptive meshing in the context of Cartesian IB methods for compressible flows have also been a subject of study by researchers. De Tullio and co-workers proposed a robust and versatile IB approach with local grid refinement for moderate Reynolds number flows [69]. They showed that their approach could accurately compute flows employing a semi-structured Cartesian mesh in subsonic, transonic and supersonic regimes. Arslanbekov et al. [70] have carried out detailed studies on the role of adaptive Cartesian meshes for high-speed compressible flows and report that local grid refinement near the surface of the body can offer great improvement in computing skin friction and surface heat fluxes. They recommend that the cell Reynolds number (defined based on the **local conditions, speed of sound** and local grid resolution) be less than 5 for accurate estimation of the skin friction and wall shear stress distributions.

A deeper look at numerical studies that have used sharp interface IB methods for compressible viscous flows shows that they have been largely employed for problems in the high subsonic/low supersonic flow regimes [65, 66, 69, 71]. The use of IB methods for high Mach number viscous flows is more challenging and therefore less prevalent with the numerical studies in [70, 72, 73] being some of the noteworthy efforts in this direction. Surprisingly, there has however been no emphasis on the ability of these methods to accurately compute skin friction and heat transfer estimates. To the best

of our knowledge, the only efforts to understand the ability of Cartesian IB methods for problems involving hypersonic viscous flows are the works of Sekhar and Ruffin [74] and Arslanbekov et al.[70]. While these studies do address the issue of skin friction and heat flux predictions, they are mostly restricted to laminar flows at low and moderate Reynolds numbers.

1.3 Multi-fidelity framework for optimisation/design problems

The Practical design of hypersonic vehicles is a multi-disciplinary effort that requires a trade-off between several conflicting objectives and constraints to arrive at the final prototype. While the current application of hypersonic vehicles are targeted at space missions and defense applications, there research interests have also been directed towards design of futuristic transport vehicles [75, 76]. The designer is therefore faced with a complex multi-disciplinary optimisation problem that involves a large number of decision variables. Deriving the optimal shapes of geometries that optimise certain metrics of aerodynamic/aero-thermodynamic performance is a challenging sub-problem in the entire design cycle. The earliest attempts at obtaining optimal shapes involved simple geometries and analytical techniques involving simple theories [77–79]. However, the limitations of the underlying theories and geometric complexities paved the way for numerical techniques to solve optimisation problems. In particular, the advent of computational fluid dynamics (CFD) codes and evolutionary techniques such as genetic algorithms have led to the development of generic and accurate optimisation frameworks.

The problem of finding the optimal shape in hypersonic flows is relevant in the design of aeroshells, missiles, waveriders and next-generation launch vehicles. Several researchers have tackled this problem under varied objectives and constraints by implementing efficient shape optimisation strategies in the recent past. Seager and Agarwal [80] coupled turbulent computations of hypersonic flows with a multi-objective genetic algorithm (MOGA) to determine blunt shapes with low drag and heat transfer. Their approach of multi-objective optimisation led to a Pareto optimal front, from which the designer could choose one of the several optimal shapes depending on the relative importance of either cost function. Deepak and co-workers [81] employed a single-point minimisation of the total drag using viscous simulations and genetic algorithms (GA) for an experimental hypersonic vehicle. Their work, which also investigated off-design performance of the optimal geometry, highlighted the importance of the avoiding slope

discontinuities at the nose region.

Multi-objective optimisation has also been performed for re-entry aeroshells by Theisinger and Braun [82], using both single and multi-objective optimisation where parameters such as volumetric efficiency, static stability and convective heating rates were addressed in addition to drag. Studies on optimal blunt leading edges with least peak heat flux were carried out by Cui and Hu, [83] who employed the mini-max optimisation model along with viscous simulations. Efforts have been made to determine optimal configurations for reacting flows and in rarefied environments as well. While Neville and Candler [84] investigated the maximum drag–minimum heat transfer aeroshell shape in a nine-species environment, Huang et al. [85] employed modified Burnett equations to obtain minimum drag–minimum heat transfer shapes in high Knudsen number flows with both research groups employing a combination of genetic algorithms and robust viscous, compressible flow solvers. Eyi and Yumusak [86] also considered the problem of minimum drag blunt geometry in hypersonic flow with low aerodynamic heating with finite-rate chemistry. Unlike other efforts in this direction, they employed a gradient-based approach using adjoint method for sensitivity calculations and carried out a single objective constrained optimisation accounting for heat transfer through an explicit geometric constraint. Other notable efforts in hypersonic shape optimisation include hypersonic lifting bodies using correlation-based transition models and MOGA [87] and the surrogate-assisted multi-objective design optimisation of inlet and combustor in scramjet engines using an inviscid reacting flow solver [88].

A critical requirement of a good shape optimisation framework, particularly in the early phases of vehicle design, is to provide the designer with a knowledge on how various factors would influence the optimal geometry and their performance. It is also likely that the designer wishes to perform several studies by incorporating one or more constraints. In such cases, the use of CFD and GA driven frameworks become computationally expensive requiring several hours which can hamper the design cycle making the process practically infeasible [89]. While parallel computations to reduce design times appear to be an obvious solution, it is not always practically feasible and alternative approaches need to be sought. Surrogate-based optimisation strategies adopted in [81, 88] can reduce computational cost and time as compared to the non-surrogate counterparts, but still incurs considerable cost in the early phases of design. A useful alternative to the very accurate but expensive high-fidelity frameworks is the use of fast and quick approaches with less accuracy which may be collectively referred to as low-fidelity frameworks. While some researchers [90] actually employ

a cheaper variant of the high-fidelity framework, by using an inviscid solver instead of a viscous one and reducing convergence levels, others have made use of suitable reduced model(s) to determine the cost function(s) and possibly simpler approaches for optimisation. Newtonian impact theory was employed to calculate wave drag in the three-dimensional aeroshell optimisation studies in [82] and also by Sahai et al. [91] to study the role of fineness ratio on the shape of axisymmetric bodies in hypersonic flows. However, while the latter study used a gradient-based optimisation approach, the work of Theisinger and Braun [82] employed NSGA-II to handle multiple objectives. More recently, Hinman and co-workers [92] have considered aero-thermal optimisation of two-dimensional leading edges using both reduced models and compressible Navier-Stokes solvers.

In this context, it is desirable to construct a hybrid of high and low fidelity frameworks for aerodynamic, aero-thermal and aero-thermodynamic shape optimisation. Such a multi-fidelity framework is in effect an “optimal” combination that provides accurate solutions at reasonable computing cost and time. The key idea is to employ simple, physics-driven reduced models in conjunction with inexpensive and fast gradient-based optimisation approaches to arrive at an intermediate optimal configurations starting from a baseline geometry, which is then refined further using compressible flow solvers in conjunction with a host of optimisation strategies. Similar low-fidelity framework can also be employed for generating preliminary design configurations.

1.4 Objectives of the thesis

In the light of extensive literature survey that has been carried out in the previous section, the overall objective of the thesis is the development of a simple, robust and efficient immersed boundary finite volume (IB-FV) framework for compressible flows its application towards design and optimisation. The specific aims of the thesis are elaborated below.

1. **Development of a novel gradient reconstruction:** We discuss the development of a new cell-centered gradient reconstruction scheme on arbitrary polygonal meshes. The utility of this scheme which is referred to as Modified Green Gauss (MGG) reconstruction, is studied for test problems involving inviscid and viscous compressible flows.
2. **Sharp interface immersed boundary finite volume framework for Euler flows:** We devise a sharp-interface based immersed boundary finite volume

(IB-FV) solver employing the Inverse Distance Weighting (IDW) based reconstruction. Efficacy of this approach for high speed flows with stationary and moving bodies are investigated. The important issue of discrete conservation and the role of solution reconstruction on the accuracy are also discussed.

3. **Development of a hybrid Cartesian immersed boundary finite volume solver for viscous compressible flows:** Sharp interface immersed boundary solver that employs one-dimensional local reconstruction has been developed for compressible flows. The solver is validated using canonical problems in laminar high-speed problems with specific emphasis towards the accurate estimation of wall heat-flux as well as skin-friction coefficient. Studies are performed for a large range of Mach number and Reynolds number flows to gain insight into the advantages and limitations of the approach.
4. **Application to design and optimisation:** The finite volume and the immersed boundary finite volume frameworks are combined with physics driven reduced models and fast gradient based optimisation approaches to evolve multi-fidelity frameworks to enable design and optimisation in high-speed flows. Three different problems involving axisymmetric nose cone, optimal supersonic nozzle and mixed compression intakes are studied to highlight the advantage of the IB-FV solver and the multi-fidelity approach.

1.5 Outline of the thesis

The remainder of the thesis is organised as follows. Chapter 2 provides a brief overview of the governing equations for compressible flows and also highlights the finite volume discretisation in an unstructured framework. Chapter 3 details the implementation of an alternative gradient reconstruction strategy and its assessment for compressible flows. This is followed by Chapter 4 wherein we describe the implementation and validation of a sharp interface immersed boundary finite volume framework for inviscid compressible flows. The immersed boundary philosophy has been extended employing a one dimensional reconstruction approach for **high-speed** viscous flows in Chapter 5, which also discusses a large number of canonical test problems with specific emphasis on accurate estimation of heat flux and skin-friction. Chapter 6 details the set of diagnostic approaches to probe the inaccuracies associated with the sharp interface immersed boundary finite volume flow solver for hypersonic laminar flow computations. The finite volume/ immersed boundary-finite volume framework has then been applied to design and optimisation problems in Chapter 7. Lastly, Chapter 8 discusses the salient contributions of the thesis and directions for future research.

CHAPTER 2

GOVERNING EQUATIONS AND MATHEMATICAL PRELIMINARIES

“Observing and understanding are two different things”

- Mary E. Pearson, *The miles between*

We give a brief overview of the governing conservation laws for compressible inviscid and viscous flows. The finite volume discretisation and the development of the cell-centered compressible flow solver in an unstructured finite volume framework are described. Implementation of the boundary conditions and the spatial and temporal discretisation are also discussed.

2.1 Navier-Stokes equations

Governing conservation laws for the compressible viscous flows are the Navier Stokes equations. These equations may be cast in a conservative form in two-dimensions which reads,

$$\frac{\partial \mathbf{U}}{\partial t} + \frac{\partial \mathbf{F_I}}{\partial x} + \frac{\partial \mathbf{G_I}}{\partial y} + \frac{\partial \mathbf{F_V}}{\partial x} + \frac{\partial \mathbf{G_V}}{\partial y} + \alpha(\mathbf{S_I} - \mathbf{S_V}) = 0 \quad (2.1)$$

where,

$$\mathbf{U} = \begin{bmatrix} \rho \\ \rho u \\ \rho v \\ \rho E \end{bmatrix}; \quad \mathbf{F_I} = \begin{bmatrix} \rho u \\ \rho u^2 + p \\ \rho uv \\ \rho u \left(E + \frac{p}{\rho} \right) \end{bmatrix}; \quad \mathbf{G_I} = \begin{bmatrix} \rho v \\ \rho uv \\ \rho v^2 + p \\ \rho v \left(E + \frac{p}{\rho} \right) \end{bmatrix}$$

$$\mathbf{F_V} = \begin{bmatrix} 0 \\ \tau_{xx} \\ \tau_{xy} \\ u\tau_{xx} + v\tau_{xy} - q_x \end{bmatrix}; \quad \mathbf{G_V} = \begin{bmatrix} 0 \\ \tau_{xy} \\ \tau_{yy} \\ u\tau_{xy} + v\tau_{yy} - q_y \end{bmatrix}$$

the vectors $\mathbf{S_I}$ and $\mathbf{S_V}$ are the inviscid and viscous source terms respectively and are relevant only for axisymmetric flows. These may be expressed as,

$$\mathbf{S_I} = \frac{1}{y} \begin{bmatrix} \rho v \\ \rho uv \\ \rho v^2 \\ \rho v \left(E + \frac{p}{\rho} \right) \end{bmatrix}$$

$$\mathbf{S_V} = \frac{1}{y} \begin{bmatrix} 0 \\ \tau_{xy} - \frac{2}{3}y \frac{\partial}{\partial x}(\mu v/y) \\ \tau_{yy} - \tau_{\theta\theta} - \frac{2v}{3y}\mu - \frac{2}{3}y \frac{\partial}{\partial y}(\mu v/y) \\ u\tau_{xy} + v\tau_{yy} - q_y - \frac{2\mu v^2}{3y} - \frac{2y}{3} \frac{\partial}{\partial y}(\mu v^2/y) - \frac{2y}{3} \frac{\partial}{\partial x}(\mu uv/y) \end{bmatrix}$$

where,

$$q_x = -k \frac{\partial T}{\partial x}; \quad q_y = -k \frac{\partial T}{\partial y} \quad (2.2)$$

$$\tau_{xx} = \mu \left(\frac{4}{3} \frac{\partial u}{\partial x} - \frac{2}{3} \frac{\partial v}{\partial y} \right); \quad \tau_{yy} = \mu \left(\frac{4}{3} \frac{\partial v}{\partial y} - \frac{2}{3} \frac{\partial u}{\partial x} \right); \quad \tau_{xy} = \mu \left(\frac{\partial u}{\partial y} + \frac{\partial v}{\partial x} \right) \quad (2.3)$$

$$\tau_{\theta\theta} = \mu \left(-\frac{2}{3} \left(\frac{\partial u}{\partial x} + \frac{\partial v}{\partial y} \right) + \frac{4v}{3y} \right)$$

We set $\alpha=1$ for axisymmetric simulations while for planar two-dimensional studies $\alpha=0$. In the above equations, \mathbf{U} represents the vector of conserved variables (mass, momentum and energy) and $\mathbf{F_I}$ and $\mathbf{G_I}$ denote the inviscid fluxes while $\mathbf{F_V}$ and $\mathbf{G_V}$

represent the viscous fluxes. The terms q_x and q_y are components of heat flux whereas τ_{xx} , τ_{yy} and τ_{xy} which depend on the velocity gradients are the components of the symmetric viscous stress tensor. Symbol k refers to thermal conductivity of the fluid and μ refer to the dynamic viscosity of the fluid and is evaluated using Sutherland's equation as,

$$\mu = \mu_{ref} \left(\frac{T}{T_{ref}} \right)^{3/2} \left(\frac{T_{ref} + S}{T + S} \right) \quad (2.4)$$

where, T_{ref} and μ_{ref} refer to the reference temperature and dynamic viscosity and are equal to 273.15 K and 17.17×10^{-6} Ns/m². The constant S is the Sutherland's constant for air and is taken as $S=110.56$. The system of equations is closed by taking into account the equation of state. We assume the fluid behaves like a perfect gas and therefore the equation of state is given by,

$$p = \rho RT \quad (2.5)$$

where, the symbol p , ρ and T refer to pressure, density and temperature, respectively whereas R refer to gas constant.

2.2 Finite volume formulation

The computational domain is divided into finite number of non-overlapping control volumes and the governing equations described in the previous section is integrated over each individual control volume, referred to as a cell. The integral form of the governing equations can therefore be written as,

$$\int_{\Omega} \left(\frac{\partial \mathbf{U}}{\partial t} + \frac{\partial(\mathbf{F_I} - \mathbf{F_V})}{\partial x} + \frac{\partial(\mathbf{G_I} - \mathbf{G_V})}{\partial y} + \alpha(\mathbf{S_I} - \mathbf{S_V}) \right) d\Omega = 0 \quad (2.6)$$

where, Ω refers to the volume of an individual cell. The above equation can now be arranged as,

$$\int_{\Omega} \frac{\partial \mathbf{U}}{\partial t} d\Omega = - \int_{\Omega} \left(\frac{\partial(\mathbf{F_I} - \mathbf{F_V})}{\partial x} + \frac{\partial(\mathbf{G_I} - \mathbf{G_V})}{\partial y} + \alpha(\mathbf{S_I} - \mathbf{S_V}) \right) d\Omega \quad (2.7)$$

The various terms appearing in Eq. 2.7 may be approximated as described below.

The temporal may be discretised as,

$$\int_{\Omega} \frac{\partial \mathbf{U}}{\partial t} d\Omega = \frac{\partial}{\partial t} \int_{\Omega} \mathbf{U} d\Omega = \frac{d}{dt} (\bar{\mathbf{U}} d\Omega) = \Omega \frac{d\bar{\mathbf{U}}}{dt} \quad (2.8)$$

where we define $\bar{\mathbf{U}} = \frac{\int_{\Omega} \mathbf{U} d\Omega}{\int_{\Omega} d\Omega}$ as a cell averaged value, that is lumped at the centroid of a cell. The RHS of Eq. 2.7 can be written in a compact form as,

$$\int_{\Omega} \left(\frac{\partial(\mathbf{F}_I - \mathbf{F}_V)}{\partial x} + \frac{\partial(\mathbf{G}_I - \mathbf{G}_V)}{\partial y} + \alpha(\mathbf{S}_I - \mathbf{S}_V) \right) d\Omega = \int_{\Omega} (\nabla \cdot (\mathbf{H}_I - \mathbf{H}_V) + \alpha(\mathbf{S}_I - \mathbf{S}_V)) d\Omega \quad (2.9)$$

Defining the vector \mathbf{H} as,

$$\mathbf{H} = \mathbf{H}_I - \mathbf{H}_V \quad (2.10)$$

and employing the Gauss Divergence theorem gives,

$$\int_{\Omega} \nabla \cdot \mathbf{H} d\Omega = \int_S \mathbf{H} \cdot \hat{n} dS \quad (2.11)$$

The symbol S represents the bounding surface bounding the control volume and \hat{n} represents the unit normal to the surface. The surface integral may now be approximated in a discrete manner as,

$$\int_S \mathbf{H} \cdot \hat{n} dS = \sum_J \mathbf{H}_J \cdot \hat{n}_J \Delta S_J = \sum_J \mathbf{H}_{\perp J} \Delta S_J \quad (2.12)$$

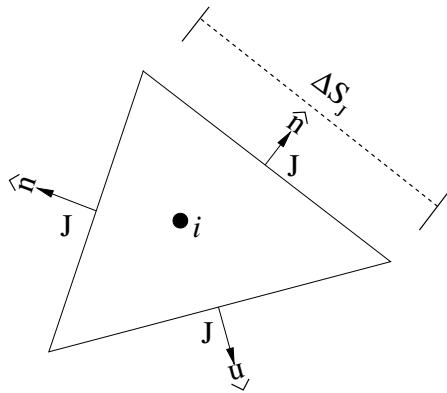


Figure 2.1: Cell nomenclature

where the summation is over faces J of the control volume. In Eq. 2.12, ΔS_J represents the length of the face J of a control volume (see also Figure 2.1) while \mathbf{H} refers to the total flux normal to the face and includes both inviscid and viscous contribution.

$$\mathbf{H}_{\perp} = \mathbf{H}_{I\perp} - \mathbf{H}_{V\perp}$$

$$\mathbf{H}_\perp = \begin{bmatrix} \rho u_\perp \\ \rho uu_\perp + pn_x \\ \rho vu_\perp + pn_y \\ (\rho e + p)u_\perp \end{bmatrix} - \begin{bmatrix} 0 \\ n_x \tau_{xx} + n_y \tau_{xy} \\ n_x \tau_{yx} + n_y \tau_{yy} \\ n_x \theta_x + n_y \theta_y \end{bmatrix} \quad (2.13)$$

Here, $u_\perp = un_x + vn_y$, $\theta_x = u\tau_{xx} + v\tau_{xy} - q_x$, $\theta_y = u\tau_{yx} + v\tau_{yy} - q_y$. The source terms appearing in Eq. 2.9 can also be handled in an analogous manner as,

$$\int_{\Omega} \alpha(\mathbf{S}_{\mathbf{I}} - \mathbf{S}_{\mathbf{V}}) d\Omega = \alpha \cdot \bar{\mathbf{S}} \quad (2.14)$$

where $\bar{\mathbf{S}} = \bar{\mathbf{S}}_{\mathbf{I}} - \bar{\mathbf{S}}_{\mathbf{V}}$ is the cell-averaged value of the source term which is also lumped at the centroid of the cell. Using these simplifications, the semi-discrete form of the governing conservation laws can be written as ,

$$\frac{d\bar{\mathbf{U}}_i}{dt} = -\frac{1}{\Omega_i} \sum_{J \in i} \mathbf{H}_{\perp J} \Delta S_J - \alpha \bar{\mathbf{S}}_i = \mathbf{R}(\bar{\mathbf{U}}_i) \quad (2.15)$$

Here, summation is over all faces of the cell i and term $\mathbf{R}(\bar{\mathbf{U}}_i)$ is referred to as the residual term. This semi discrete flux formula contains viscous and convective flux contributions which are evaluated at the face mid-point. This amounts to the use of a single point Gauss quadrature for evaluating the integral and is therefore important for a nominally second order accurate flow solver.

2.3 Inviscid and viscous flux computations

The evaluation of the convective and viscous fluxes appearing in Eq. 2.13 are now discussed below.

2.3.1 Inviscid flux discretisation

The inviscid flux computation is based on the solution of an approximate Riemann problem oriented normal to the interface. There are several flux formulations possible that include central and upwind schemes. In the present study we employ van Leer [93] and AUSM [94] schemes. The flux formula corresponding to these scheme are provided in Appendix A. For further details of implementation corresponding to these schemes and several others, one may refer to [95].

Solution reconstruction

In order to have nominal second order accuracy, the states required for the approximate Riemann solver need to be obtained using a linear reconstruction procedure. According to the Godunov Barrier theorem [96], the use of a simple linear interpolation can lead to loss in monotonicity. In order to achieve monotone numerical solutions, one needs to use slope limiters which leads to limited linear reconstruction that defines the left and right states as,

$$V_L = V_i + \psi(\nabla V_i \cdot \mathbf{r}_L) \quad (2.16)$$

$$V_R = V_j + \psi(\nabla V_j \cdot \mathbf{r}_R) \quad (2.17)$$

Here, \mathbf{r}_L and \mathbf{r}_R represent the vectors pointing from the cell-centroid towards the face centroid as shown in the Figure 2.2. In the above expression, V_L and V_R are the primitive variables (density, velocity, pressure, temperature) and ∇V_i and ∇V_j are the gradient of V at the cell centres. The cell centroidal gradient are calculated by either Standard Green Gauss (SGG) reconstruction [97] or Modified Green Gauss (MGG) reconstruction [98], whose details are provided in Chapter 3.

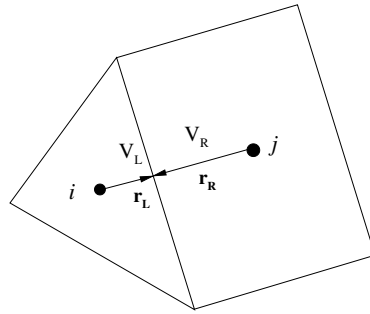


Figure 2.2: Linear reconstruction for the cell centered scheme

In the present solver we employ Venkatakrishnan's limiter [97] which ensures good convergence characteristics to steady state and the limiter function is defined by,

$$\psi = \begin{cases} \frac{1}{\Delta^2} \left[\frac{(\Delta_{1,max}^2 + \epsilon^2)\Delta_2 + 2\Delta_2^2\Delta_{1,max}}{\Delta_{1,max}^2 + 2\Delta_2^2 + \Delta_{1,max}\Delta_2 + \epsilon^2} \right] & \text{if } \Delta_2 > 0 \\ \frac{1}{\Delta^2} \left[\frac{(\Delta_{1,min}^2 + \epsilon^2)\Delta_2 + 2\Delta_2^2\Delta_{1,max}}{\Delta_{1,max}^2 + 2\Delta_2^2 + \Delta_{1,max}\Delta_2 + \epsilon^2} \right] & \text{if } \Delta_2 < 0 \\ 1 & \text{if } \Delta_2 = 0 \end{cases}$$

where $\Delta_{1,max} = V_{max} - V_i$ and $\Delta_{1,min} = V_{min} - V_i$. Here, V_{max} and V_{min} are the maximum and minimum values of all surrounding cells j , including the cell i itself, and are expressed as,

$$V_{max} = \max(V_i, \max_j V_j)$$

$$V_{min} = \min(V_i, \min_j V_j)$$

where the term Δ_2 is calculated as,

$$\Delta_2 = |\Delta_2| + 10^{-12} \quad (2.18)$$

Further, the parameter $\epsilon^2 = (K\Delta h)^3$ is the controlling factor for limiting where Δh is a characteristic length scale for the cell. The value of K which is typically chosen between 2 to 10 but an optimal choice depends on the mesh and the problem being solved. **For the studies carriedout in Chapter 4 till Chapter 7, value of K has been taken as 2.**

2.3.2 Viscous flux discretisation

Evaluation of the viscous flux at the face requires computations of the first derivatives at the faces. This requires the use of flow quantities at the face mid-points if standard Green Gauss reconstruction as described in Chapter 3 is employed. This requires the use of a suitable interpolation procedure and in the present work we use a simple mathematical averaging as defined by,

$$V_J = \frac{1}{2}(V_i + V_j) \quad (2.19)$$

The gradients can also be computed based on variants based on the Green-Gauss divergence theorem whose details are described in greater detail in Chapter 3.

2.4 Temporal discretisation

The ODE's represented by the semi-discrete finite volume update formula shown in Eq. 2.15 are marched in time to obtain the numerical solution either to steady state or upto a finite time for unsteady problem. In the present study, we make use of an explicit time integration procedure which include the first order accurate Euler scheme and the higher order accurate Runge-Kutta scheme [97]. The first order accurate Euler scheme which is used for steady state problems only, leads to a fully discrete finite volume update that reads,

$$\mathbf{U}_i^{n+1} = \mathbf{U}_i^n - \frac{\Delta t}{\Omega_i} \sum_{J \in i} \mathbf{H}_{\perp J} \Delta S_J - \alpha \bar{\mathbf{S}}_i \quad (2.20)$$

$$\mathbf{U}_i^{n+1} = \mathbf{U}_i^n + \mathbf{R}(\bar{\mathbf{U}}_i)^{(n)}$$

where the quantity n and $n + 1$ refer to the current and next time step.

For unsteady problem which require higher order accuracy in time, we employ the explicit five stage Runge-Kutta scheme. The implementation is as follows,

$$\mathbf{U}_i^{(0)} = \mathbf{U}_i^{(n)}$$

$$\mathbf{U}_i^{(m)} = \mathbf{U}_i^{(0)} - \alpha_m \Delta t \mathbf{R}(\bar{\mathbf{U}}_i)^{(m-1)} \quad ; m = 1, 2, \dots 5$$

$$\mathbf{U}_i^{(n+1)} = \mathbf{U}_i^{(5)}$$

The stage coefficients α_m are tuned to improve stability and damping properties and in the present solver are chosen as,

$$\alpha_1 = 1/4; \quad \alpha_2 = 1/6; \quad \alpha_3 = 3/8; \quad \alpha_4 = 1/2; \quad \alpha_5 = 1$$

2.5 Implementation of boundary conditions

Proper implementation of boundary condition is essential to obtain stable and accurate numerical solutions. Specification of inappropriate boundary conditions may also cause instabilities that corrupt the solution. In the following sub-sections, we detail the various boundary conditions encountered in high speed flows.

2.5.1 Supersonic inlet & outlet

For supersonic inlet, the primitive variables are fixed to their corresponding freestream values while for supersonic outlet, all variables are extrapolated from the interior cells adjacent to the boundary faces.

2.5.2 No-slip walls

The no-slip boundary condition is imposed by setting the normal and tangential velocities at the surface to zero. For isothermal walls, the temperature is set to a constant value whereas for the adiabatic walls, the temperature gradient is set to zero.

2.5.3 Inviscid wall or symmetry boundary

In this boundary condition, we merely set the normal component of velocity to zero as a consequence of the impermeable wall boundary condition. The implementation of this boundary condition may be realised by one of the following two approaches.

Mirror or Ghost cell approach

In this approach we construct a virtual ghost cell for each boundary cell and the ghost cell values are populated as defined below,

$$\begin{aligned} u_{\perp g} &= -u_{\perp I} \\ u_{\parallel g} &= u_{\parallel I} \\ p_g &= p_I \\ \rho_g &= \rho_I \end{aligned}$$

Here ‘ g ’ and ‘ I ’ refers to ghost state and interior states respectively. These states are used in the same flux formula that is used to compute the inviscid fluxes in the interior of the domain.

Pressure gradient extrapolation

An alternate approach is to directly enforce the normal velocity to zero in the expres-

sion for inviscid fluxes. In such a case, the flux vector simplifies as,

$$\mathbf{H}_\perp = \begin{bmatrix} 0 \\ pn_x \\ pn_y \\ 0 \end{bmatrix}$$

The unstructured cell-centered finite volume flow solver that has been described herein, is the basic workhorse for this particular study. This solver has been extensively validated for hypersonic inviscid and viscous flows [95]. We have attempted to improve the robustness of this flow solver through the implementation of a novel gradient reconstruction approach and this solver has also been combined with sharp interface immersed boundary methods to obtain a generic and accurate numerical framework as described in the subsequent chapters of this thesis.

CHAPTER 3

MODIFIED GREEN-GAUSS RECONSTRUCTION

“Essentially, all models are wrong, but some are useful”

- George Box, 1976

We describe a new and simple strategy based on the Gauss divergence theorem for obtaining centroidal gradients on unstructured meshes. Unlike the standard Green–Gauss (SGG) reconstruction which requires face values of quantities whose gradients are sought, the proposed approach reconstructs the gradients using the normal derivative(s) at the faces. The new strategy, referred to as the Modified Green–Gauss (MGG) reconstruction depends on the accuracy of discretisation of the normal derivatives at faces and this necessitates an iterative approach for gradient computation on non-orthogonal meshes. We show via the use of non-iterative piggybacking that MGG reconstruction encounters nearly the same computational cost as SGG reconstruction, even when non-orthogonal corrections are employed. Furthermore, it was observed that solutions from MGG reconstruction results in lesser numerical dissipation as compared to SGG reconstruction and also serves as a robust choice for complex practical flow problems in hypersonic flows.

Use of unstructured finite volume solvers on adaptive grids necessitates a generic method for gradient estimation with the latter being used for convective and viscous flux calculations. Studies till now have been predominantly carried out using Least-Square and Green-Gauss approaches and there are no definitive answers on which

The contents of this chapter are published in “**A new Green–Gauss reconstruction on unstructured meshes. Part I: Gradient reconstruction**”, Journal of Computational Physics (2018) and is joint work with Mr. Mandeep Deka [99]

gradient reconstruction is the best. Hence, this chapter is devoted to the development and investigation of a novel gradient reconstruction approach rooted in the Gauss divergence theorem and which therefore belongs to the class of Green–Gauss reconstruction. Unlike existing approaches of this category, the proposed reconstruction is unique in that it does not require face values of the solution quantities. We discuss the details of construction of the new scheme and its implementation on arbitrary polygonal meshes for gradient computations in the following sections.

3.1 Overview of Green–Gauss reconstruction

In this section, we present a brief overview of existing approaches for gradient computations which are based on the Gauss divergence theorem. For any vector field \mathbf{u} , the Gauss divergence theorem states that the net outward flux through a closed surface is equal to the volume integral of the divergence of the vector field. Stated mathematically,

$$\int_{\Omega} \nabla \cdot \mathbf{u} d\Omega = \int_{E(\Omega)} \mathbf{u} \cdot \mathbf{n} dS \quad (3.1)$$

where, $E(\Omega)$ is the closed surface enclosing a volume Ω with \mathbf{n} representing the unit outward normal to the surface (see Figure 3.1(a)). Substituting $\mathbf{u} = \phi \mathbf{a}$, where \mathbf{a} is any arbitrary constant vector and ϕ is a scalar field, we obtain after simplification,

$$\int_{\Omega} \nabla \phi d\Omega = \int_{E(\Omega)} \phi \mathbf{n} dS \quad (3.2)$$

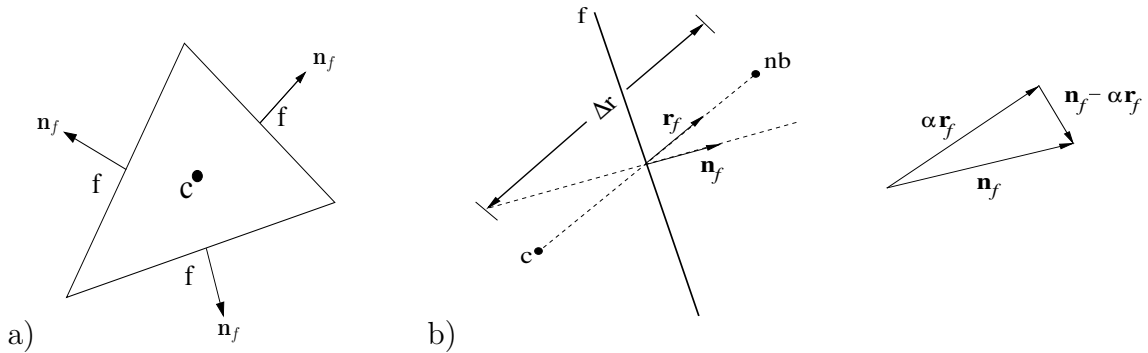


Figure 3.1: (a) Cell geometry (b) nomenclature for non-orthogonal grid

One can obtain an expression for the centroidal gradient in a finite volume frame-

work by replacing the integrals in Eq. 3.2 by their discrete analogues. The volume integral defines the cell-averaged gradient and can be shown to be a second-order approximation to the centroidal value. We therefore have,

$$(\nabla\phi)_c = \frac{1}{\Omega} \int_{\Omega} \nabla\phi d\Omega + O(h^2) \quad (3.3)$$

where h is representative of the cell dimension, and c represents the cell center. For a polygonal (polyhedral) volume, the surface integral can be evaluated as the sum over all faces as,

$$\int_{E(\Omega)} \phi \mathbf{n} dS = \sum_f \left(\int_f \phi dS \right) \mathbf{n}_f \quad (3.4)$$

where \mathbf{n}_f represents the outward unit face normal of a face f of the polygon (polyhedron). Employing a single-point Gauss quadrature to evaluate the integral over each face gives,

$$\int_f \phi dS = \phi_f \Delta S_f + O(h^2) \Delta S_f \quad (3.5)$$

where, ΔS_f represents the face area. It must be realised that the single-point Gauss quadrature requires evaluating the scalar values only at the face center and is exact for constant and linear functions only, which explains the second-order error in Eq. 3.5. Using Eqs. 3.3 and 3.5 in Eq. 3.2 one can compute the gradient of ϕ as,

$$(\nabla\phi)_c = \frac{1}{\Omega} \sum_f \phi_f \mathbf{n}_f \Delta S_f \quad (3.6)$$

The expression for gradient computation defined by Eq. 3.6 must, therefore, be necessarily viewed as a numerical approximation to the first derivative which leads to consistent gradients on any mesh topology if the “true” values at the faces ϕ_f are known. This is seldom the case, with the solution known only at the cell centers and therefore needing some interpolation to obtain the face center values. Consequently, the reconstruction defined by Eq. 3.6 has approximation errors that are dependent on the chosen interpolation strategy. The various existing approaches in practice, collectively referred to as GG reconstruction, merely differ in the methodology adopted to evaluate the face-centered value.

As stated earlier, all quantities are stored at the cell centers on collocated grids and therefore GG reconstruction necessitates the use of a suitable interpolation to obtain the face-centered values from the cell center quantities. One of the approaches, which is very prevalent, is to obtain the face values as the weighted average of the centroidal values in cells sharing the face using volume or inverse volume weighting or inverse distance weighting (linear interpolation) [13, 15]. A second approach employs an analogous weighted interpolation to first estimate the quantities at nodes from those at the cells and then the face values are determined from the nodal values by simple averaging [14]. Both these class of approaches invariably require interpolation and the accuracy of the gradients are therefore dependent on the accuracy of the interpolation. It can be easily demonstrated that simple interpolation practices involving volume and/or inverse volume weighting would in general lead to gradient errors that do not diminish with grid refinement on genuinely unstructured grids thus rendering the gradient estimates inconsistent [15, 20]. Inverse distance-weighted (or linear) interpolation can lead to consistent gradients but only if the line joining the cell-centers passes through face center, which is not possible in general on arbitrary polygonal meshes. It must be pointed out that most interpolation approaches, except the Laplacian strategy of [16], the nodal least-squares approach in [14] and auxiliary control volume approach in [18] do not lead to consistent gradients on unstructured meshes. In essence, for Green-Gauss reconstruction to lead to consistent gradients, the interpolation of values from cell centers to face centers need to be at least second order accurate, and such approaches, as discussed are only a few and are not free from numerical issues and/or implementation either. Since the study in this Chapter is devoted to the development and investigation of a new alternative for gradient reconstruction derived from similar roots as GG reconstruction, we shall effect comparisons with the GG reconstruction to highlight the improvements from the proposed approach. To this end, we shall assume that the face values are obtained from centroidal values using volume-weighted averaging and refer to this calculation methodology as SGG reconstruction. Mathematically, the interpolation can be expressed as,

$$\phi_f = \frac{\phi_{C1}\Omega_{C1} + \phi_{C2}\Omega_{C2}}{\Omega_{C1} + \Omega_{C2}} \quad (3.7)$$

where, C_1 and C_2 are the cells sharing the face f . It must be remarked that one can choose to use a linear interpolation for computing the face values, although a greater effort would be necessary to realise it on arbitrary polygonal meshes that could be both skewed and non-orthogonal. The use of linear interpolation for computing the face values in SGG reconstruction could be advantageous on few mesh topologies

but volume-weighted averaging is a more simpler choice in multi-dimensions and the conclusions drawn herein with this choice of interpolation for the SGG reconstruction are not different from those when other interpolation approaches are employed, except in a handful of cases.

3.2 Modified Green Gauss reconstruction

The biggest advantage of Green–Gauss reconstruction, including SGG reconstruction, is that it offers a closed-form expression involving a compact stencil for gradient calculations. Despite the gradients on unstructured meshes being inconsistent, SGG reconstruction has been employed with good success for engineering computations of compressible and incompressible fluid flows. In this section, we describe the new gradient reconstruction strategy which is based on the Green–Gauss theorem and therefore inherits many of the advantages offered by SGG reconstruction. The new strategy, which we refer to as Modified Green–Gauss reconstruction (or simply MGG), is however different from SGG reconstruction (and related approaches) in that it reconstructs centroidal gradient from the face normal derivative instead of face-centered values and leads to consistent gradients on arbitrary polygonal meshes. The approach to compute gradients using MGG reconstruction has its roots in the reconstruction of centroidal values from scalar quantities defined on faces on unstructured staggered meshes as discussed in [100]. These scalars are in fact the projections of the vector quantities along the normal vector to the faces. Consider the Gauss divergence theorem applied to $\mathbf{u} = (\mathbf{a} \cdot \mathbf{x})\mathbf{v}$, where \mathbf{a} represents an arbitrary constant vector, \mathbf{x} represents the position vector in a stationary reference frame and \mathbf{v} represents a vector field. One can see that Eq. 3.1 therefore becomes,

$$\int_{\Omega} \nabla \cdot [(\mathbf{a} \cdot \mathbf{x})\mathbf{v}] d\Omega = \int_{E(\Omega)} (\mathbf{a} \cdot \mathbf{x})\mathbf{v} \cdot \mathbf{n} dS \quad (3.8)$$

This may be simplified as,

$$\int_{\Omega} (\mathbf{a} \cdot \mathbf{x}) \nabla \cdot \mathbf{v} d\Omega + \int_{\Omega} \mathbf{v} \cdot \nabla (\mathbf{a} \cdot \mathbf{x}) d\Omega = \int_{E(\omega)} (\mathbf{a} \cdot \mathbf{x})\mathbf{v} \cdot \mathbf{n} dS \quad (3.9)$$

Writing the above in tensorial form we get,

$$\int_{\Omega} (a_j x_j) \frac{\partial u_i}{\partial x_i} d\Omega + \int_{\Omega} v_i \frac{\partial (a_j x_j)}{\partial x_i} d\Omega = \int_{E(\omega)} (a_j x_j) v_i n_i dS \quad (3.10)$$

Since a_j is a constant vector,

$$a_j \left[\int_{\Omega} x_j \frac{\partial u_i}{\partial x_i} d\Omega + \int_{\Omega} v_i \frac{\partial x_j}{\partial x_i} d\Omega - \int_{E(\omega)} x_j v_i n_i dS \right] = 0 \quad (3.11)$$

The term inside the parenthesis vanishes identically, since a_j is an arbitrary vector

$$\int_{\Omega} x_j \frac{\partial u_i}{\partial x_i} d\Omega + \int_{\Omega} v_i \frac{\partial x_j}{\partial x_i} d\Omega = \int_{E(\omega)} x_j v_i n_i dS \quad (3.12)$$

Also,

$$\frac{\partial x_j}{\partial x_i} = \delta_{ij}$$

$$\int_{\Omega} x_j \frac{\partial u_i}{\partial x_i} d\Omega + \int_{\Omega} v_i \delta_{ij} d\Omega = \int_{E(\omega)} x_j v_i n_i dS \quad (3.13)$$

or,

$$\int_{\Omega} v_j d\Omega + \int_{\Omega} x_j \frac{\partial u_i}{\partial x_i} d\Omega = \int_{E(\omega)} x_j v_i n_i dS \quad (3.14)$$

The above equation can also be written as,

$$\int_{\Omega} \mathbf{v} d\Omega + \int_{\Omega} (\nabla \cdot \mathbf{v}) \mathbf{x} d\Omega = \int_{E(\omega)} (\mathbf{v} \cdot \mathbf{n}) \mathbf{x} dS \quad (3.15)$$

Dividing Eq. 3.15 through by Ω and rearranging gives,

$$\frac{1}{\Omega} \int_{\Omega} \mathbf{v} d\Omega = \frac{1}{\Omega} \int_{E(\omega)} (\mathbf{v} \cdot \mathbf{n}) \mathbf{x} dS - \frac{1}{\Omega} \int_{\Omega} (\nabla \cdot \mathbf{v}) \mathbf{x} d\Omega \quad (3.16)$$

Realising that $\mathbf{x} = \mathbf{x}_c + \mathbf{x}_r$ where \mathbf{x}_c is the position vector of the cell centroid allows us to rearrange Eq. 3.16 as,

$$\begin{aligned} \frac{1}{\Omega} \int_{\Omega} \mathbf{v} d\Omega &= \frac{1}{\Omega} \int_{E(\Omega)} (\mathbf{v} \cdot \mathbf{n})(\mathbf{x} - \mathbf{x}_c) dS + \frac{1}{\Omega} \int_{E(\Omega)} (\mathbf{v} \cdot \mathbf{n}) \mathbf{x}_c dS \\ &\quad - \frac{1}{\Omega} \int_{\Omega} (\nabla \cdot \mathbf{v}) \mathbf{x}_c d\Omega - \frac{1}{\Omega} \int_{\Omega} (\nabla \cdot \mathbf{v}) \mathbf{x}_r d\Omega \end{aligned} \quad (3.17)$$

It must be remarked that the above equation is exact and we shall now attempt to evaluate the integrals appearing in Eq. 3.17 in a discrete setting.

The first integral is a volume integral that precisely defines the cell-averaged value of the vector. However, the cell averaged values are “lumped” at the cell centroids in a collocated framework and this makes the cell-averaged value a second-order approximation to the centroidal value, similar to Eq. 3.3. We therefore have,

$$\frac{1}{\Omega} \int_{\Omega} \mathbf{v} d\Omega = \mathbf{v}_c + O(h^2) \quad (3.18)$$

where \mathbf{v}_c is the value at the centroid of the cell. The second integral is a surface integral that needs to be evaluated over the faces forming the cell. This integral may be approximated as,

$$\frac{1}{\Omega} \int_{E(\Omega)} (\mathbf{v} \cdot \mathbf{n})(\mathbf{x} - \mathbf{x}_c) dS = \frac{1}{\Omega} \sum_f \left[(\mathbf{x}_f - \mathbf{x}_c) \mathbf{v}_f \Delta S_f \right] \cdot \mathbf{n}_f + O(h^2) \quad (3.19)$$

where the surface integral over each face has been evaluated using a single-point Gauss quadrature similar to Eq. 3.5 which is second-order accurate, in general. It is easy to see that the third and fourth integrals cancel one another. The fifth integral which is again a volume integral is not amenable for further simplification but can be evaluated in certain cases. A little effort shows that, in general, the integral is zero if and only if $\nabla \cdot \mathbf{v}$ is a constant. The case of a constant vector or a solenoidal field both of which give $\nabla \cdot \mathbf{v} = 0$ are special cases, with the latter resulting possibly from a conservation law. However, for arbitrary \mathbf{v} , this integral has a non-zero contribution. Expanding the integrand about its value at the cell-center using Taylor’s series gives,

$$\nabla \cdot \mathbf{v} = (\nabla \cdot \mathbf{v})_c + O(h) \quad (3.20)$$

Substituting Eq. 3.20 into the integral and simplifying by invoking the definition of the centroid leads to,

$$\frac{1}{\Omega} \int_{\Omega} (\nabla \cdot \mathbf{v}) \mathbf{x}_r d\Omega \sim O(h^2) \quad (3.21)$$

which essentially means that the numerical evaluation of the fifth integral introduces approximation errors which are $O(h^2)$ similar to those incurred from the approximation of the first two integrals. We, therefore, obtain the numerical analogue of Eq. 3.16 which reads,

$$\mathbf{v}_c = \frac{1}{\Omega} \sum_f V_f (\mathbf{x}_f - \mathbf{x}_c) \Delta S_f + O(h^2) \quad (3.22)$$

where $V_f = (\mathbf{v}_f \cdot \mathbf{n}_f)$ is a scalar quantity, \mathbf{x}_f and \mathbf{x}_c refer to the position vector of the face and cell centers respectively and all other geometric quantities have standard

meanings as defined previously. However, this assumes that the face values V_f are exactly known, which is seldom the case in collocated frameworks. In most problems, it is necessary to approximate the face values from the cell-center values using suitable interpolation. Assuming that $V_f = \tilde{V}_f + O(h^m)$ where \tilde{V}_f is the interpolated value of the scalar at the face and m is the order of accuracy of the interpolation,

$$\mathbf{v}_c = \frac{1}{\Omega} \sum_f \tilde{V}_f (\mathbf{x}_f - \mathbf{x}_c) \Delta S_f + O(h^{\min(m,2)}) \quad (3.23)$$

The numerical estimate of the centroidal vector quantity can, therefore, be obtained by neglecting the approximation errors and defines the MGG reconstruction,

$$\mathbf{v}_c = \frac{1}{\Omega} \sum_f \tilde{V}_f (\mathbf{x}_f - \mathbf{x}_c) \Delta S_f \quad (3.24)$$

We must emphasise that Eq. 3.24 must, therefore, be necessarily viewed as an at-most second-order approximation to the “true” value of the centroidal vector. It must be remarked that this reconstruction has been previously employed to reconstruct the velocity components at cell centers from face normal velocities on unstructured staggered frameworks in [101–103].

The MGG gradient reconstruction simply follows the vector reconstruction expression obtained in Eq. 3.24 to derive an expression for the centroidal gradients of any scalar ϕ by considering $\mathbf{v} = \nabla\phi$. The approximate gradient reconstruction then reads,

$$(\nabla\phi)_c = \frac{1}{\Omega} \sum_f \left. \frac{\partial\phi}{\partial n} \right|_f (\mathbf{x}_f - \mathbf{x}_c) \Delta S_f \quad (3.25)$$

While one can employ several possible approximations for the normal derivative [104] in Eq. 3.25, we employ the Zwart’s approach [105] on generic unstructured meshes. This is done by first decomposing the normal derivative as,

$$\left. \frac{\partial\phi}{\partial n} \right|_f = \nabla\phi|_f \cdot (\alpha \mathbf{r}_f) + \overline{\nabla\phi}|_f \cdot (\mathbf{n}_f - \alpha \mathbf{r}_f) \quad (3.26)$$

where, \mathbf{r}_f is an unit vector from c to the cell center of the face-sharing neighbour cell denoted as nb (See Figure 3.1) and $\alpha = (\mathbf{n}_f \cdot \mathbf{r}_f)$ is a scaling factor. This calculation of the normal derivative may, therefore, be interpreted as the sum of an orthogonal component and associated non-orthogonal correction, which are respectively represented by the first and second terms (on the right hand side) in Eq. 3.26. One can easily see that α is bounded between 0 and 1 and becomes unity on orthogonal

meshes, causing the second term in Eq. 3.26 to identically vanish on such meshes. The orthogonal and non-orthogonal contributions in Eq. 3.26 may be numerically evaluated as,

$$(\nabla\phi)_f \cdot (\alpha \mathbf{r}_f) = \alpha \left(\frac{\phi_{nb} - \phi_c}{\Delta r} \right) \quad (3.27)$$

$$\overline{\nabla\phi}|_f \cdot (\mathbf{n}_f - \alpha \mathbf{r}_f) = \frac{1}{2} ((\nabla\phi)_c + (\nabla\phi)_{nb}) \cdot (\mathbf{n}_f - \alpha \mathbf{r}_f) \quad (3.28)$$

where Δr represents the distance between the centroids c and nb (See Figure 3.1(b)). A quick look at Eqs. 3.27 and 3.28 show that the gradient computation becomes implicit on non-orthogonal meshes. This is because the non-orthogonal correction requires the use of gradients at the cell-centers which are in fact the desired quantities themselves. **This paradoxical situation can be resolved by using an iterative approach where the gradients appearing in the correction term are lagged.** The normal derivative calculations then become,

$$\frac{\partial\phi}{\partial n}\Big|_f^{k+1} = \alpha \left(\frac{\phi_{nb} - \phi_c}{\Delta r} \right) + \frac{1}{2} ((\nabla\phi)_c^k + (\nabla\phi)_{nb}^k) \cdot (\mathbf{n}_f - \alpha \mathbf{r}_f) \quad (3.29)$$

where it must be recognised that the gradients appearing in the non-orthogonal correction are approximate values determined using MGG reconstruction and that the accuracy of interpolation of the face normal derivative defined by Eq. 3.29 would, in turn, determine the gradient accuracy. The iterative algorithm for computing gradients may be summarised in Table 3.1.

Table 3.1: The algorithm for MGG reconstruction

Algorithm: MGG gradient reconstruction	
1	Set iteration counter, $k = 0$ and cell-center gradients, $\phi = 0$ at all cells.
2	Compute the terms in Eqs. 3.27 and 3.28
3	Obtain face normal derivatives by employing quantities from step 2 in Eq. 3.29
4	Reconstruct the cell center gradients using MGG reconstruction using Eq. 3.25
5	Convergence? If yes, terminate else set $k = k + 1$ and go to step 2.

The iterations are assumed to be converged when the L_2 norm of the gradient correction, $\|\nabla\phi^{k+1} - \nabla\phi^k\|_2$ become lesser than a pre-defined tolerance ϵ_{res} which is set equal to 10^{-8} . This can also be ensured by having sufficient number of sub-iterations (usually less than 10). We remark that while other approaches to take into account non-orthogonality effects [104] may be employed, we have found the Zwart's approach to be the most robust on highly non-orthogonal meshes. This choice is motivated by the investigations in [23] and the specific choice of α accounts for the mesh non-orthogonality and also serves as an under-relaxation parameter that aids in iterative

convergence.

The iterative nature of the MGG reconstruction shown in Table 3.1 means that it encounters significant computational overhead as compared to SGG reconstruction. In order to mitigate the cost associated with MGG reconstruction on non-orthogonal meshes, we propose that the reconstruction in transient (and pseudo-transient) flow solvers be implemented in a non-iterative manner. While iterative approaches are inherent in computing fluid flows, we distinguish them as “inner” iterations, which are associated with the solution to the linear system of equations and “outer” iterations. The outer iterations are routinely employed when a transient/pseudo-transient procedure is adopted (in a time-marching approach until a finite time) and for non-transient problems as well, if some of the terms in the equations are treated with a deferred correction approach. Inspired by the recent efforts of Syrakos et al. [20], we compute the gradients in a single-step as,

$$(\nabla\phi)_c^l = \frac{1}{\Omega} \sum_f \left. \frac{\partial\phi}{\partial n} \right|_f (\mathbf{x}_f - \mathbf{x}_c) \Delta S_f \quad (3.30)$$

where the normal derivative is evaluated as,

$$\left. \frac{\partial\phi}{\partial n} \right|_f = \alpha \left(\frac{\phi_{nb}^l - \phi_c^l}{\Delta r} \right) + \frac{1}{2} ((\nabla\phi)_c^{l-1} + (\nabla\phi)_{nb}^{l-1}) \cdot (\mathbf{n}_f - \alpha \mathbf{r}_f) \quad (3.31)$$

where the index l denotes the outer iteration. It is easy to see that the calculation of the normal derivative in Eq. 3.31 is dependent on the most recently available values of the gradients (at $l - 1$ which need to be stored), thereby avoiding any iterations in the derivative computation. It must be emphasised that one must employ this approach only when the gradients are repetitively computed (several numbers of times) during the course of the solution process on grids that are genuinely non-orthogonal. This occurs when higher-order convective schemes are employed and also for viscous computations, both of which necessitate the determination of velocity gradients. The above approach herein is referred to as “non-iterative piggybacking” and we make use of this approach to evaluate its utility for practical problems of interest, with a measure of the computational cost associated with it.

3.3 Numerical studies

In the following sections we discuss the utility of the proposed gradient reconstruction technique named Modified Green Gauss reconstruction and compare its performance against Standard Green Gauss reconstruction. Three test case are taken for this

purpose and for each test case, we identify salient features which distinguish MGG and SGG reconstructions. All the test cases performed herein are using the in-house finite volume solver [106] as described in Chapter 2.

3.3.1 Supersonic vortex flow

We begin with the supersonic vortex flow test case [107] which has an analytical solution and describes the inviscid, isentropic flow between concentric circular arcs. The inner arc has a radius of unity whereas the outer arc has a radius of 1.384 (Figure 3.2). The analytical solution for this problem is,

$$\rho = \rho_i \left[1 + \frac{\gamma - 1}{2} \left(1 - \frac{R_i^2}{r^2} \right) M_i^2 \right]^{\frac{1}{\gamma-1}}$$

Here, ρ_i and M_i are density and Mach number respectively at an inner radius R_i . This expression gives density (ρ) at any radius r . In the present test case, M_i is set equal to 2.25 while ρ_i is kept at 1 for the inner radius. The velocity components and pressure are given by

$$u = U_{Ri} \frac{y R_i}{r^2}; \quad v = -U_{Ri} \frac{x R_i}{r^2}$$

$$p = p_i \left[1 + \frac{\gamma - 1}{2} \left(1 - \frac{R_i^2}{r^2} \right) M_i^2 \right]^{\frac{\gamma}{\gamma-1}}$$

$$U_{Ri} = M_i a_i; \quad a_i = \sqrt{\frac{\gamma p_i}{\rho_i}}$$

The test case being shock free isentropic flow, presence of any physical dissipative mechanism is not expected. However, this test case being simulated numerically, we expect some numerical dissipation to be generated, especially with the effect of the curvature of the boundaries. This provides the opportunity to test the gradient reconstruction methods in terms of a technique which yields lowest-numerical dissipation. We evaluate the numerical dissipation produced in the steady-state solution in terms of the difference between the maximum and minimum entropy generation ΔS , as

$$\Delta S = S_{max} - S_{min}$$

$$S = \frac{P}{\rho^\gamma}$$

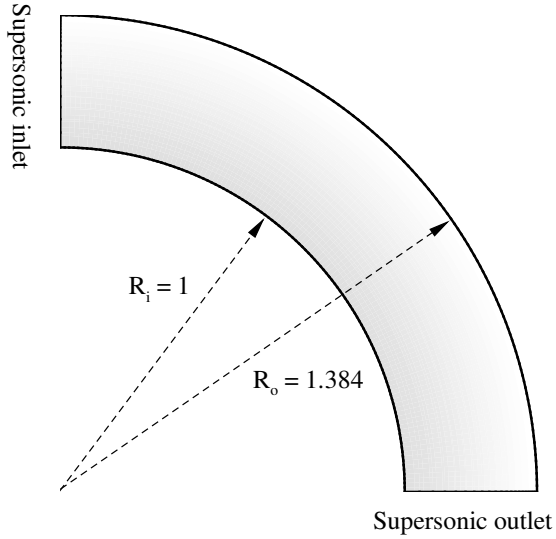


Figure 3.2: Schematic for the supersonic vortex flow computational domain

where, S , P and ρ are the entropy, pressure and density, respectively. It is noteworthy that numerical dissipation is also dependent on the computational grid adopted and thus we adopt for three different grid viz. uniform, unstructured triangulated and curvilinear stretched (Figure 3.3). The total number of control volume nc for the stretched and uniform are kept same i.e. $nc = 2541$, whereas for the unstructured triangulated grid, total control volumes amount to $nc = 6632$. A minor stretching factor is applied in the radial direction for the stretched grid whereas uniform spacing is provided along the circumferential direction of the circular arcs.

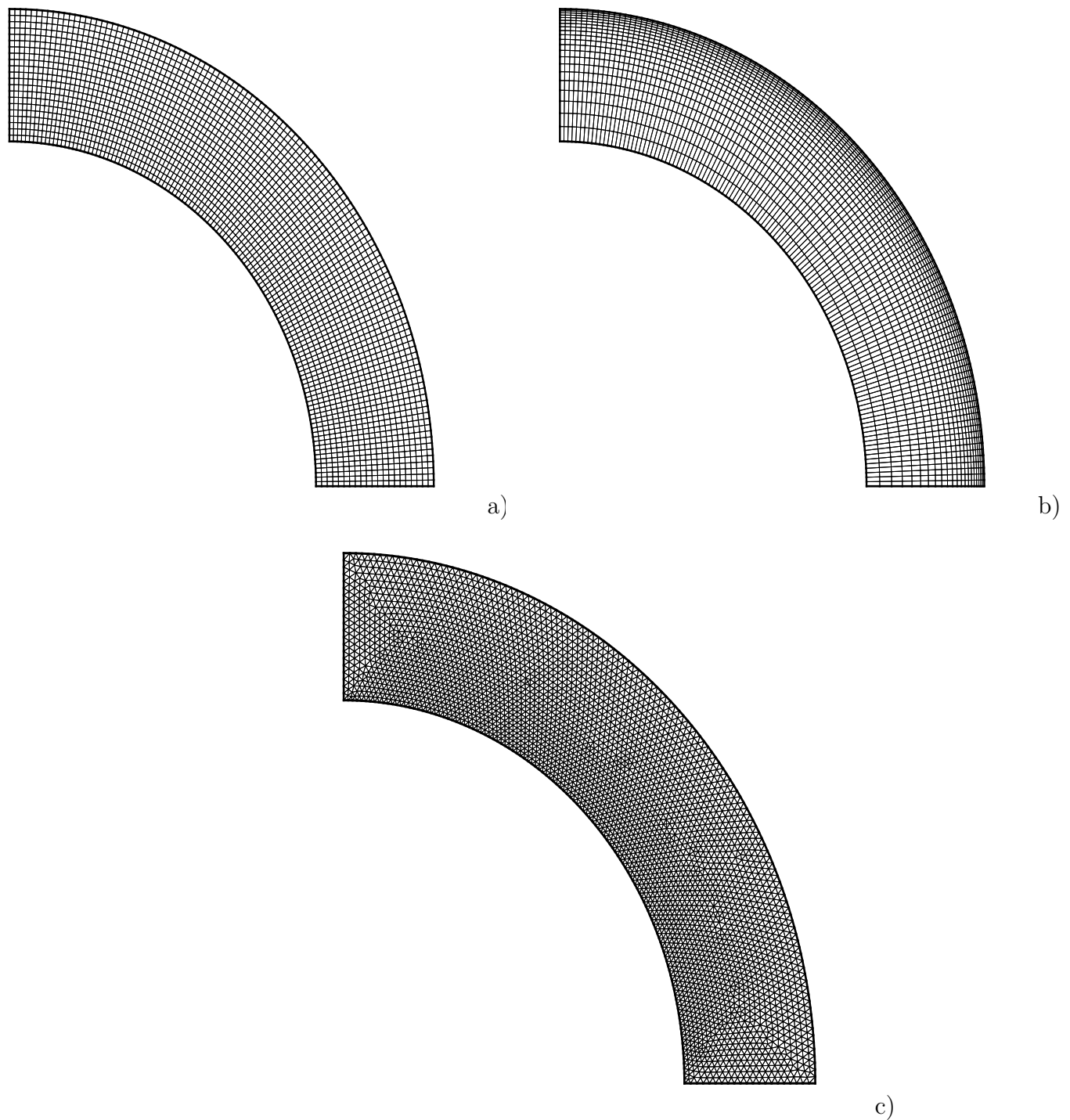


Figure 3.3: Computational grid adopted (a) uniform (b) stretched (c) triangulated

Table 3.2: Numerical dissipation produced in terms of ΔS

Gradient reconstruction method	Type of grid		
	Uniform	Triangulated	Stretched
SGG	0.005453	0.002156	0.009453
MGG	0.005453	0.001404	0.009045

The results obtained in terms of ΔS for the three grids for both MGG reconstruction (without non-orthogonality correction) and SGG reconstruction is reported in the Table 3.2. It is clear that for the uniform grid, the numerical dissipation produced ΔS is exactly equal for both SGG and MGG reconstructions, which is expected for a uniform grid. Interestingly, for both the stretched and the triangulated grid, we observe that MGG reconstruction generates lesser numerical dissipation as compared to SGG reconstruction, even though their magnitude wise difference are not significantly large. Moreover, with the influence of the curved boundaries coming into play, we cannot draw a conclusion. This observation motivated the next test-case, where we studied the decay rate of the minimum pressure for a isentropic vortex decay test case, as described in the next section.

3.3.2 Grashof vortex

We simulate the decay of an isentropic vortex to evaluate the performance of MGG reconstruction in compressible flows. We solve the Euler equations for this smooth flow problem for which the exact solution is known [108].

$$\rho(r) = \left(1 - \frac{\gamma - 1}{2} M_v^2 e^{1-r^2}\right)^{\frac{1}{\gamma-1}} \quad (3.32)$$

$$p(r) = \frac{\rho^r}{r}; u_r = 0; u_\theta = M_v r e^{\frac{1-r^2}{2}} \quad (3.33)$$

where, $r = \sqrt{(x - x_0)^2 + (y - y_0)^2}$ is the local radius of the vortex with its centre at $(x_0, y_0) = (0, 0)$. $M_v = 0.25$ is the vortex strength while $\gamma = 1.4$ is the ratio of specific heats. We employ a $[4, 4] \times [4, 4]$ computational domain discretised using a triangular mesh of 8098 elements. Initialization is carried out using the exact solution which is also applied at the boundaries. Numerical simulations are carried out for long times up to $t = 100$ with a constant time step of 0.01. Although the solution should remain invariant, one can observe a decay in the vortex strength which is due

to numerical dissipation. Studies are also carried out with and without limiters to identify the role played by limiting on the vortex decay. The limiters are applied to the gradients which are calculated using SGG or MGG reconstruction and these have a non-trivial influence on the numerical dissipation.

Figure 3.4(a) shows vortex decay with time, quantified by the decrease in pressure which is computed as $(P_{ref} - P_{min})/P_{ref}$ where, $P_{ref} = 1$ and P_{min} is the minimum pressure in the domain (which occurs at the vortex center) [15]. It is evident that the first-order scheme is very dissipative compared to the second-order counterparts. Among the SGG and MGG reconstructions, we observe that the MGG reconstruction introduces marginally lesser numerical dissipation than SGG reconstruction. This observation is however in cases devoid of limiters and when limiting is employed, there are no appreciable differences between the two reconstructions. The vortex decay is however at a much slower and acceptable rate when either gradient reconstruction strategies are employed, although MGG reconstruction exhibits superior dissipation characteristics compared to SGG reconstruction.

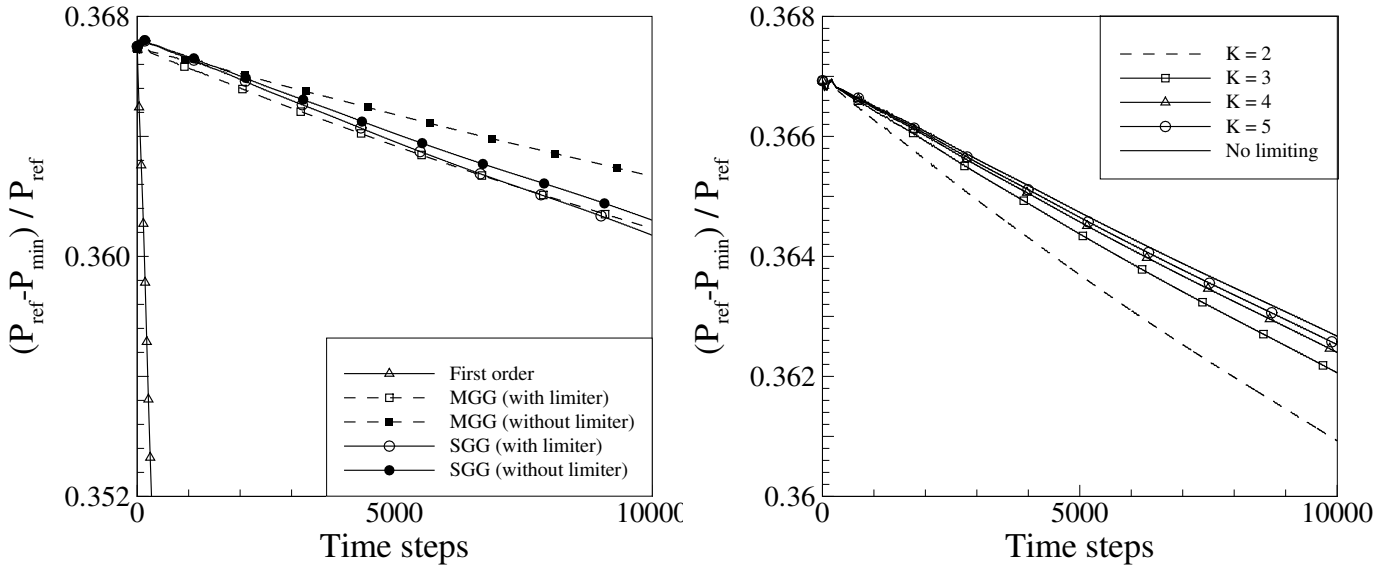


Figure 3.4: (a) Numerical dissipation for inviscid isentropic vortex (b) behaviour of numerical dissipation with limiter constant K

We further analyse the role of limiter in numerical dissipation for MGG reconstruction. Figure 3.4(b) shows the vortex decay with time for different values of the parameter K in the Venkatakrishnan limiter. It must be recalled that very low values of K would mean full limiting (with the scheme approaching first-order) while very high values of K denote minimal limiting (fully second-order scheme). The typical values

of K are in the range from 2–10 and are employed in compressible flows with discontinuities. We see from Figure 3.4(b) that the case of no limiting introduces the least numerical dissipation and the decay rate increases as K decreases. Although there are no discontinuities in this test case, the observations from this study indicate that the MGG reconstruction with limiting using values of K in the range of 3–5 can introduce sufficient numerical dissipation to impart robustness without unduly compromising the solution accuracy which could be important in simulations of compressible flows with shocks. It must also be mentioned that this study used 5 iterations for the MGG reconstruction and did not employ the “non-iterative piggybacking” strategy.

3.3.3 Hypersonic flow past compression ramp

We now assess the MGG reconstruction for practical compressible flow scenarios by considering the challenging case of laminar hypersonic flow past a compression ramp which has also been studied experimentally in [109]. The test case consists of a hypersonic free-stream with $M_\infty = 11.63$ and $Re_\infty = 552116/\text{m}$ flowing past a 15° compression ramp. Simulations are carried out on a 180×80 non-uniform body-fitted mesh (Figure 3.5) with the flow assumed to be laminar, with fixed CFL (global time-stepping). We choose the first grid point normal to the surface at 10^{-4} m with the K value for the Venkatakrishnan limiter chosen equal to 5. The steady-state convergence history (with the residual computed on energy) for CFL number of 0.1 and 0.175 are shown in Figures 3.6(a) and 3.6(b) respectively, for both SGG and MGG reconstructions. It is easy to observe that while the MGG reconstruction results in a smooth convergence history for both Courant numbers, the solver fails to converge at the larger CFL when SGG reconstruction is employed. One can, therefore, see that while the MGG reconstruction remains numerically stable up to a CFL number of 0.175, the flow solver encounters numerical instability for CFL numbers exceeding 0.1 with SGG reconstruction. The numerical solutions from the MGG reconstruction at higher CFL are also reasonably accurate as can be seen from Figures 3.7(a) and 3.7(b) which show a comparison of the skin friction and surface pressure respectively with the experimental data of Holden [109]. These results demonstrate the performance of MGG reconstruction in flows requiring the use of limiters and show that the proposed gradient reconstruction allows the use of a larger CFL (for an explicit solver) without affecting the solution accuracy.

Table 3.3: Comparison of computational time to achieve steady-state solution using SGG and MGG reconstructions for hypersonic flow past compression ramp. The blanks indicate that the solution process did not converge

Reconstruction	CFL = 0.1	CFL = 0.1	CFL = 0.175	CFL = 0.175
	Iterations	time/iterations (in s)	Iterations	time/iterations (in s)
SGG	335191	0.057	-	-
MGG (8 iterations)	368685	0.154	210679	0.135
MGG (no iterations)	369108	0.064	210922	0.056

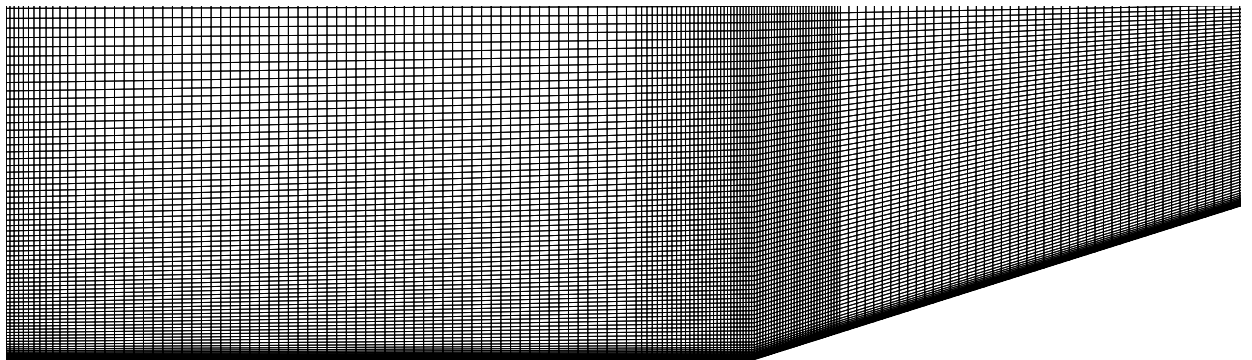


Figure 3.5: Computational grid adopted for flow past ramp

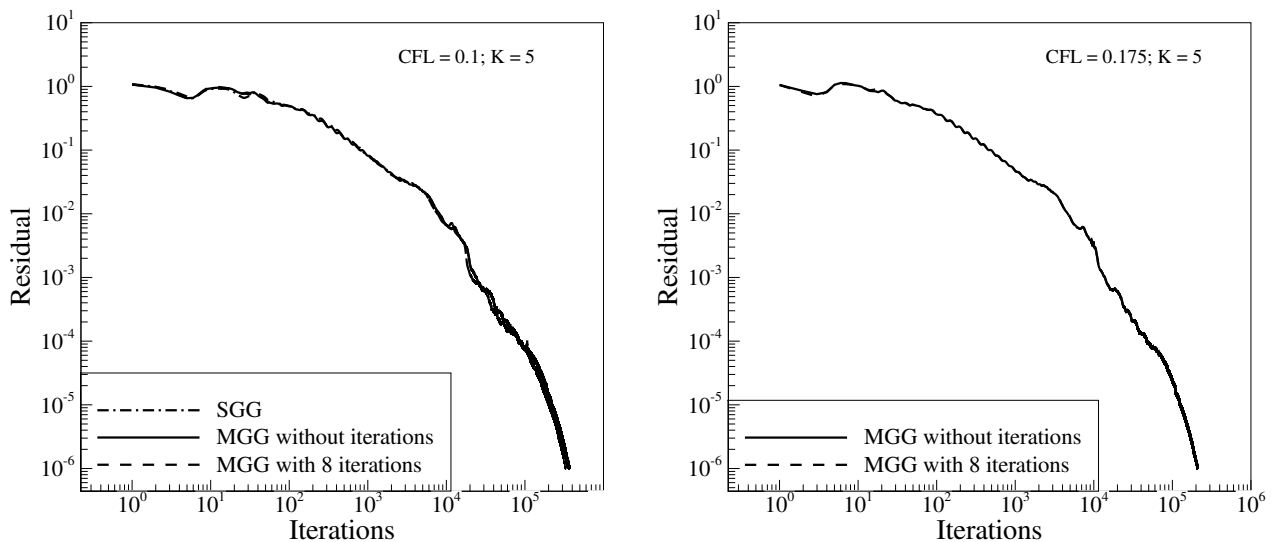


Figure 3.6: Steady-state convergence for flow past compression ramp at (a) $\text{CFL} = 0.1$ (b) $\text{CFL} = 0.175$

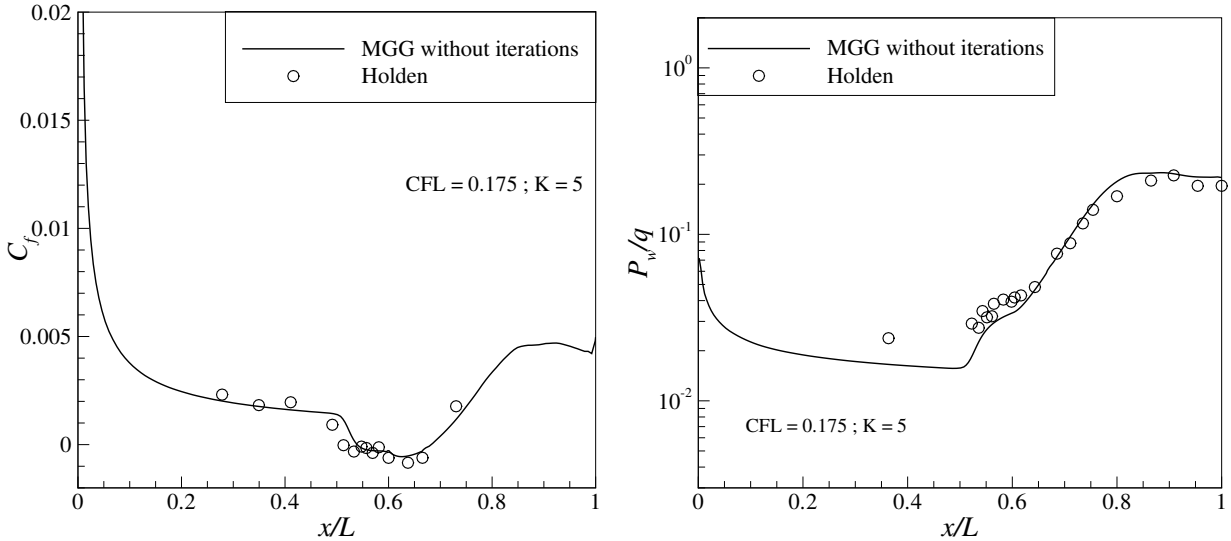


Figure 3.7: (a) C_f distribution for flow past compression ramp (b) P_w/q distribution for flow past compression ramp

We also show in Table 3.3 the time required to obtain the steady-state solution at both CFL numbers using SGG and MGG reconstructions. It must be emphasised that the MGG reconstruction has been carried out both with an iterative approach with a fixed number of iterations (chosen as 8) as well as the “non-iterative piggy-backing” approach for this test case. While the solutions from MGG reconstruction using both iterative and non-iterative approach are not different and agree well with those from SGG reconstruction and the experimental measurements, the time taken to reach steady-state convergence is clearly different. Employing MGG reconstruction with the iterative approach is clearly more expensive and incurs approximately twice the cost (per solver iteration) of SGG reconstruction. On the other hand, the CPU time per iteration using the non-iterative MGG reconstruction is quite comparable to that from SGG reconstruction without compromising on the solution accuracy. The use of the non-iterative approach in conjunction with MGG reconstruction marginally decreases the robustness (as compared with MGG reconstruction using an iterative approach) but results in a reconstruction that is more robust than SGG reconstruction and leads to accurate solutions at a computational cost comparable to SGG reconstruction. The accuracy of the MGG reconstruction for gradient computations on different mesh topologies with varying aspect ratio and skewness have been studied in detail in [98] where studies have also been performed for fluid-flow and heat-transfer problem in incompressible regime.

3.4 Summary

In this chapter we propose a simple and novel gradient reconstruction strategy referred to as Modified Green–Gauss (MGG) reconstruction. Derived from the Gauss divergence theorem, the MGG reconstruction has a compact stencil and gives a closed-form expression for numerical gradients on orthogonal meshes. However, on more generic meshes with non-orthogonality, the reconstruction requires an iterative approach to determine the gradients. A cost-effective strategy of MGG reconstruction devoid of iterations for use in finite volume solvers has been proposed and it performs well for a range of compressible flow problems. The results from the extensive numerical investigations in this study highlight the MGG reconstruction as a simple, robust and cost-efficient approach for gradient computations on generic unstructured meshes.

CHAPTER 4

SHARP INTERFACE IMMERSED BOUNDARY FOR INVISCID FLOWS

“It doesn’t matter how beautiful your theory is. If it doesn’t agree with experiment, it’s wrong”

- Richard Feynman, *The Feynman lectures on physics*

A new finite-volume flow solver based on the hybrid Cartesian immersed boundary (HCIB) framework is developed for the solution of high-speed inviscid compressible flows. The immersed boundary method adopts a sharp interface approach, wherein the boundary conditions are enforced on the body geometry itself. A key component of the present solver is a novel reconstruction approach, in conjunction with inverse distance weighting, to compute the solutions in the vicinity of the solid-fluid interface. We show that proposed reconstruction leads to second-order spatial accuracy while also ensuring that the discrete conservation errors diminish linearly with grid refinement. Investigations of supersonic and hypersonic inviscid flows over different geometries are carried out for an extensive validation of the proposed flow solver. Studies on cylinder lift-off in supersonic flows further demonstrate the efficacy of the flow solver for computations with moving geometry. These studies conclusively highlight the capability of the proposed immersed boundary methodology as a promising alternative for robust and accurate computations of compressible fluid flows on non-conformal Cartesian meshes.

The contents of this chapter are published in “A sharp interface immersed boundary framework for simulations of high speed inviscid compressible flows”, International Journal of Numerical Methods in Fluids (2018)

Body conformal flow-solvers as discussed in Chapter 3, inspite of numerous advantages, are plagued with significant limitations. Some of the prominent limitations are associated with creation of good quality computational grid that can cater to complex geometries within reasonable user time, ease of handling moving bodies as well as shape morphing/changing geometries, requirement of greater data storage etc. These limitations pave way for Immersed Boundary (IB) solvers however, most studies concerning IB solvers have been subjected to incompressible flows and low-speed compressible flows. This provides a motivation to investigate the use of sharp interface IB solvers for high-speed compressible flows for complex geometries and is precisely the focus of the present study. Although the principle of discrete forcing in the present study is similar to the one in [67], we borrow aspects of interpolation strategies from [110] for the proposed immersed boundary method. The IB strategy is embedded within an unstructured data based finite volume flow solver for compressible flows to enable numerical simulations of inviscid high-speed flows with stationary and moving geometries of varying complexity. We focus on the important yet less-addressed issue of discrete conservation in sharp interface IB frameworks. The remainder of the chapter is organised as follows. The sharp interface IB is dealt with in detail in Section 4.1. Sections 4.2 and 4.3 are devoted to two important issues pertaining to the IB framework - discrete conservation and spatial accuracy. Various test problems which involve steady and unsteady flows are presented in Section 4.4.

4.1 Sharp interface immersed boundary method

We discuss the details and implementation of the sharp interface immersed boundary (IB) method in the FV framework, discussed in Chapter 2. The proposed approach is rooted in the immersed boundary philosophy wherein the computational domain is discretised using a background mesh and rigid solid bodies are simply “immersed” into the mesh. This leads to a non-conformal approach, unlike traditional CFD solvers, with the mesh not conforming to the shape of the solid body with the challenge being the transmission of the boundary condition on the solid surface to the background mesh. The background grids are typically Cartesian or curvilinear with the geometry discretised using a set of linear segments¹. The key principle of the sharp interface IB method is that the “sharp” representation of the geometric interface needs to be preserved (and hence utilised) in the course of computations of the discrete numerical solution. The IB approach can be considered as a two-step process with two distinct steps viz. classification and reconstruction.

¹In three dimensions, the surface is triangulated, but we consider only two-dimensional problems in this study

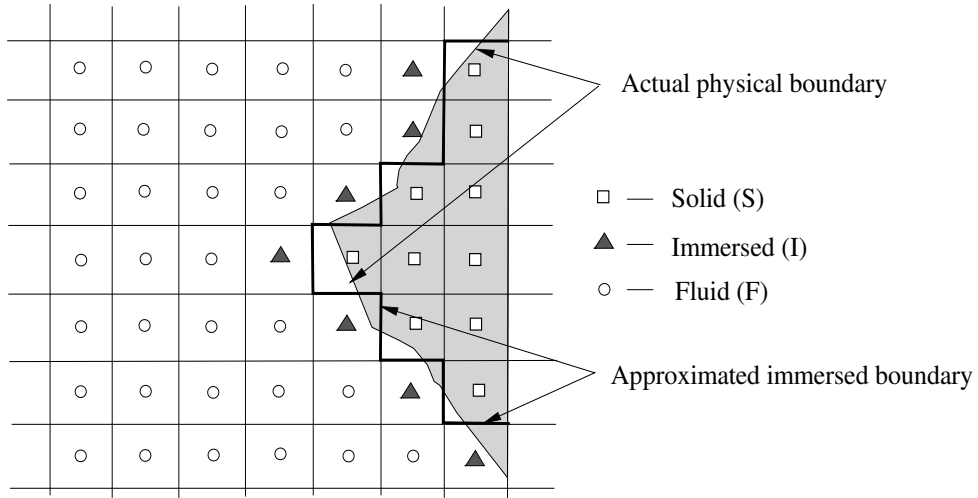


Figure 4.1: Classifications of cells in the immersed boundary finite volume (IB-FV) solver

4.1.1 Classification

The first step in HCIB approach is to identify the cells (or control volumes) that lie within the fluid and solid as well as in the vicinity of fluid–solid interface. We use an efficient ray–casting algorithm [65] to identify cells as solid (S), fluid (F) and immersed (I). Cells whose centroids lie within the body are classified as *S* while those lying outside the body are marked as *F*. The immersed cells are those *F* cells which share at-least one face with a *S* cell. This three–way classification is a critical step in the IB approach as it distinguishes between cells where the Euler equations need not be solved (*S* and *I* cells) and the cells where the discrete equations are employed to obtain the numerical solution (*F* cells). Figure 4.1 shows a typical Cartesian mesh with the immersed solid and the classification of cells in the vicinity of the body. It is evident that the classification ensures that no *F* cells share a face with a *S* cell and vice-versa. This is of consequence in moving body simulations, where the time-step is chosen such that any *S* cell that becomes a *F* cell (as the body moves) or vice-versa does not do so without becoming an *I* cell.

4.1.2 Reconstruction

The second and arguably the more critical step in the IB methodology is the reconstruction process. As mentioned earlier, the solution in the immersed cells (*I* cells) are not obtained from the governing differential equations. Rather, we employ a simple algebraic approach to “reconstruct” the solution in these cells using the solution in

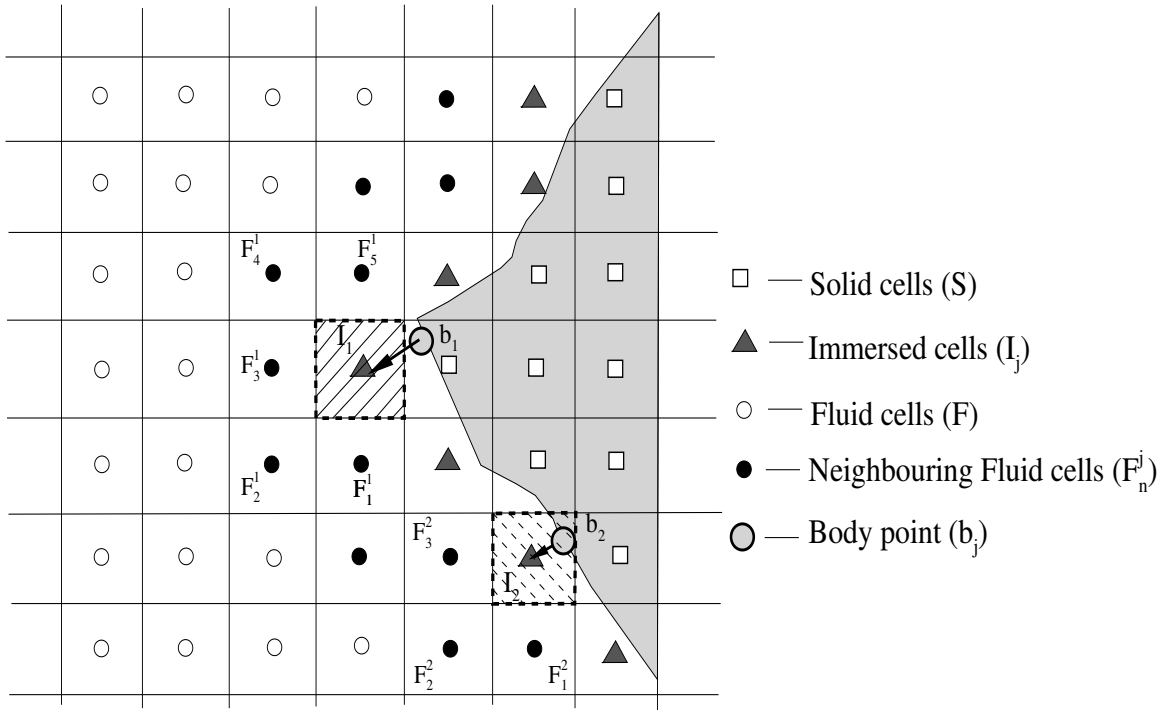


Figure 4.2: Schematic of reconstruction scheme where subscript j refers to the immersed cell

F cells along with the physical boundary condition on the sharp geometric interface. The IB reconstruction may itself be described as a three-stage process and can be seen as a modification of the approach in [110] for compressible flows.

The first stage consists of identifying the neighbourhood for each I cell. We define in this study the neighbourhood for the I cell as the set of all F cells that share atleast a node with the I cell. These node-sharing neighbours are clearly depicted in Figures 4.2 and 4.3. The present choice of neighbourhood is compact, preserves data locality, has atleast 3–5 neighbours, as also recommended in [50] and suffice for accurate computations. In the second stage, a local normal is drawn from the centroids of each of the ‘ I ’ cells so as to intersect the discretised geometry at the point ‘ b ’, which is referred to as the body point. The third and final stage effects the reconstruction by calculating the value of primitive variables in the immersed cells. This is achieved by employing inverse-distance weighting (IDW) in conjunction with the solutions available in the neighbourhood and the physical boundary condition (Figure 4.3, where other immersed/solid cells in the vicinity are non-participating). The approach of using IDW in the framework of IB methods is not entirely new and has been previously employed in [50]. It must also be remarked that the use of inverse-distance

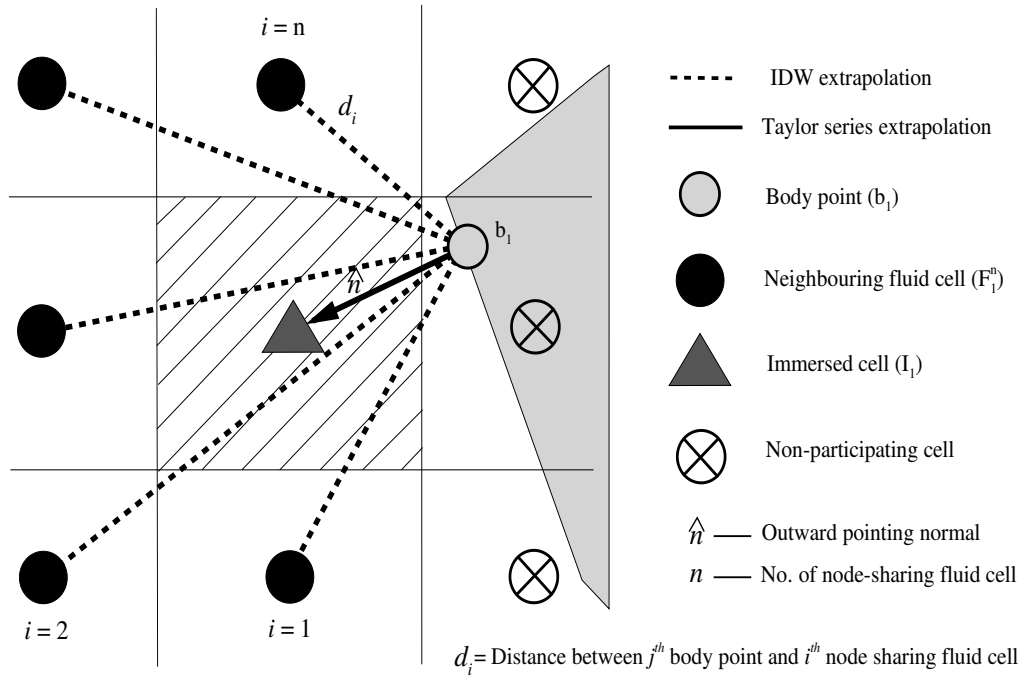


Figure 4.3: Computational stencil for inverse-distance weighting (IDW) reconstruction

weights gives more prominence to the cells that are closer to ‘ b ’ than the farther ones, ensuring that data locality is not getting lost. However, the specific implementation of IDW for sharp-interface IB solvers in the context of compressible flows has not been reported previously to the best of the our knowledge making it a novel contribution of the present study. We shall now discuss the specific details of this implementation which forms the core of the reconstruction process and therefore of the proposed IB–FV solver.

The reconstruction process first uses the IDW to calculate fluid properties and their gradients at b as,

$$\phi_b = \frac{\sum_{i=1}^{i=n} w_i \phi_i}{\sum_{i=1}^{i=n} w_i} \quad (4.1)$$

$$\nabla \phi_b = \frac{\sum_{i=1}^{i=n} w_i \nabla \phi_i}{\sum_{i=1}^{i=n} w_i} \quad (4.2)$$

where, $w_i = 1/|d_i|$, $|d_i|$ being the distance between the centroids of the i^{th} neighbour (which is a F cell) and b . Here, n represents the total number of cells in the neighbourhood of the immersed cell. Recall also that every I cell is associated with

an uniquely defined b point. Subsequently, one can compute the values of the fluid properties and their gradients at I cells using a truncated Taylor series expansion as,

$$\phi_I = \phi_b + \nabla\phi_b \cdot \mathbf{r}_{I-b} \quad (4.3)$$

$$\nabla\phi_I = \nabla\phi_b \quad (4.4)$$

where, \mathbf{r}_{I-b} is the vector joining the centroid of the I cell and its corresponding body point. It is easy to see that the solution gradients at the immersed cells are same as that at the body point and follows a constant polynomial reconstruction unlike the solution itself which employs a linear reconstruction. We choose to do so because the evaluation of the Hessians if they were to be used for a high-order reconstruction of solution gradients at the I cells, would become a computationally expensive task. Furthermore, we show in the subsequent sections that the simplification of using non-identical truncated Taylor series for the solution and its first derivatives does not adversely affect the spatial accuracy of the flow solver. **For all studies presented hereafter, we employ SGG reconstruction for computing the gradients.**

At this juncture, it is important to discuss the implementation of the boundary conditions and its role in reconstruction. It must be emphasised that the physical boundary conditions need to be suitably accounted in any non-conformal approach for physically consistent solutions. Importantly, in the present study, these conditions are enforced on the sharp interface itself and therefore are considered to be known at the respective b points of each I cell. It is therefore evident that the reconstruction process defined in Eqs. 4.3 and 4.4 must employ the known values of the fluid property or its gradients rather than those calculated using IDW in Eqs. 4.1 and Eqs. 4.2. For Dirichlet boundary conditions, one must use the known values of ϕ at the b points in Eq. 4.3 instead of employing Eq. 4.1, although the gradients at the b points would still rely on IDW through the use of Eq. 4.2. In the case of Neumann boundary conditions, the values of fluid properties at the b point are obtained using IDW via Eq. 4.1 while the gradients appearing in the reconstruction (Eqs. 4.3 and 4.4) are imposed from the boundary conditions rather than using Eq. 4.2.

While the approach of enforcing the boundary conditions within the IB-FV solver is generic, we now discuss the specifics of its implementation for Euler flows. We choose to evaluate the pressure and its gradients at b points using IDW and reconstruct them to the I cells. This is in contrast to approaches that specify a curvature-corrected non-homogeneous Neumann BC for the pressure [65]. We adopt an analogous approach for

density as well, in contrast to approaches that enforce a zero normal entropy gradient [67]. The latter is an incorrect choice when curved shocks are involved and we shall demonstrate that our approach in handling pressure and density through the IDW and subsequent reconstruction leads to physically consistent numerical solutions. Unlike the scalars, the reconstruction of the velocity field needs to be addressed with more care. In the case of inviscid flows, there exists only a Dirichlet BC on the normal velocity, $u_{\perp b} = 0$, which follows from the impermeability condition on the rigid solid surface. To employ this physical BC, we first transform the (u, v) components to those normal and tangential to the surface $(u_{\perp}, u_{\parallel})$. It is easy to see that,

$$\begin{aligned} u_{\perp b} &= u_b n_x + v_b n_y \\ u_{\parallel b} &= u_b t_x + v_b t_y = u_b n_y - v_b n_x \end{aligned} \quad (4.5)$$

where n_x and n_y are the components of the unit normal while t_x and t_y are those of the unit tangent at the solid surface. Recall that for stationary bodies $u_{\perp} = 0$, while in case of moving bodies they are either specified or follow from the solution to equations governing body motion (as is the case in this chapter). The gradients of u and v velocity components at the b points are evaluated using IDW and can be transformed into gradients of u_{\perp} and u_{\parallel} in a manner analogous to the components themselves. The reconstruction process then computes the normal and tangential components at the I cells instead of u and v components, enforcing the Dirichlet BC during this stage. The velocity components (u, v) at the I cells can then be obtained by a reverse transformation that reads,

$$\begin{aligned} u_I &= u_{\parallel I} t_x + u_{\perp I} t_y \\ v_I &= u_{\parallel I} t_y - u_{\perp I} t_x \end{aligned} \quad (4.6)$$

where the quantities in the rights hand side have been evaluated by the IB reconstruction. In case of moving bodies where the motion is induced by the flow, the velocity components of the body are evaluated by solving the second-order ODEs describing Newton's second law of motion. This gives,

$$\begin{aligned} u_b^{k+1} &= u_b^k + \frac{\Delta t}{M_b} F_x^k \\ v_b^{k+1} &= v_b^k + \frac{\Delta t}{M_b} F_y^k \end{aligned} \quad (4.7)$$

where k and $k + 1$ represent the present and next time step, respectively and M_b is the mass of the body. The force components (F_x, F_y) are evaluated by integrating the pressure exerted on the solid surface(s) using single point Gauss quadrature. It

must be remarked that since the IB approach is non-conformal, we choose the contour of integration as the set of grid faces in the vicinity of the body, which leads to an approximated domain stair-step representation as in [111]. The pressure at those faces are simple the cell-centroidal value from the corresponding immersed cell. The errors from this approximation reduces as the grid resolution in the near-solid regions increases and our studies show that for the grid resolutions considered herein these errors insignificantly influence the force calculations.

4.2 Discrete Conservation

A major issue in non-conformal approaches including immersed boundary methods, particularly for compressible flows, is that of discrete conservation. Since the governing partial differential equations represent conservation of mass, momentum and energy, numerical techniques used to solve them at the discrete level should also preserve this property. While the lack of conservation in IB solvers for incompressible flows has been addressed to some extent [112], there have been no dedicated efforts in this direction for their compressible counterparts. It is clear that the use of IB reconstruction, which employs an algebraic approach to compute the solution at I cells rather than the solution to the weak form of the conservation laws (as done in F cells) raises questions of both conservation and overall accuracy. We deal with the latter in section 4.3 while the former is discussed here using two different test problems viz. transonic flow past 10% thick bump and supersonic flow past wedge.

4.2.1 Transonic flow past bump

We first study the transonic flow past a bump inside a channel where the expansion on the bump surface is followed by a strong normal standing shock. We choose the Ni's test case [113] with a circular arc bump of unit length and 10% thickness in a domain of size 3×1 , as shown in Figure 4.4 and an inlet Mach number $M_\infty = 0.675$. For this test case, we fix the outlet static pressure as $P_{out} = 0.737$, which causes a standing shock to be formed nearly three-quarters from the leading edge of the bump. We compute the numerical solutions on four different uniform but non-conformal Cartesian meshes viz. 150×50 , 225×75 , 300×100 and 450×150 using the proposed IB-FV solver. Computations are also carried out on body-fitted curvilinear meshes of similar resolution using the unstructured finite volume solver. Figures 4.5(a)-(d) show the Mach contours which clearly show the standing normal shock on the surfaces. While the results on the coarser meshes are smeared for both, the shock is more crisply resolved on the finer meshes. Interestingly, the results show that the shock locations predicted by the

IB-FV solver is different from that on the curvilinear body-fitted grid. A closer look at Figures 4.5(b)-(d) also show that the error in shock locations diminish as the grid becomes finer. This is also reflected in Figure 4.6(a) which shows the C_p distributions on the four Cartesian grids, compared with that of the solution on the body-fitted mesh. The IB-FV results on the finest mesh shows a less-diffused shock closer to that predicted by the unstructured FV solver (on the body-fitted mesh) while the results on progressively coarser meshes are more diffused and show a farther shock location. In contrast, the C_p distributions over the bump in Figure 4.6(b) for the body-fitted meshes show that the “average” shock location is indeed the same, independent of the grid resolution.

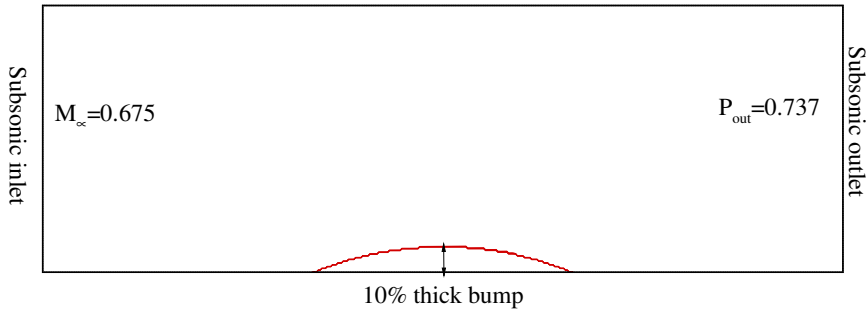


Figure 4.4: Computational domain for transonic flow past bump along with boundary condition

One can infer from these observations that the IB-FV results approach those obtained on conformal meshes using the unstructured FV solver as $h \rightarrow 0$ where h is the characteristic length scale². It must be realised that the unstructured FV approach is discretely conservative on all meshes, which explains why the shock location is correctly predicted on all four curvilinear meshes. The IB-FV solver predicts a different shock location on each mesh and even on the finest mesh, the shock location shows a deviation from that predicted by the unstructured FV solver, although the differences in the predictions are evidently smaller than those on the coarser meshes. It follows therefore that the IB-FV solver is not discretely conservative but the conservation errors do diminish as the grid is refined.

²On uniform Cartesian meshes, $h = \Delta x = \Delta y$ while on unstructured meshes we consider $h=1/\sqrt{nc}$ where nc is the total number of cells in the mesh

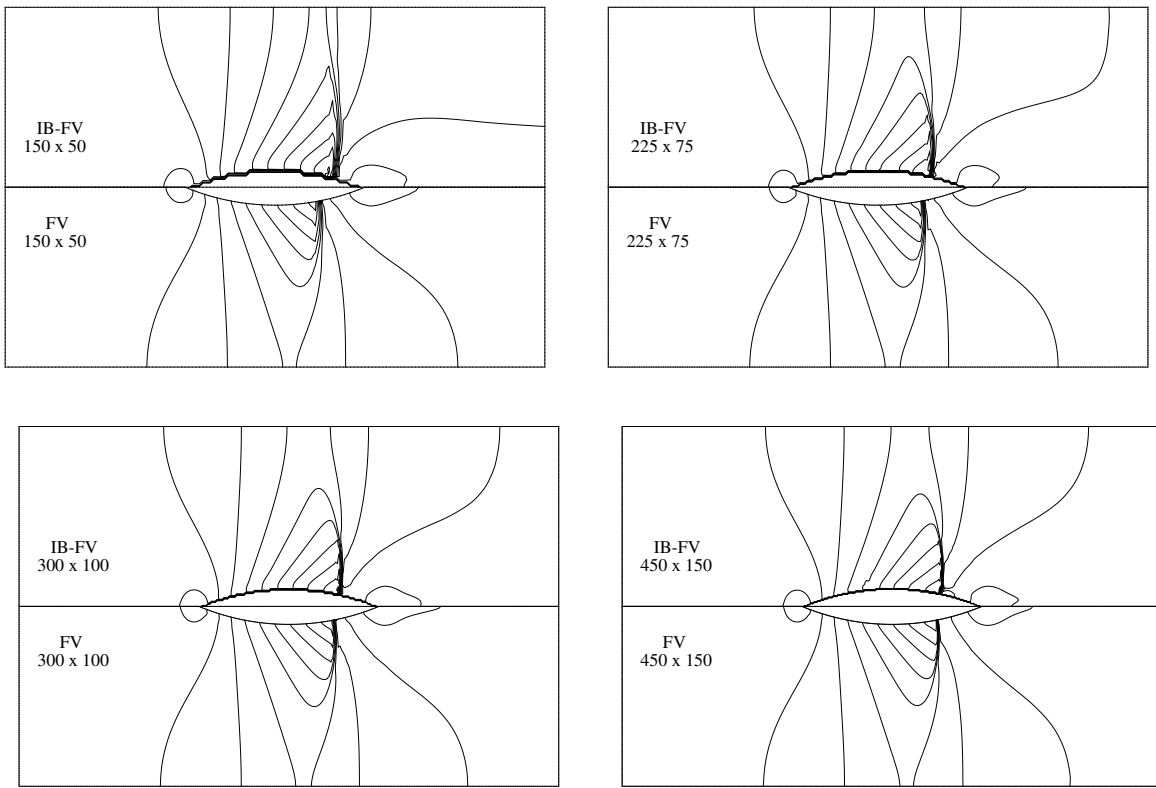


Figure 4.5: Mach contours depicting normal standing shock for different grid (a) 150×50 (b) 225×75 (c) 300×100 (d) 450×150 (Min: 0, $\Delta : 0.117$, Max: 1.52) (Top:- IB-FV solver; Bottom:- FV solver on body fitted mesh)

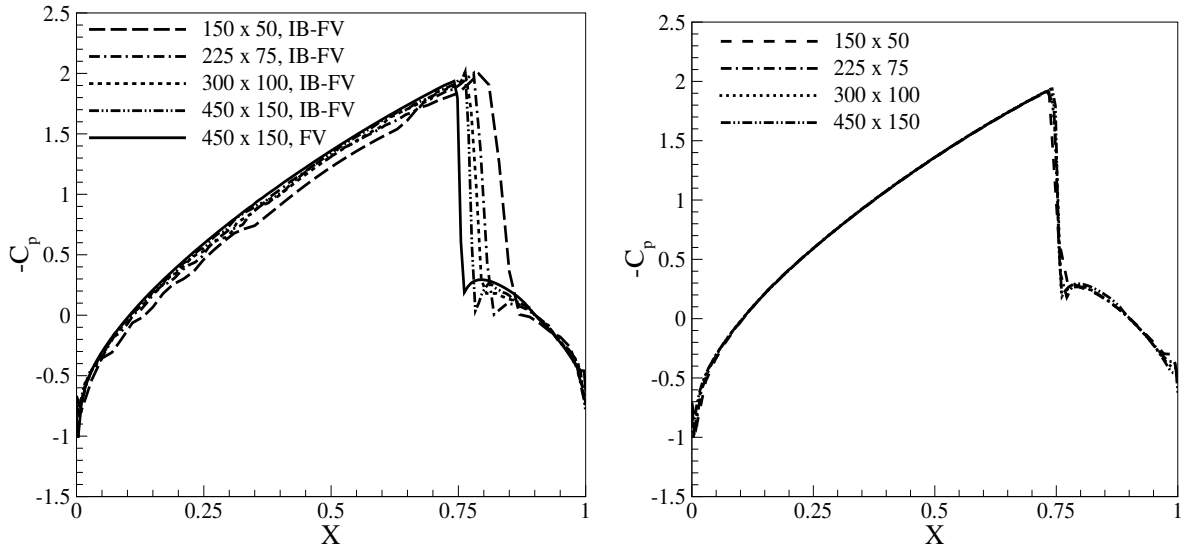


Figure 4.6: Coefficient of pressure distribution along the surface of the body from (a) IB-FV solver on non-conformal grid (b) FV solver on conformal grid

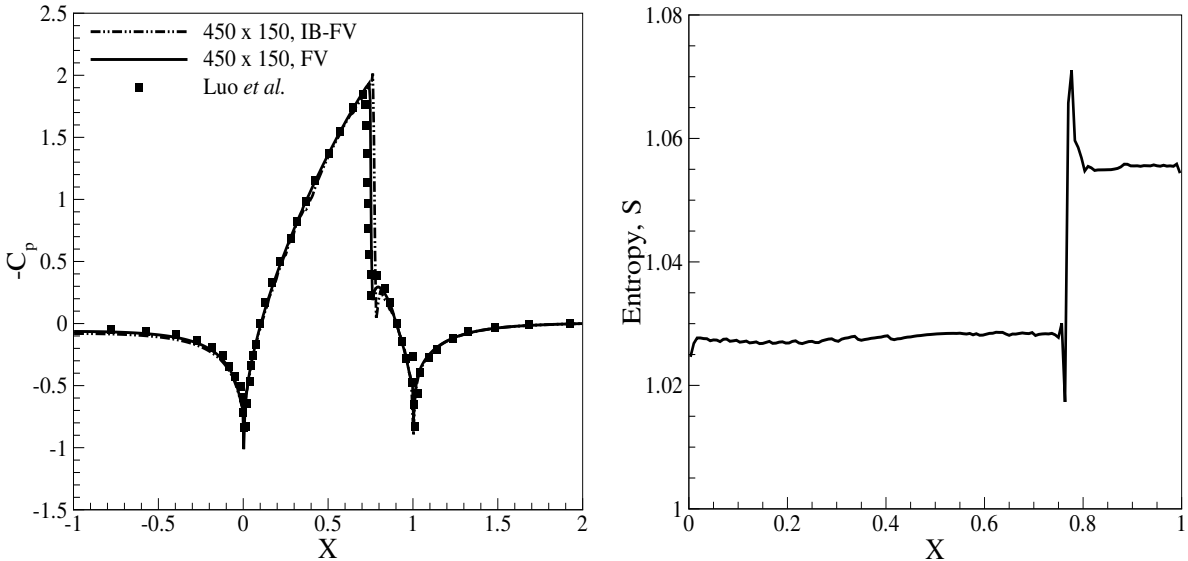


Figure 4.7: (a) Coefficient of pressure distribution along the surface of the body on conformal and non-conformal mesh (b) Numerical entropy generation along immersed cells

This test case also serves to study the efficacy of the IB approaches for problems with a non-conformal geometry and strong compression. One can see from Figure 4.7(a) that the pressure distribution on the surface of the bump using the IB-FV solver on the 450×150 grid agrees well with those computed by Luo et al. [114] as well as that obtained using the unstructured FV solver on body-fitted mesh of equivalent resolution. The distribution of numerical entropy $S = P/\rho^\gamma$ in Figure 4.7(b), on the surface of the bump clearly indicates a jump at the location of the standing shock, which makes it a good indicator of discontinuities in compressible flows. This test problem effectively achieves the twin-objectives of investigating discrete conservation and validating the solver on flow past curved geometries **with strong compression**. Our results show that discrete conservation can only be achieved in the limit as the grid size tends to zero and on sufficiently fine meshes the IB-FV solver does compute the numerical solution to reasonable accuracy.

4.2.2 Supersonic flow past wedge

As a second test case in analysing the issue of discrete conservation, we simulate the supersonic flow past a wedge of semi-vertex angle of 20° at freestream Mach number $M_\infty=2$. While the geometry for this test case is quite simple, the use of IB-FV solver with a uniform Cartesian mesh means that the **body is not aligned** with the background mesh. Moreover, the flow creates an **attached shock at the leading edge which is also not aligned with the grid**. We carry out simulations on four different meshes on a

domain of size 0.1×0.15 maintaining unit aspect ratio cells on all grids. The details of all grids are shown in Table 4.1 along with their respective characteristic lengths. For all these simulations, we also compute the mass defect defined by

$$\Delta m = \sum \rho_f U_{\perp,f} \Delta S_f \quad (4.8)$$

where the summation is over all the boundary faces of the domain as well as the interior faces shared by S and I cells. In other words, Eq. 4.8 is a summation of the mass fluxes through the inlet and outlet as well as the body surface, which is approximated by the stair-step representation in Figure 4.1. On body-conforming grids, the mass flux through the body surface would be zero and the mass fluxes through the inlet and outlet would differ by an amount which is of the order of residual at steady-state, which we also observed in our numerical studies (not reported here for sake of brevity). This is a consequence of the discrete mass preservation of FV solvers. In the case of IB-FV solvers, the solutions at I cells are reconstructed as opposed to F cells where they are “solved” and there would be a finite mass defect on any mesh even when steady-state solutions are obtained. Table 4.1 shows this mass defect on the four meshes at steady-state convergence, defined by the relative residual (in energy) becoming 10^{-6} or lesser. On the backdrop of observations in Section 4.2.1, it is not surprising to see mass defects that are three orders of magnitude larger than the residual errors. This clearly shows that the IB-FV solver does not discretely conserve mass on any mesh but the errors do diminish as the grid becomes finer. Figure 4.8 shows that the discrete conservation errors, which are quantified by the mass defect at steady-state in this case, indeed decrease linearly with grid refinement. A similar result was obtained for a class of meshfree methods with regard to mass conservation [115]. This study reinforces the fact that there is a finite $O(h)$ conservation error for the IB-FV approach and it is strictly conservative only in the limit as the grid spacing tends to zero.

Table 4.1: Mass defect Δm on different grids

Grid	h	Δm
100×150	$1/100$	0.058
150×225	$1/150$	0.039
200×300	$1/200$	0.028
250×375	$1/250$	0.022

The lack of machine-zero conservation errors on any mesh using the IB-FV approach means that it is necessary that the Cartesian/curvilinear meshes employed for compressible flows are “sufficiently” fine in the vicinity of the bodies to keep con-

servation errors to acceptably low values. This may be achieved using local grid refinement. We emphasise that the studies on discrete conservation (and its errors) conducted herein for sharp interface IB methods is likely the first comprehensive exposition of this issue, unlike other studies which often ignore the problem or even implicitly assume that the use of fine meshes guarantee conservation.

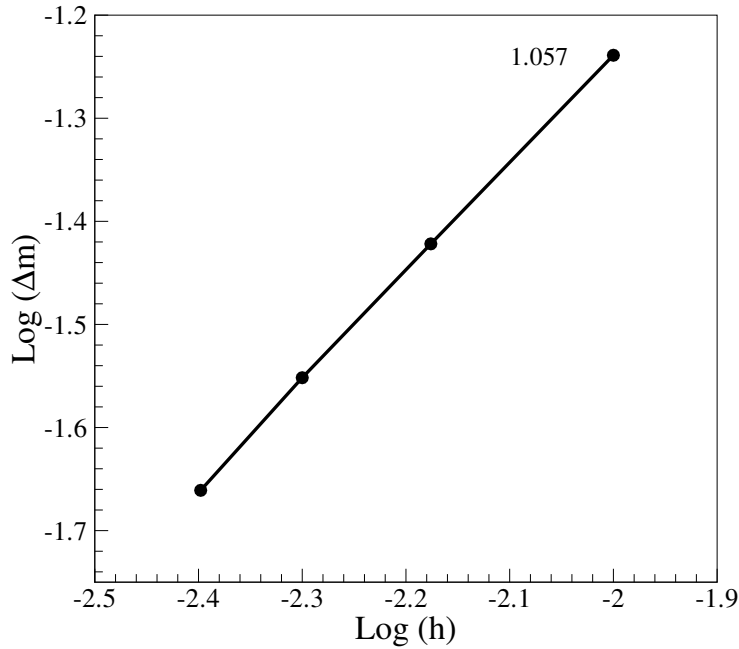


Figure 4.8: Variation of mass defect Δm with grid refinement

4.3 Order of accuracy study

A key concern, apart from conservation, in IB methods pertains to the order of accuracy. We investigate the order of accuracy of the IB–FV solver by considering the case of a supersonic vortex. The problem, which has an analytical solution, describes the **inviscid, isentropic flow between concentric circular arcs**. For the purpose of simulation, we immerse the channel into a square domain of size 1.5×1.5 which is discretised using a series of Cartesian meshes. It must be noted that the channel is defined by arcs of radii 1 and 1.384 respectively (Figure 4.9) and cells inside the channel (where the solution is desired) are marked as F cells and those outside of it as S cells, with a layer of I cells separating them. The analytical solution for this problem is,

$$\rho = \rho_i \left[1 + \frac{\gamma - 1}{2} \left(1 - \frac{R_i^2}{r^2} \right) M_i^2 \right]^{\frac{1}{\gamma-1}}$$

Here, ρ_i and M_i are density and Mach number respectively at inner radius R_i .

This expression gives density (ρ) at any radius r . In the present test case, M_i is set equal to 2.25 while ρ_i is kept at 1 for the inner radius. The velocity components and pressure are given by

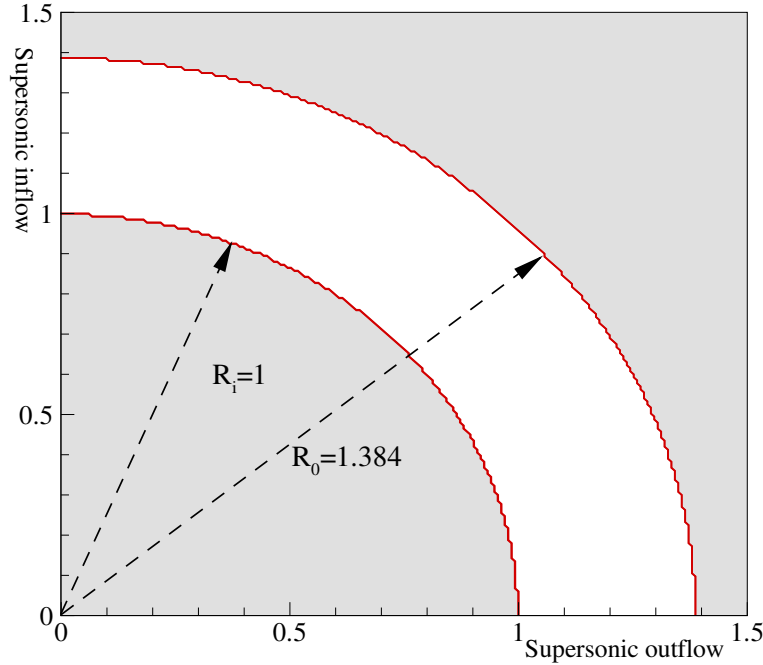


Figure 4.9: Computational domain for supersonic vortex flow

$$u = U_{Ri} \frac{y R_i}{r^2}; \quad v = -U_{Ri} \frac{x R_i}{r^2}$$

$$p = p_i \left[1 + \frac{\gamma - 1}{2} \left(1 - \frac{R_i^2}{r^2} \right) M_i^2 \right]^{\frac{\gamma}{\gamma-1}}$$

$$U_{Ri} = M_i a_i; \quad a_i = \sqrt{\frac{\gamma p_i}{\rho_i}}$$

$$\begin{aligned} \epsilon_2 &= \sqrt{\frac{\sum_{i=1}^{nc} (\rho_i - \rho_{exact})^2}{nc}} \\ \epsilon_\infty &= \max_i |(\rho_i - \rho_{exact})| \end{aligned} \tag{4.9}$$

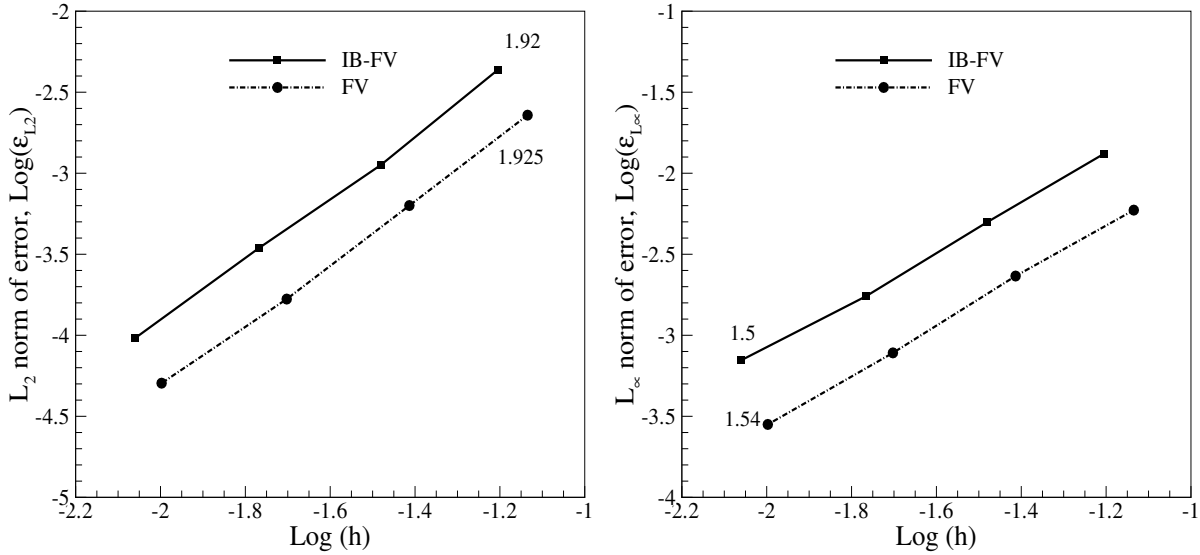


Figure 4.10: Order of accuracy for IB-FV (non-conformal grid) and FV (conformal grid) using (a) L_2 norm (b) L_∞ norm

We use four uniformly refined meshes starting from a coarse 25×25 grid. The unstructured finite volume solver was also employed on four body-fitted curvilinear meshes of similar resolution as the uniform Cartesian meshes in the IB-FV solver. The L_2 and L_∞ norms of error are calculated using Eq. 4.9 on all four meshes after steady-state convergence is achieved and the results are presented in Figures 4.10 (a) and (b). We see from Figure 4.10 (a) that the order of accuracy in the L_2 norm for both IB-FV and the body-fitted solver is approximately 2, which is indicative of the fact that the IB reconstruction does not degrade the nominal second-order global accuracy of the finite volume solver. The L_∞ norm in Figure 4.10 (b) however decreases with grid refinement at a marginally lower rate of 1.5 for both the IB and body-fitted solvers, with the error values from the Cartesian meshes (IB-FV solver) higher than those from its curvilinear counterparts. It must be remarked that the L_∞ error norm is a stringent test on the accuracy of the flow solver and reflects the largest errors in the domain (which are likely due to boundary treatment) in case of smooth flows such as those studied herein. Nevertheless, even in the L_∞ norm, the IB-FV solver shows an order of accuracy between 1 and 2 and therefore one can conclude that the proposed flow solver is second-order accurate.

4.4 Numerical investigations

In this section, we discuss the application of the compressible IB-FV solver for a number of test problems in the supersonic and hypersonic flow regimes. The test cases considered include both internal and external steady inviscid flows with one or more

solid bodies which may be stationary or moving. In order to realise the potential of the proposed solver, we also demonstrate its ability to accurately predict the trajectory of a moving body in an unsteady flow-field.

4.4.1 Supersonic flow past a cone

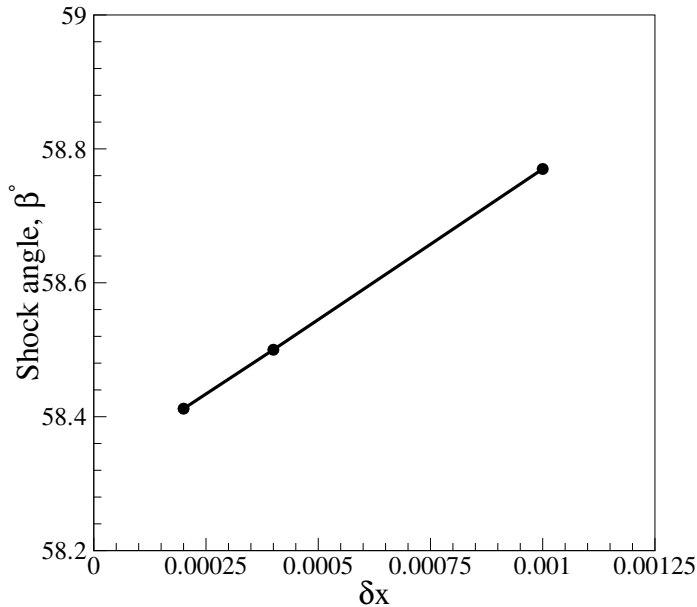


Figure 4.11: Shock wave angle β with grid refinement

We consider the flow past a slender cone of semi–vertex angle 20° , which is immersed in a domain of 0.1×0.15 . Three progressively refined uniform Cartesian grids viz. 100×150 , 250×375 and 500×750 are employed for the inviscid simulation at $M_\infty = 1.321$. Figure 4.11 shows the dependence of shock angle on the grid spacing with refinement. It can be seen that the value of shock angle approaches the analytical value of 58° as the grid is progressively refined and that the solutions on 250×375 mesh can be considered grid-independent. The pressure distribution on the conical surface obtained from the IB-FV solver on a 250×375 grid is compared with the pressure distribution obtained from the FV solver on a conformal mesh of similar resolution as well as with the exact solution for conical flows [116] in Figure 4.12 (a). It can be seen that the pressure distribution obtained from IB-FV solver shows a fair agreement with those obtained on body-fitted meshes as well as with the theoretical estimates from Taylor and MacColl [116]. However, the pressure distribution obtained from IB-FV solver is seen to be oscillatory at the apex of the cone with the amplitude of oscillations reducing along the length of the cone. This oscillatory nature of the surface pressure distribution found in the IB-FV results appears to reduce as the mesh

resolution is increased (Figure 4.12 (b)). It must also be remarked that we have carried out numerical studies for this configuration at higher Mach numbers where the oscillations in the surface pressure distributions, even on the 250×375 mesh, are significantly smaller. The numerical and experimental Schlieren images are compared in Figure 4.13 and show excellent agreement with the numerical estimate of shock angle deviating from the experimental value of 58° by about 1%. The solver also resolves the attached oblique shock crisply which is a manifestation of the high-resolution second-order convective scheme embedded in the IB-FV solver.

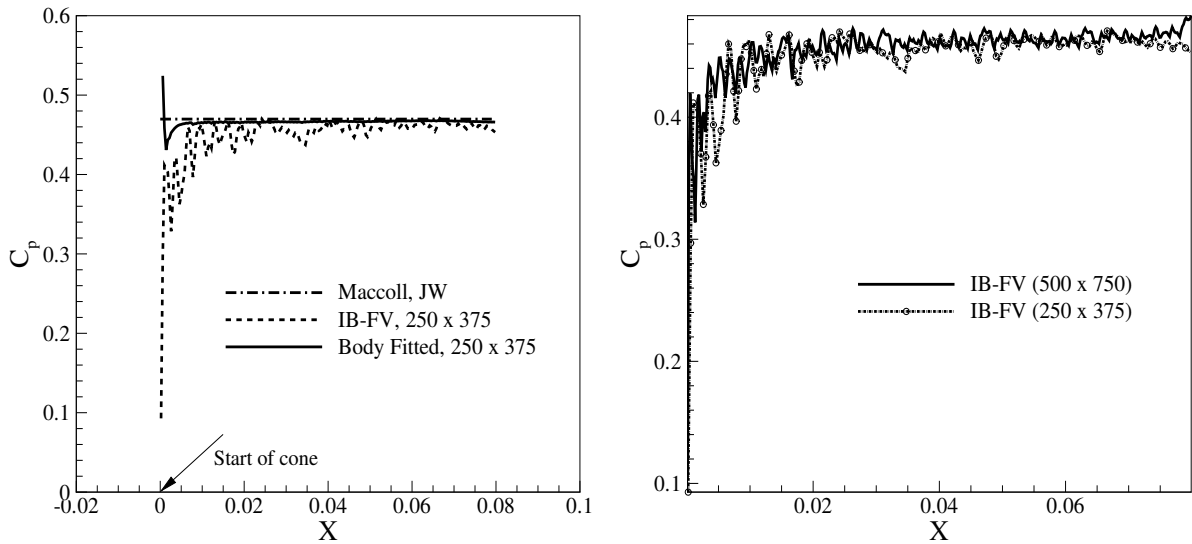


Figure 4.12: (a) Comparison of coefficient of pressure distribution with theoretical correlation and body-fitted FV result (b) Coefficient of pressure distribution using IB-FV solver on two different grid resolution (zoomed view)

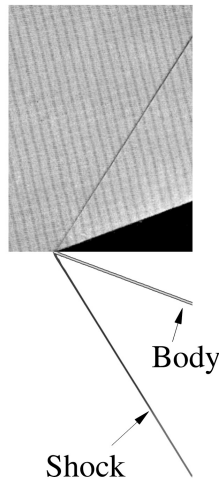


Figure 4.13: Comparison of numerical Schlieren (below) and experimental Schlieren (top) [116] for supersonic flow over cone

4.4.2 Hypersonic Flow past Sphere

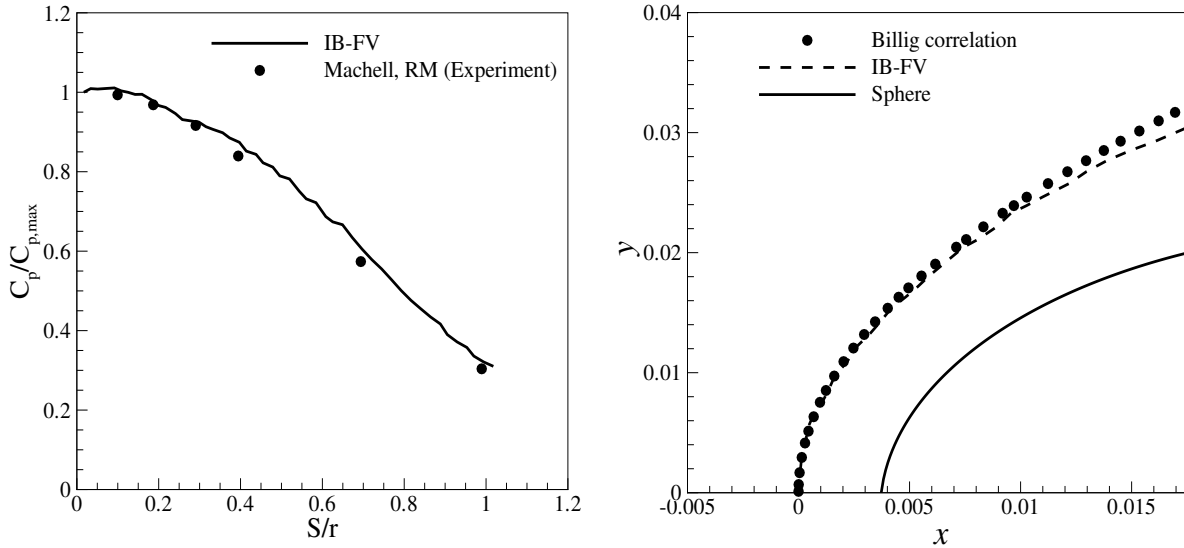


Figure 4.14: Comparison of (a) coefficient of pressure distribution obtained using IB-FV solver with experimental data (b) shock shape obtained using IB-FV solver with theoretical correlation

We now assess the ability of the solver to handle hypersonic flow past bluff bodies using this test case. A sphere of radius $r = 23.65$ mm is immersed in the same computational domain as described in section 4.4.1. The grid resolution employed for this inviscid test problem at $M_\infty = 5.8$ is also identical to those used for the conical body earlier. The results from the solver are summarised in Figures 4.14 (a) and (b) which respectively show the pressure distribution on the surface and the shape of the detached bow shock. One can see that the surface pressure distribution agrees quite well with the experimental measurements of Machell [117] while the numerically predicted shock shape agrees excellently with the one obtained from Billig correlation [118]. Figure 4.15 which compares the experimental visualisation and numerical Schlieren also provides additional evidence that the proposed IB-FV solver can accurately compute hypersonic flow past axisymmetric geometries.



Figure 4.15: Comparison of numerical Schlieren (below) and experimental Schlieren (top) [117] for hypersonic flow over sphere

4.4.3 Hypersonic flow past a double ellipse

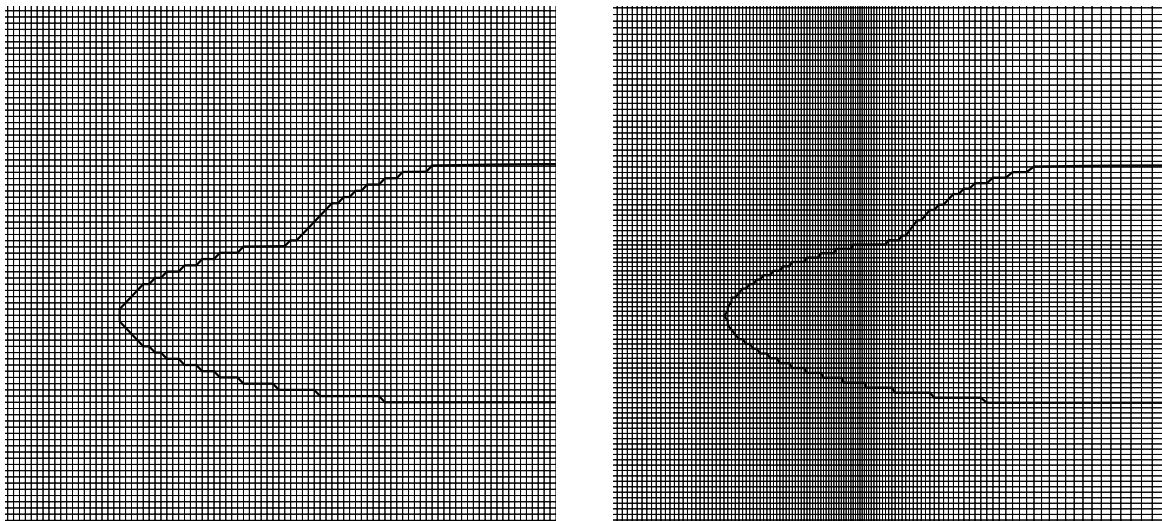


Figure 4.16: (a) Uniform (b) non-uniform Cartesian grid employed in IB-FV solver for flow over double-ellipse

All the test cases discussed earlier demonstrate the ability of the proposed flow solver to handle inviscid high-speed flows past supersonic or hypersonic configurations and also serve as validation tests for the IB-FV solver with the numerical solutions showing good agreement with theoretical estimates and/or experimental results. To investigate the ability of the solver to resolve flow phenomena at **high angles of attack** past complex geometries, we consider the $M_\infty = 8.15$ flow past a double ellipse. The flow is at

an angle of attack $\alpha = 30^\circ$ to the horizontal and the ellipse whose dimensions are same as those in [119] is immersed into a computational domain of size $[-0.1, 0.1] \times [-0.1, 0.1]$. Two different Cartesian meshes, one which is uniform and the other non-uniform, but with the same number of control volumes (equal to 36000) are used for the simulations as shown in Figure 4.16.

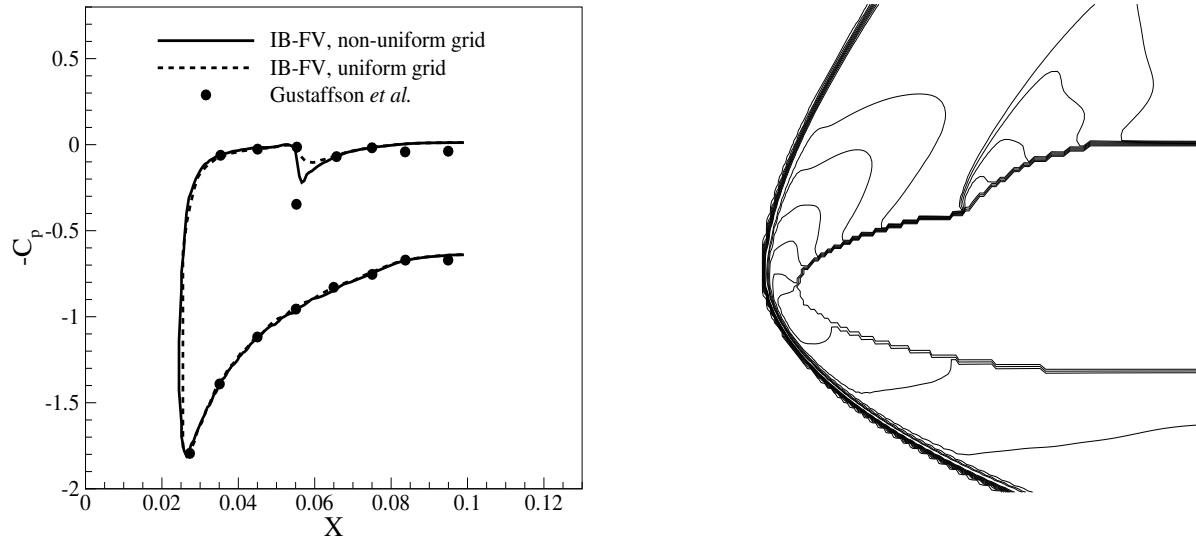


Figure 4.17: (a) Coefficient of pressure distribution (b) Mach contours for double ellipse (Min: 0, Δ : 0.5, Max: 8.15)

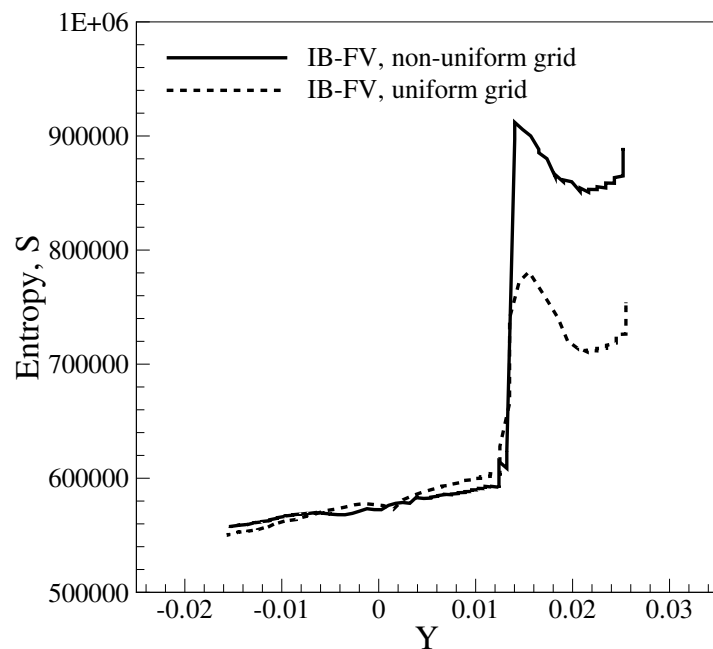


Figure 4.18: Entropy distribution on uniform and non-uniform grid

The importance of the non-uniform mesh in the context of IB-FV solver is evident from the surface pressure distribution shown in Figure 4.17 (a). It is clear that the jump across the canopy shock is smeared on the uniform mesh while the non-uniform grid resolves the weaker canopy shock quite accurately. This is also reflected in the Mach contours (on the non-uniform mesh), where both the stronger bow-shock and weaker canopy shock are adequately resolved (Figure 4.17 b). Additionally, we also present the entropy distribution along the surface of the body on both meshes in Figure 4.18 and one can notice a sharp rise in entropy in the canopy region which corresponds to the weak shock. Moreover, it can be observed that the peak value of entropy is also under-predicted when a uniform grid is employed to resolve the jump discontinuity. This justifies the choice of non-uniform mesh near the canopy region to sharply capture the entropy rise, due to the presence of shock. In other words, this also suggests that the ability of IB reconstruction to resolve weaker features is strongly dependent on the grid resolution in the near-wall regions and for this problem critical in resolving the geometric slope discontinuity and subsequent weak shock.

4.4.4 Hypersonic flow in a scramjet intake

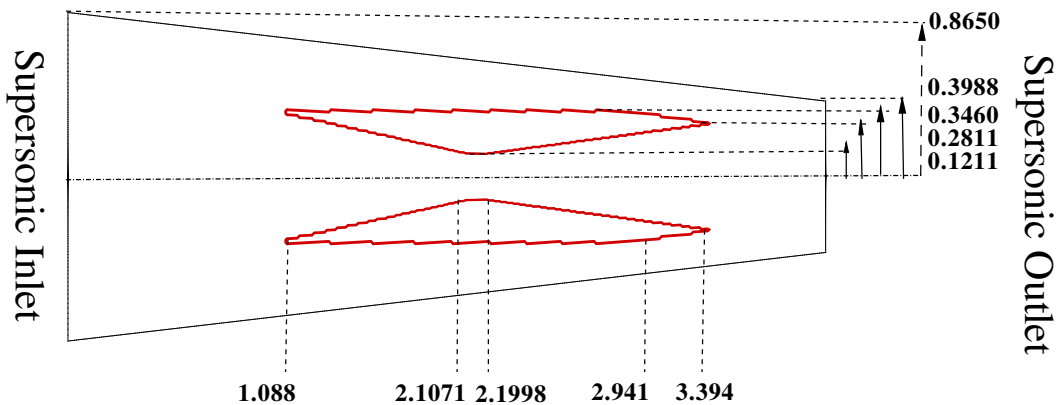


Figure 4.19: Scramjet geometry

We consider the inviscid flow through a scramjet intake at a freestream Mach number of $M_\infty = 5$. The scramjet geometry is shown in Figure 4.19 and for purpose of simulation, the struts are immersed into the convergent computational domain. The presence of multiple struts allow the testing of the solver with more than one objects and the domain naturally demands a non-Cartesian structured grid. A non-uniform curvilinear mesh of 158400 volumes is used for the studies (Figure 4.20) and the Mach contours obtained are shown in Figure 4.21. It is easy to see that the flow solver accurately

captures all relevant flow phenomena including the shock reflections from the strut surfaces and domain boundaries. In addition, one can also notice the expansion fans and slip stream as well as their interactions with the shock. Due to the coarseness of the mesh away from the struts, these interactions, as well as the shock reflections from the domain boundaries are relatively diffused. The center-line Mach number distribution from the present study, therefore compares well with those of Praveen and Deshpande [120] as can be seen from Figure 4.22 (a). We also show the surface pressure distribution along the surface of the top and bottom wall of the strut in Figure 4.22 (b). The surface pressure distribution is devoid of any oscillations and the sudden jumps are indicative of the various shock interactions taking place along both the top and bottom walls of the struts. This test serves to demonstrate the ability of the sharp interface IB approach to work well on non-Cartesian grids with multiple bodies while adequately resolving multiple interactions in hypersonic regime. It must be stressed that present test case would show sharper flow features and better resolved interactions when solution-adaptive mesh refinement is employed, which is a matter of future work.

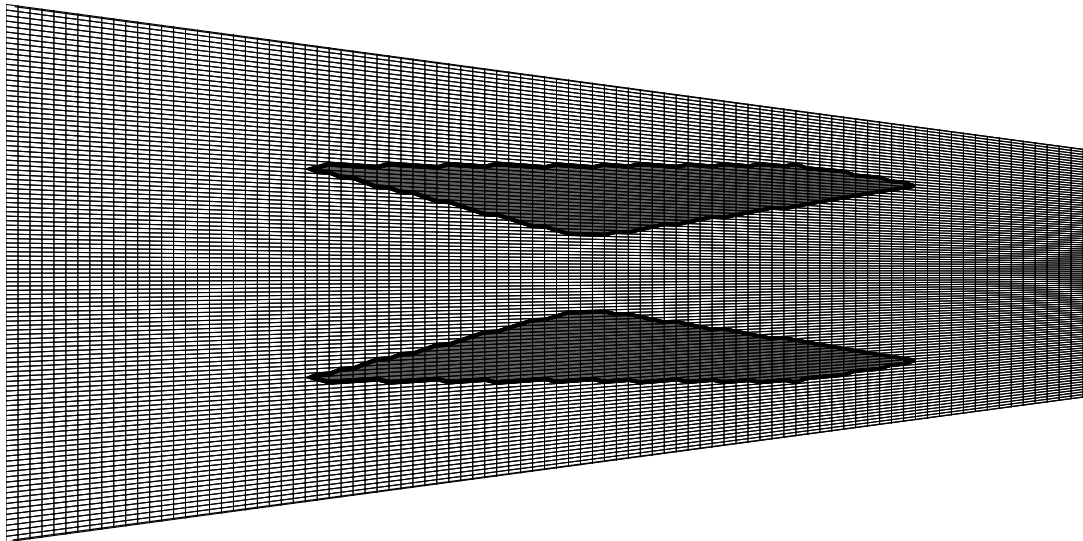


Figure 4.20: Curvilinear grid used with struts immersed in it (every fourth grid line shown)

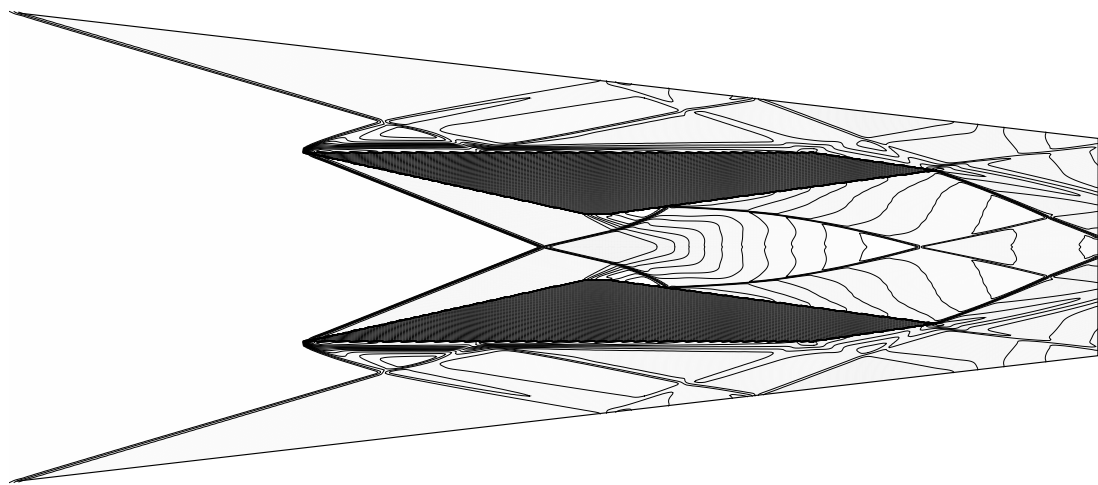


Figure 4.21: Mach contours for scramjet simulations (Min: 0, Δ : 0.22, Max: 5.4)

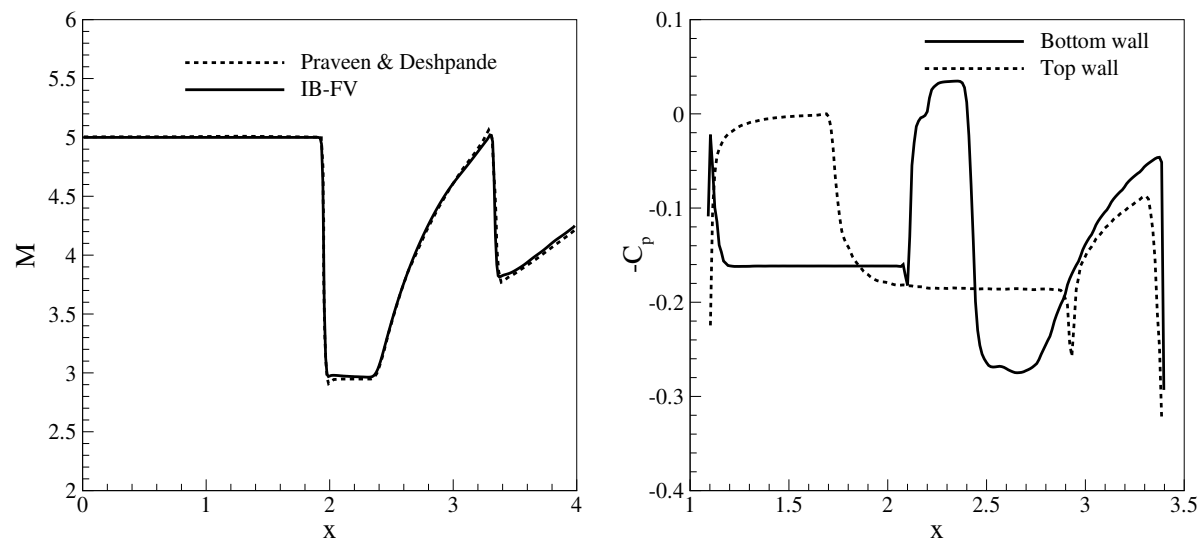


Figure 4.22: (a) Center-line Mach number variation (b) Pressure coefficient distribution along the surface of scramjet struts

4.4.5 Supersonic flow with moving bodies: Cylinder lift-off

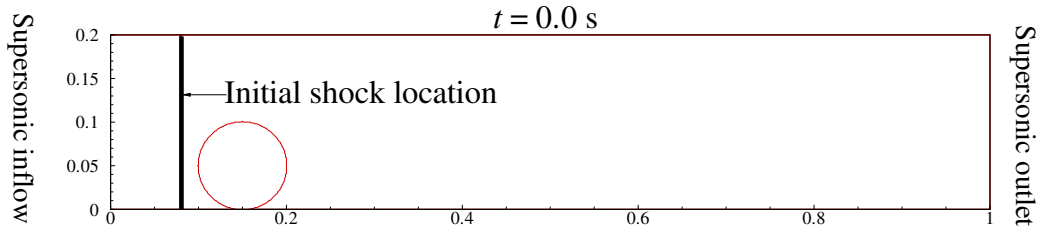


Figure 4.23: Location of body and shock at time $t = 0$ s

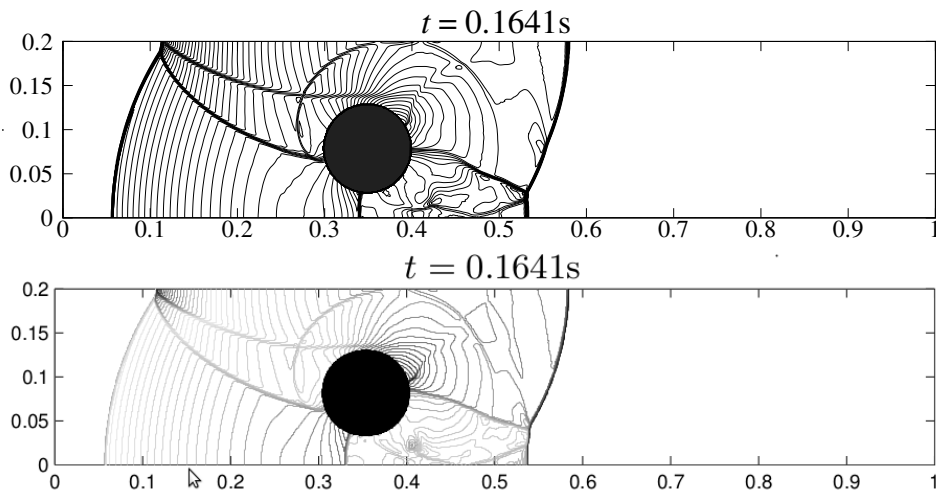


Figure 4.24: Pressure contours at $t = 0.1641$ s from (a) IB-FV solver (Min: 0, $\Delta : 0.51$, Max: 28.3) (b) Shyue, KM [121], ($\Delta x = \Delta y = 1/1000$)

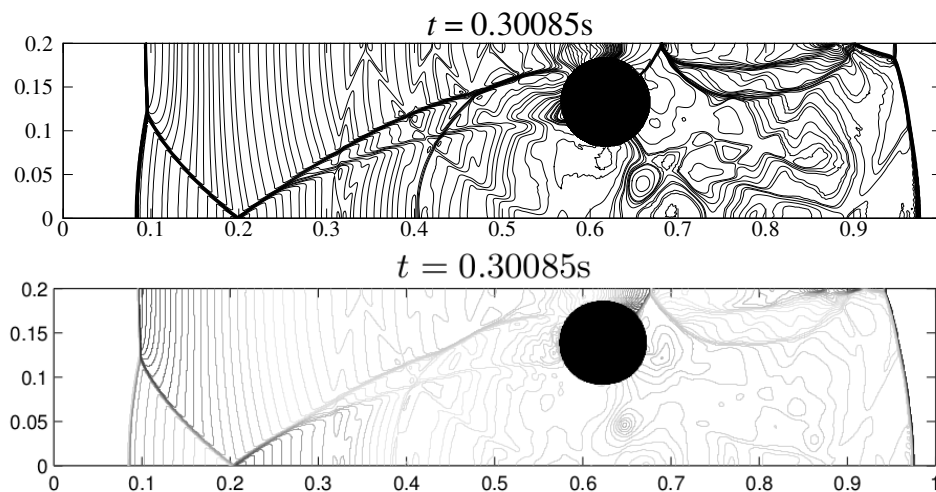


Figure 4.25: Pressure contours at $t = 0.30085$ s from (a) IB-FV solver (Min: 0, $\Delta : 0.4$, Max: 19.22) (b) Shyue, KM [121], ($\Delta x = \Delta y = 1/1000$)

The studies of flow past stationary objects can be handled using a conformal FV solver and do not necessitate the use of an IB–FV solver. The IB–FV solver, however, holds a significant advantage over conventional FV solvers for moving body problems, both due to the simplicity in mesh generation as well as the use of a fixed background mesh that does not demand re-meshing/deforming meshes. In order to demonstrate the capability of the proposed solver for moving body problems, we consider the interaction of a Mach 3 shock with a cylinder at rest in a channel. The channel has dimensions of 1×0.2 and is taken as the computational domain. The cylinder of radius 0.05 m has a density of $\rho_b = 10.77 \text{ kg/m}^3$ and is initially placed at $(0.15, 0.05)$ (Figure 4.23). The shock which is located at $x = 0.08$ at $t = 0$, interacts with the cylinder causing it to lift-off and subsequently resulting in complex interactions. The density and pressure in the pre-shock state are maintained at $\rho = 1.4 \text{ kg/m}^3$ and $p = 1 \text{ Pa}$ while the left boundary is maintained at post-shock state. Studies have been conducted using uniform Cartesian grids of three different resolutions as shown in Table 4.2, which compares the centroidal locations at $t = 0.30085$ with those in Shyue [121]. The motion of the cylinder, which is considered rigid, is induced by the pressure forces acting on the cylinder and we neglect the effects of gravity in the present simulations to allow for quantitative comparisons with other studies [121, 122] which make the same assumption. The results from the present simulations are found to agree quite well with those in [121], both qualitatively and quantitatively. The pressure contours at two different time instants are shown in Figures 4.24 and 4.25 where they are also compared with the numerical results obtained by Shyue [121]. There is a fair agreement in terms of the flow features between the present results and those in [121] and small discrepancies may be attributed to the differences in specific methodologies employed for the study. It is evident from the present results that the IB–FV approach can resolve the complex unsteady flow phenomena excellently, lending credence to its applicability for challenging problems involving one or more solids in supersonic streams. The temporal history of trajectory of the cylinder is compared with literature [122] in Figure 4.26 (a). It can be clearly seen that, the location of the centre of mass of the cylinder with time from the present solver for the finest mesh has an excellent agreement with that reported in [122]. The good agreement between results from present simulations and those in literature [121, 122] underscore the ability of the proposed solver to accurately handle moving bodies in compressible flows with relative ease. Finally, we also plot the temporal history of forces (lift and drag) in Figure 4.26 (b). It may be observed that the force histories are free of any spurious oscillations that are known to plague sharp interface IB methods in moving body problems [123]. Unfortunately, there is no data available to compare the force histories but the overall agreement of the cylinder trajectory with the computations of Puscas and Monasse

[121, 122] is an indirect proof that the force histories are quite accurate.

Table 4.2: Position of centre of mass of cylinder (in m) at time $t = 0.30085$ s

Present IB-FV solver			Shyue, KM [121]	
h	X	Y	X	Y
1/500	0.613	0.1239	0.6203	0.1368
1/1000	0.6173	0.1312	0.6231	0.1389
1/1600	0.6199	0.1349	-	-

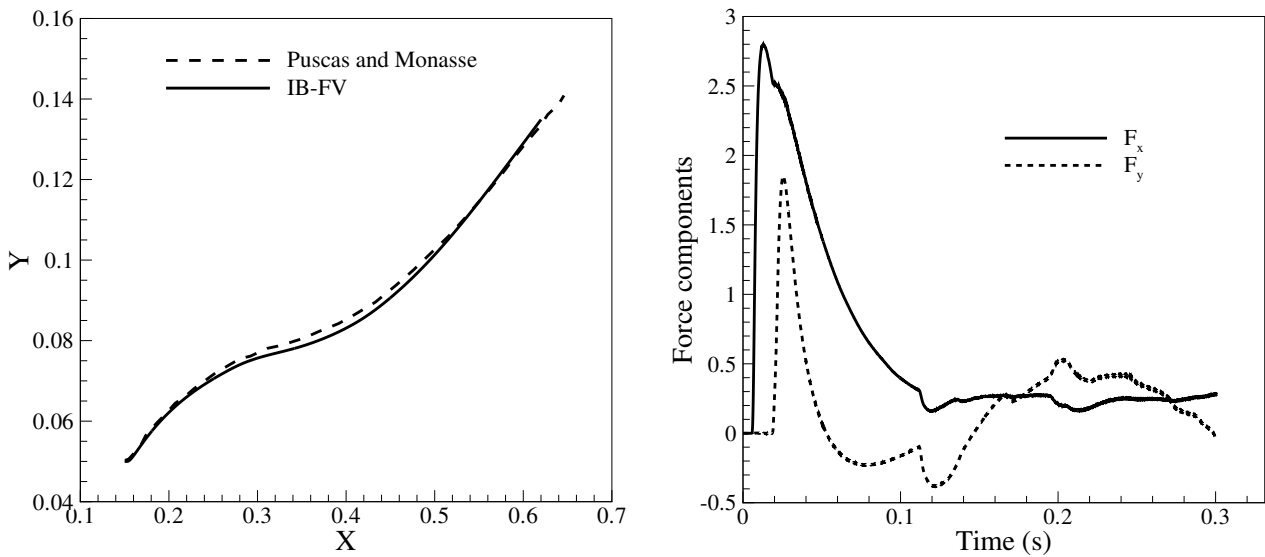


Figure 4.26: (a) Trajectory of the centre of mass of cylinder (b) Temporal history of force components, on 1600×320 grid

4.4.6 Shape optimisation: Minimum drag geometries in hypersonic flow

As a final test case to demonstrate the versatility of the IB-FV solver, we apply it to the problem of finding the axisymmetric fore-body of minimum drag in hypersonic flows. We consider an inviscid hypersonic flow scenario corresponding to a freestream Mach number of 5 and numerically investigate the power-law body of least drag in this flow. While traditional conformal approaches would have required re-generation (or modification) of meshes to conform with the geometry at every optimisation cycle, the IB-FV solver clearly and easily circumvents this difficulty.

We consider the problem of determining the minimum drag axisymmetric geometry of fixed length and base area described using the power-

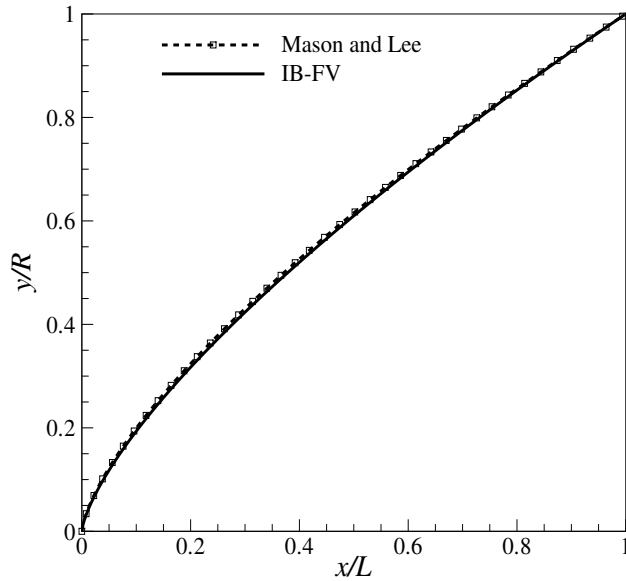


Figure 4.27: Optimal configuration of the axisymmetric forebody

law $y/R = a(x/L)^n$. We begin with a half-cone, corresponding to $n = 1$, which is immersed in a computational domain of size 0.1×0.15 unit. The wave drag, neglecting base pressure drag is computed using the IB–FV solver and serves as the cost function for an optimisation algorithm, which as described in [124] generates the new shape at every optimisation cycle. To avoid further complexities, we consider a fixed radius–to–length ratio of $R/L = 0.25$ (in fact, the radius and length are fixed as well) and the optimal shape obtained is shown in Figure 4.27. Our results show that the axisymmetric power–law body for least drag has an exponent close to 0.71, which is in excellent agreement with those predicted by Mason and Lee [125], who employed a brute–force approach with a finite volume solver on the body–fitted grids. This investigation, while limited in scope, nevertheless serves as a proof–of–concept study which suggests that the IB–FV solver could be a cost–efficient yet accurate high–fidelity solver for shape optimisation frameworks in more complex scenarios. This study employing the sharp interface IB for shape optimisation in high–speed inviscid flows is also the first such attempt to the best of our knowledge, making it a novel contribution of the present work.

4.5 Summary

We propose a new immersed boundary–finite volume flow solver with a sharp interface representation of the geometry for high speed compressible inviscid flows and the salient contributions from the present study can therefore be summarised as follows:

- The use of inverse-distance weighting based reconstruction for the solution of cells in the vicinity of the body that suitably accounts for both Dirichlet and Neumann boundary conditions has been proposed for compressible flows. While this idea has been previously employed in the context of incompressible flows, the present study herein marks the first comprehensive investigation of the approach for high-speed compressible flows.
- The IB-FV solver is shown to be spatially second-order accurate and a thorough investigation of the discrete conservation errors is carried out. It is demonstrated through numerical experiments that the errors diminish linearly with grid refinement.
- The proposed sharp-interface immersed boundary method is found to be versatile, robust and capable of accurately computing compressible inviscid flows with complex geometries in the supersonic and hypersonic regimes. Our investigations also reveal that the methodology is capable of handling stationary as well as moving bodies with equal ease **and can be seamlessly integrated into an aerodynamic shape optimisation framework**.

The study in this chapter is predominantly targeted at supersonic and hypersonic flows, unlike previous research efforts which focussed largely on subsonic, transonic and low supersonic flows. The extensive numerical investigations that have been presented in this chapter conclusively establish the proposed IB–FV solver as a viable and generic alternative to conventional finite volume solvers in handling stationary and moving boundary problems involving complex geometries in high–speed flows in a robust and cost–effective manner. We believe that the present strategy holds a lot of promise and when equipped with adaptive grid refinement, can become a powerful computational tool for fluid flow simulations and analysis at high Mach number regimes. We have made use of this particular philosophy for viscous high-speed compressible flows as well with a specific interest of accurately estimating near wall skin-friction and wall heat-flux values in the following chapters.

CHAPTER 5

SHARP INTERFACE IMMERSED BOUNDARY FOR VISCOUS FLOWS

“Programs must be written for people to read, and only incidentally for machines to execute”

- Harold Abelson, *Structure and Interpretation of Computer Programs*

We discuss the development of a sharp interface immersed boundary (IB) method for viscous compressible flows and assessment of its ability to accurately compute wall shear and heat fluxes in laminar hypersonic flows. We describe the implementation of Hybrid Cartesian Immersed Boundary (HCIB) in an unstructured Cartesian finite volume (FV) framework for compressible flows with embedded geometries having isothermal or adiabatic walls. The HCIB approach resolves the geometric interface sharply on the non-conformal mesh through the direct imposition of boundary conditions made possible by a local reconstruction approach that determines the solution in the vicinity of the body using a suitable interpolation strategy. The efficacy of the IB-FV solver is investigated for canonical high-speed viscous flows over a range of Mach numbers. The numerical results indicate that the surface pressure and shear stress distributions are computed with reasonable accuracy whereas inaccuracies in surface heat flux computations are observed in some cases. Interestingly, for aerodynamically blunt configurations with isothermal walls, the stagnation heat flux is found to be severely under-predicted by the IB-FV solver and results in poor estimation of surface heat flux distribution.

Contents of this chapter are part of the manuscript titled “**Development and assessment of a new sharp interface immersed boundary method for hypersonic viscous flows**”, (under review)

As mentioned in Chapter 1, despite the obvious importance of stagnation heat transfer as well as skin friction and wall heat flux distributions in hypersonic laminar flows, the investigations on the efficacy of IB methods for such flows particularly at higher Reynolds numbers are currently non-existent. Furthermore, most studies using IB approaches rarely focus on skin friction and heat transfer instead choosing to present pressure distributions. This constitutes an incomplete and somewhat incorrect assessment of the approach since the accuracy of estimation of heat loads and wall shear are important at high speeds. The motivation of the present study is to assess the performance of sharp interface IB solvers for hypersonic flows with a specific emphasis on computation of wall heat flux and skin friction in high Reynolds number hypersonic flows past generic configurations. In the contents of the present Chapter, we discuss a novel Hybrid Cartesian Immersed Boundary (HCIB) approach for compressible viscous flows and its utility for laminar hypersonic flows past configurations of fundamental and practical interest. The remainder of the Chapter is organised as follows. Section 5.1 describe the numerical framework of the HCIB approach while numerical experiments using IB methodology on adaptive Cartesian meshes are discussed in Section 5.2.

5.1 Hybrid Cartesian Immersed Boundary Method

We now discuss the details and implementation of the sharp interface Hybrid Cartesian Immersed Boundary (HCIB) method in this section. The HCIB was first proposed by Gilmanov and Sotiropoulos [37] for incompressible fluid flows and we shall extend this approach to compressible inviscid and viscous flows in the present study. In this approach, the solid body is embedded or immersed into an underlying Cartesian mesh which may be uniform or non-uniform. The solid boundary is discretised using linear line segments in two dimensions (surface triangulated in three dimensions) and the key feature of the IB strategy is to ensure that the sharpness of the geometric interface is always preserved. The mesh does not conform to the geometry as in the traditional body-fitted CFD solvers and therefore the accurate calculation of the near-wall numerical solution is central to the success of any IB strategy. The HCIB approach has been implemented in the finite volume framework described previously in Chapter 2 and constitutes two distinct stages viz. *classification* (same as discussed in Chapter 4) and *reconstruction*.

The solution reconstruction is the stage of the HCIB approach where the numerical solution in the near vicinity of the solid body is obtained by enforcing the boundary conditions while preserving the sharp interface of the geometry. It is evident following the classification stage that the numerical solution needs to be computed only in the

F and I cells which belong to the fluid domain. The solution in the F cells which lie completely in the fluid region (they never contain geometric interfaces) are completely determined by solving the Navier-Stokes equations in the same manner as in conventional continuum solvers. This is possible because these cells are “interior” to the domain and not in the immediate vicinity of the interface. The process of obtaining the solution in the I cells is different and is termed as the solution reconstruction stage.

We shall now discuss the solution reconstruction for viscous compressible flows in greater detail, with an emphasis on its practical implementation, for geometries with isothermal as well as adiabatic walls. In the HCIB approach, the solution reconstruction is effected by an interpolation strategy along the direction locally normal to the interface as shown in Figure 5.1, while exploiting the fact that the boundary conditions are enforced directly at the sharp interface. To effect the interpolation, we first identify the nearest face on the solid boundary for each I cell. Subsequently, we obtain the points b and f on the sharp interface and the fluid domain respectively which lie on a line parallel to the interface normal \hat{n} but passing through the centroid of the I cell. It may be noted that while b is the point of intersection of this line with the geometric boundary, point f is the closest point on this line that cuts a connector joining two F cells as shown in Figure 5.1. However, in some scenarios such as sharp trailing edges, it may not be possible to obtain the b point by this approach in which case the nearest face node is chosen as the b point. The values of primitive variables at b points follow from the prescribed boundary conditions on the sharp interface. On the other hand, the values of these primitive variables at the f point are obtained by a linear interpolation of the values in the two fluid cells F_1 and F_2 as,

$$\phi_f = \phi_{F1} + \frac{d_1}{d_2}(\phi_{F2} - \phi_{F1}) \quad (5.1)$$

where, d_1 and d_2 are the distances of f point from the centroids of cells F_1 and F_2 . The reconstruction approach then obtains the estimate of primitive variables at the centroid of the I cell by a suitable interpolation of their values at b and f points. The reconstruction could involve either a polynomial or non-polynomial interpolation and the choice of interpolation need not necessarily be identical for all primitive variables. We shall now describe the specifics of the reconstruction for velocities, pressure and temperature for viscous flows past geometries with isothermal as well as adiabatic walls.

The process of solution reconstruction employing a linear polynomial interpolation is detailed below. Denoting the variable of interest as ϕ , one can write its variation

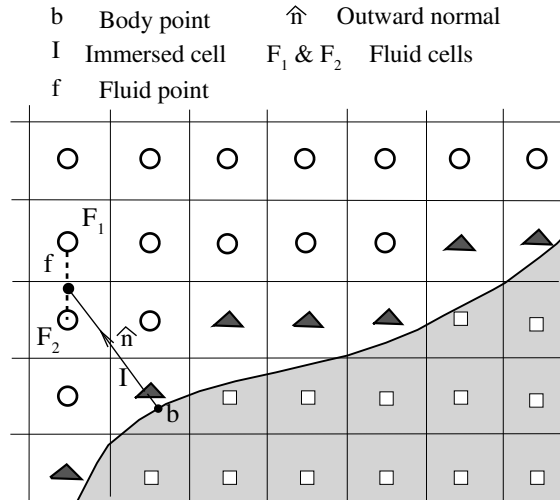


Figure 5.1: Reconstruction for obtaining ϕ at immersed cells

along the normal direction as,

$$\phi = C_1 r + C_2 \quad (5.2)$$

where r is the distance measured from the b point on the sharp interface along the direction of the outward local normal. Subsequently, if the unknowns C_1 and C_2 can be uniquely determined from two independent conditions then the value at the I cell may be computed as,

$$\phi_I = C_1 r_{bI} + C_2 \quad (5.3)$$

The constants C_1 and C_2 are typically evaluated using the boundary conditions at ' b ' and the interpolated solution at ' f '.

5.1.1 Reconstruction for velocities

The velocities at the surface in viscous flows must satisfy the no-slip boundary condition $u_{\parallel b} = 0$ and impermeability condition $u_{\perp b} = 0$. The quantities u_{\parallel} and u_{\perp} denote the components of velocity vector along the local tangential and local normal directions respectively and may be determined as,

$$u_{\parallel} = u_f n_y - v_f n_x \quad (5.4)$$

$$u_{\perp} = u_f n_x + v_f n_y \quad (5.5)$$

where n_x and n_y now refer to the components of the normal to the interface along which the one-dimensional solution reconstruction is effected. The values of these velocity components at the f point may be computed using Eq 5.1 where ϕ is chosen as u_{\parallel} or u_{\perp} . The use of the known values at b and f points helps to compute the values of u_{\parallel} and u_{\perp} at the I cells using Eq 5.3 and one can obtain the Cartesian velocity components at the cell centers using the reverse transformation that reads,

$$u_I = (u_{\parallel I} n_y) - (u_{\perp I} n_x) \quad (5.6)$$

$$v_I = (-u_{\parallel I} n_x) - (u_{\perp I} n_y) \quad (5.7)$$

5.1.2 Reconstruction for pressure

The pressure at the cell I is obtained by invoking the boundary layer approximation that holds for non-separated flows which dictates that $\frac{\partial p}{\partial r} = 0$. This allows one to impose the pressure outside the boundary layer on the surface and thus to obtain $p_b = p_I = p_f$, with p_f obtained using Eq 5.1. While this condition would be strictly valid only for thin layers and un-separated flows, they have been used for inviscid flows as shown in Chapter 4 and appear to work even in scenarios with flow separation.

5.1.3 Reconstruction for temperature

While the value of temperature at the f point, T_f may be computed using Eq 5.1, the temperature at the b point depends on whether the wall is isothermal or adiabatic, both of which can be handled with relative ease. For isothermal walls, the wall temperature T_w is known and typically constant which gives $T_b = T_w$. The value of temperature T_I at the centroids of the immersed cells can then be obtained using Eq 5.3. While one can also use a linear temperature variation in the case of adiabatic walls, the zero wall heat flux condition applied to Eq 5.2 would give $C_1 = 0$ which in turn means that the temperatures at b point as well as the I cell are both equal and identical to the value at the f point. Simply stated, this gives $T_b = T_I = T_f$ similar to the reconstruction of pressure, which also satisfies the homogeneous Neumann boundary condition at the interface.

It must be emphasised however that a mathematically consistent approach to enforcing homogeneous Neumann BCs for pressure and temperature (in case of adiabatic walls) at the b points is to employ a quadratic interpolation for these quantities. This

variation is described as,

$$\phi = C_1 r^2 + C_2 r + C_3 \quad (5.8)$$

where $\phi = p, T$ and the three unknowns in Eq 5.8 need to be evaluated using three independent conditions. These three conditions are the values of $\frac{\partial\phi}{\partial r}$ at the b point (where it is zero) and at the f point (where they are obtained by using Eq 5.1 for the gradient quantities and then projecting it along the local normal direction) as well as the value of ϕ_f . One can see with a little effort that $C_2 = 0$ but the variation of pressure and/or temperature remains parabolic with finite non-zero values for C_1 and C_3 . The pressure and/or temperature at the immersed cells may be easily obtained as,

$$T_I = T_f + \frac{1}{2r_{bf}} \left. \frac{\partial T}{\partial r} \right|_f (r_{bI}^2 - r_{bf}^2) \quad (5.9)$$

$$p_I = p_f + \frac{1}{2r_{bf}} \left. \frac{\partial p}{\partial r} \right|_f (r_{bI}^2 - r_{bf}^2) \quad (5.10)$$

5.1.4 Reconstruction for density

The density at I cells follows from the equation of state (EOS) for a perfect gas and is computed as,

$$\rho_I = \frac{p_I}{RT_I} \quad (5.11)$$

where R is the gas constant and p_I as well as T_I follow from suitable reconstruction approaches as described in Sections 5.1.2 and 5.1.3.

We must mention that while only polynomial reconstruction approaches (linear and quadratic) have been discussed herein, non-polynomial interpolation are also possible and these alternate reconstructions, particularly for temperature, and their impact shall be discussed in Chapter 6. Although the present work has an exclusive focus on viscous compressible flows, it is also instructive to briefly look at the solution reconstruction for inviscid flows for sake of completeness. In case of Euler flows, the only boundary condition is $u_{\perp b} = 0$ and the viscous fluxes are all zero. We still employ a linear variation for all relevant quantities viz. u_{\perp}, u_{\parallel} and ρ , but the values at b points for the latter two are obtained from the values at F cells in a specified neighbourhood using an inverse-distance weighted interpolation as described in the Chapter 4. The

pressure at the I cells are imposed directly from the values at the f point like for viscous flows and the temperature (which is not necessary though) can be computed using the equation of state.

The philosophy of one-dimensional solution reconstruction along the local normal direction is adopted from [37] and consequently the primitive variables are reconstructed. The conserved variables in the I cells which are required to define the states for flux computations in neighbouring F cells are then obtained from the reconstructed quantities. One can also envisage a solution reconstruction approach for the conserved variables in the I cells. This is not a trivial proposition however and has not been investigated in the present study. It may be noted that the reconstruction approach used in this study closely resembles the extended extrapolation technique in [126] except that the normal velocity varies linearly in our approach as opposed to the quadratic variation in the extended extrapolation method.

5.1.5 Calculation of wall pressure, shear stress and heat flux

The major quantities of interest in viscous computations are the surface distribution of pressure, viscous stresses and heat transfer. We provide a concise description of the computation of these parameters in the IB-FV solver to enable reproducibility of results in the following sections.

The pressure at the wall, by virtue of the homogeneous Neumann BC, is $p_w = p_I = p_f$ and may also be quantified using the coefficient of pressure defined by,

$$C_p = (p_w - p_\infty)/(0.5\rho_\infty V_\infty^2)$$

The wall heat flux is obtained is related to the temperature gradients at the wall and is defined as,

$$q_w = k_w \frac{\partial T}{\partial r} \Big|_w$$

where the fluid thermal conductivity k_w at the wall is a function of the wall temperature T_b and is obtained from Sutherland's law. The temperature gradient at the wall may be approximated using a simple finite differencing for the linear solution variation in the near-wall regions. The heat flux on the surface then follows as,

$$q_w = k_w \frac{T_I - T_w}{r_{bI}}$$

However, for other solution reconstructions, we differentiate the expression for temperature variation $T(r)$ with respect to the local normal direction r and then compute the value of this directional derivative at $r = 0$, to obtain the temperature gradient and subsequently the wall heat flux. A non-dimensional wall heat flux may also be defined in terms of Stanton number (St),

$$St = q_w / (0.5\rho_\infty V_\infty c_p (T_o - T_w))$$

where, T_o is the total temperature corresponding to the freestream temperature and c_p is the constant pressure specific heat capacity.

The wall shear stress, like the wall heat flux, is a scalar quantity whose distribution over the surface is desired to obtain the viscous drag acting on the body. The wall shear stress is obtained by adding up all components of the viscous force along the local tangential direction and is given by,

$$\tau_w = (\tau_{xx} n_x + \tau_{xy} n_y) t_x + (\tau_{xy} n_x + \tau_{yy} n_y) t_y$$

where $t_x = n_y$ and $t_y = -n_x$ denote the components of the local tangent vector and n_x and n_y are the components of the local normal to the surface. The conventional representation is to use the non-dimensional wall shear stress, which is referred to as the skin friction coefficient (or simply skin friction), C_f defined as,

$$C_f = \tau_w / (0.5\rho_\infty V_\infty^2)$$

One important aspect in computing C_f is the need to obtain the viscous stress components at the body faces. These may be obtained by identifying a neighbourhood of F cells associated with each b point (and therefore a unique I cell) and then using an inverse-distance weighted averaging of the velocity gradients in these F cells to obtain an estimate at the b point (see Chapter 4) which is consequently employed to calculate the viscous stresses. It may be noted that the viscous stresses require the dynamic viscosity at the wall which is also a function of temperature and is obtained from the Sutherland's law.

It must be remarked that the Stanton number distribution is indicative of the heat loading and the skin friction and pressure contribute to the aerodynamic forces acting on the geometry. These quantities are therefore measures of aerothermodynamic performance and their accurate estimation in the immersed boundary framework constitutes the primary focus of the present study. In summary, the overall solution

process consists of solving the Navier-Stokes equations using the finite volume discretisation in all F cells at every time step and consequently using this solution along with the boundary conditions in the reconstruction stage to determine the numerical solution at the I cells. We shall now explore the efficacy and versatility of the IB-FV solver that employs the HCIB strategy in an unstructured finite volume framework in estimating aerodynamic forces and heat loads for canonical laminar hypersonic flows.

5.2 Numerical investigations

We devote this section to numerical experiments using the IB-FV solver for viscous flows in the subsonic, supersonic and hypersonic regimes involving both internal and external flows. These test problems help to understand the ability of the non-conformal mesh and the associated solution reconstruction in computing pressure, skin friction and heat flux distributions.

5.2.1 Inviscid hypersonic flow past a hemisphere

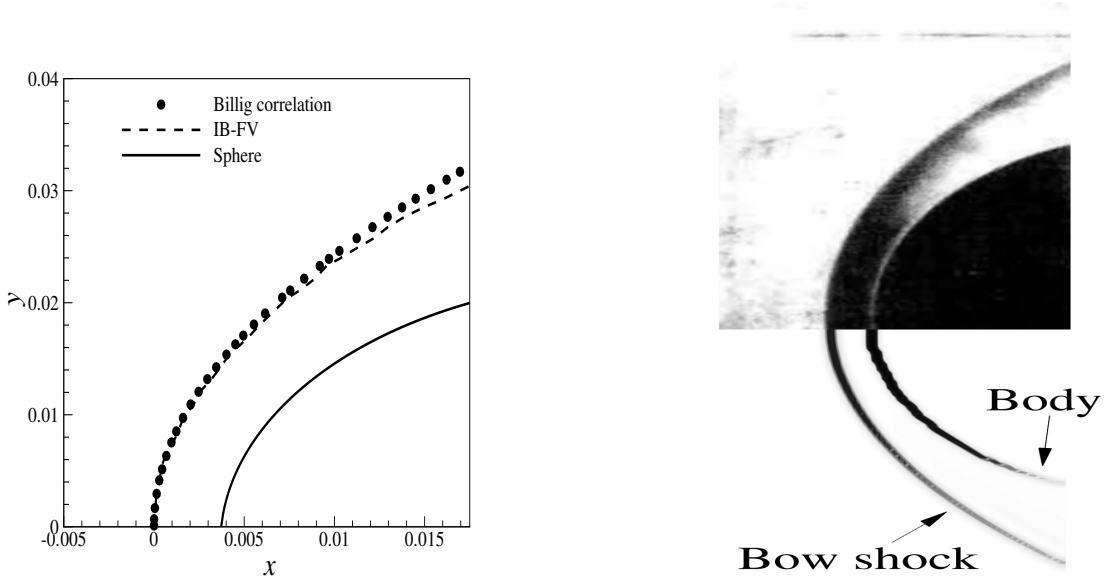


Figure 5.2: (a) Comparison of shock shape with Billig correlation [118] (b) comparison of numerical (bottom) and experimental (top) Schlieren

The first test case is the numerical simulation of inviscid hypersonic flow past a hemisphere which is carried out as a preliminary validation of the HCIB approach, albeit to Euler flows. The freestream Mach number of the flow is $M_\infty = 5.8$ and the cylinder of radius 23.65 mm is immersed into a uniform Cartesian mesh with 93750 cells that

spans a domain of size $0.1 \text{ m} \times 0.15 \text{ m}$. The simulations are carried out for an axisymmetric flow and the steady-state solution consists of a detached bow shock upstream of the hemisphere. Figure 5.2(a) is a comparison of the shock shape obtained from the IB-FV solver with the theoretical prediction proposed by Billig [118] and one can notice that the agreement is quite good. The shock can also be seen clearly in the numerical Schlieren from the present computations and the computed shock location agrees quite well with that observed in the experimental Schlieren in Figure 5.2(b). The ability of the IB-FV solver in computing inviscid flows is also underlined by the fact that the computed pressure coefficient C_p over the surface of the hemisphere compares excellently with the experimental results of [117] as can be seen from Figure 5.3. These results point to the ability of the HCIB approach in computing pressure distribution over blunt bodies in inviscid flow and lend confidence in the application of the approach for more complex flow problems involving laminar flows.

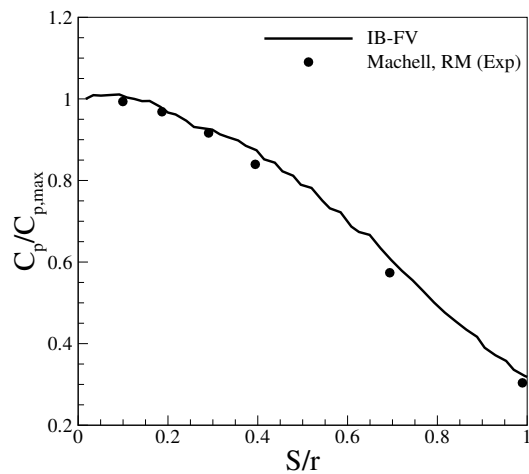


Figure 5.3: Comparison of normalised pressure coefficient with experimental data [117]

5.2.2 Subsonic flow past NACA0012 airfoil

We begin the viscous test cases for subsonic flow with a well documented test problem i.e. subsonic flow past a NACA 0012 airfoil. NACA0012 airfoil is a symmetric airfoil with the chord length C is taken as unity and the thickness of the airfoil is 12% C . Considering the freestream conditions for this test problem, the computational domain is taken significantly large i.e. $40C \times 40C$ (see Figure 5.4(a)) where the airfoil wall is maintained as adiabatic wall, inlet boundary as subsonic inlet and rest of the boundaries are kept as subsonic outlet. The freestream conditions are $M_\infty=0.5$ and $Re_\infty=5000$ with zero angle of attack. The initial (unadapted) grid contains 108900 computational cells (see Figure 5.4(b)) whereas the final adapted grid contains 204882 control volumes. The grid-adaptation is performed along the near vicinity of the body

which also contains the boundary layer. The nature of grid adaptation is purely geometric where the parent cell gets divided into 4 children cells and no solution based refinement is performed. Figure 5.5(a) and (b) shows the adapted grid leading edge and trailing edge region of the airfoil.

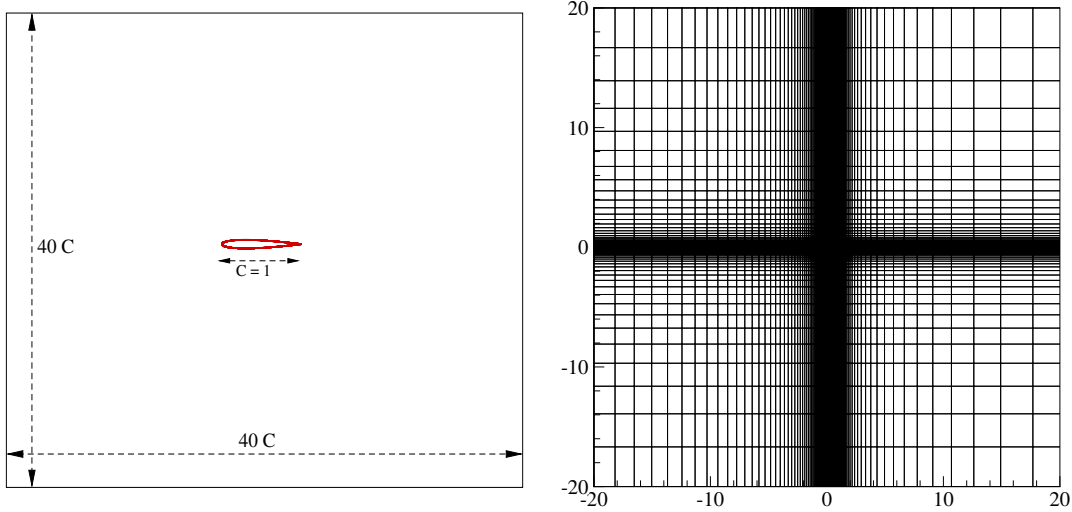


Figure 5.4: (a) Computational domain (not to scale) (b) Non-uniform initial grid

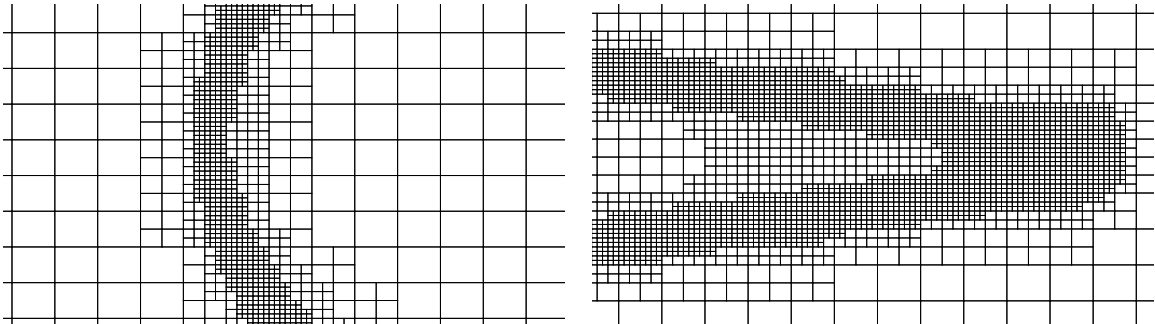


Figure 5.5: Three levels of refinement across the NACA0012 airfoil at (a) leading-edge portion (b) trailing-edge region

Table 5.1: Comparative study showing point of separation and force coefficients

	ΔX_{min}	ΔY_{min}	l_{sep}	C_d
IB-FV, level 1 grid	1.2×10^{-3}	1.0×10^{-3}	0.85	0.049
IB-FV, level 2 grid	6.0×10^{-4}	5.0×10^{-4}	0.826	0.0545
IB-FV, level 3 grid	3.0×10^{-4}	2.5×10^{-4}	0.812	0.0588
Swanson and Langer <i>et al.</i> [128]	2.3×10^{-3}	3.1×10^{-5}	0.808	0.0557
Mondal <i>et al.</i> [33]	-	-	0.813	0.0616

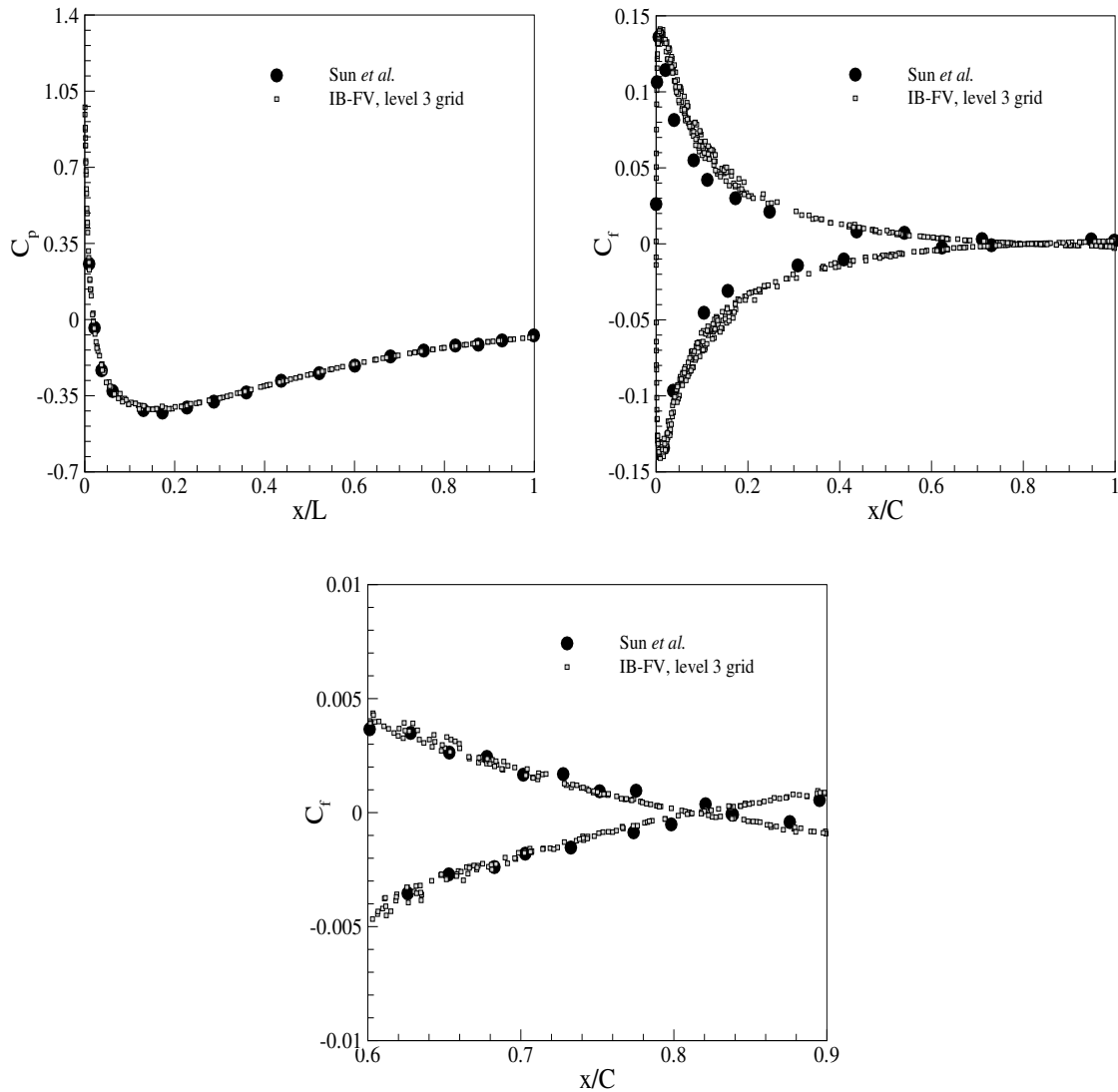


Figure 5.6: Surface distribution of (a) pressure coefficient C_p (b) skin-friction C_f (c) C_f along region of separation

We now show a comparative study where we present the solution obtained along the wall for the level three adapted grid. Figure 5.6(a) clearly indicates that the variation of pressure coefficient C_p along the wall agrees very well with the available data [127] whereas Figure 5.6(b) shows that the skin-friction coefficient also has a good agreement with the point of separation being correctly captured (Figure 5.6(c)). Moreover, it is evident that C_p distribution remains invariant with mesh resolution whereas wall C_f distribution is quite sensitive on mesh resolution. In Table 5.1 we highlight the quantitative variation of point of separation l_{sep} and drag coefficient C_d for three consecutive levels of adapted grids. It is seen that for the final adapted grid, both l_{sep} and C_d are in agreement with the available data of [128] and [33].

5.2.3 Transonic flow past biplane NACA0012 airfoil

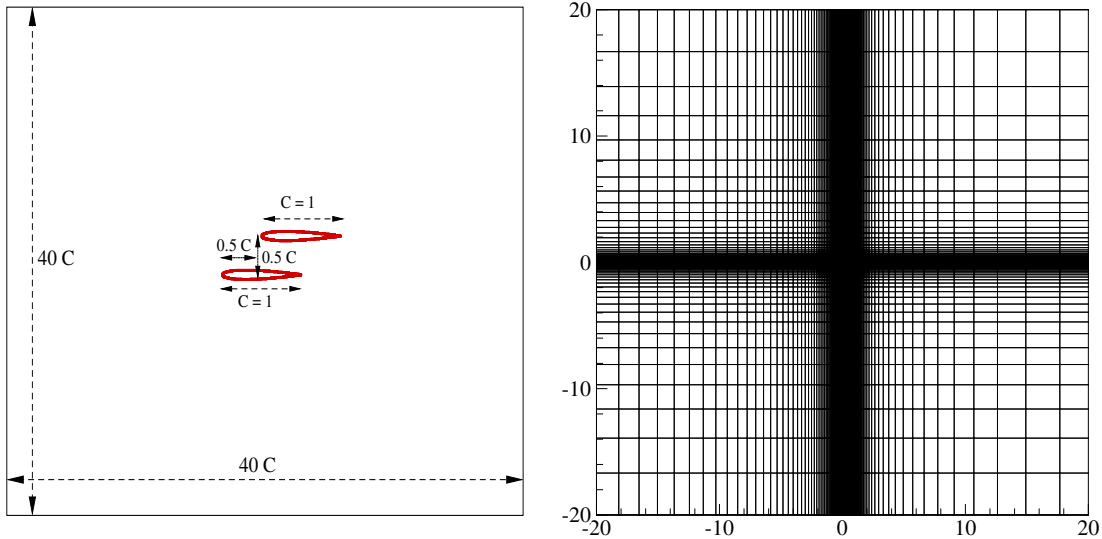


Figure 5.7: (a) Computational domain (not to scale) (b) Non-uniform initial grid

We now numerically simulate the transonic flow for the NACA 0012 airfoil as in the previous test case however, for the present test problem, we adopt the biplane configuration that is arranged in a staggered manner (see Figure 5.7(a)). We adopt the same computational domain as in the previous test case but the wall boundary is maintained as isothermal. The freestream conditions are $M_\infty=0.8$, $Re_\infty=500$ at 10° angle of attack. The initial (unadapted) grid contains 121500 cells (see Figure 5.7(b)) whereas the final adapted grid (adapted upto two levels) contains 152511 control volumes.

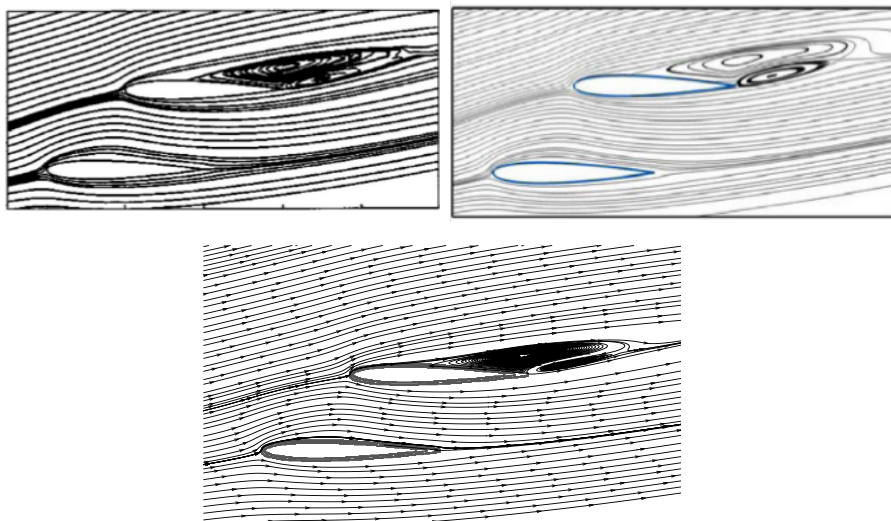


Figure 5.8: Streamlines for flow past NACA0012 staggered airfoil (a) Jawahar and Kamath [129] (b) Qiu et al. [130] (c) IB-FV

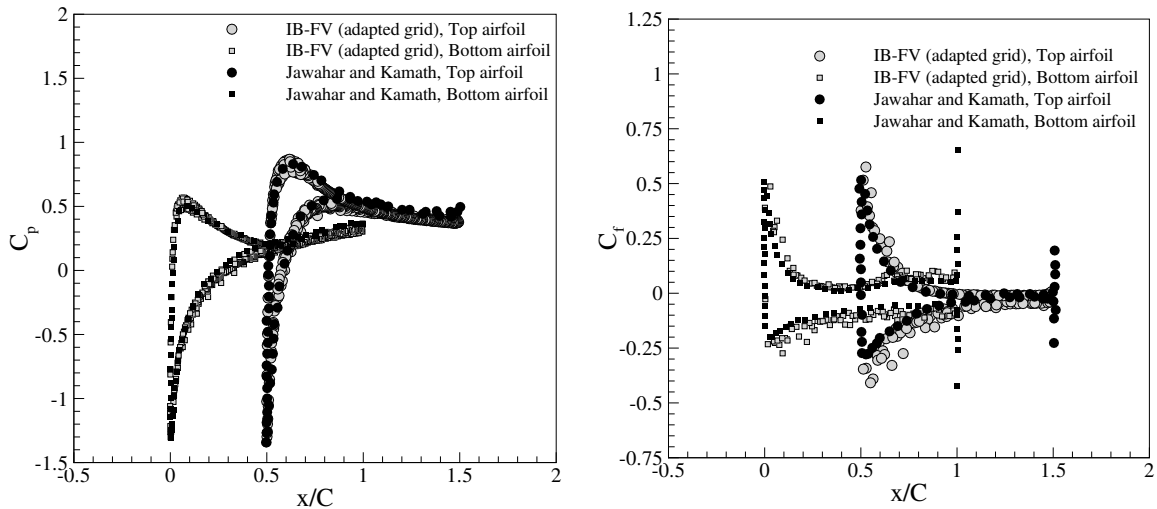


Figure 5.9: Comparison of surface distribution of (a) pressure coefficient C_p and (b) skin-friction coefficient C_f

We compare the streamlines obtained from present solver on the adapted grid with that of streamlines reported by Jawahar and Kamath [129] and Qie et al. [130] (Figure 5.8). It can be seen that present solver is able to accurately predict the double “separation bubble” present in the trailing edge portion of the top airfoil. Moreover, it is seen that the surface distribution of pressure coefficient C_p compares really well with existing literature in Figure 5.9(a) whereas reasonable agreement can be observed for skin-friction coefficient C_f distribution with significant oscillations for the top airfoil using the IB-FV approach, as highlighted in Figure 5.9(b). This oscillatory nature of the C_f distribution needs to be investigated in the future.

5.2.4 Low supersonic flow past a 4% thick bump

We now consider the supersonic flow past a 4% thick bump in a channel which is an interesting test case to gauge the efficacy of the IB-FV solver for separated low Reynolds number flows. The freestream Mach and Reynolds numbers are 1.4 and 8000 respectively. The computational domain shown in Figure 5.10 (a) is discretised using a non-uniform Cartesian mesh (see Figure 5.10(b)). To facilitate better grid resolution near the bump walls which are considered adiabatic, local grid refinement is carried out in the region around the bump as can be seen from the enlarged view of the grid depicted in Figure 5.10(c). The total number of cells in the adapted Cartesian mesh is 14781. The Mach contours shown in Figure 5.11 indicate that the IB-FV solver is capable of resolving the complex flow features for this problem reasonably accurately. The Mach reflection of the incident shock is captured quite well as also the lifting of the boundary layer due to the interaction with the reflected shock. The slipstream near the top wall and compression waves emanating from the separated

boundary layer are weakly captured, partly due to the lack of solution adaptive mesh refinement. Nevertheless, the IB-FV solver is able to predict the skin friction distribution quite accurately as can be observed from Figure 5.12. In particular, we see that the separation point agrees quite well with those from the finite volume computations in [131] although the IB approach predicts a marginally earlier reattachment and thus a slightly shorter re-circulation bubble. We believe that further grid refinement in the vicinity of the bump could improve the skin friction predictions further, although the results from the present computations are clearly encouraging. One can therefore conclude that the HCIB strategy does well to compute the wall shear stress in supersonic flows past geometries with adiabatic surfaces.

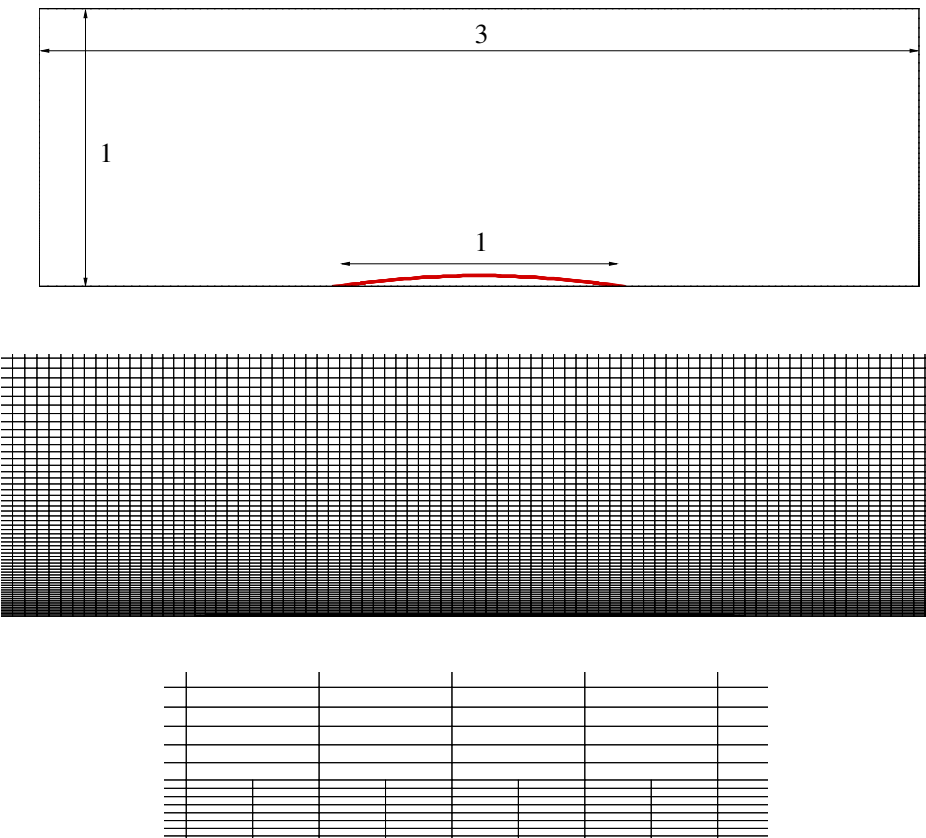


Figure 5.10: (a) 4% thick bump in a channel configuration (b) non-uniform computational grid (c) enlarged portion of the bump with adapted grid

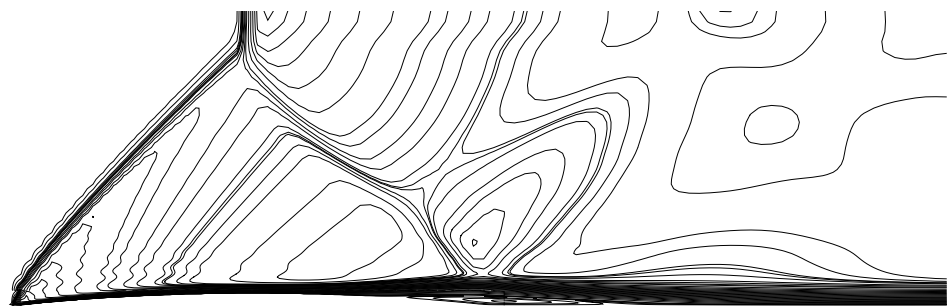


Figure 5.11: (a) Mach contour (Min: 0, Δ : 0.04, Max: 1.42)

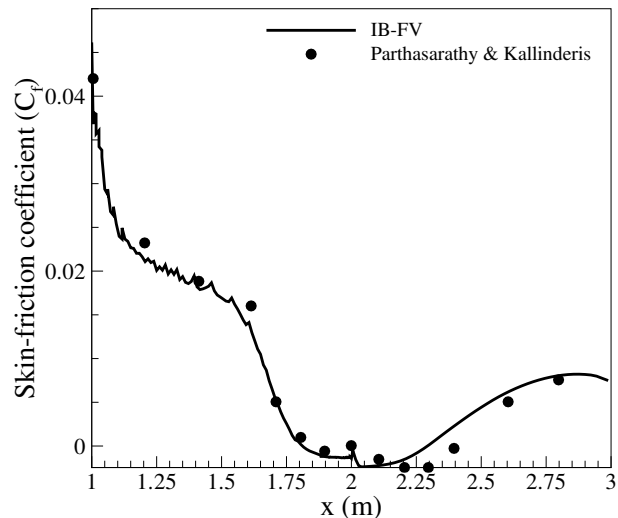


Figure 5.12: Comparison of skin-friction coefficient C_f along the bump and wall with [131]

5.2.5 Supersonic flow past NACA0012 airfoil

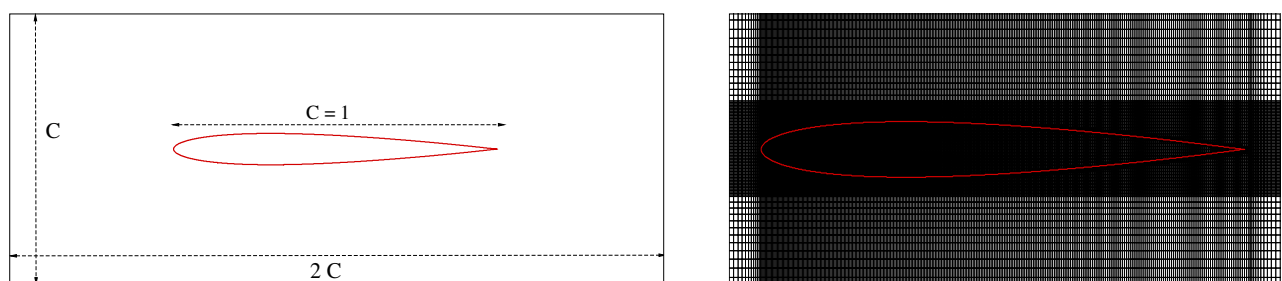


Figure 5.13: (a) Computational domain (not to scale) (b) non-uniform adapted grid

For the next test case we numerically simulate a supersonic flow past NACA 0012 airfoil at freestream conditions of $M_\infty=2$, $Re_\infty=1000$ and 10° angle of attack. Due to

the nature of the boundary condition, this problem was simulated on a much smaller domain of size 2×1 (divided into 9 blocks, Figure 5.13 (a) and (b)) with 33165 cells on the initial (unadapted) grid and has 43932 cells in the final adapted grid. The inlet is maintained as supersonic inlet whereas rest of the walls are kept as supersonic outlet. The wall of the NACA 0012 airfoil is maintained as adiabatic wall.

In Figure 5.14 we show the Mach contour of the final obtained solution on the adapted grid. It is seen that the flow results in a detached bow-shock at the leading edge which is crisply captured using the IB-FV solver. In Figure 5.15, we compare the surface distribution of pressure coefficient C_p and skin-friction coefficient C_f on the adapted grid. It was noticed that the solution obtained from IB-FV solver agrees well with the reported data of Marshall and Ruffin [132]. The surface distribution of C_f is oscillatory as also observed in the Section 5.2.3. This is not extremely surprising because C_f is obtained as a derivative of a primitive variable on meshes which are non-conformal in nature in case of IB solvers. These oscillations however are likely to reduce on sufficiently fine mesh resolutions near the body boundary.

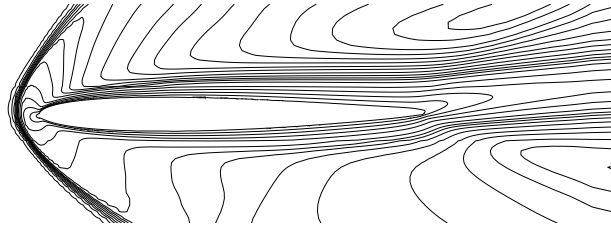


Figure 5.14: Mach contour (Min: 0.2, Δ : 0.11, Max: 2.18)

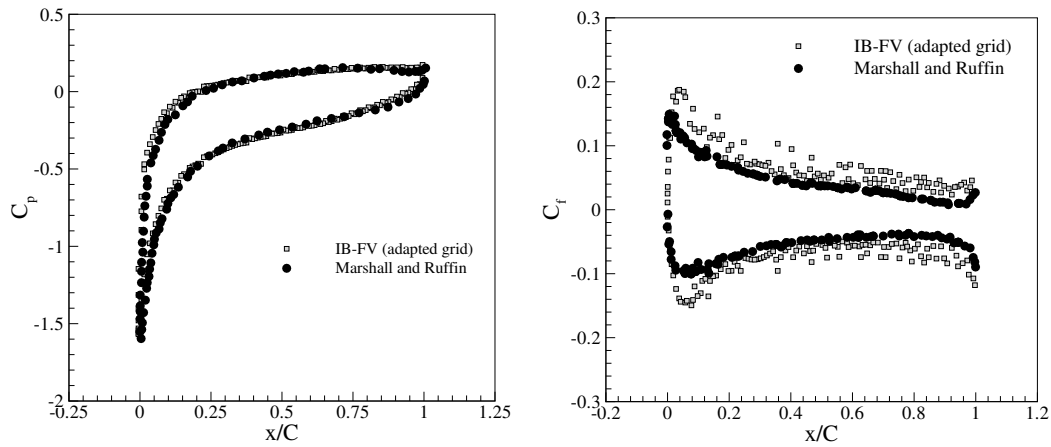


Figure 5.15: Comparison of surface distribution of (a) pressure coefficient C_p and (b) skin-friction coefficient C_f

5.2.6 Hypersonic flow past a flat plate

We now numerically simulate a viscous compressible flow past a flat plate of length $L=0.5334\text{m}$ at a freestream Mach number $M_\infty=6$. While the geometry is of trivial nature, the extremely high freestream Reynolds number $Re_\infty=1.4 \times 10^7$ makes it an interesting case to test the ability of the IB-FV solver in accurately predicting the wall property distribution. The freestream pressure and temperature are taken as $P_\infty = 2211.56 \text{ Pa}$ and $T_\infty=65 \text{ K}$, respectively. The surface of the flat plate is maintained as isothermal wall with constant temperature of $T_w=100 \text{ K}$ and the computational domain of size $0.1 \times 0.5334 \text{ m}$ is divided into 50000 control volumes (i.e. 250 grid points along the length of the body and 200 grid points in the direction normal to the body with clustering near the wall surface). A minimum grid spacing of $\Delta y_{min} = 4 \times 10^{-6}$ is taken. The computations have also been performed using the FV solver for the sake of comparison.

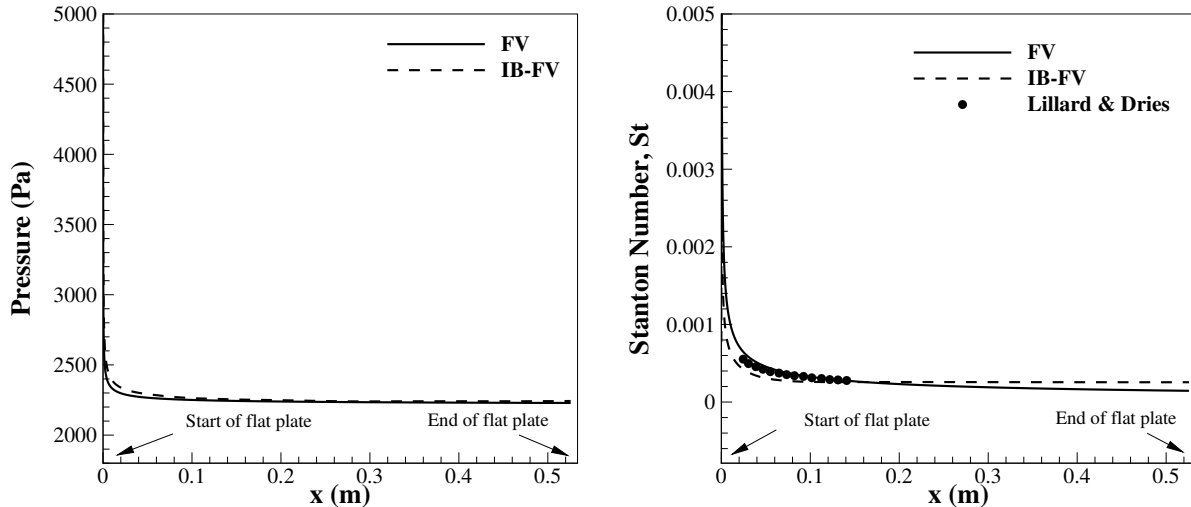


Figure 5.16: Distribution along the surface of the wall for (a) wall pressure (b) Stanton number with experimental data of Lillard and Dries [133]

In Figure 5.16(a) we compare the pressure distribution along the surface of the flat plate obtained from the IB-FV and the FV solvers. It can be noticed that the results from the present IB-FV approach compares excellently well with the results of the FV solver. In Figure 5.16(b) we compare the results for Stanton number from both the approaches with the experimental data of Lillard and Dries [133]. It can again be noticed that both the approaches compares really with the experimental data. It must be remarked here that while both the IB-FV and the FV solvers,

for this test case, employs the same computation grid, the former essentially reconstructs the solution along the wall surface (i.e. the I cells). The excellent comparison of the wall pressure as well as Stanton number is testament to the efficacy of the present reconstruction approach in accurately handling hypersonic flows at high Reynolds number, albeit for geometry that conforms to the background grid. We now investigate additional test cases in the subsequent sections.

5.2.7 Hypersonic flow past a compression ramp

The hypersonic laminar flow past a compression ramp has been studied in the past both numerically as well as experimentally [109]. The configuration is described by a flat plate of length $L = 0.4394$ m followed by the ramp of vertex angle $\theta = 15^\circ$ as shown in Figure 5.17(a). We choose the freestream Mach and Reynolds numbers consistent with the experimental conditions as $M_\infty = 11.63$ and $Re_\infty = 552216/\text{m}$. The freestream temperature is $T_\infty = 67.05$ K with the ramp wall maintained at a constant temperature of $T_w = 294.38$ K. We embed the ramp in a uniform Cartesian mesh with a minimum grid spacing of $\Delta y = 3.2 \times 10^{-4}$ m and has 67500 cells. To improve the resolution of the thin boundary layer near the ramp surface for the non-conformal mesh, we carry out geometric refinement in the vicinity of the ramp (upto four levels) and the final adapted mesh, shown in Figure 5.17(b), consists of 229338 volumes with a minimum grid spacing equal to $\Delta y = 2 \times 10^{-5}$ m. This corresponds to a cell Reynolds number (based on freestream conditions and local grid resolution) equal to ~ 11 .

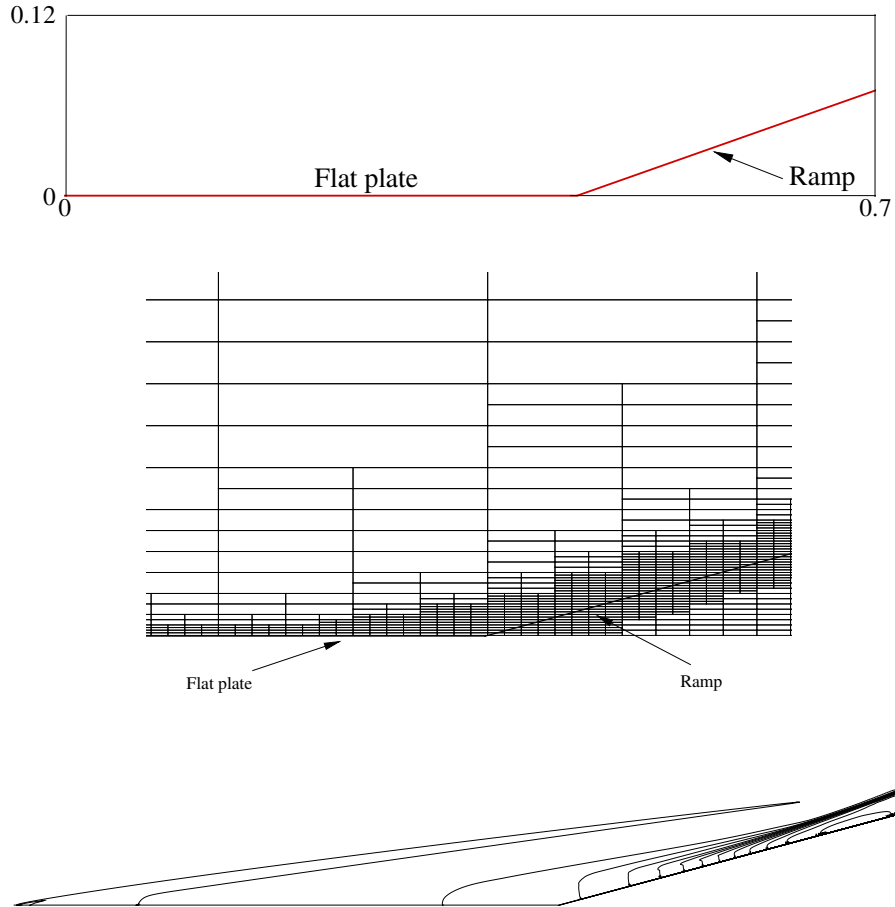


Figure 5.17: (a) Ramp geometry (b) locally adapted grid (c) pressure contour for flow past compression ramp (Min: 0, Δ : 51.66, Max: 620)

Figure 5.17(c) shows the pressure contour for this test case where the leading edge shock striking the ramp is clearly visible and this region corresponds to the maximum pressure on the ramp surface. Of particular interest for this test problem are the computed distributions (along the ramp) of skin friction and heat flux. It is evident that the computed pressure coefficient distribution in Figure 5.18(a) shows excellent agreement with experimental measurements. Furthermore, the computed skin friction and Stanton number distributions in Figure 5.18(b)(c) also compare reasonably well with experimental data demonstrating that the IB-FV solver can be employed with adequate grid resolution to accurately predict the shear stress and heat transfer in viscous flows over compression ramps.

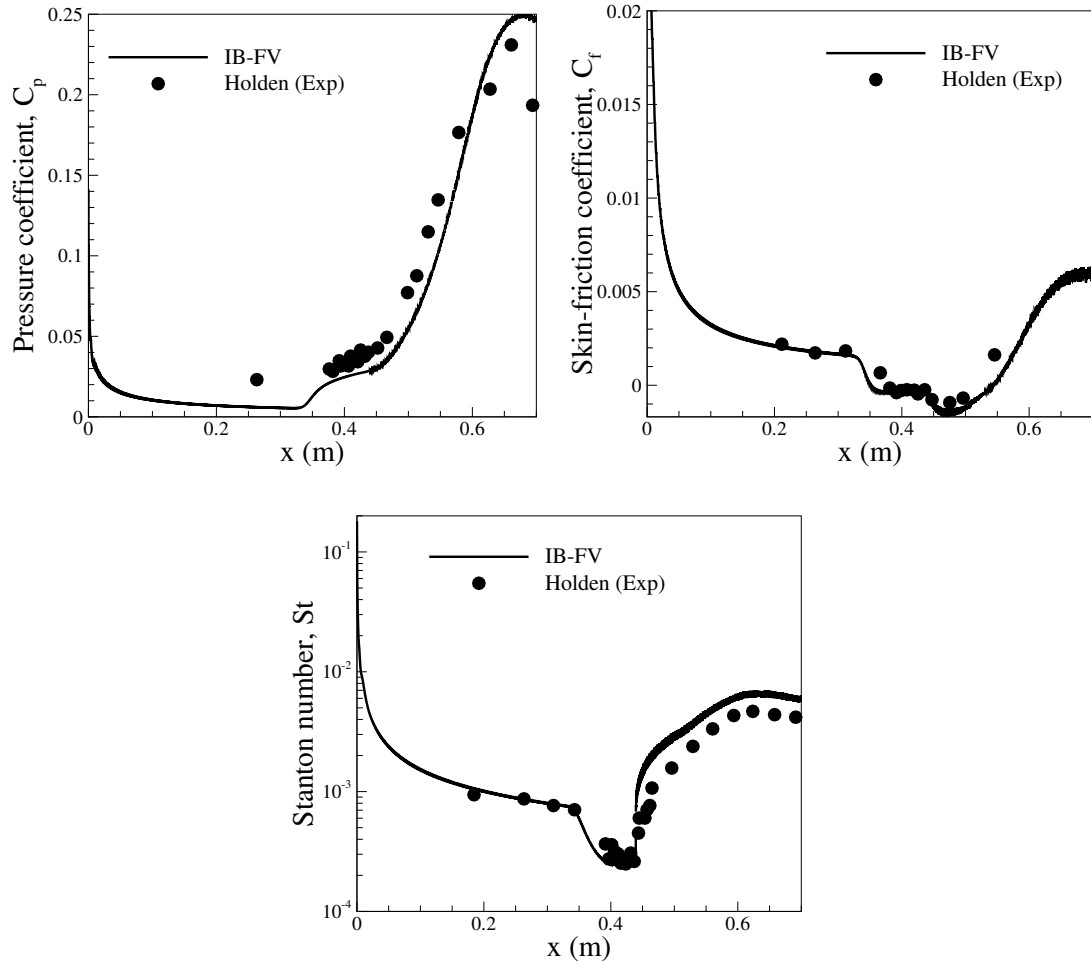


Figure 5.18: Comparison of (a) pressure coefficient C_p (b) skin-friction coefficient C_f (c) Stanton number St with experimental data [109]

5.2.8 Hypersonic flow past a cylinder

The hypersonic viscous flow past a semi-cylinder constitutes a well-studied test case but this simple geometry is also representative of aerodynamically blunt configurations typical of nose cones of hypersonic vehicles. We simulate the laminar flow at $Re_\infty = 1.835 \times 10^5$ past a semi-cylinder of radius 0.0381 m where the freestream corresponds to a hypersonic Mach number $M_\infty = 8.03$ and temperature $T_\infty = 124.94$ K. The cylinder wall is considered isothermal with a constant wall temperature of $T_w = 294.44$ K. The steady-state solution consists of a strong curved shock away from the leading edge which however does not interact with the boundary layer on the cylinder walls. As in the previous test case, we start from a uniform Cartesian mesh in a $0.07 \text{ m} \times 0.14 \text{ m}$ computational domain (see Figure 5.19(a)) with a grid spacing of 2.3×10^{-4} m into which the cylinder is immersed. The grid resolution near the surface of the cylinder is significantly increased by four levels of geometric mesh refinement resulting in a near

wall resolution of 1.43×10^{-5} m and an adapted unstructured Cartesian mesh with 244433 volumes.

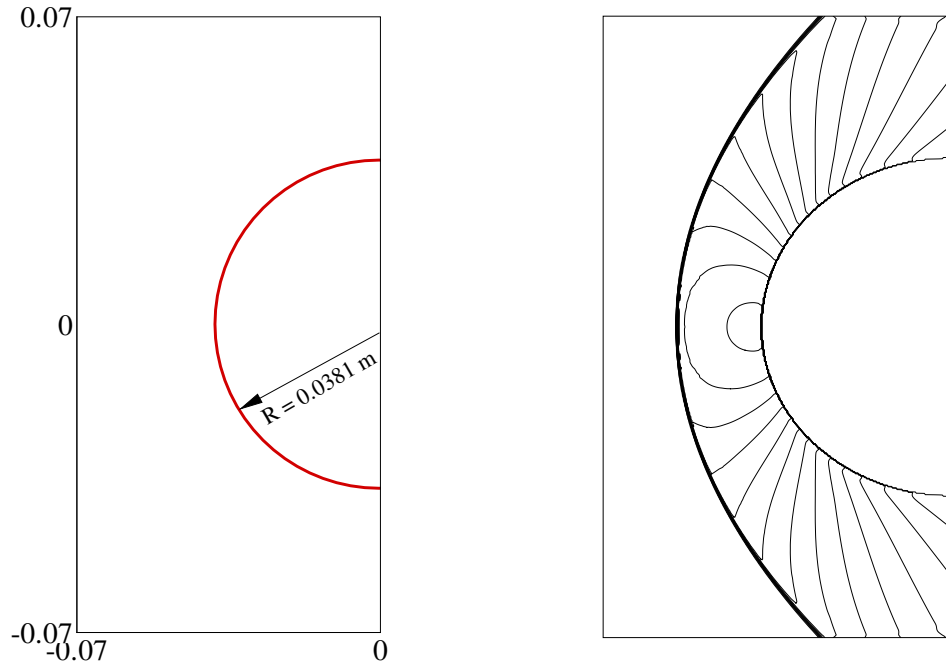


Figure 5.19: (a) Cylinder geometry (b) pressure contour for flow past cylinder (Min: 0, Δ : 5087, Max: 71220)

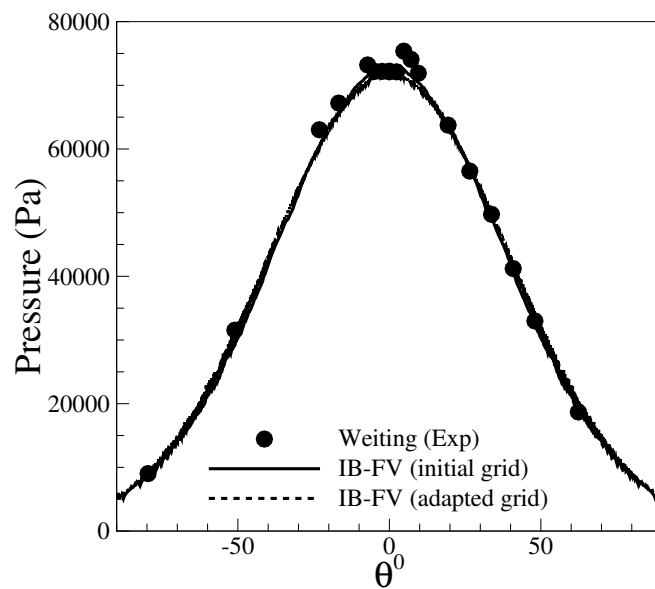


Figure 5.20: Pressure distribution along the cylinder and its comparison with experimental data [134]

Table 5.2: Comparison of stagnation point heat flux q_o

Method	q_o (W/cm ²)
Weiting[134] (Exp)	72
IB-FV (initial grid)	0.876
IB-FV (adapted grid)	5.58

The pressure contours corresponding to the steady-state solution is presented in Figure 5.19(b) where the detached bow shock is clearly visible. The distribution of pressure on the surface of the cylinder compares quite well with the experimental data of Weiting [134] as shown in Figure 5.20. Interestingly though, Table 5.2 shows that the absolute value of stagnation point heat flux is severely under-predicted by the IB-FV solver when compared with those reported in the experiments of Weiting et al. [134]. Moreover, one can notice that while grid refinement does improve the stagnation heat flux estimate around six-fold times, it remains atleast an order of magnitude smaller than the measured heat flux. This is in stark contrast to the performance of the solver for the test case in Section 5.2.7, where the Stanton number distribution on the ramp surface was quite accurately predicted. **It should be noted that in this case shock anomalies also start to appear, dependent on the mesh topology, convective schemes etc., which in turn can affect the peak heat flux prediction [135].** However, we have tried to understand the inaccurate estimation of surface heat fluxes in Chapter 6 only from the point of view of immersed boundary methods.

5.2.9 Hypersonic flow past a sphere-cone model

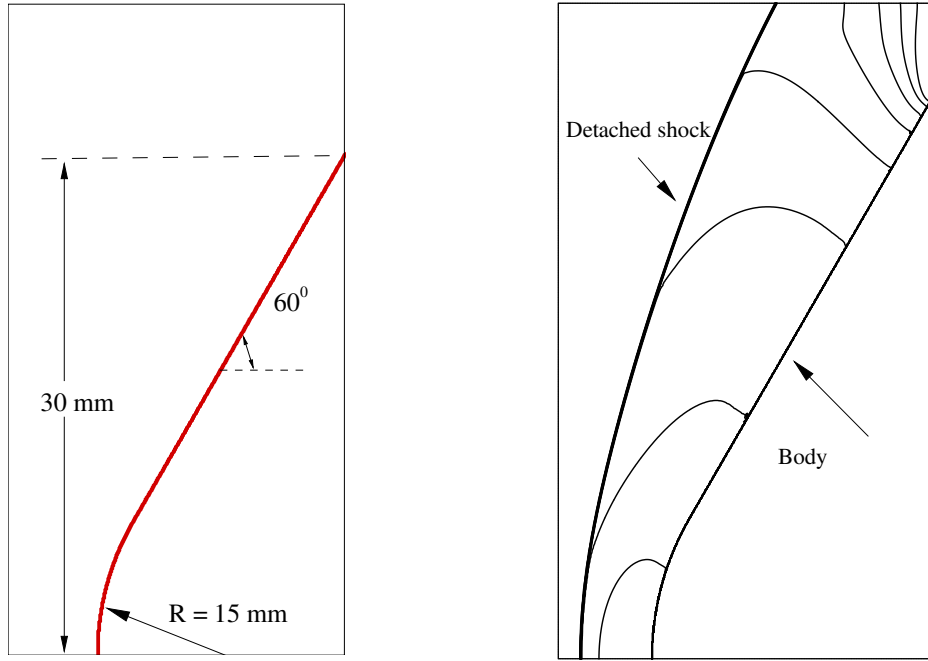


Figure 5.21: (a) Sphere-cone model (b) pressure contour for flow past the sphere-cone model (Min: 0, Δ : 5700, Max: 74930)

The final test problem that we investigate using the IB-FV solver is the hypersonic flow past a sphere-cone model shown in Figure 5.21(a). The flow is assumed to be axisymmetric in this case and the model consists of a hemisphere of radius 15 mm followed by a cone of 60° semi-vertex angle with other relevant dimensions as shown in the figure. We choose a domain of size $0.035 \text{ m} \times 0.02 \text{ m}$ which is discretised into a uniform Cartesian mesh with a grid spacing equal to $5.7 \times 10^{-5} \text{ m}$ that ensures a near-wall cell Reynolds number of ~ 280 . While one may consider employing local adaptation for improving the grid resolution, we study this test problem only on initial uniform grid. The flow conditions correspond to a freestream Mach number of 6 and temperature of 157.7 K while the Reynolds number is equal to 1.48×10^5 . These are identical to the experimental conditions in [136] where the isothermal wall has a fixed temperature equal to 300 K. The sphere-cone model is immersed into the mesh with 213500 volumes.

Table 5.3: Comparison of total force on the body

Method	F (N)
Satheesh[136] (Exp)	$167.56 \pm 2.8\%$
Truitt correlation[137]	164.44
IB-FV	166.1

Table 5.4: Comparison of stagnation point heat flux q_o

Method	q_o (W/cm ²)
Satheesh[136] (Exp)	$90 \pm 5\%$
Fay & Riddell correlation[138]	87
IB-FV	2.22

The pressure contours in Figure 5.21(b) depicts the strong detached bow shock that is typical of flow past blunt bodies akin to the test case studied in Section 5.2.1. It may be noted however that although the bow shock does not interact with the boundary layer, there is indeed a strong expansion of the flow on the surface of the body. While no direct measurements of skin friction, the total drag force on the body has been experimentally measured. Table 5.3 shows the drag computed from the IB-FV solver along with those from experiments and Truitt correlation [137]. The agreement is excellent and may be construed as evidence that the wall pressure and skin friction distribution (that contribute to the drag) are accurately estimated as well. However, we observe that stagnation point heat flux from the computations using the immersed boundary method (Table 5.4) are significantly smaller (by around 40 times) from those determined from experimental measurements while the latter shows a good agreement from the estimates obtained using the Fay-Ridell correlation [138]. This under-prediction for heat flux estimation in a high Reynolds number flow past a blunt configuration has also been observed for the cylinder test case (see Table 5.2) even when a higher mesh resolution were employed and reinforces the fact that the IB-FV solver may not always estimate the wall heat flux distributions to reasonable accuracy. Considering the fact that the conservation laws are solved in a coupled manner, except in the near vicinity where the primitive variables are all reconstructed, it is surprising that only the heat fluxes for the high Re hypersonic flows past blunt geometries are heavily under-estimated.

5.3 Summary

In this chapter a sharp-interface immersed boundary method (HCIB) for compressible viscous flows has been developed in an unstructured Cartesian mesh framework. The IB-FV solver treats the geometry as a sharp interface with the boundary conditions directly enforced using a one-dimensional solution reconstruction process. The solution reconstruction involves interpolation of primitive variables in the near vicinity of the body and is therefore not discretely conservative. From several numerical studies it was observed that the IB-FV solver can accurately estimate wall pressure distributions even at coarse grid resolutions. Accurate predictions of skin friction are possible with acceptable levels of grid refinement which signifies that the estimates of aerodynamic coefficients using this approach are reliable although wall heat fluxes may or may not be computed accurately. It must however be noted that on coarser mesh resolutions, the skin-friction estimates while reasonably accurate, can be significantly oscillatory. The inaccuracies in heat flux predictions are observed in case of blunt geometries where the Mach and Reynolds numbers are high as well. An in-depth analysis is desired in this regard to delineate the reason for the under-prediction and the next chapter is intended for this purpose.

CHAPTER 6

REVISITING THE SHARP INTERFACE IMMersed BOUNDARY FOR VISCOUS FLOWS

“Debugging is twice as hard as writing the code in the first place. Therefore, if you write the code as cleverly as possible, you are, by definition, not smart enough to debug it”

- Brian Kernighan, *Kernighan’s Law*

Employing a set of carefully designed experiments and simple diagnostic tools, we probe the possible causes for the under-prediction in heat flux. We show that there exist two sources of error in the HCIB approach - one due to grid non-conformality and resolution while the other arises from the solution reconstruction in the cells in the vicinity of the sharp interface. Our investigations show that the errors due to **solution reconstruction** are more prominent than those **due to grid resolution** and are primarily responsible for the observed under-prediction in heat flux. Moreover, we demonstrate that **these errors can be linked to the loss in discrete conservation** and are not significantly mitigated by a finite number of grid refinements. Studies also reveal that the heat flux estimates from the IB-FV solver **remain largely independent of the temperature reconstruction** and that the under-prediction is severe in case of flows with higher Mach and Reynolds numbers. The errors due to temperature reconstruction are found to persist even when the walls are adiabatic with the skin temperatures predicted from the IB-FV solver found to be lesser than those obtained with a finite volume solver on

Contents of this chapter are part of the manuscript titled “**Development and assessment of a new sharp interface immersed boundary method for hypersonic viscous flows**”, (under review)

a conformal mesh with equivalent mesh resolution. The investigations present strong evidence in support of the claim that anomalous heat transfer estimates are a consequence of inaccuracies in solution reconstruction and that accurate estimation of heat transfer for high Reynolds number flows would necessitate unacceptably large number of mesh refinements. On the basis of these studies, we conjecture that current state-of-art sharp interface IB approaches are likely to be inaccurate for heat transfer predictions in high Reynolds number hypersonic flow past generic configurations while being able to accurately compute the aerodynamic forces.

In continuation with the efforts of chapter 5, this section has been devoted towards a set of simple diagnostic approaches and utilise them to probe and understand the likely sources of error that lead to inaccurate heat flux predictions in flows past blunt geometries. To this end, we shall choose the hypersonic laminar flow past a cylinder discussed in the earlier chapter as a representative test problem to perform the diagnosis. The geometry and freestream conditions for this test case are identical to those in Section 5.2.8 of Chapter 5, unless otherwise specified.

6.1 Resolution and reconstruction errors

The Cartesian immersed boundary approach discussed in the present study is implemented within the framework of an unstructured finite volume (FV) flow solver. This means that one could employ the FV solver with a body-fitted structured mesh in which case the conservation laws are solved in all control volumes. On the contrary, the IB-FV solver uses a Cartesian mesh which does not conform to the geometry with the conserved quantities in the near vicinity of the *body obtained using an interpolation rather than as a solution to the governing partial differential equations.* It is therefore possible to hypothesise that there are two kinds of errors when employing IB-FV solver on non-conformal Cartesian meshes. While the body-fitted grids resolve the boundary layers using large aspect ratio cells aligned with the body, the use of Cartesian mesh would mean that the thin shear layer is being resolved using nearly unit aspect ratio volumes that do not conform to the geometry. The errors that arise due to the use of a non-conformal Cartesian mesh in capturing the viscous layer close to the walls are termed as “*resolution errors*”. Furthermore, while the finite volume approach is inherent to the IB-FV solver, it is applied almost everywhere except in the close vicinity of the walls which is *precisely where the thin boundary layer forms.* The use of a simple interpolation for the conserved quantities in the near-wall region using the IB-FV approach would mean that these quantities would not necessarily satisfy discrete conservation that is inherent to the construction of the FV solver. The errors

resulting from this loss of discrete conservation as a consequence of the solution reconstruction strategy are referred to as “*reconstruction errors*”. One must appreciate at this juncture that the immersed boundary approach is merely a philosophy that is employed in conjunction with a suitable discretisation of the conservation laws, which in this study is the finite volume method.

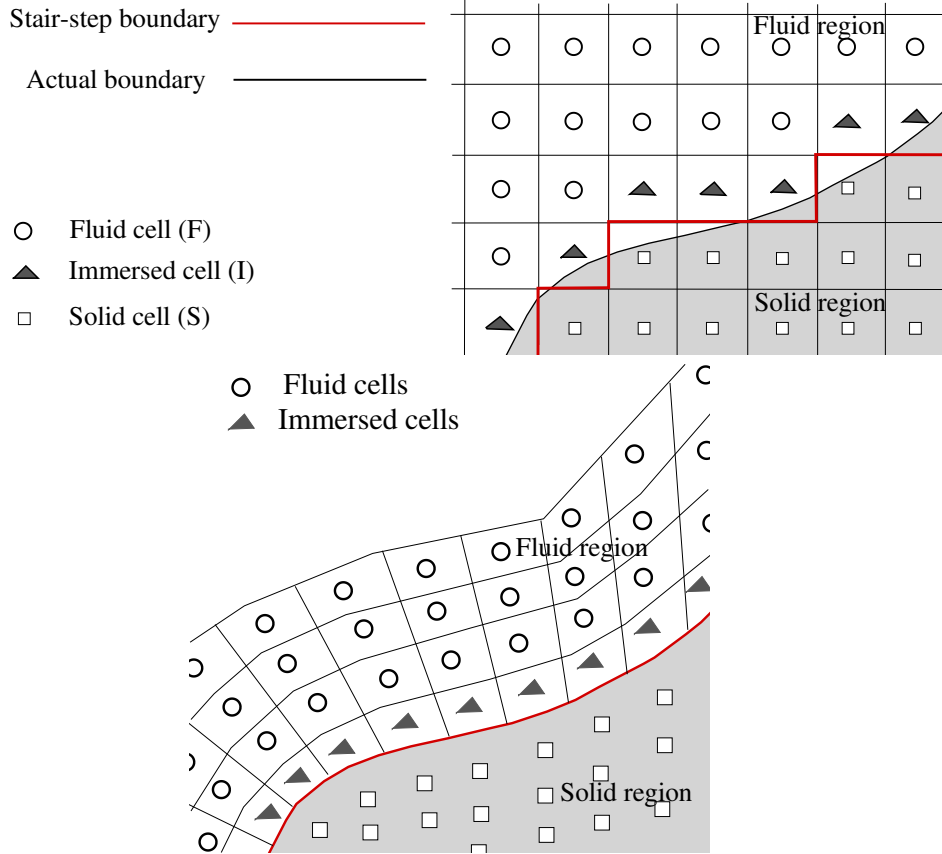


Figure 6.1: (a) Stair-step boundary (b) body conformal grid

In order to isolate the role of these errors in estimation of relevant physical parameters, we therefore propose two approaches in addition to the body-fitted finite volume method (referred to as FV herein) and the Cartesian mesh based IB-FV solver (referred to as IB-FV herein). The first is the “stair-step FV” approach which uses a Cartesian mesh similar to that in the IB-FV solver. However, the geometry in this case is represented using a “stair-step approximation” (see Figure 6.1(a)) with the boundary conditions directly enforced on the faces of the Cartesian mesh that approximate the true shape of the body. The second approach is the “conformal IB” approach wherein the geometry is immersed into a hybrid mesh (see Figure 6.1(b)) such that the fluid domain is discretised using a structured mesh with the geometry coincident with the grid lines. Even though the mesh now conforms to the geometry, we obtain

the solution in a manner akin to the IB-FV solver with the conserved variables in the near-wall cells computed using the solution reconstruction approach (**the near-wall properties corresponds to the cell-centroid values of the ‘I’ cells or cells adjacent to the surface of the body**). It must be remarked that while the “stair-step FV” and “conformal IB” are not viable solution methodologies in practice they are valuable tools to analyse the resolution and reconstruction errors. In particular, the “stair-step FV” approach is devoid of reconstruction errors and can thus highlight the role of grid resolution while the “conformal IB” approach may be used to explore the influence of solution reconstruction on a conformal mesh. We also remark that the IB-FV and stair-step FV approaches employ the same Cartesian mesh, the nature of structured mesh resolving the boundary layer and other flow features in the domain is identical between the FV and conformal IB solvers.

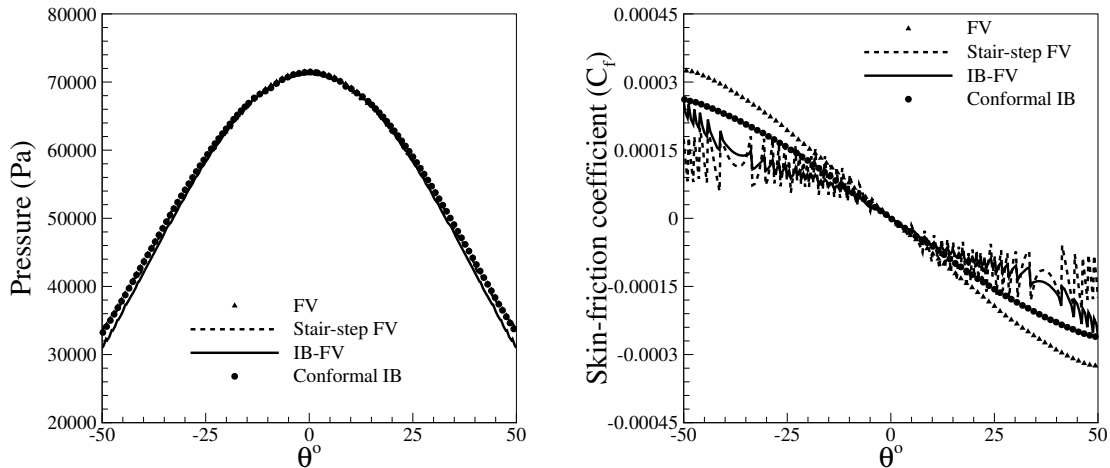


Figure 6.2: Comparison of (a) pressure (b) skin-friction coefficient C_f

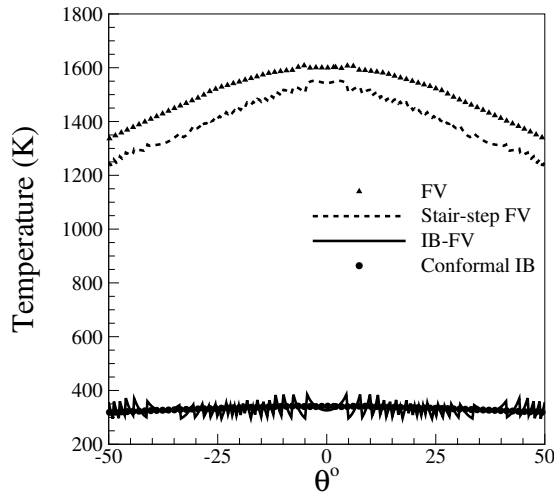


Figure 6.3: Distribution of near wall temperature

Table 6.1: Comparison of stagnation point heat flux q_o

Method	q_o (W/cm ²)
FV	29.3
Stair-step FV	28.3
IB-FV	0.87
Conformal IB	1.05

Figure 6.2(a) shows the pressure distribution for flow past the cylinder using these four approaches and the mutual agreement of the computed pressures is not surprising. The skin friction estimates from the four methods show a fair agreement as well although some differences can be observed with the use of a Cartesian mesh when compared with a body-fitted grid (Figure 6.2(b)). It may be remarked that the grid resolution of the Cartesian and body-fitted meshes are comparable although the meshes employed are not sufficiently fine to ensure grid-independent solutions. However, we observe that the predictions of near-wall temperature depicted in Figure 6.3 are quite different, with those obtained using FV and stair-step FV approaches exhibiting a good agreement among themselves while also being higher than those computed using conformal IB and IB-FV methods. If the numerical estimates from the FV approach is treated as the benchmark, it is easy to see that the stair-step FV approach is clearly superior to the conformal IB approach. This suggests that the inaccuracies in wall heat flux computations, quantified by the deviation from the FV results, are largely a manifestation of the solution reconstruction. This is because the near-wall temperature distribution on a conformal mesh (also employed for the FV solver) computed using solution reconstruction at the boundaries is significantly lesser than that predicted with a Cartesian mesh and approximated stair-step like geometry.

despite the nearly unit aspect ratio quadrilateral cells in the latter not aligned with the boundary layer. We can therefore conclude that the loss in discrete conservation near the boundaries that is a consequence of solution reconstruction in the conformal IB approach is responsible for the under-estimation of the heat flux when compared with the FV benchmark. The good agreement of stagnation point heat flux estimates from the stair-step FV approach with those from the FV approach in Table 6.1, even when the grids are different, may therefore be attributed to the fact that both approaches are discretely conservative everywhere in the domain.

6.2 Studies with local grid refinement

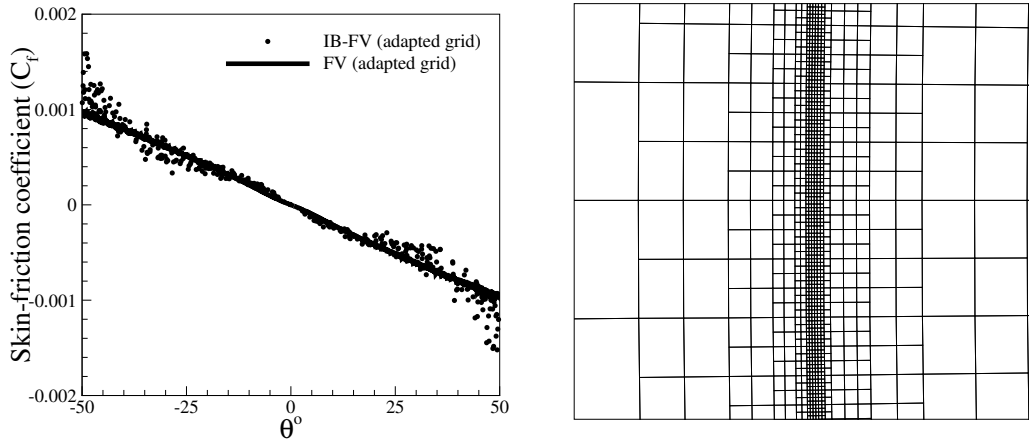


Figure 6.4: (a) Comparison of skin-friction coefficient C_f on adapted grid (b) enlarged view of adapted grid

Table 6.2: Comparison of stagnation point heat flux q_o in adapted grid

Method	q_o (W/cm ²)
Weiting (Exp) [134]	72
FV (adapted grid)	61.7
FV (initial grid)	29.3
Conformal IB (adapted grid)	4.9
Conformal IB (initial grid)	1.05

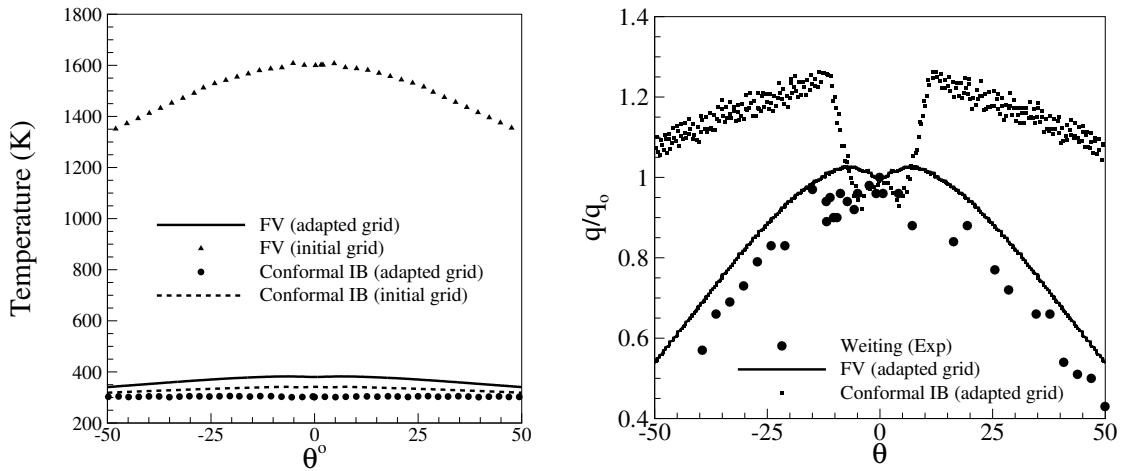


Figure 6.5: Distribution of (a) near wall temperature (b) normalised wall heat flux q/q_o

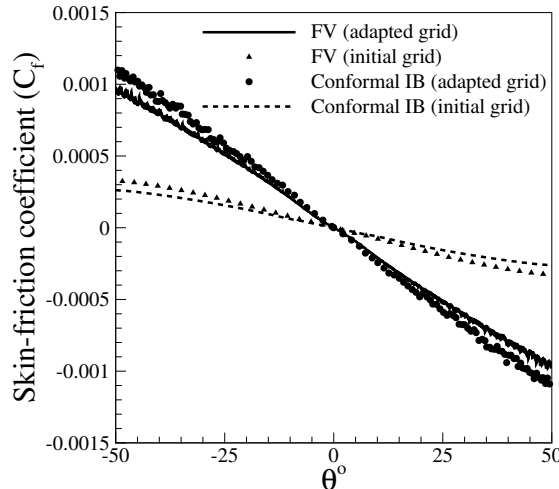


Figure 6.6: Comparison of skin-friction coefficient C_f along the cylinder on the adapted grid

The lack of discrete conservation is clearly inherent in the immersed boundary approach, but it does lead to reasonably accurate estimates of skin friction (see Figure 6.4(a)) and in some cases, even heat transfer (see Figure 5.18(c), Chapter 5). The lack of mass conservation in sharp-interface IB methods has been shown to be proportional to the grid spacing [139] and this motivates the study of adaptive mesh refinement in the context of IB approaches. Specifically, we try to address the issue of whether increasing the near-wall grid resolution can improve the estimates of wall heat flux. Towards this objective, we compare the numerical solutions obtained on the same structured mesh using FV and conformal IB approaches on unadapted as well as locally adapted meshes. The initial unadapted grid consists of 29000 cells with a near-

wall spacing of 2.283×10^{-4} m and is adapted to five levels in the vicinity of the solid wall as shown in Figure 6.4(b). We carry out an isotropic grid refinement where each quadrilateral cell is divided into four smaller quads. The final adapted grid has 102200 cells with the cell Reynolds number being ~ 35 . The results using the FV approach on the initial and adapted grids clearly show marked improvement with the stagnation heat flux on the adapted mesh being close to the experimental value of 72 W/cm^2 . It must be noted that the FV simulations on the final adapted mesh were performed with van Leer scheme for the convective computations. The results from the conformal IB approach show improved estimates on grid refinement; however the estimates on the adapted mesh are significantly lower than those from the FV approach (see Table 6.2). This is consistent with the near-wall temperature distributions (Figure 6.5(a)) wherein one can see that the temperatures obtained with the conformal IB approach show a qualitative trend different from those obtained with the FV approach, while also being considerably lesser in magnitude and closer to the wall temperature. Figure 6.5(b) shows the normalised heat flux distribution on the adapted mesh using both approaches. The estimates from FV approach show a reasonable agreement with the experimental data whereas the normalised heat fluxes from the IB-FV approach are anomalous. In fact, the stagnation point heat transfer from the IB-FV approach is not clearly the expected maxima which is likely due to the erroneous near-wall temperatures which translate into incorrect wall heat fluxes. Interestingly, the skin friction distribution on the adapted mesh using these approaches in Figure 6.6 are in good agreement, indicating that the solution reconstruction does not adversely affect the wall shear stress estimates.

The importance of this study is that it strongly reveals the overwhelming dominance of “reconstruction” errors in estimating wall heat fluxes while using an immersed boundary approach. The study demonstrates that the heat flux estimates even on a conformal mesh but using solution reconstruction does not improve significantly with increasing grid resolution. While one could perform further levels of grid refinement, it is not difficult to see that a finitely large number of mesh refinements would be necessary, even with a conformal IB approach, to achieve the accuracy of solutions obtained on an adapted mesh with five levels of refinement using the FV approach. Consequently, the number of levels of grid refinement on a non-conformal mesh that employs the IB-FV approach would be even higher and therefore not feasible in practice. One must contrast this observation with the studies in [70, 74] where the use of local grid refinement upto 14 levels (leading to a cell Reynolds number of ~ 1 resulted in quite accurate estimates of skin friction and heat flux. It must however be remarked that these studies were limited to low Reynolds number flows (less than 2000) and do

not consider high Re viscous flows as considered in this study. Our observations for this test case therefore point to the fact that local grid refinement has a weak influence on heat flux estimates obtained with IB-FV solvers and that while it is possible to obtain accurate estimates of wall shear stress with acceptably finite number of grid refinements, the predictions of wall heat fluxes could be practically infeasible with such an approach.

6.3 Selective solution reconstruction

The investigations using the conformal IB approach have highlighted the role of solution reconstruction on the numerical solution in the near-wall region and therefore on the wall heat flux calculations. In order to understand this aspect further, we employ a selective reconstruction approach for the variables in the immersed cells. The approach of selective reconstruction implies that we do not reconstruct all the primitive variables as in the conformal IB approach discussed earlier. Since the grid is conformal to the body, we first obtain the solution everywhere in the domain (including the near-wall I cells) using the finite volume approach. Subsequently, we reconstruct *select* primitive variables in the I cells while the values for the remaining variables are retained from those obtained using the finite volume method.

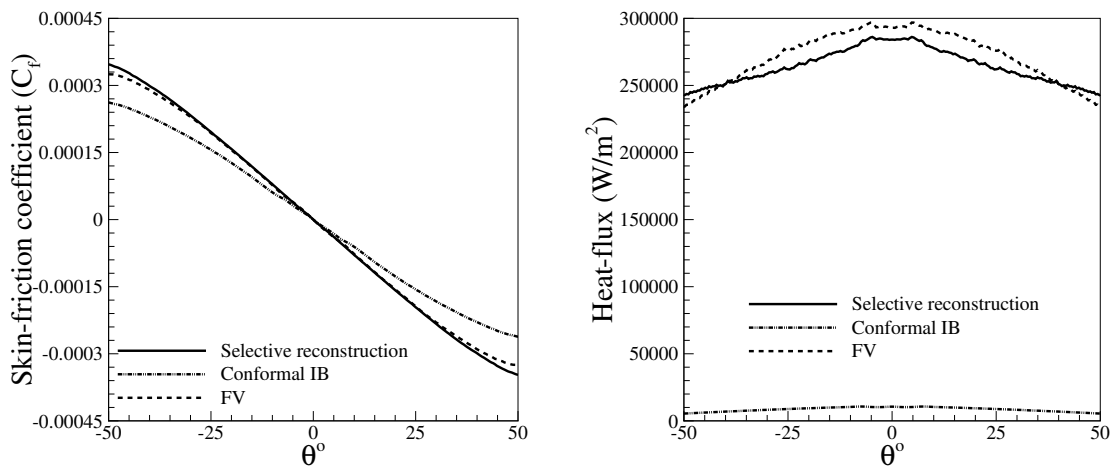


Figure 6.7: Comparison of (a) skin-friction coefficient C_f (b) wall heat-flux

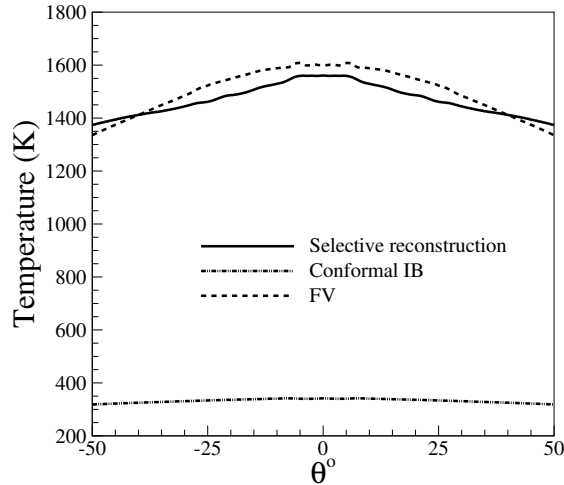


Figure 6.8: Comparison of near wall temperature along the cylinder

Recognising that it is the reconstruction of temperature that led to inaccurate wall heat flux predictions, we consider the scenario where all variables except the temperature are reconstructed. Figures 6.7(a) and 6.7(b) show the skin friction and heat flux distributions obtained using the selective reconstruction approach on the coarsest mesh. The choice of the coarsest grid resolution is a matter of convenience and the conclusions arrived at herein hold good even on adapted meshes. A comparison of these predictions with those from the FV and conformal IB approaches is very illuminating. It may be observed that the skin friction predictions are qualitatively similar and the quantitative differences that exist are likely to mitigate with grid refinement (see Figure 6.4(a)). Surprisingly, the stagnation heat flux estimates obtained from the selective reconstruction is much closer to those predicted by the FV approach and this is reflected in the near-wall temperature distributions shown in Figure 6.8. This is in contrast to the conformal IB approach where the reconstruction of all variables including temperature led to under-prediction in stagnation point heat transfer (see Table 6.2). One may therefore conclude that the errors in discrete conservation of energy is the source of inaccurate estimates of heat transfer although the lack of discrete conservation of mass and momentum do not appear to overwhelmingly affect the estimates of surface pressure and wall shear stress. This study reaffirms the fact that the temperature reconstruction is strongly linked to the lack of discrete energy conservation and we investigate the possibility of employing non-linear and non-polynomial reconstruction approaches in a bid to improve discrete energy conservation in immersed boundary methods.

6.4 Alternate reconstruction approaches

In light of the conclusions from investigations in Sections 6.1 and 6.3 wherein the importance of solution reconstruction was highlighted, we consider three alternate reconstruction approaches for the temperature in the conformal IB approach. We reiterate that the reason behind using conformal IB approach instead of the IB-FV approach is to isolate the reconstruction errors from the resolution errors. Furthermore, the interpolation approaches we discuss in this section are limited to temperature alone; all other primitive variables are reconstructed using linear interpolation.

The temperature variation can be described using non-linear and non-polynomial interpolants, but the choice of specific interpolants is limited by the number of points in the fluid domain whose information is necessary. Furthermore, there is strictly no solid basis for the choice of linear interpolant except that it is simple to use and works for most scenarios, particularly in incompressible flows where immersed boundary methods have found favour. While the linear interpolants have been used in compressible IB approaches [140], it is clearly desirable to employ physics-based interpolation approaches for temperature and even other primitive variables in compressible laminar flows, akin to the power-law interpolation for velocities in case of incompressible turbulent flows. We discuss the following three interpolants as alternatives to linear interpolation for the reconstruction of temperature in the I cells.

1. Quadratic interpolation defined by,

$$T_I = T_b + \left[\frac{1}{r_{bf}} \frac{\partial T}{\partial r} \Big|_f - \frac{1}{r_{bf}^2} (T_f - T_b) \right] r_{bI}^2 + \left[\frac{2}{r_{bf}} (T_f - T_b) - \frac{\partial T}{\partial r} \Big|_f \right] r_{bI} \quad (6.1)$$

This is a second-order accurate non-linear polynomial interpolation and the basis of its choice is purely mathematical with the expectation that it would perform better than the linear interpolation.

2. Power-law interpolation defined by,

$$T_I = T_b (cr + 1)^{\frac{1}{\omega+1}}; \quad c = \frac{\left[\left(\frac{T_f}{T_b} \right)^{\omega+1} - 1 \right]}{r_{bf}} \quad (6.2)$$

where, r is the distance along the outward local normal from the body point b and the viscosity variation is also described using a power-law given by,

$$\frac{\mu}{\mu_\infty} = \left(\frac{T}{T_\infty} \right)^\omega$$

where, $\omega = 0.72$. This interpolant is inspired by the studies in [141] which remark that the temperature variation in hypersonic laminar boundary layers may be described using a power-law variation.

3. Non-polynomial interpolation defined by,

$$\frac{T_I}{T_f} = \frac{T_b}{T_f} + \left[\left(1 - \frac{T_b}{T_f} + \frac{r(\gamma - 1)}{2\gamma RT_f} u_{||f}^2 \right) \left(\frac{r_{bI}}{r_{bf}} \right)^k \right] - \frac{r(\gamma - 1)}{2\gamma RT_f} u_{||f}^2 \left(\frac{r_{bI}}{r_{bf}} \right)^{2k} \quad (6.3)$$

This non-polynomial interpolant follows from the Walz correlation for compressible boundary layers where we use $k = 1$ for the case of laminar flows and the recovery factor r is chosen equal to \sqrt{Pr} . This correlation has been used previously in the framework of immersed boundary methods in [71], but the focus therein was not on heat transfer/skin friction estimates. A similar interpolant can be employed even if the walls are adiabatic and reads,

$$\frac{T_I}{T_f} = 1 + \frac{r(\gamma - 1)}{2\gamma RT_f} u_{||f}^2 \left(1 - \left(\frac{r_{bI}}{r_{bf}} \right)^{2k} \right) \quad (6.4)$$

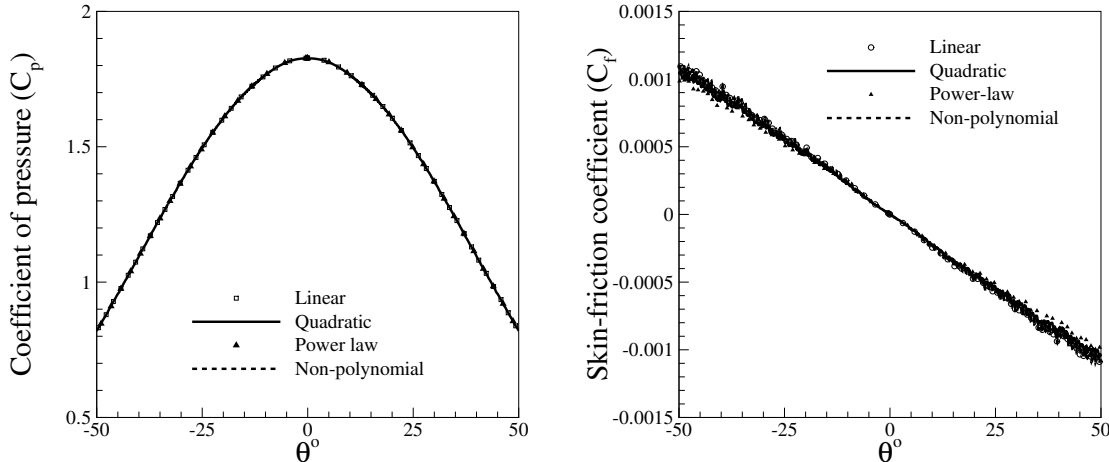


Figure 6.9: Comparison of (a) pressure coefficient C_p (b) skin-friction coefficient C_f , along the cylinder

We carry out studies on the adapted mesh with highest near-wall resolution using the conformal IB approach with these alternate reconstruction approaches for temperature. One can easily see that the pressure coefficient and skin friction are not very different even when quadratic or non-polynomial interpolants discussed above are employed (see Figures 6.9(a) and (b)). This is expected, but the surprising result is that the use of power-law interpolation and the Walz correlation do not improve the stagnation heat transfer estimates over those obtained using a simple linear in-

terpolation (see Table 6.3). This is despite the fact that these non-polynomial interpolants are derived from physical considerations for temperature distribution in high-speed boundary layers. Interestingly, the quadratic interpolation is seen to further under-estimate the stagnation heat flux values which may however be attributed to the nature of computed parabolic variation. We have seen that the numerical fit for the quadratic interpolant turns out to be a concave parabola for all I cells (not shown here for brevity) which means the temperatures of the immersed cells are lesser than those obtained using a linear interpolant. Consequently, the computed wall heat fluxes are smaller as well which explains why the linear interpolation outperforms the quadratic interpolation while the naive expectation would be otherwise. One may consider imposing a very high-degree polynomial interpolant (say five or higher) to describe the temperature variation but computing the unknown polynomial coefficients would require data from more points (analogous to f) in the fluid domain and would be computationally expensive. Moreover, the failure of interpolants rooted in physical basis in accurately predicting wall heat fluxes does not augur well for mathematically-inspired high-degree polynomial interpolants which are unlikely to perform any better.

Table 6.3: Comparison of stagnation point heat flux q_o on the adapted grid

Method	q_o (W/cm ²)
FV	62
Conformal IB, Linear	4.97
Conformal IB, Quadratic	0.64
Conformal IB, Power-law	5.04
Conformal IB, Non-polynomial	4.96

6.5 Dependence on freestream and wall conditions

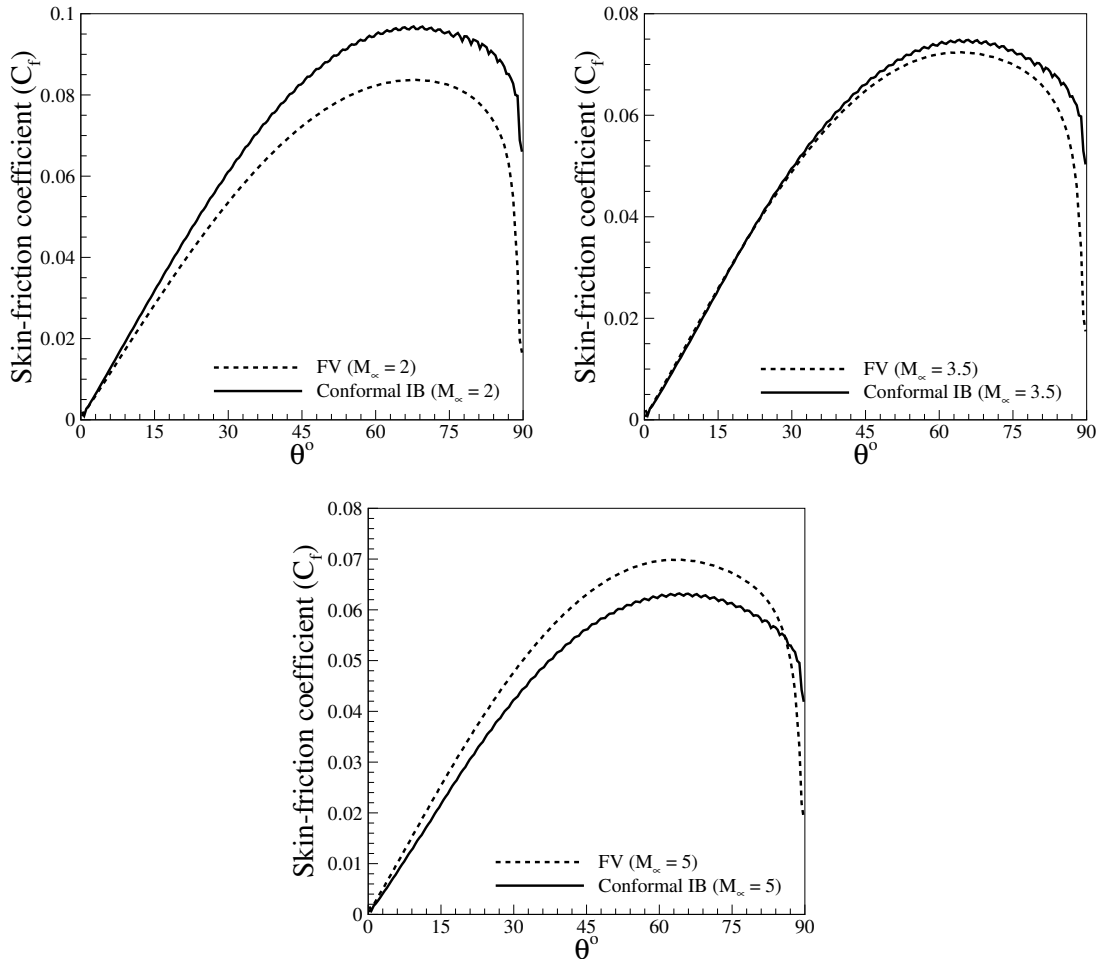


Figure 6.10: Comparison of skin-friction C_f along the cylinder for freestream Mach number (a) 2.0 (b) 3.5 (c) 5.0

The use of adaptive mesh refinement to improve the accuracy of predicted wall heat flux and shear stress estimates has been shown to be ineffective for moderate levels of refinement in the studies in Section 6.2. However, there have been limited studies [70, 74] where 14 levels of refinement have been employed for flow past a cylinder with the computed estimates for heat transfer and skin friction showing good agreement with experimental data. However, these studies have been largely restricted to low Reynolds number flows and this motivates us to investigate the effect of freestream and wall conditions on the numerical solutions obtained using the immersed boundary approach. We continue to employ the conformal IB approach on a coarse structured mesh and compare the solutions with those obtained using a FV approach which is treated as a benchmark. It may be noted that the results of either approaches are not grid-independent but the focus of these studies is on the effect that freestream Mach

and Reynolds numbers have on the differences between the computed estimates using the two approaches for the same grid resolution.

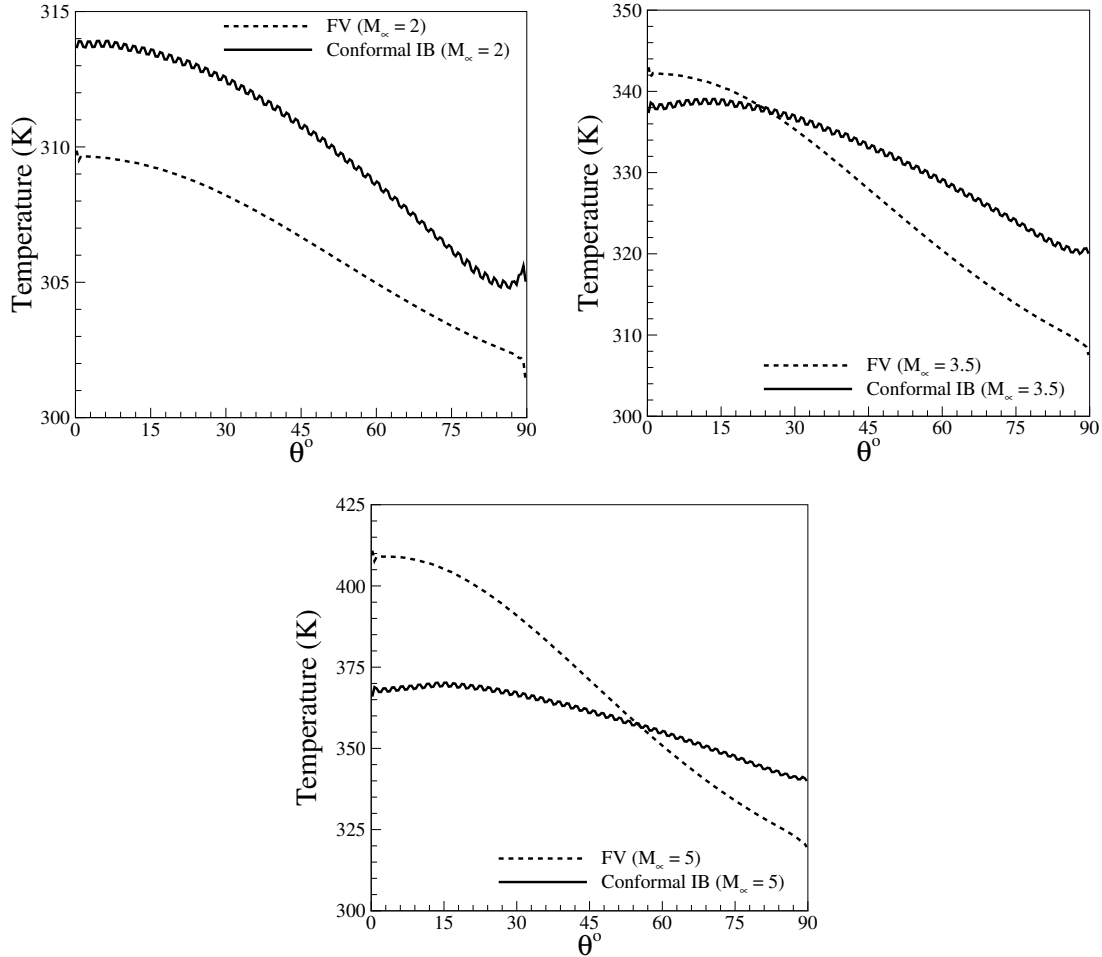


Figure 6.11: Comparison of near wall temperature distribution for freestream Mach number (a) 2.0 (b) 3.5 (c) 5.0

We first study the influence of freestream Mach number for a fixed Reynolds number $Re_\infty = 500$ by considering three different Mach numbers. The surface skin friction distribution are shown for $M_\infty = 2, 3.5$ and 5 respectively in Figure 6.10 where one can see that the estimates from FV and conformal IB show a qualitative agreement and the deviation is relatively more prominent at the lowest and highest values of Mach number. While the results from the two approaches for the wall shear are not expected to agree, the deviation in the results are not too significant and the results from the conformal IB approach can be improved through adaptive mesh refinement, which is however not shown herein. The near-wall temperature distribution for the three Mach numbers are shown in Figure 6.11 and one can clearly discern the differences. Noticing that the temperature scales differ in these plots, one can see that the disagreement between the computed estimates from the approaches tend to increase as the Mach

number increases, which would consequently appear as deviation in wall heat fluxes. Therefore, one can conclude that the heat flux estimates of the conformal IB solver tend to be further off from those predicted using the conservative FV approach as the freestream Mach number increases.

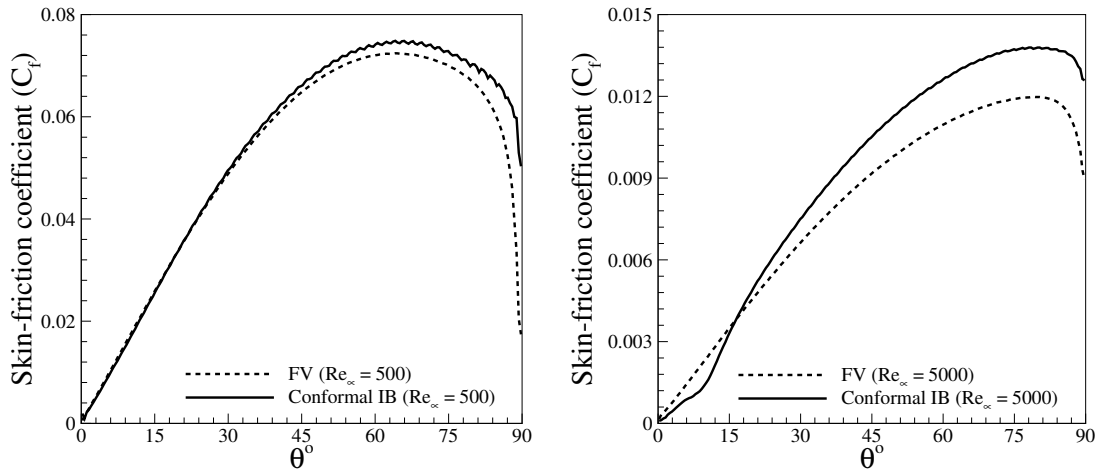


Figure 6.12: Comparison of skin-friction C_f along the cylinder for freestream Reynolds number (a) 500 (b) 5000

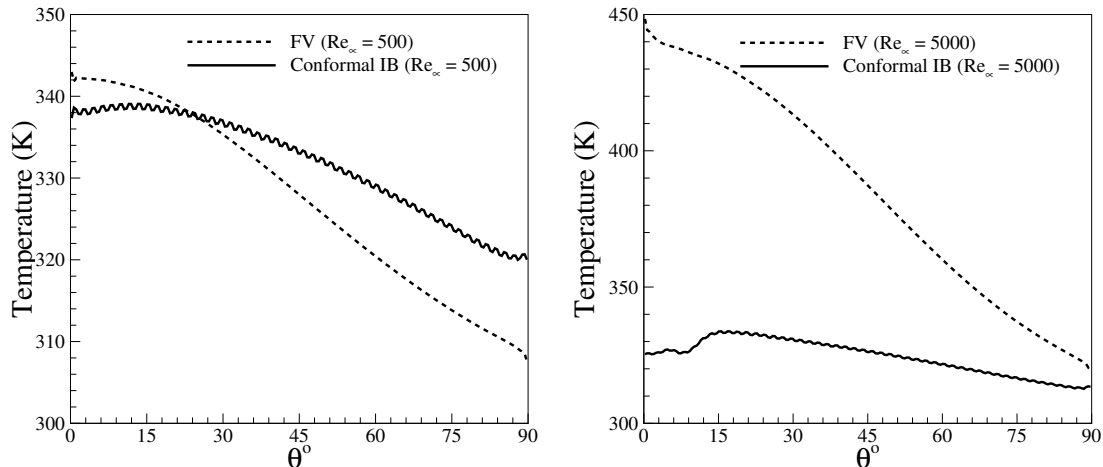


Figure 6.13: Comparison of near wall temperature distribution for freestream Reynolds number (a) 500 (b) 5000

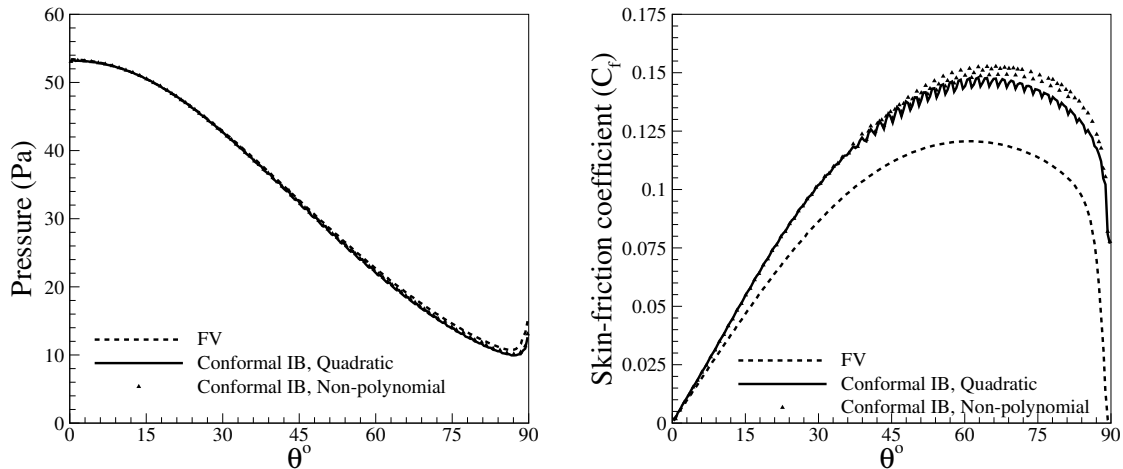


Figure 6.14: Comparison of (a) pressure (b) skin-friction coefficient C_f , along the cylinder

The second study we carry out is to understand the role of freestream Reynolds number for high-speed flows for which we choose two Reynolds numbers viz. $Re_{\infty} = 500$ and 5000 respectively. We keep the freestream Mach number constant at 3.5 for these computations and the skin friction and near-wall temperature distributions for the two cases are shown in Figures 6.12 and 6.13. While one can notice that the discrepancy between the FV and conformal IB solutions for skin friction distribution is not considerable at either Reynolds numbers, the near-wall temperatures are different between the two methods with the differences being significantly higher for the case of higher Reynolds number (see Figure 6.13). The near-wall temperatures for the isothermal cases are directly linked to the wall heat flux estimates and the lesser estimates of these temperatures at $Re_{\infty} = 5000$ would translate into under-prediction of wall heat fluxes as well when compared to the estimates from the FV approach.

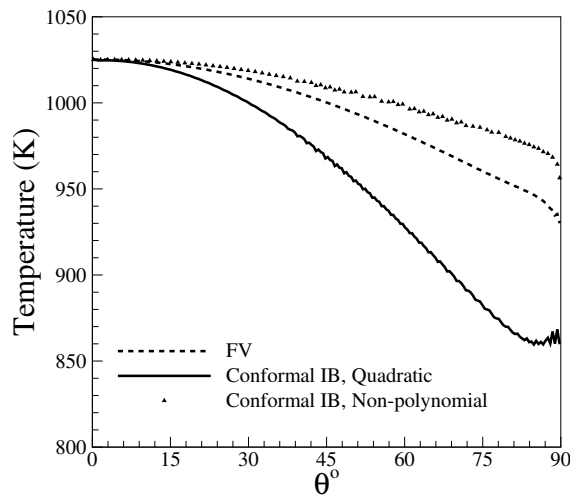


Figure 6.15: Distribution of skin temperature

To assess the influence of wall conditions, we consider the same test case of laminar hypersonic flow past the cylinder except that the wall is considered adiabatic instead of isothermal. The flow conditions correspond to $M_\infty = 3.5$, $Re_\infty = 500$ and $T_\infty = 300$ K, for a cylinder with radius of 0.1 m. A naive argument would be that since the wall heat flux is zero by definition, the IB approaches would work well for the case of adiabatic surfaces. It may be noted that the temperature variation is assumed to be either quadratic (see Section 5.9) or one could employ the Walz correlation (see Section 6.4). One can see from Figures 6.14(a) that the wall pressure distribution from the conformal IB approach using either temperature reconstructions agrees excellently with those computed using the FV solver. The agreement of the skin friction distribution is fair (Figure 6.14(b)), although one would require a greater near-wall grid resolution when the conformal IB is employed for the estimates to agree excellently with those obtained from the FV approach. Although the wall heat flux is zero, the estimate of skin temperatures (or the wall temperatures) clearly highlight the inaccuracies inherent in the solution reconstruction as can be observed from Figure 6.15. The largest difference between the FV and conformal IB estimates is around 110 K when the quadratic interpolant is employed while the non-polynomial interpolation based on Walz correlation shows a better agreement with a maximum difference of 30 K. Moreover, while the non-polynomial interpolation over-predicts the skin temperatures compared with the FV benchmark, the use of quadratic interpolation leads to an under-prediction. It must be emphasised that the adiabatic test case considered here is however at a relatively low Reynolds number and investigations at higher Reynolds numbers are necessary to make substantial conclusions related to the performance of IB approaches for hypersonic viscous flows with adiabatic walls.

These studies show that the non-conservative approach inherent to the sharp-interface IB approach could lead to smaller heat flux estimates (for isothermal surfaces) than those from the conservative FV approach with the differences being more prominent at higher Mach and Reynolds numbers. The solution reconstruction is also found to influence the skin temperatures in case of adiabatic walls. These studies may also be construed as evidence in support of the under-prediction of stagnation point heat transfer observed for the studies in Sections 5.2.8 and 5.2.9 wherein the flows are at high Reynolds numbers (of the order of 10^6) and hypersonic Mach numbers (greater than 5).

6.6 Discussions and remedial approaches

We summarise in this section the salient findings from the numerical investigations pertaining to the sharp-interface immersed boundary approach and discuss its ramifications for simulations of realistic hypersonic flows. The major observations that can be made from the numerical experiments including the diagnostic studies are enumerated below.

1. The solution reconstruction approach inherent to sharp-interface IB methods introduce conservation errors that heavily influence the heat transfer while the pressure is least sensitive to these errors. The use of local grid refinement can compensate for these conservation errors only to the extent that while accurate estimates of wall shear stress with an acceptably finite number of local mesh refinements is possible the wall heat fluxes may still be under-predicted. One can therefore estimate aerodynamic forces and moments with reasonable accuracy but not necessarily the stagnation point heat transfer.
2. The choice of interpolants for solution reconstruction does not always have a strong physical basis. The use of non-linear and non-polynomial interpolants are found to as non-conservative as the linear interpolation in hypersonic viscous flows. Despite the use of interpolations that follow from empirical correlations that have a physical basis, the wall heat flux estimates from the IB approach are consistently poorer than those from the FV approach for the same grid resolution.
3. The use of a simple linear interpolation would likely suffice, in conjunction with adaptive mesh refinement, for accurate predictions of wall heat flux and shear stresses at lower values of freestream Mach and Reynolds numbers. This would require cell Reynolds number values ~ 20 (based on freestream velocity) and can be realised using local grid refinement near the body vicinity to an acceptable number of levels. In contrast, for hypersonic laminar flows at higher Reynolds numbers, the number of levels of mesh refinements could become enormously large and therefore not feasible in practice.

One can therefore conclude that the sharp-interface immersed boundary methods are not necessarily accurate for near-wall resolution of heat fluxes although skin friction estimates can be reasonably accurate. While we have been able to use adaptive Cartesian meshes and the IB-FV approach to accurately estimate the skin friction and

Stanton number distribution in the flow past a compression ramp, the estimates of wall heat fluxes for the flow past blunt geometries have been quite poor despite the use of locally refined grids. From a conventional viewpoint, it may be argued that Cartesian IB-FV approaches would not perform well for viscous flows owing to their inability to resolve the boundary layers accurately unlike body-fitted meshes in the FV approach. We must stress that our studies herein have shown that this is not entirely true and that solution reconstruction plays a more dominant role in determining the gradient estimates in the near-wall regions. It must also be asserted that adaptive grid refinement to acceptable number of levels does not necessarily compensate for the non-conservation errors arising from temperature reconstruction. Even in case of geometries with adiabatic walls where surface heat transfer is zero, the reconstruction of temperature can possibly cause inaccuracies in estimation of skin temperatures with the inaccuracies likely compounded when the freestream Reynolds and Mach numbers are higher. It must be reiterated that our findings are far from trivial and may be encapsulated, albeit based on the limited number of numerical experiments, in the following conjecture.

Conjecture: *"It is not always possible to accurately estimate wall heat fluxes or wall temperatures (for isothermal and adiabatic walls respectively) at acceptably finite near-wall grid resolutions using the present sharp-interface immersed boundary approach."*

The inability to have accurate estimates of wall heat flux while being able to make quite accurate numerical predictions of wall shear stress may appear to be a violation of Reynolds analogy. However, it must be recognised that the Reynolds analogy applies to zero pressure-gradient boundary layers and no generalisations for flows past arbitrary geometries are available. We are also of the conviction that this conjecture would apply to all immersed boundary approaches that belong to the sharp-interface category such as those in [66, 72] as well as several meshfree approaches. This is because most meshfree approaches and current state-of-art sharp-interface IB approaches do not satisfy discrete conservation principles in the near-wall regions and though there have been no studies that discuss the performance of these approaches for laminar hypersonic flows, we speculate that they would perform no better than the HCIB approach discussed in this study.

The inaccurate estimation of wall heat transfer in high Re flows past blunt geometries using the immersed boundary approach may be viewed as a significant limitation from an engineering viewpoint. This is because the stagnation heat transfer and heat

loading are critical to design of thermal protection systems of hypersonic vehicles. It is therefore imperative to discuss alternatives that does not compromise on the ease and simplicity offered by the immersed boundary approach while ensuring accurate estimations of skin friction and heat transfer in all scenarios. While mitigating the problem of under-prediction is neither a trivial task nor in the scope of this study, we do outline a few possible remedial strategies.

1. Quasi-conservative immersed boundary approach: The idea behind this strategy is to employ the conservation laws even in the near-wall regions, but ensuring that the boundary conditions are suitably accounted for. This can be realised by adopting a diffuse interface approach such as the one in [41] or the Brinkman penalisation technique in [47]. In fact, [47] has employed this methodology wherein “unified” conservation laws are solved everywhere in the domain for compressible flows although its utility for hypersonic viscous flows has not yet been explored. We call this approach as “quasi-conservative” because the conservation equations are constructed by combining the Navier-Stokes equations with the boundary conditions (based on some scalar parameter such as permeability in [47]) thereby leading to a diffusion of the true interface.
2. Overset grid/immersed boundary approach: In this approach, a curvilinear mesh may be generated in the vicinity of the geometry that resolves the boundary layer quite accurately. The body with this “viscous padding” may then be immersed into a background Cartesian mesh with the curvilinear mesh overlapping with the Cartesian mesh. The solution to the near-wall region can then be obtained akin to a body-fitted mesh and the solution reconstruction then “shifts” from the near-wall region to away from it at the edge of the structured mesh. However, this necessitates solution interpolation between the overlapping meshes and a very similar approach has only been studied for limited number of very low-speed viscous flows recently in [142].
3. Virtual sub-grid approach: This methodology uses a virtual discretisation in the normal direction to the body along which a reduced form of the energy equation (say, steady without convection terms) may be solved using a finite volume approach so as to approximately ensure conservation. This is inspired by the work in [143] for low-speed turbulent flows where an efficient wall model is developed with the inner layer virtually resolved and a simplified form of the thin boundary layer equations solved.

The quasi-conservative approach sacrifices the sharpness of the interface while the overset grid/immersed boundary technique does not lend itself to complete automation, requiring an “immersed grid” (body with a conformal structured viscous layer).

The third approach is therefore the only methodology that is in the true spirit of the sharp-interface immersed boundary approaches. While these three strategies broadly fall within the Cartesian immersed boundary framework, they remain obviously unexplored for hypersonic flows. We do believe that these approaches would be remedial because they are all bound by the same principle - of enforcing conservation, although the specific means and the extent are quite different. Furthermore, it is also important to investigate the existing class of sharp-interface IB approaches (and these possible remedial strategies) on a wide range of canonical flows past generic configurations such as the HB2 geometry [144] and the double cone configuration [145] among others, to gain a greater insight into the strengths and limitations of different variants for complex hypersonic flow problems.

6.7 Summary

In this chapter an in-depth investigation using novel diagnostic approaches reveals that the non-conservation due to reconstruction of temperature is the main cause of under-prediction in wall heat fluxes and that unacceptably high mesh resolutions using adaptive mesh refinement would be necessary for accurate estimation of stagnation point heat transfer. The studies also show that the use of non-linear and non-polynomial solution reconstruction do not mitigate the conservation errors and sharp-interface IB approaches therefore cannot always estimate wall heat transfer to reasonable accuracy. The issue of non-conservation in the near-wall region also has implications even for adiabatic surfaces where skin temperatures show a strong dependence on the choice of reconstruction. The investigations help to discover limitations of the HCIB approach for high-speed viscous flows and offer a conclusive answer corroborated by strong numerical evidence to the question posed in the earlier chapter. A few possible research directions to evolve remedial approaches in the Cartesian IB framework are outlined while these appear promising, extensive numerical experiments are essential to assess their viability and versatility for realistic flow scenarios.

CHAPTER 7

APPLICATIONS TOWARDS DESIGN AND OPTIMISATION

“A designer knows when he has achieved perfection not when there is nothing left to add, but when there is nothing left to take away”

- Antoine de Saint-Exupery, *Terre des Hommes*

We discuss the application of finite volume and immersed boundary-finite volume frameworks for design and optimisation using variable fidelity framework. Specifically, we focus on three test-cases namely, aerodynamic shape optimisation (ASO) of bodies of revolution in hypersonic flows, design of scramjet inlets in hypersonic flows and optimal nozzle contour for supersonic flows. In each case, we employ a physics driven low-fidelity framework (LFF) which is a computationally cheap methodology for preliminary design. In problems where multi-fidelity frameworks (MFF) are employed, solutions from the low-fidelity framework are used as initial guesses to a high fidelity framework based on accurate finite volume continuum CFD based solvers. The use of multi-fidelity frameworks reduce the total turn-around time from initial guess to final optimal solution. It was observed that while the low-fidelity framework was used as a computationally inexpensive approach for the design of scramjet inlets, multi-fidelity frameworks that incorporate the immersed boundary finite volume approaches can also be easily devised for shape optimisation problems.

Contents of this chapter are part of the manuscript titled “**On Maximum Ballistic Coefficient Axisymmetric Geometries in Hypersonic Flows**”, Journal of Spacecraft and Rockets (2018) and “Comment on “**A new approach for the design of hypersonic scramjet inlets**”, Physics of Fluids 24, 086103 (2012)”, (under review)

Practical design of hypersonic vehicles is a multi-disciplinary effort that requires a trade-off between several conflicting objectives and constraints to arrive at the final prototype. While certain design problems pose itself as an optimisation task (such as 2D axisymmetric nose cone, nozzle configuration etc.), necessitating an iterative approach to arrive at that final prototype, others often portray them simply as a design problem while being subjected to multiple constraints (such as scramjet intake). We have focused our attention to attempt some of those questions while using MFF or LFF, predominantly for high-speed flows. The present chapter is arranged as follows: Section 7.1 discusses the ASO of two-dimensional axisymmetric configurations, for two objective functions: namely minimum drag and maximum ballistic coefficient bodies. This is followed by Section 7.2 where a physics based Low-Fidelity (LF) Framework is proposed for the design of scramjet inlets with multiple internal and external ramps. Lastly, in Section 7.3 where we discuss the design of optimal nozzle configurations using quasi one-dimensional approach in conjunction with immersed boundary finite volume IB-FV approach.

7.1 Aerodynamic shape optimisation of nose cone

Of the several parameters of interest for high-speed flight vehicles, an important quantity of interest is the total drag, C_d . An equally important design objective within the optimisation community is the ballistic coefficient β [146], defined as,

$$\beta = \frac{m}{C_d A} \quad (7.1)$$

where, m and A are the mass and reference area of the body, respectively. The choice of low or high β therefore depends on the vehicle of interest and, while re-entry modules favour the former, most missiles are inclined towards the latter design. Despite its importance in design, β has seldom been employed as a design parameter [77, 147, 148].

The study in this section discusses the use of a multi-fidelity framework and a novel strategy of shape optimisation where one would perform multi-objective optimisation of C_d and volume V with a scalar objective function created from their ratio. We attempt to separately minimise C_d and maximise β and study their cross-objective performance as well as heat transfer characteristics.

We briefly describe the salient features of the proposed multi-fidelity aerodynamic shape optimisation framework (MFF) below,

Computing the objective function

In this present study, we choose two different objective functions for the study viz. C_d and β . The latter is related to C_d via the Eq. 7.1. The low-fidelity approach employs the modified Newtonian theory [1] which defines the pressure coefficient on the surface based on the local inclination (θ) as,

$$C_p = C_{p,max} \sin^2 \theta \quad (7.2)$$

$$C_{p,max} = \frac{P_0 - P_\infty}{\frac{1}{2} \rho_\infty V_\infty^2} \quad (7.3)$$

where, P_0 and P_∞ are the stagnation pressure and freestream pressure, respectively and ρ_∞ and V_∞ are freestream density and velocity. The drag coefficient follows by a direct integration over the curved, convex surface of the body with a fixed base radius R .

$$C_d = \frac{\int_0^R C_p \sin \theta 2\pi r dr}{\pi R^2} \quad (7.4)$$

The integral is then numerically evaluated using a single-point Gauss quadrature with the surface discretised using a large number of linear segments (usually 500) to ensure sufficient accuracy. While one could make use of a IB-FV flow solver as described in this thesis in Chapters 4 or 5, we have employed the continuum CFD solver (ANSYS FLUENT v14.5 [149]) primarily because we have carried out laminar and turbulent simulations particularly from the view point of heat-transfer. The integration of pressure and viscous stresses over the body surface, obtained using the above density based solver, directly lead to the force coefficients. The calculation of β then follows as,

$$\beta = \frac{V}{C_d A} \quad (7.5)$$

where, m is replaced by V , as a constant vehicle packaging density equal to unity is assumed. The volume V , for any body of revolution is calculated by summing up the elemental volumes which are calculated as,

$$\delta V = \pi \int_{x_1}^{x_2} \left(\frac{r_2 - r_1}{l} x + r_1 \right)^2 dx \quad (7.6)$$

where, r_1 and r_2 are the radii at locations x_1 and x_2 of the elemental frustum of length $dx = x_2 - x_1$ and the integral is numerically evaluated using a single point Gauss quadrature.

Geometric representation

We employ cubic Bezier curves to provide excellent local control of the forebody shapes, following the recommendations of [91], that may be represented as,

$$\mathbf{r}(u) = \sum_{i=0}^3 \binom{3}{i} (1-u)^{3-i} u^i \mathbf{P}_i \quad 0 \leq u \leq 1 \quad (7.7)$$

where P_i are the control points of the Bezier control polygon. Of the four control points needed for the representation, we keep the first and last control points fixed in this study for any given fineness ratio l/d . The co-ordinates of the remaining two control points are the decision variables which need to be optimised, resulting in four decision variables. There are no explicit constraints to enforce convexity but the co-ordinates of the control points are bounded by the length l and radius R of the body.

Optimisation strategy

In this present study, we adopt the steepest descent/ascent method for optimisation. The decision variables are iteratively updated following the scheme below.

$$X_i^{k+1} = X_i^k \pm \lambda^k \frac{\partial \phi}{\partial X_i} \quad (7.8)$$

where ϕ represents the objective function, k is the optimisation cycle and \pm sign refers to ascent/descent depending on the nature of the problem. The objective function is computed as a discrete numerical value and its sensitivities are therefore obtained using a forward finite difference approximation. To accelerate the convergence towards the optimal solution, an adaptive learning rate λ^k was adopted. For each optimisation cycle using steepest ascent, λ^k was defined as,

$$\lambda^k = \begin{cases} \alpha_1 \lambda^{k-1} & \text{if } \phi^k > \phi^{k-1} \\ \alpha_2 \lambda^{k-1} & \text{otherwise} \end{cases}$$

where $\alpha_1 = 1.1$ and $\alpha_2 = 0.5$, with the inequality in the Eq. above reversed for a steepest descent approach.

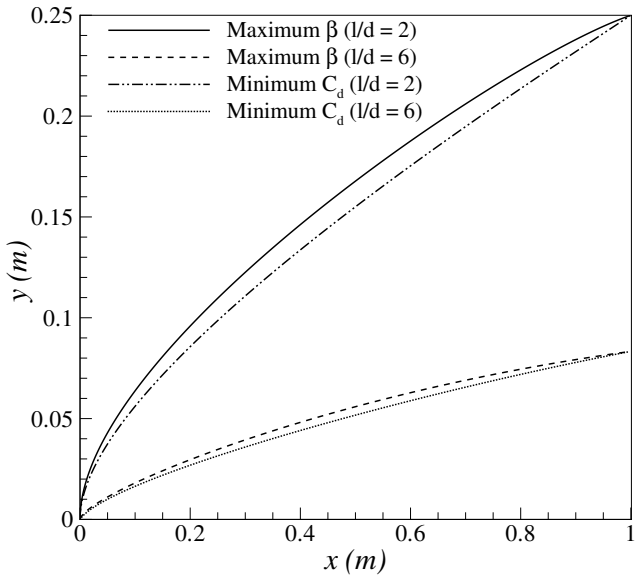
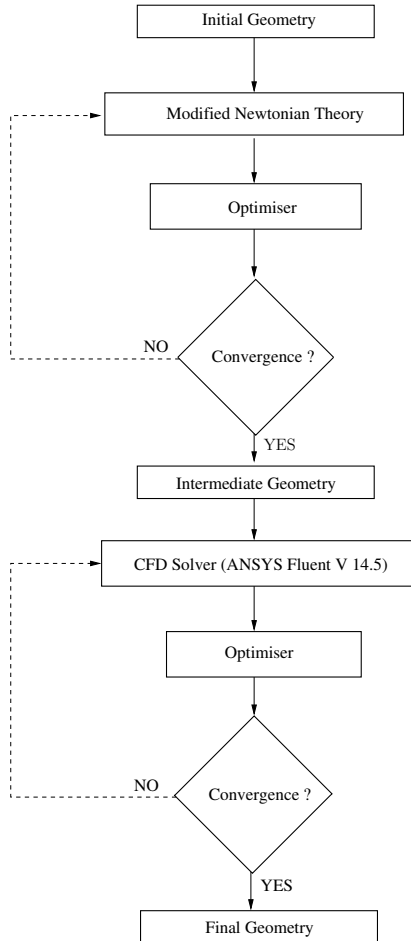
Figure 7.2: Optimal bodies at different l/d

Figure 7.1: Flowchart describing the proposed multi-fidelity optimisation framework

The proposed multi-fidelity shape optimisation framework (MFF) is a seamless combination of low-fidelity (LFF) and high-fidelity frameworks (HFF), which differ only in the solution approaches to calculate the objective function, as described in Figure 7.1. We begin with an initial configuration, typically chosen as the right circular cone (for sake of convenience) and the optimal shape from the LFF (denoted as intermediate geometry in the flowchart) is first obtained, which then acts as an initial guess to the HFF that leads to the final optimal geometry. The convergence criterion for the optimisation frameworks are $\epsilon_{LFF} = 10^{-10}$ and $\epsilon_{HFF} = 10^{-5}$ respectively, with the latter being absolute and the former being relative difference of the objective function between consecutive optimisation cycles. The flow field is assumed steady and structured meshes with approximately 60,000 volumes are employed for evaluation of the objective function in the HFF. We have ensured that the solutions are grid-independent and the grids in this study are generated using ICEM CFD v14.5 [150], including the use of ICEM scripts to reduce complexity, similar to the approach

adopted by Seager and Agarwal [80]. Second-order accurate AUSM scheme is used for convective flux computations. For the case of viscous computations, finer meshes resolving the near-wall region are employed and turbulence is modelled with the $k-\omega$ SST model. For the turbulent simulations a sufficiently low y^+ is maintained at the wall and a 1% turbulence intensity at the inlet is used. All computations assume that air may be treated as an ideal gas with ratio of specific heats as 1.4 at flow conditions tabulated in Table 7.1. The freestream Reynolds number Re_∞ is calculated based on the length of the body l , which is fixed equal to 1 m, while the base diameter d of the body follows from the chosen l/d . While some of the assumptions herein may not be realistic, the present choice allows the demonstration of the proof-of-concept of the proposed framework.

Table 7.1: Flow conditions

Flow conditions	Value
Freestream Mach number	5
Freestream Reynolds number	4.76×10^6
Freestream density (kgm^{-3})	0.04626
Freestream pressure (Pa)	2930
Freestream temperature (K)	220.65
Wall temperature (K)	300

Minimum C_d and maximum β axisymmetric geometries

We now proceed to study the optimal axisymmetric forebodies that minimise and maximise C_d and β , respectively. The aerodynamic performance as well as stagnation point heat transfer characteristics of these geometries are evaluated and salient conclusions are drawn. A systematic validation of the present optimisation framework was carried out separately, where it was also observed that optimal shapes derived from Euler simulations are almost identical to those obtained using viscous simulations. This observation has also been reported by other researchers [86, 125] and we therefore use Euler simulations for the optimisation framework with a view to minimising the total computational cost.

We investigate the minimum C_d and maximum β axisymmetric bodies in hypersonic flow using the proposed multi-fidelity framework. While the minimum C_d body would also have a maximum β for a fixed A and V , we only constrain A during optimisation, for a given l/d . In this work, we therefore consider bodies of varying l/d from 2 to 7. Figure 7.2 shows the minimum C_d and maximum β bodies for $l/d=2$ and $l/d=6$. A closer look at the geometries reveal the dependence of the optimal shape on the given l/d . In particular, we plot the leading edge angle θ_{LE} for the optimal geometries

for varying l/d in Figure 7.3. One can classify the shapes as being “aerodynamically sharp” or “aerodynamically blunt” by identifying if the axisymmetric body admits an attached or detached shock. This is done using Shanbhag’s [151] expression that relates the limiting leading edge semi–vertex angle θ_m , below which the shock remains attached, to the freestream Mach number as,

$$\gamma \sin^2 \theta_m = \left(1 - \frac{1.66811133}{M_\infty^2} - \frac{1.80290197}{M_\infty^4} + \frac{13.5947703}{M_\infty^6} - \frac{28.844018}{M_\infty^8} + \frac{27.247824}{M_\infty^{10}} - \frac{9.527563}{M_\infty^{12}} \right) \quad (7.9)$$

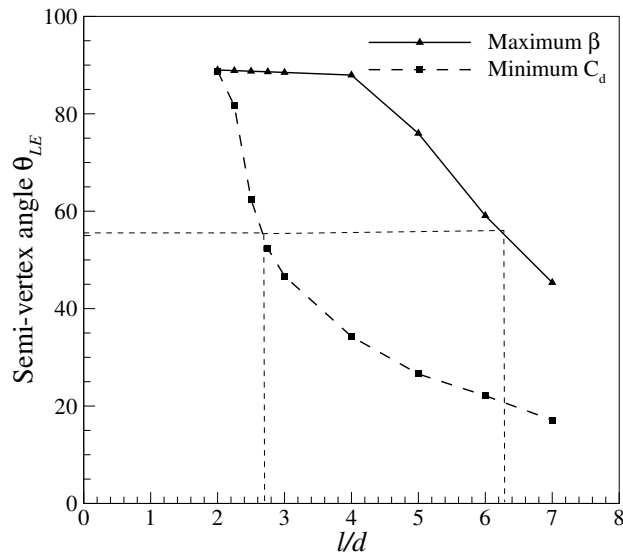


Figure 7.3: Semi–vertex angle θ_{LE} of optimal bodies for different l/d

For the chosen flow conditions, θ_m is approximately 56° . It is therefore clear that for both objective functions, the optimal geometries transform from “aerodynamically blunt” to “aerodynamically sharp” as the l/d increases. This “transition” l/d for minimum C_d bodies is found to be close to 2.7, in fair agreement with the results of Sahai *et al.* [91], while the transition l/d is a much higher value of 6.1 for maximum β bodies. The proposed multi–fidelity framework is as accurate as a fully high–fidelity framework but is at least 3–5 times faster (Figure 7.4 and 7.5), leading to considerable savings in terms of computational cost. This can be easily understood from Table 7.2 which shows the number of HFF optimisation cycles and total computational time for one complete optimisation study using the multi–fidelity (MFF) and fully high–fidelity approaches (HFF). Figure 7.6 and 7.7 shows the optimal configurations for minimum C_d and maximum β body obtained at $l/d=2$ and 6 respectively.

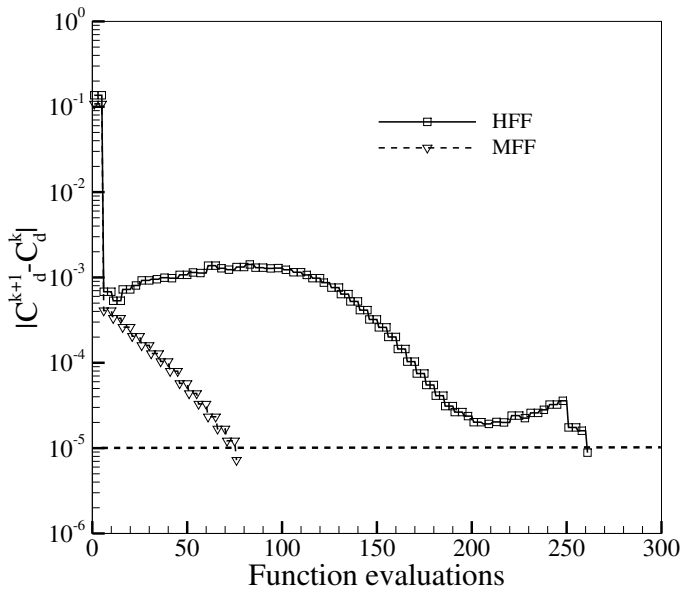


Figure 7.4: Convergence acceleration for maximum C_d body at $l/d=2$

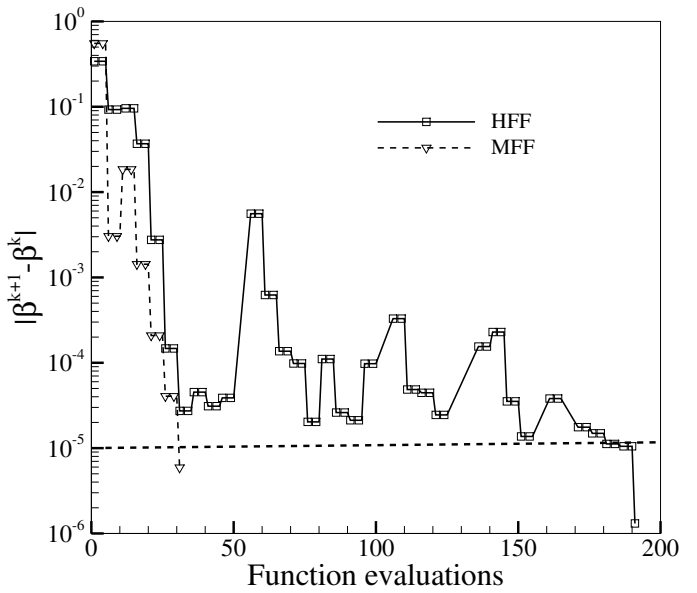


Figure 7.5: Convergence acceleration for minimum β body at $l/d=6$

Table 7.2: Total computational time in hours for MFF and HFF frameworks. The number of optimisation cycles is indicated in parentheses

Framework	Min. C_d body	Max. β body
	$l/d = 2$	$l/d = 6$
MFF	2.5 (15)	1.2 (6)
HFF	8.7 (52)	6.4 (38)

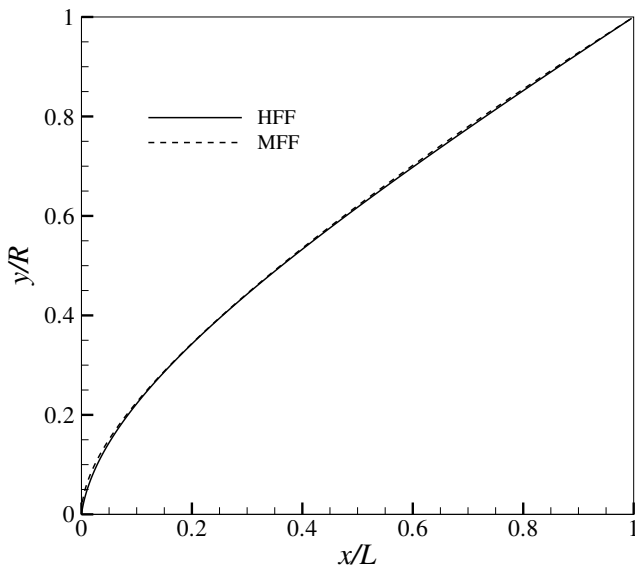


Figure 7.6: Min. C_d body at $l/d = 2$

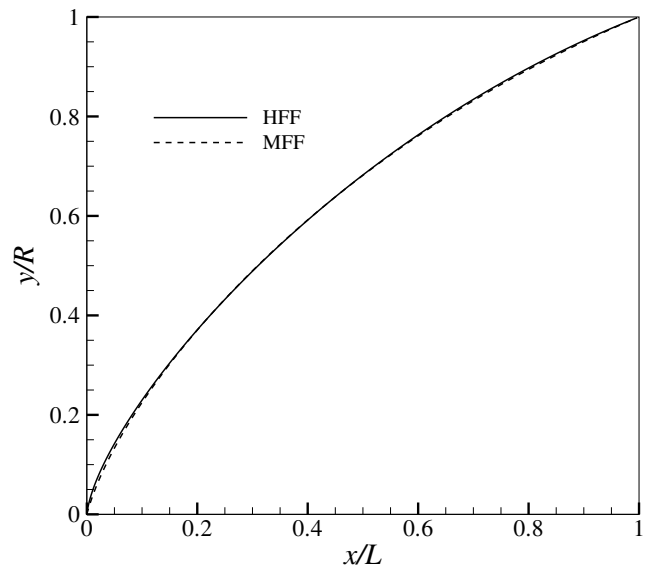


Figure 7.7: Max. β body at $l/d = 6$

Cross-objective performance of optimal shapes

One of the interesting questions that we address is the performance of optimal configurations for objective functions for which they not actually are optimised for. To the best of our knowledge, while there have been studies on off-design performance of optimal shapes, there has been no real efforts to assess cross-objective performance. We define a penalty parameter for either objective function as,

$$P_\phi = \frac{|\phi - \phi_{ideal}|}{\phi_{ideal}} \times 100 \quad (7.10)$$

where ϕ is the value of objective function for the geometry optimised for a different objective and ϕ_{ideal} is the value of objective function for the geometry optimised for the same objective, both of them being calculated for identical l/d . The penalty in C_d/β that one would incur if one were to use the maximal β /minimal C_d body is illustrated in Figure 7.8. A closer examination shows that at low l/d , penalty on the objective function is smallest. For instance, for $l/d=2$, the minimum C_d body has only 5% lesser β than the maximum β body, which in turn has only 5% more C_d than the minimum C_d body. For $l/d = 2$, the two geometries are also “aerodynamically blunt”, with comparable leading angles. As the l/d increase, we can see that penalty in C_d actually decreases for the maximum β body. For the higher l/d , the performance of the minimum C_d body in terms of the β becomes poorer, leading to increased penalties and it then represents a non-optimal geometry in terms of β .

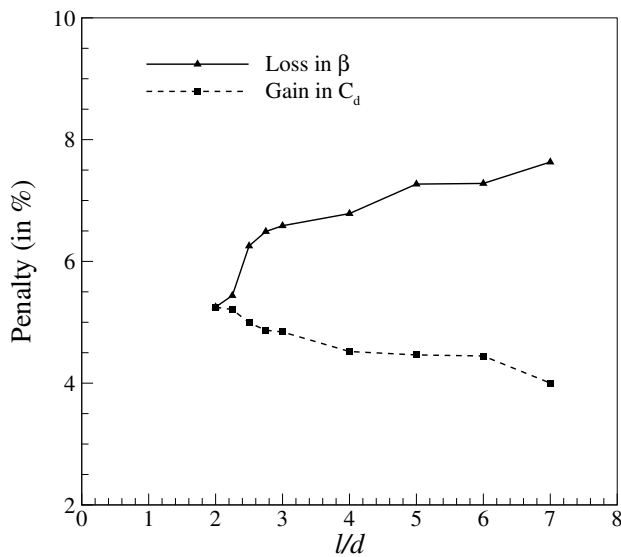


Figure 7.8: Cross-objective performance for different l/d

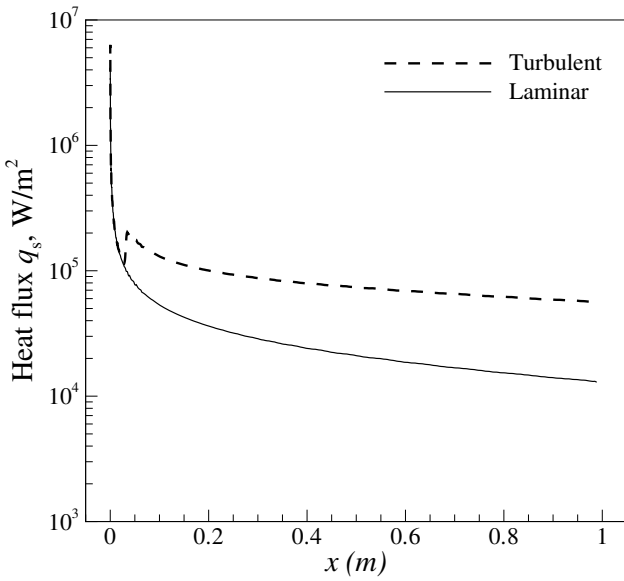


Figure 7.9: Heat flux distribution along the length of the maximum β body at $l/d=6$

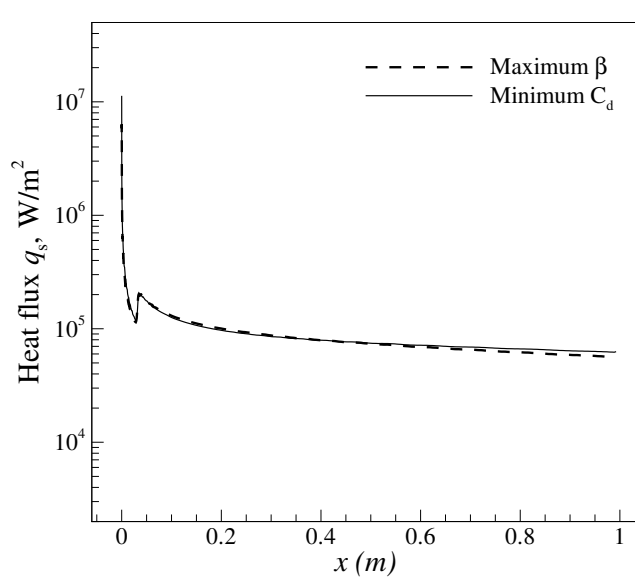


Figure 7.10: Heat flux distribution for optimal bodies at $l/d=6$

Heat transfer considerations

One of the salient aspects in aerodynamic design for hypersonic flows is the heat transfer to the body. It must be recalled that neither geometries have been optimised for heat transfer and that absolute aerodynamic performance parameters are dependent on the nature of the flow. In this regard, we investigate the heat transfer for the minimum C_d and maximum β bodies obtained at $l/d=2$ and $l/d=6$ by carrying out viscous simulations to obtain the true estimate of stagnation point heat transfer, q_o and total heat load, q_L . The heat flux distribution over the length of the maximum β body at $l/d=6$ obtained from laminar and turbulent simulations is depicted in Figure 7.9. It can be observed that the heat flux predictions from turbulent simulations are higher than those from laminar simulations, except in the vicinity of the stagnation region. Since hypersonic flows at similar Reynolds number have been modelled as being fully turbulent previously [81], we carry out turbulent simulations for minimum C_d and maximum β bodies for $l/d=6$. One can see that the heat flux distribution over both bodies, shown in Figure 7.10 are largely comparable except at the stagnation point. This is also reflected in Table 7.3 which shows that the q_o for the optimal shapes derived from either objective function do not significantly differ for the lower l/d but the minimum C_d body has a larger q_o than the maximum β body at higher l/d . The total q_L from both optimal bodies at $l/d=6$ are however not very different as can be seen from Table 7.3. The result that the maximum β body has a lower q_o for a given l/d is not entirely surprising though, because the q_o is known to be inversely

Table 7.3: Stagnation point heat flux and heat load at $l/d = 2$ and 6

Geometry	Stagnation point heat flux, q_0 (W/m²)		Heat load, q_L (kW)
	$l/d=2$	$l/d=6$	$l/d=6$
Minimum C_d	2.293×10^6	1.05×10^7	23.03
Maximum β	2.184×10^6	6.33×10^6	23.7

proportional to the square of the leading edge radius in hypersonic flows [138]. A larger leading edge radius would mean a larger leading edge semi–vertex angle and the maximum β bodies being “blunter” than their minimum C_d counterparts at $l/d=6$ would predictably lead to lower q_o .

Salient conclusions from the investigations are summarised below:

1. Minimum C_d bodies have high β and maximum β bodies have low C_d at lower l/d . This cross–objective performance at higher l/d is retained only by the maximal β geometries.
2. Minimum C_d and maximum β geometries are both blunt–nosed for smaller l/d and sharp–nosed for higher l/d . The transition from blunt to sharp happens earlier (at l/d values lesser than 3) for the minimum C_d geometries than for the maximum β geometries (where it occurs at l/d values above 6).
3. Maximising β can lead to lower values of q_o than for minimising C_d for a given l/d .

The study in this section discusses the use of a multi–fidelity framework and a novel strategy of shape optimisation where one would perform multi–objective optimisation of C_d and V with a scalar objective function created from their ratio. The single scalar objective function is to maximise β which leads to shapes that have both low C_d and lower q_o than the corresponding minimum C_d body. This is an interesting observation and while this study is limited to axisymmetric geometries, it hints at the possibility of exploiting similar physically–inspired single objective cost functions to obtain geometries that could perform favourably in terms of one or more different objectives. We now employ similar low-fidelity frameworks to examine its utility in designing much complex shapes with external and internal flow such as scramjet intake and nozzle, respectively in the following sections.

7.2 Design of scramjet inlets

We discuss the design of mixed compression scramjet intakes using a one-dimensional low-fidelity framework. While we do not carryout aerodynamic shape optimisation using MFF, the design strategy is based on one-dimensional gas dynamics principle is targeted at maximising total pressure recovery (TPR) while also ensuring low non-uniformity in the isolator. We use the immersed boundary finite volume (IB-FV) solver discussed in Chapter 4 as the high-fidelity solver however, this does not form part of any optimisation strategy in this study. The IB-FV solver herein is used to compute the numerical solution on the final design obtained from the one-dimensional design approach and to evaluate the efficacy of the design strategy in designing two-dimensional planar intakes. This is motivated by the use of physics based low-fidelity frameworks that have been recently proposed [152].

Low-Fidelity Framework

We make use of 1D gas dynamics Eqs. as a LF Framework to estimate the quantities of interest for a particular scramjet intake. The schematic of the scramjet intake is shown in Figure 7.11. The shock that emerge from the leading edge of the external ramps were enforced to meet at the cowl-lip to satisfy the *shock-on-lip* criterion, whereas the shocks that emanate from the cowl lip, were constrained to hit the ramp shoulder to satisfy the *shock-on-shoulder* criterion. The shock-on-lip criterion ensures maximum capture area and no air is spilled outside the inlet. The shock-on-shoulder constraint reduces the non-uniformity of the flow entering the isolator. To enable a uniform flow that is parallel to the exit of the isolator, we impose a *flow-deflection* angle, θ correction wherein the summation of the external flow-deflection angles is equal to the summation of the internal flow-deflection angles and is implemented as,

$$\sum_{i=1}^n \theta_{i,\text{ext}} = \sum_{i=1}^m \theta_{i,\text{int}} \quad (7.11)$$

where, n and m denote the number of external and internal shocks, respectively. In the studies of Raj and Venkattasubbaiah [152] who also uses similar approach, it must be noted that the flow-deflection angle correction is not enforced which could lead to non-uniformities in the isolator. For the present test case, we shall highlight the importance of enforcing this criterion in the design.

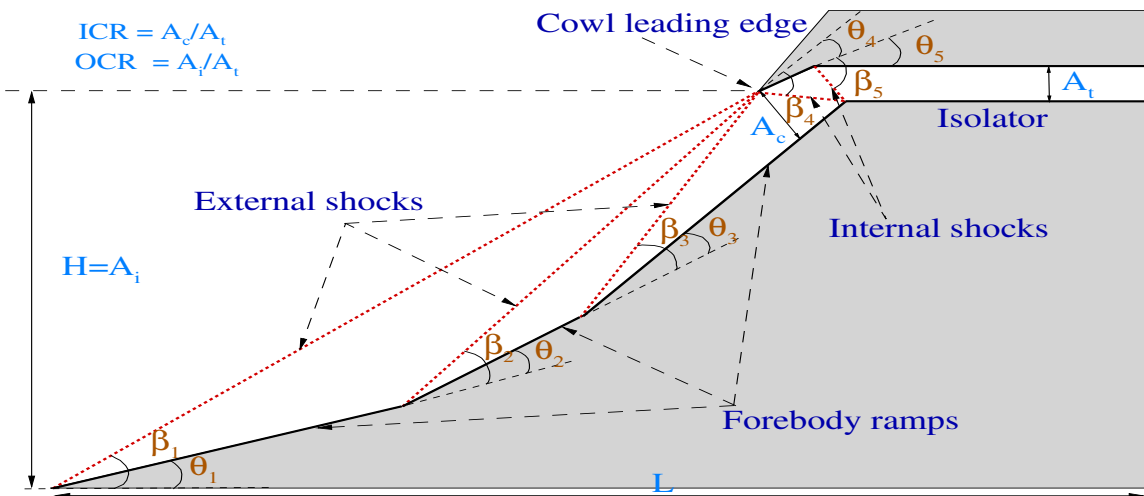


Figure 7.11: Scramjet inlet schematic representation where β and θ represent the shock and flow-deflection angle respectively

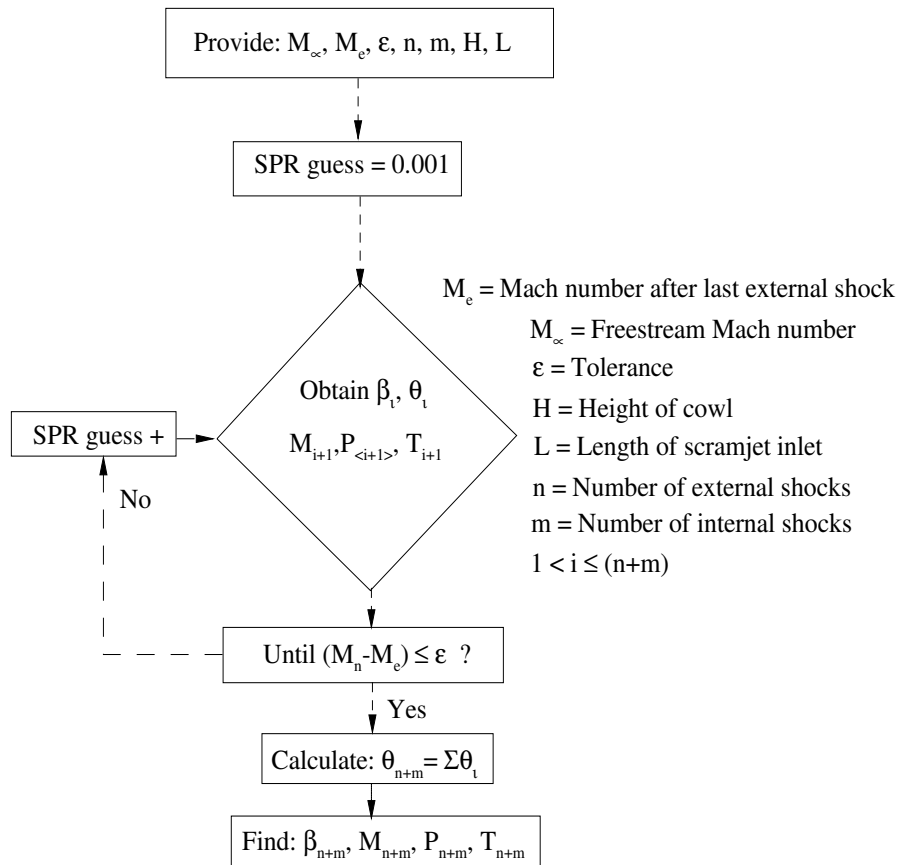


Figure 7.12: Low-fidelity flowchart

Once the freestream properties are fixed, the ramp angles and the pre-post shock conditions are determined using standard isentropic and oblique shock relations as

highlighted in the flowchart shown in Figure 7.12. The Mach number after the last external shock or M_e value was determined based on a study whose details are provided in later section. We also effectuate the *Oswatitsch* criterion, where the static pressure ratio across all external shocks were kept equal and the same is also true for multiple internal shocks as well. This was done following the report of Smart [153] where he observed that the scramjet inlets which resulted in maximum Total Pressure Recovery (TPR), were having external shocks of equal strengths. For the studies in the present section, we define some quantities of interest such as Static Pressure Ratio (SPR) and TPR as,

$$\text{SPR}_i = P_2/P_1 \quad \text{TPR}_i = \frac{P_{02}}{P_2} \frac{P_2}{P_1} \frac{P_1}{P_{01}} \quad (7.12)$$

$$\text{Total Pressure Recovery} = \prod_{i=1}^{n+m} \text{TPR}_i \quad (7.13)$$

$$\beta = \sin^{-1} \left[\sqrt{\frac{((\text{SPR} - 1)(\frac{\gamma+1}{2\gamma})) + 1}{M_1^2}} \right] \quad (7.14)$$

$$\theta = \tan^{-1} \left[2 \cot \beta \left(\frac{M_1^2 \sin^2(\beta) - 1}{M_1^2 (\gamma + \cos 2\beta) + 2} \right) \right] \quad (7.15)$$

$$M_2 = \frac{\sqrt{\frac{M_1^2 \sin^2(\beta) + \frac{2}{\gamma-1}}{\frac{2\gamma}{\gamma-1} M_1^2 \sin^2 \beta - 1}}}{\sin(\beta - \theta)} \quad (7.16)$$

where, subscripts 1 and 2 represent the pre-post shock conditions respectively across a single shock i . P_1 , P_{01} , γ and M refer to static pressure, total pressure, ratio of specific heats and Mach number respectively. In our studies we choose the value of Mach number after the last external shock $M_e=0.75$.

The IB-FV flow solver discussed in Chapter 4 is used to compute the flow for the final design obtained using the one-dimensional approach described earlier. This is done by merely immersing the final geometry into the same mesh which enables fast and robust simulations owing to reduced costs for mesh generation. We consider flow

to be necessarily inviscid and solve the steady Euler equations using the AUSM flux-splitting scheme with explicit time stepping. Computations are performed on 1000×120 Cartesian mesh with a CFL of 0.4.

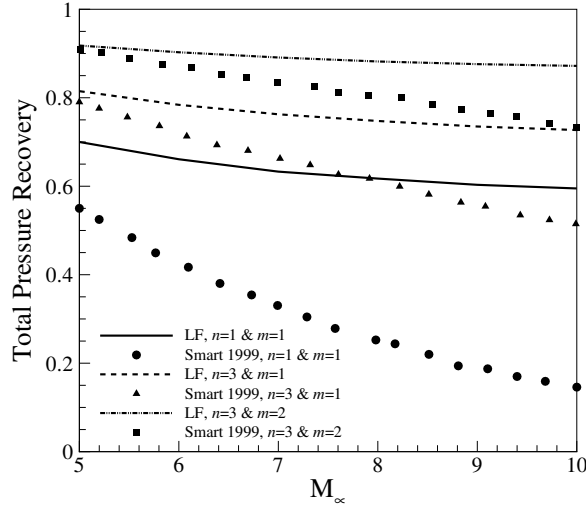


Figure 7.13: Total pressure recovery obtained from LF framework

For different intake configurations with combinations of internal and external ramps, the TPR obtained from the LFF is compared with those of Smart [153] in Figure 7.13. It can be seen that for all cases our results indicate higher TPR than that of Smart at all Mach number and all configurations, although the differences basically diminish as the number of ramps increases. Moreover, it can also be noticed that TPR is nearly invariant with M_∞ . This is considered a positive trait for the scramjet inlet as their performance do not degrade for different freestream Mach number M_∞ .

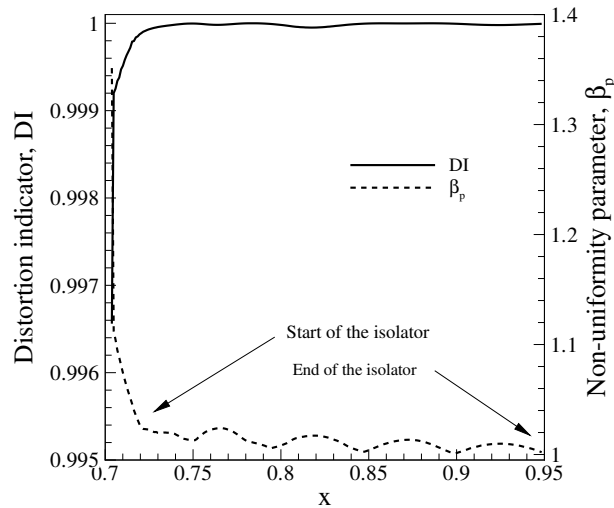


Figure 7.14: Flow non-uniformity in the isolator

In order to verify the results obtained from the one-dimensional low-fidelity framework are indeed meaningful, we now carryout two dimensional numerical simulation making use of the IB-FV solver for the configuration $n=3$ and $m=1$, at freestream mach number $M_\infty=8$. The non-uniformity in the isolator is studied in terms of parameters known as velocity non-uniformity parameter, β_p [154] and distortion-indicator, DI [155]. Figure 7.14 shows the variation of β_p and DI along the isolator surface. At the start of the isolator location, due to the striking of the cowl shock, there is a sudden jump in β_p and DI. However, along the stream-wise direction, both β_p and DI considerably reduces and approached a value ≈ 1 , signifying uniform flow at the isolator exit. The low non-uniformity at the isolator is not entirely surprising, considering that the flow-deflection correction renders a uniform flow parallel to the isolator. Thus, contrary to the reports of [156], it can be suggested that the present design methodology for scramjet inlets leads to high-contraction ratio and at the same time, suffers from less non-uniformity in the flow. Figure 7.15 is the depiction of the Mach contours for two scramjet inlet configurations, where the external and internal shocks are clearly visible. Moreover, it can be seen that the shock-on-lip and shock-on-shoulder criterion is also satisfied.

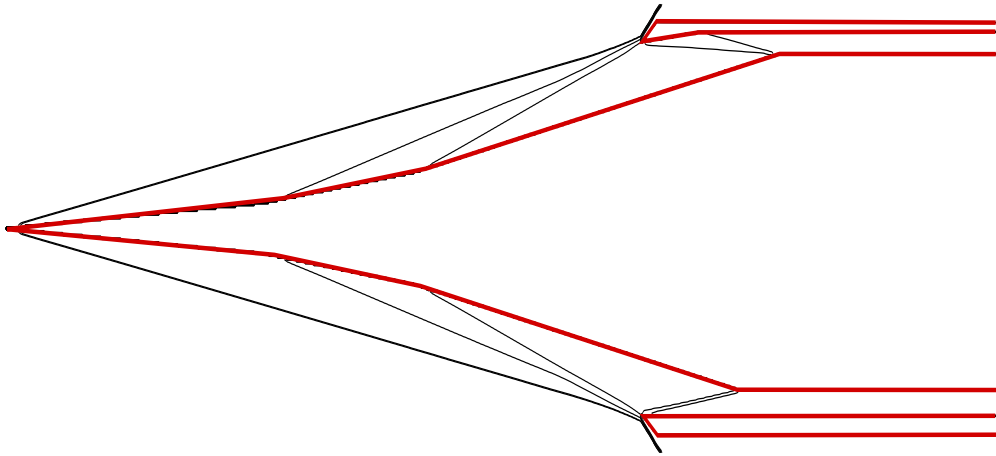


Figure 7.15: Mach contour for the scramjet intake configuration (a) $n=3$, $m=1$ (bottom) (b) $n=3$, $m=2$ (top) (Min: 0, Δ : 0.888, Max: 8.0)

Table 7.4: Comparison of LF and HF frameworks at $M_\infty=8$ for the $n=3$ and $m=2$ configuration

M_∞	8 (LF) Present	8 (HF) Present	8 (LF) Ref. [152]	8 (HF) Ref. [152]
SPR	22.58	20.423	50.05	66.41
TPR	0.883	0.8423	0.829	0.68
M_{is}	4.725	4.769	4.0	3.75

We also quantitatively verify the 1D solutions from the Low-fidelity framework by comparing those obtained using the IB-FV solver as shown in Table 7.4. It can be observed that the quantities of interest at the isolator agree well from both the LF and HF framework. This is not entirely surprising as the HF framework is based on the inviscid dynamics of the flow. We have observed some difference with [152], which is likely because of the different M_e/M_∞ value and flow-deflection angle correction. Raj and Venkattasubbaiah [152] attribute the difference between their LF and HF solutions to the two-dimensionality effects however, in contrary to their report, we have noticed an excellent agreement between the solutions form LF and HF framework. It is also worth reporting that this difference between LF and HF is not due to the flow-deflection correction, as has been seen in our numerical investigations (not shown here for brevity).

From the studies carried out in this section, we see that the scramjet inlet captures full inlet air-stream, generates sufficiently high compression ratio unlike reported literature. The scramjet inlet configurations generates high TPR which were not strongly sensitive on freestream Mach number. Moreover, the deflection angle correction enables uniform flow in the isolator of the scramjet inlet. The computations performed using the IB-FV solver clearly highlight the utility of the design framework based on the one-dimensional approach. Nevertheless, one can make use of the multi-fidelity framework which uses the optimal shape shown herein as an initial guess and carries out a shape optimisation to optimise one or more cost functions. This is however beyond the scope of the present study and may be taken up in the future.

7.3 Design of optimal nozzle for supersonic flows

As a final test case, we now consider the design of a contoured axisymmetric nozzle for supersonic flows. The requirement in this particular study is to design contoured diverging nozzle using quasi one-dimensional approaches which has minimum radial velocity at the exit and thereby maximises the streamwise velocity at the outlet of the nozzle.

Low-Fidelity Framework

We describe the rationale behind the choice of LF flow solver adopted, namely quasi-one dimensional approach. The concept of isentropic relations embedded in the quasi one-dimensional flow is often used for nozzle to determine the axial variation of flow properties. Considering the isentropic subsonic–supersonic flow past a variable

area nozzle (Figure 7.16), we can arrive at an useful “area-Mach number relation” as given in equation [1],

$$\left(\frac{A}{A^*}\right)^2 = \frac{1}{M^2} \left[\frac{2}{\gamma + 1} \left(1 + \frac{\gamma - 1}{2} M^2 \right) \right]^{\frac{\gamma+1}{\gamma-1}} \quad (7.17)$$

where, γ is the ratio of specific heats. Eq. 7.17 is referred to as the *Area-Mach number* relation and is used to determine the flow properties across any cross-section inside the nozzle. This idea is now employed as shown in the algorithm detailed in Table 7.5.

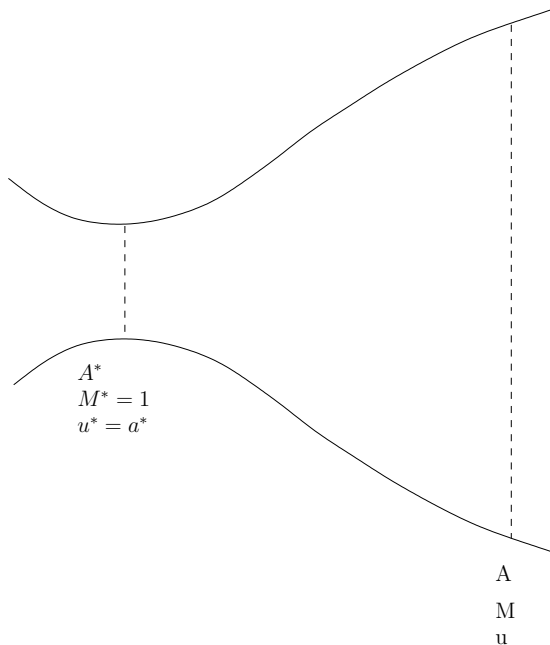


Figure 7.16: Variable area nozzle

Table 7.5: Low-fidelity flow solver

Algorithm: LF Flow solver

- 1 Fix the inner and outer radius r_i , r_o of the nozzle, respectively (Figure 7.17)
 - 2 Fix the inlet Mach number M and ratio of specific heats γ
 - 3 Parameterise the geometry using cubic Bezier curve, (shown in section 7.1)
 - 4 Evaluate the RHS of Eq. 7.17
 - 5 Increment the Mach number M by small value (10^{-6}).
 - 6 If difference between LHS and RHS $\leq \epsilon$ Terminate. Or repeat steps 4-5 above
-

We now incorporate the IB-FV solver, as also done in Section 7.2, to evaluate the design obtained using the quasi one-dimensional approach. As opposed to study in Section 7.2 which involves planar scramjet intakes, we reiterate that studies herein are necessarily involving axisymmetric geometries and axisymmetric flow.

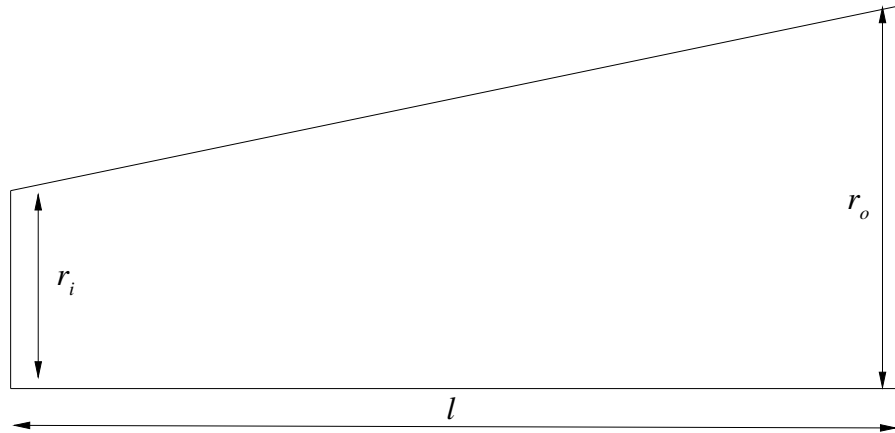


Figure 7.17: Schematic of the nozzle configuration

We choose an initial shape in terms of a conical frustum and carryout optimisation to minimise the radial velocity at the exit of the nozzle defined as, v_r/V_t , which ensures that the flow is parallel at the exit of the nozzle, necessary for maximising the positive thrust. We start by fixing the inlet radius and outer radius as $r_i=0.02$ and $r_o=0.045$ and the length of the nozzle l is taken as $l=0.1$. The optimisation process (carried out using steepest descent, as elaborated previously in section 7.1) is terminated after 200 iterations or when the difference between the cost functions becomes lesser than 10^{-3} , whichever happens earlier. The inlet Mach number is fixed at 1.001 (small positive perturbation above the Mach number of unity guarantees that the flow accelerates to supersonic flow at the exit).

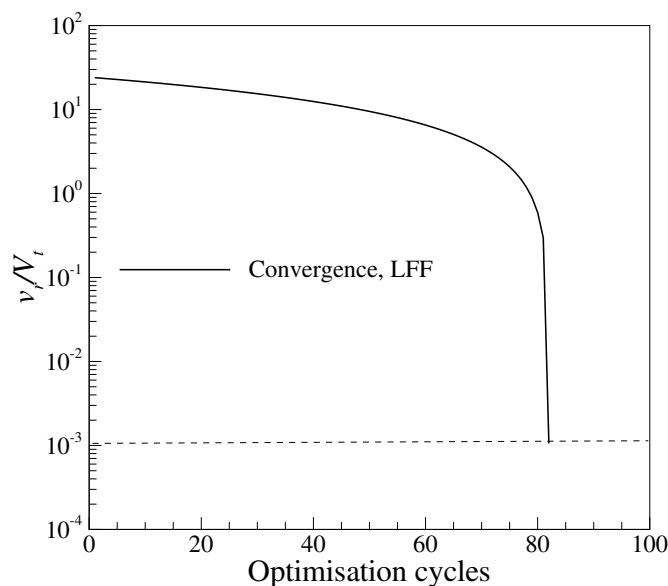


Figure 7.18: Convergence history

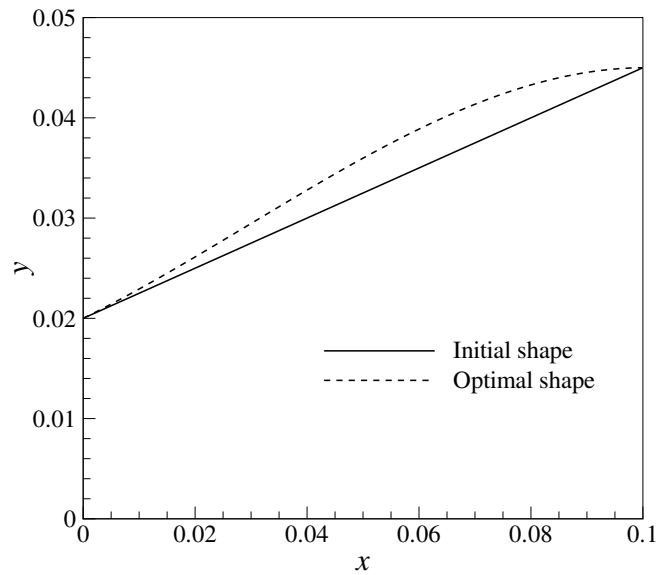


Figure 7.19: Optimal nozzle configuration obtained from LFF

The convergence plot in Figure 7.18 obtained using the LFF shows monotonic decrease in the cost function (i.e v_r/V_t). Figure 7.19 shows the optimal nozzle configuration obtained from LFF and its comparison with the initial shape. It can be seen that the optimal nozzle shape resembles a “bell-shaped” contoured nozzle with seamless transition from the leading edge to the trailing edge, allowing for reduction in the radial velocity at the exit. This reduction can yet again be confirmed Figure 7.18 where the cost function reduces by nearly 4 orders. This study is in contrast to the remarks in [1] where they mention that the utility of the quasi one-dimensional approach is only restricted to the determination of axial distribution of flow properties.

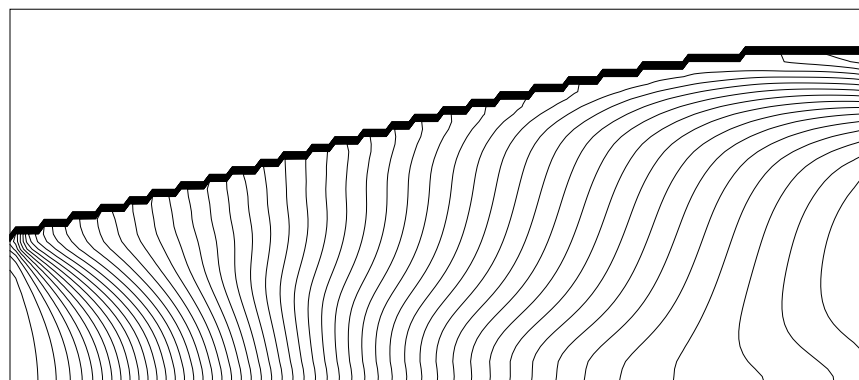


Figure 7.20: Mach contour obtained from IB-FV flow solver for the optimal nozzle configuration (Min: 0.05, Δ:0.0493, Max: 3.45)

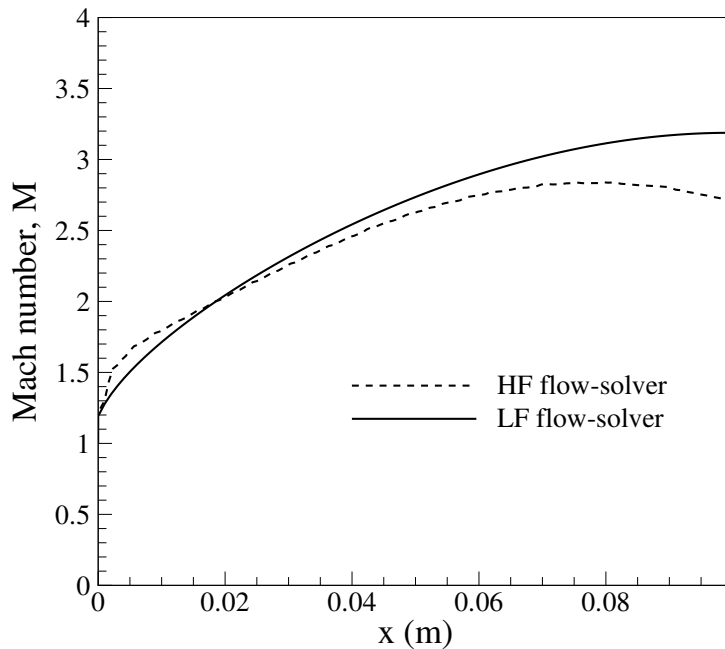


Figure 7.21: Comparison of Mach number obtained from both flow solvers

We now carry out studies by immersing this optimal nozzle shape in a Cartesian grid that employs 150×50 control volumes along with AUSM flux splitting scheme to compute the inviscid flow within the nozzle. In Figure 7.20 Mach contour are shown and Figure 7.21 shows the Mach number distribution over the nozzle wall wherein small differences between the low-fidelity approach and IB-FV can be seen. However, the exit Mach number obtained from low-fidelity flow solver is 3.19 while the IB-FV flow solver gives an average exit Mach number 3.35. One can see that the quantitative agreement for the average exit Mach number is good, similar to what has been observed in the scramjet intake studies as well (see Table 7.4).

7.4 Summary

It can thus be summarised from the studies carried-out herein that design of optimal contoured nozzle can be carried out using a one-dimensional framework. Moreover, the IB-FV solvers employed as standalone continuum CFD codes do indeed verify the efficacy of the lower dimensional approach. As also remarked earlier, it is definitely possible to develop multi-fidelity framework wherein the low-fidelity solution is fed in to a high-fidelity optimisation framework, which employs the IB-FV approach as a flow solver and arrive at configurations that are truly optimal. It must however be remarked that one-dimensional approaches do give nearly optimal configuration and therefore

constitutes a cheap design framework for finding nozzle shapes. The importance of IB-FV strategy as a flow solver in a high-fidelity framework is that as opposed to conventional CFD solvers such as ANSYS Fluent, it allows for a automated, robust and more flexible multi-fidelity strategy since it does not have any issues with grid generation and the shapes that are generated are merely immersed into an underlying grid. The design of such multi-fidelity frameworks that employs such IB-FV solver for problems that have been discussed in this thesis and for other problems in hypersonic flows are part of future scope and are detailed in the next chapter.

CHAPTER 8

CONCLUSIONS AND FUTURE SCOPE

“There is always room at the top”

- Daniel Webster,

This thesis discusses the development and application of immersed boundary finite volume framework for compressible flows. The framework has been developed by combining an unstructured data based finite volume flow solver in conjunction with a sharp interface immersed boundary approach which allows the use of adaptive Cartesian meshes. Numerical investigations of high speed inviscid and viscous flows over a wide range of Mach and Reynolds numbers have been carried out using this numerical framework. Studies have also been carried out to understand the role of discrete conservation on the accuracy of the framework in computing inviscid and laminar high speed flows. In this chapter, we shall present the salient contributions from the present study and provide directions for future research.

8.1 Conclusions

The accuracy of the solution obtained using FV approaches is determined by the discretisation of the convective and diffusive fluxes, which themselves are directly affected by the accuracy of the solution gradients. We have proposed a novel cell-centered gradient reconstruction method referred to as Modified Green Gauss reconstruction (MGG) on arbitrary polygonal meshes. This method employs a variant of the Gauss divergence theorem that is devoid of any interpolations on purely orthogonal meshes (like uniform or non-uniform non-orthogonal Cartesian grids). However, the methodology requires interpolation and an iterative approach on non-orthogonal meshes, which

could be computationally expensive for time marching problems. In order to cut down the cost and its applicability to adaptive Cartesian meshes typical of IB-FV framework, we have also employed a non-iterative variant that is accurate and robust. The numerical investigations show that the MGG reconstruction is less dissipative than the Standard Green Gauss (SGG) reconstruction and allows for the use of a larger Courant number than the SGG reconstruction. MGG reconstruction, therefore, may be viewed as a strategy that may devoid of iterations and results in a fast, robust and accurate approach for compressible flows.

The focal point of study in this thesis is the development of an in-house Immersed Boundary Finite Volume (IB-FV) framework for compressible flows. We have devised a sharp interface immersed boundary approach that employs a non-conservative reconstruction in the vicinity of the body. Two techniques, one employing an employing Inverse Distance Weighting (IDW) based reconstruction for inviscid flows and the other employing one-dimensional reconstruction for viscous flows have been proposed in this work. The IB-FV framework has been employed to solve a large range of flow problems involving hypersonic inviscid and laminar flows, including those with moving bodies. The salient findings from the numerical investigations are summarised below.

1. The IDW reconstruction approach accounts for both Dirichlet and Neumann boundary conditions and directly enforces the boundary conditions on the surface of the body, thereby preserving the sharp interface.
2. Numerical studies show that the mass conservation errors remain non-zero on finite mesh resolutions. However, these errors tend to decrease with grid refinement, decaying at a rate close to unity.
3. The use IDW reconstruction approach preserves the nominal second-order accuracy of the finite volume flow solver, despite a lack of conservation in the near vicinity of the body. This clearly indicates that the reconstruction approach does not degrade the accuracy of the solution in the computational domain.
4. Despite the use of a non-conservative approach, the wall pressure and skin-friction distribution were computed with reasonable accuracy. While the pressure distributions could be computed accurately on relatively coarser meshes, accurate estimates of skin-friction necessitated local grid refinement near the vicinity of the body.
5. The computations of wall heat fluxes and stagnation point heat transfer are dependent on the geometry and flow conditions. While accurate results were

obtained for flow past a compression ramp, studies on aerodynamically blunt geometries yielded under-predicted heat fluxes. The problem was more severe on higher Mach and Reynolds numbers and also persist in adiabatic flows where the skin temperatures were incorrectly estimated.

6. An in-depth investigation into the underprediction of heat flux/skin temperature indicated that the errors are largely due to the non-conservative nature of the one-dimensional reconstruction approach employed. The inability of the IB approach to discretely conserve the energy in the near wall cells manifests as an under prediction in stagnation point heat flux for such cases. The problem was found to increase as Reynolds number increases for a given Mach number and as Mach number increases for a given Reynolds number, indicating a failure of the methodology to accurately predict the heat loads in hypersonic laminar regimes. The use of non-polynomial and non-linear interpolation as opposed to linear interpolation previously employed, was found to be equally non-conservative and inaccurate for heat-flux prediction.

The finite volume/immersed boundary framework has also employed in conjunction with variable fidelity framework for design and optimisation problems that included aerodynamic shape optimisation of axisymmetric nose cone, design of planar scramjet intakes and optimal axisymmetric nozzle configurations. The conclusions from these findings are enumerated below.

1. The use of a multi-fidelity framework comprising of a computationally inexpensive low-fidelity framework and computationally accurate high-fidelity framework leads to a significant reduction in turn-around time from initial guess to final optimal solution.
2. The maximum ballistic coefficient bodies are found to lead to lower stagnation point heat transfer while also having a low drag value than minimum drag geometries.
3. The quasi one-dimensional low-fidelity frameworks based on gas dynamic principles are found to be quite useful for the design of nozzle and scramjet intake. In case of scramjet intakes, this approach leads to a design with high total pressure recovery (TPR) while leading to low non-uniformity in the isolator. Similarly, these approaches have also been used successfully to design optimal contoured nozzles that minimise the radial velocity at the exit.
4. The IB-FV solver have been employed to verify the results from the quasi one-dimensional design approach. Studies show that the two-dimensional computations agree well the one-dimensional estimates.

The numerical investigations in this thesis have attempted to address some of the important issues concerning IB-FV solvers such as discrete conservation and its accuracy for skin-friction and heat-transfer estimates in hypersonic flows. The IB-FV approach is also a promising alternative that can be used in conjunction with high-fidelity frameworks for design and optimisation. It must however be noted that while the framework is quite accurate for inviscid compressible flows, there are issues in employing this solver in viscous compressible regime, that needs to be looked into more deeply. The present work should be seen as the first step in a thorough investigation towards the development of a robust and accurate industry level flow solver and some of the directions for future research are discussed below.

8.2 Scope of future work

In view of the limitations and drawbacks of the IB-FV flow solver and its possibilities for design and optimisation, we elaborate some of the possible directions for future research.

1. **Quasi-conservative Immersed Boundary approach:** The sharp interface IB-FV flow solver is inaccurate for heat transfer computations due to its non conservative nature near the body. It is thus worthwhile to investigate diffuse interface immersed boundary approaches such as those in [41], for compressible viscous flows.
2. **Wall modelling approach:** A near-wall modelling approach similar to the work by Posa and Balaras [157] can be employed to accurately capture skin friction and wall heat flux estimates for high-speed flows.
3. **Non-linear velocity and temperature reconstruction:** The use of non-linear near-wall velocity model in conjunction with a non-linear temperature reconstruction needs to be examined for high Reynolds number flow past blunt configurations.
4. **Post-processing and data reconstruction:** Wall distribution of gradient based quantities such as skin friction coefficient and Stanton number from non-conformal solvers are often oscillatory. This aspect of the near-wall data reconstruction and its post-processing needs to be further looked at.
5. **Immersed Boundary Finite Volume based Multi-Fidelity Framework:** The IB-FV solver has been used in these studies only to verify the one-dimensional

designs obtained using a low fidelity framework. However, one can also make use of the IB-FV solver as part of a high-fidelity framework to carry out aerodynamic shape optimisation of scramjet intakes and other geometries. Use of such a framework would lead to a fast shape optimisation strategy due to the ease and automation associated with generating Cartesian grids.

6. **Multi Objective Optimisation:** It is also desired to incorporate multi-objective problems with more than two objectives while employing evolutionary algorithm based optimisation techniques. This is considered important especially because of the limitation of gradient based optimisation techniques for multi-modal problems.
7. **Turbulence and Parallelisation:** The studies in this thesis were limited to high speed laminar flows and it is vital to investigate transitional and turbulent flows as well. A possible line of research could therefore be towards incorporating RANS model into the compressible IB-FV solver proposed in this thesis. Extensional to three-dimensional problems would necessarily require parallelisation of the flow solver. This is deemed important for investigation of configurations relevant to aerospace industry wherein the optimal solutions are desired in realistic turn around times.

Appendix A

Table A: The flux formulas for the vanLeer and AUSM scheme are given in the Table below

Scheme	Flux formula	Terms
vanLeer [93]	<p>Interface flux, $H_{I\perp} = H_I^+ + H_I^-$</p> $H_{I\perp} = \begin{bmatrix} \rho u_\perp \\ \rho uu_\perp + pn_x \\ \rho vu_\perp + pn_y \\ (\rho e + p)u_\perp \end{bmatrix}$ <p>$H_I^+ = H_{I\perp}$, $H_I^- = 0$ if, $M_\perp \geq 1$</p> <p>$H_I^- = H_{I\perp}$, $H_I^+ = 0$ if, $M_\perp \geq -1$ if $M_\perp < 1$</p> $H_I^\pm = \begin{bmatrix} f_{mass}^\pm \\ f_{mass}^\pm [u + n_x(-u_\perp \pm 2c)/\gamma] \\ f_{mass}^\pm [v + n_y(-u_\perp \pm 2c)/\gamma] \\ f_{energy}^\pm \end{bmatrix}$	$M_L^+ = \begin{cases} M_L, & \text{if, } M_L \geq 1 \\ \frac{1}{4}(M_L + 1)^2 & \text{if, } M_L < 1 \\ 0 & \text{if, } M_L \leq -1 \end{cases}$ $M_R^- = \begin{cases} 0 & \text{if, } M_R \geq 1 \\ \frac{1}{4}(M_R + 1)^2 & \text{if, } M_R < 1 \\ M_R & \text{if, } M_R \leq -1 \end{cases}$ $M_{\perp L} = \frac{u_{\perp L}}{c_L}, \quad M_{\perp R} = \frac{u_{\perp R}}{c_R}$ $f_{mass}^+ = +\rho_L c_L \frac{(M_L + 1)^2}{4}$ $f_{mass}^- = -\rho_R c_R \frac{(M_R - 1)^2}{4}$ $f_{energy}^\pm = f_{mass}^\pm \left\{ \frac{[(\gamma - 1)u_\perp \pm 2c]^2}{2(\gamma^2 - 1)} + \frac{u^2 + v^2 - u_\perp^2}{2} \right\}_{L/R}$

Continued on next page

Table A – *Continued from previous page*

Scheme	Flux formula	Terms
AUSM [94]	<p>Interface flux,</p> $H_{I\perp} = (M_n)_{I+\frac{1}{2}} \begin{bmatrix} \rho c \\ \rho cu \\ \rho cv \\ (\rho e + p)c \end{bmatrix}_{L/R} + \begin{bmatrix} 0 \\ pn_x \\ pn_y \\ 0 \end{bmatrix}_{I+\frac{1}{2}}$ <p>where</p> $(M_n)_{I+\frac{1}{2}} = M_L^+ + M_R^-$ $(p)_{I+\frac{1}{2}} = p_L^+ + p_R^-$ $(M_n)_{I+\frac{1}{2}} = M_L^+ + M_R^-$ $(\cdot)_{L/R} = \begin{cases} (\cdot)_L & \text{if, } M_{nI+\frac{1}{2}} \geq 0 \\ (\cdot)_R & \text{Otherwise} \end{cases}$	$p_L^+ = \begin{cases} p_L & \text{if, } M_L \geq +1 \\ \frac{p_L}{4}(M_L + 1)^2(2 - M_L) & \text{if, } M_L < 1 \\ 0 & \text{if, } M_L \leq -1 \end{cases}$ $p_R^- = \begin{cases} 0 & \text{if, } M_R \geq +1 \\ \frac{p_R}{4}(M_R - 1)^2(2 + M_R) & \text{if, } M_R < 1 \\ p_R & \text{if, } M_R \leq -1 \end{cases}$ <p>$M_{\perp L} = \frac{u_{\perp L}}{c_L}, \quad M_{\perp R} = \frac{u_{\perp R}}{c_R}$</p> <p>To avoid zero advection Mach number $(M_n)_{I+\frac{1}{2}}$ is modified as,</p> $ M_{nI+\frac{1}{2}} = \begin{cases} M_{nI+\frac{1}{2}} & \text{if, } M_{nI+\frac{1}{2}} > \delta \\ \frac{M_{nI+\frac{1}{2}}^2 + \delta^2}{2\delta} & \text{if, } M_{nI+\frac{1}{2}} \leq \delta \end{cases}$

PUBLICATIONS

Peer Reviewed Journal:

- Brahmachary S, Natarajan G, Kulkarni V, Sahoo N. **A sharp interface immersed boundary framework for simulations of high speed inviscid compressible flows.** *International Journal of Numerical Methods in Fluids*, 86:770–791, (2018)
- Brahmachary S, Natarajan G, Sahoo N. **On the Quasi–Optimality of Axisymmetric Geometries in Hypersonic Flows.** *Journal of Spacecrafts and Rockets*, 55:518–522, (2018)
- Deka M, Brahmachary S, Ramakrishnan T, Dalal A, Natarajan G. **A new Green-Gauss reconstruction on unstructured meshes, Part I: Gradient reconstruction.** *Journal of Computational Physics* (accepted)
- Brahmachary S, Natarajan G, Kulkarni V, Sahoo N, Ashok V, Kumar V. **Development and assessment of a new sharp interface immersed boundary method for hypersonic viscous flows.** (under review)
- Brahmachary S, Natarajan G, Kulkarni V, Sahoo N. “**Comment on “A new approach for the design of hypersonic scramjet inlets”**”, *Physics Of Fluids* 24, 086103 (2012)”. (under review)

Book Chapter:

- Brahmachary S, Natarajan G, Sahoo N. A Hybrid Aerodynamic Shape Optimization Approach for Axisymmetric Body in Hypersonic Flow. ***Fluid Mechanics and Fluid Power – Contemporary Research***, 301–311, (2017)

Conferences:

- S. Brahmachary, G. Natarajan and N. Sahoo, Aerodynamic Shape Optimisation of a two dimensional body, for minimum drag using simulated annealing

method, *Proceedings of International Conference on Advanced Engineering Optimization Through Intelligent Techniques* (AEOTIT), SVNIT, Surat, 1-3 July, (2013)

- S. Brahmachary, G. Natarajan and N. Sahoo, Aerodynamic Shape Optimisation Studies in Hypersonic Flow, *Proceedings of 3rd National Symposium on Shock Wave (NSSLW3)*, IIT Bombay, 21-22 Feb, (2014)
- S. Brahmachary, G. Natarajan and N. Sahoo, Multi Fidelity Shape Optimization Framework for Hypersonic Flows, *Proceedings of 6th International Conference on Theoretical, Applied, Computational and Experimental Mechanics (ICTACEM)*, IIT Kharagpur, 29-31 Dec, (2014)
- S. Brahmachary, V. Kulkarni, G. Natarajan and N. Sahoo, Active and Passive Wave Drag Reduction Technique in Hypersonic Flow, *Proceedings of 1st International ISHMT-ASTFE Heat and Mass Transfer Conference*, ISRO, Thiruvananthapuram , 17-20 Dec, (2015)
- S. Brahmachary, V. Kulkarni, G. Natarajan and N. Sahoo, Numerical Investigation of Optimum Power-Effectiveness for Wave Drag Reduction, *Proceedings of 4th National Symposium on Shock Wave (NSSLW3)*, Karunya University , 25-26 Feb, (2016)
- S. Brahmachary, G. Natarajan, V. Kulkarni and N. Sahoo, A Sharp Interface Immersed Boundary Method for Inviscid Compressible Flow, *Proceedings of 6th International Congress on Computational Mechanics and Simulation (ICCMS)*, IIT Bombay, Mumbai, June 27-1 July, (2016)
- S. Brahmachary, G. Natarajan, V. Kulkarni and N. Sahoo, A Sharp-Interface Immersed Boundary Method for High-Speed Compressible flows, *Proceedings of 18th Annual CFD Symposium*, NAL, CFD Division-Aeronautical Society of India, Bangalore, 10-11 August, (2016)
- S. Brahmachary, G. Natarajan, V. Kulkarni and N. Sahoo, Hybrid Cartesian Immersed Boundary Method for High-Speed Viscous Compressible Flows, *Proceedings of 44th National Conference on Fluid Mechanics and Fluid Power (FMFP)*, Amrita University, Kollam, Kerala, 14-16 Dec, (2017)
- S. Brahmachary, G. Natarajan, V. Kulkarni, N. Sahoo and S.R. Nanda, Application of greedy and heuristic algorithm based optimisation methods towards

aerodynamic shape optimisation, *Proceedings of 7th International Conference on Soft Computing for Problem Solving* (SocPros), Indian Institute of Technology Bhubaneswar, December 23-24, (2017)

- S. Brahmachary, A. Vinod, G. Natarajan, V. Kulkarni, N. Sahoo, Physics Based Low-Fidelity Framework for Design of Scramjet Inlets, *Proceedings of the 7th International and 45th National Conference on Fluid Mechanics and Fluid Power* (FMFP), Indian Institute of Technology Bomday, December 10-12, (2018) (accepted)

REFERENCES

- [1] Anderson JD. History of high-speed flight and its technical development. *AIAA*, 39:761–771, (2001)
- [2] Richardson LF. Weather prediction by numerical process. *University Press*, (1922)
- [3] Leveque R. Finite volume methods for hyperbolic problems. *Cambridge university press*, (2004)
- [4] ANSYS FLUENT, “Software Package”, Version 19.0, ANSYS, Inc., Canonsburg, PA, (2018)
- [5] OpenFOAM, <http://www.openfoam.com/>
- [6] Palacois F, Economou TD, Aranake AC, Copeland SR, Lonkar AK, Lukaczyk TW, Manosalvas DE, Naik KR, Padron AS, Tracey B, Variyar A, Alonso KK. Stanford University unstructured (SU²): Open-source Analysis and design technology for turbulent flows. *AIAA 2014-0243*, AIAA SciTech, 52nd Aerospace Sciences Meeting, National Harbor, Maryland, (2014)
- [7] Ganesh N, Shende N, Balakrishnan N. \mathfrak{R} -parameter: a local truncation error based adaptive framework for finite volume compressible flow solvers. *Computers & Fluids*, 38:1799-1822, (2009)
- [8] Belytschko T, Krongauz Y, Organ D, Fleming M, Krysl P. Meshless methods: An overview and recent developments. *Computer Methods in Applied Mechanics and Engineering*, 139:3-47, (1996)

- [9] Ye T, Mittal R, Udaykumar HS, Shyy W. An accurate Cartesian grid method for viscous incompressible flows with complex immersed boundaries. *Journal of Computational Physics*, 156:209-240, (1999)
- [10] Mittal R, Iaccarino G. Immersed boundary methods. *Annual Reviews in Fluid Mechanics*, 37:239-261, (2005)
- [11] Diskin B, Thomas JL. Comparison of node-centered and cell-centered unstructured finite volume discretisation: inviscid fluxes. *AIAA*, 49:836-854, (2011)
- [12] Mavriplis DJ. Revisiting the least-squares procedure for gradient reconstruction on unstructured meshes. *AIAA 2003-3986*, 16th AIAA Computational Fluid Dynamics Conference, Fluid Dynamics and Co-located Conferences, Orlando, Florida, (2003)
- [13] Shima E, Kitamura K, Haga T. Green-Gauss/weighted-least-squares hybrid gradient reconstruction for arbitrary polyhedral unstructured grids. *AIAA*, 51:2740-2747, (2013)
- [14] Katz A, Sankaran V. High aspect ratio grid effects on the accuracy of Navier-Stokes solutions on unstructured meshes. *Computers & Fluids*, 65:66-79, (2012)
- [15] Sozer E, Brehm C, Kiris CC. Gradient calculation methods on arbitrary polyhedral unstructured meshes for cell-centered CFD solvers, *AIAA 2014-1440*, 52nd Aerospace Sciences Meeting, AIAA SciTech Forum, (2014)
- [16] Holmes D, Connell S. Solution of the 2D Navier–Stokes equations on unstructured adaptive grids. *AIAA 89-1392*, AIAA 9th CFD Conference, Washington, DC, (1989)
- [17] Cary AW, Dorgan AJ, Mani M. Towards accurate flow predictions using unstructured meshes. *AIAA 2009-3650*, 19th AIAA Computational Fluid Dynamics Conference, San Antonio, Texas, (2009)
- [18] Barth TJ, Jespersen DC. The design and application of upwind schemes on unstructured meshes. *AIAA 1989-366*, 27th Aerospace Sciences Meeting, Reno, Nevada, (1989)
- [19] Karimian SAM, Straatman AG. Discretization and parallel performance of an unstructured Navier–Stokes solver, *International Journal of Numerical Methods in Fluids*, 52:591-615, (2006)

- [20] Syrakos A, Varchanis S, Dimakopoulos Y, Goulas A, Tsamopoulos J. A critical analysis of some popular methods for the calculation of the gradient in finite volume methods, with suggestions for improvements *arXiv:1606.05556v2* (2016)
- [21] Correa CD. A comparison of gradient estimation methods for volume rendering on unstructured meshes. *IEEE Transactions on Visualization and Computer Graphics*, 17:305-319, (2011)
- [22] Mahesh K, Constantinescu G, Moin P. A numerical method for large-eddy simulation in complex geometries. *Journal of Computational Physics*, 197:215-240, (2004)
- [23] Ham F, Iaccarino G. Energy conservation in collocated discretisation schemes on unstructured meshes. *Annual Research Briefs*, Center for Turbulence Research, Stanford University, (2004)
- [24] de Vasconcellos JV, Maliska CR. A finite-volume method based on Voronoi discretisation for fluid flow problems. *Numerical Heat Transfer*, 45: 319-342, (2004)
- [25] Parter SV. On the overlapping grid method for elliptic boundary value problems. *SIAM Journal on Numerical Analysis* 36: 819-852, (1999)
- [26] Chung MH. Cartesian cut cell approach for simulating incompressible flows with rigid bodies of arbitrary shape. *Computers & Fluids*, 35:607-623, (2006)
- [27] Quirk JJ. An alternative to unstructured grids for computing gas dynamic flows around arbitrarily complex two-dimensional bodies. *Computers & Fluids*, 23:125-142, (1994)
- [28] Udaykumar HS, Shyy W. Simulation of interfacial instabilities during solidification—I. conduction and capillary effects. *International Journal of Heat and Mass Transfer*, 38: 2057-2073, (1995)
- [29] Yang G, Causon DM, Ingram DM, Saunders R, Batten P. A Cartesian cut-cell method for compressible flows Part A: static body problems. *The Aeronautical Journal* 101: 47–56, (1997)
- [30] Tucker PG, Pan Z. A Cartesian cut cell method for incompressible viscous flow. *Applied Mathematical Modelling* 24:591-606, (2000)
- [31] Fidkowski KJ, Darmofal DL. Review of output-based error estimation and mesh adaptation in computational fluid dynamics. *AIAA*, 49:673-694, (2011)

- [32] Hartmann D, Meinke M, Schroder W. A strictly conservative Cartesian cut-cell method for compressible viscous flows on adaptive grids. *Computer Methods in Applied Mechanics and Engineering*, 200:1038-1052, (2011)
- [33] Mondal P, Munikrishna N, Balakrishna N. Cartesian-like grids using a novel grid-stitching algorithm for viscous flow computations. *Journal of Aircraft*, 44:1598-1609, (2007)
- [34] Ashok V, Adimurthy V, Joseph G. Heat flux computation in hypersonic flow with Cartesian mesh using hybrid solution methodology. *International Review of Aerospace Engineering*, (2013)
- [35] Peskin CS. Flow patters around heart valves: A numerical method. *Journal of Computational Physics*, 10:252-271, (1972)
- [36] Luo H, Mittal R, Zheng X, Bielamowicz SA, Walsh RJ, Hahn JK. An immersed-boundary method for flow–structure interaction in biological systems with application to phonation. *Journal of Computational Physics*, 227:9303–9332, (2008)
- [37] Gilmanov A, Sotiropoulos F. A hybrid Cartesian/immersed boundary method for simulating flows with 3D, geometrically complex, moving bodies. *Journal of Computational Physics*, 207:457-492, (2005)
- [38] Borazjani I, Ge L, Le T, Sotiropoulos F. A parallel overset-curvilinear–immersed boundary framework for simulating complex 3D incompressible flows. *Computers & Fluids*, 77:76–96, (2013)
- [39] Choi JI, Oberoi RC, Edwards JR, Rosati JA. An immersed boundary method for complex incompressible flows. *Journal of Computational Physics*, 224: 757–784, (2007)
- [40] Pathak A, Raessi M. A 3D, fully Eulerian, VOF-based solver to study the interaction between two fluids and moving rigid bodies using the fictitious domain method. *Journal of Computational Physics*, 311:87-113, (2016)
- [41] Pan D. An immersed boundary method for incompressible flows using volume of body function. *International Journal of Numerical Methods in Fluids*, 50:733-750, (2006)
- [42] De AK. A diffuse interface immersed boundary method for convective heat and fluid flow. *International Journal of Heat and Mass Transfer*, 92:957-969, (2016)

- [43] Patel JK, Natarajan G. Diffuse interface immersed boundary method for multi-fluid flows with arbitrarily moving rigid bodies. *Journal of Computational Physics*, 360:202-228, (2018)
- [44] Arquis E, Caltagirone JP. Sur les conditions hydrodynamiques au voisinage d'une interface milieu fluide-milieu poreux: application à la convection naturelle. *Comptes Rendus de l'Acadie des Sciences*, 299:1-4, (1984)
- [45] Angot P, Bruneau CH, Fabrie P. A penalization method to take into account obstacles in viscous flows, *Numerische Mathematik*, 81:497-520, (1999)
- [46] Angot P. Analysis of singular perturbations on the Brinkman problem for fictitious domain models of viscous flows. *Mathematical Models in Applied Sciences*, 22: 1395-1412, (1999)
- [47] Liu Q, Vasilyev OV. A Brinkman penalization method for compressible flows in complex geometries. *Journal of Computational Physics*, 227:946-966, (2007)
- [48] Boiron O, Chiavassa G, Donat R. A high-resolution penalization method for large Mach number flows in the presence of obstacles. *Computers & Fluids*, 38:703-714, (2009)
- [49] Majumdar S, Iaccarino G, Durbin P. RANS solvers with adaptive structured boundary non-conforming grids. *CTR annual research briefs*, Stanford University, NASA Ames, (2001)
- [50] Gao T, Tseng YH, Lu XY. An improved hybrid Cartesian/immersed boundary method for fluid-solid flows. *International Journal of Numerical Methods in Fluids*, 55:1189-1211, (2007)
- [51] Chaudhuri A, Hadjadj A, Chinnayya A. On the use of immersed boundary methods for shock/obstacle interactions. *Journal of Computational Physics*, 230:1731-1748, (2011)
- [52] Tseng YH, Ferziger JH. A ghost-cell immersed boundary method for flow in complex geometry. *Journal of Computational Physics*, 192:593-623, (2003)
- [53] Mittal R, Dong H, Bozkurttas M, Najjar FM, Vargas A, von Loebbecke A. A versatile sharp interface immersed boundary method for incompressible flows with complex boundaries. *Journal of Computational Physics*, 227:4825-4852, (2008)

- [54] Lee J, You D. An implicit ghost-cell immersed boundary method for simulations of moving body problems with control of spurious force oscillations. *Journal of Computational Physics*, 233: 295-314, (2013)
- [55] Mohd-Yusof J. Combined immersed boundaries/b-splines methods for simulations of flows in complex geometries. *CTR annual research briefs*, Stanford University, NASA Ames, (1997)
- [56] Fadlun EA, Verzicco R, Orlandi P, Mohd-Yusof J. Combined immersed-boundary finite-difference methods for three-dimensional complex flow simulations, *Journal of Computational Physics*, 161:35-60, (2000)
- [57] Gilmanov A, Sotiropoulos F, Balaras E. A general reconstruction algorithm for simulating flows with complex 3D immersed boundaries on Cartesian grids. *Journal of Computational Physics*, 191:660-669, (2003)
- [58] Balaras E. Modeling complex boundaries using an external force field on fixed Cartesian grids in large-eddy simulations. *Computers & Fluids*, 33:375-404, (2004)
- [59] Verzicco R, Mohd-Yusof J, Orlandi P, Haworth D. Large eddy simulation in complex geometric configurations using boundary body forces. *AIAA*, 38:427-433, (2000)
- [60] Iaccarino G, Kalitzin G, Moin P, Khalighi B. Local grid refinement for an immersed boundary RANS solver. *AIAA 2004-0586*, 42nd AIAA Aerospace Sciences Meeting and Exhibit, Aerospace Sciences Meetings, Reno, Nevada, (2004)
- [61] Sotiropoulos F, Yang X. Immersed boundary methods for simulating fluid-structure interaction. *Progress in Aerospace Sciences*, 65:1-21, (2014)
- [62] Iaccarino G, Verzicco R. Immersed boundary technique for turbulent flow simulations. *Applied Mechanics Review*, 56:331-347, (2003)
- [63] Wang Z, Fan J, Luo K, Cen K. Immersed boundary method for the simulation of flows with heat transfer. *International Journal of Heat and Mass Transfer*, 52:4510-4518, (2009)
- [64] Patel HV, Das S, Kuipers JAM, Padding JT, Peters EAJF. A coupled volume of fluid and immersed boundary method for simulating 3D multiphase flows with contact line dynamics in complex geometries. *Chemical Engineering Science*, 166:28-41, (2017)

- [65] Palma PD, de Tullio MD, Pascazio G, Napolitano M. An immersed boundary method for compressible viscous flows. *Computers & Fluids*, 35:693-702, (2006)
- [66] Ghias R, Mittal R, Dong H. A sharp interface immersed boundary method for compressible viscous flows. *Journal of Computational Physics*, 225:528-553, (2007)
- [67] Zhang Y, Zhou CH. An immersed boundary method for simulation of inviscid compressible flows. *International Journal of Numerical Methods in Fluids*, 74:775–793, (2014)
- [68] Liu C, Hu C. An immersed boundary solver for inviscid compressible flows. *International Journal of Numerical Methods in Fluids*, 85:619-640, (2017)
- [69] de Tullio MD, Palma PD, Iaccarino G, Pascazio G, Napolitano M. An immersed boundary method for compressible flows using local grid refinement. *Journal of Computational Physics*, 225:2098-2117, (2007)
- [70] Arslanbekov RR, Kolobov VI, Frolova AA. Analysis of compressible viscous flow solvers with adaptive Cartesian mesh. *AIAA 2011-3381*, 20th AIAA Computational Fluid Dynamics Conference, Honolulu, Hawaii (2011)
- [71] Ghosh S, Choi JI, Edwards JR. Numerical simulations of effects of micro vortex generators using immersed-boundary methods. *AIAA*, 48:92-103, (2010)
- [72] Das P, Sen O, Jacobs G, UdayKumar HS. A sharp interface Cartesian grid method for viscous simulation of shocked particle-laden flows. *International Journal of Computational Fluid Dynamics*, 31:269-291, (2017)
- [73] Qu Y, Shi R, Batra RC. An immersed boundary formulation for simulating high-speed compressible viscous flows with moving solids. *Journal of Computational Physics*, 354:672-691, (2018)
- [74] Sekhar S, Ruffin SM. Predictions of convective heat transfer rates using a Cartesian grid solver for hypersonic flows. *AIAA 2013-2645*, 44th AIAA Thermophysics Conference, San Diego, CA, (2013)
- [75] Eoff B. Transportation: Destination Mars. HEDS-UP mars exploration forum. *Lunar and Planetary Institute*, (1998)
- [76] Federal Aviation Administration. *The Annual Compendium of Commercial Space Transportation*, (2016)

- [77] Miele A, Huang HY. Missile shapes of minimum ballistic factor, *Journal of Optimisation Theory and Application*, 1:151-164, (1967)
- [78] Eggers AJ, Meyer, Jr., Resnikoff M, Dennis DH. Bodies of revolution having minimum drag at high supersonic airspeeds, *NACA TN-1306*, (1957)
- [79] Oehman WI, Wallace SA. Bodies of revolution having minimum total drag in hypersonic flow, *NASA TN-5438*, (1969)
- [80] Seager C, Agarwal RK. Hypersonic blunt-body shape optimisation for reducing drag and heat transfer, *Journal of Thermophysics and Heat Transfer*, 31:48-55, (2015)
- [81] Deepak NR, Ray T, Boyce RR. Evolutionary algorithm shape optimisation of a hypersonic experiment flight nose cone, *Journal Spacecraft and Rockets*, 45:428-437, (2008)
- [82] Theisinger JE, Braun RD, Clark IG. Aerothermodynamic shape optimization of hypersonic entry aeroshells, *13th AIAA/ISSMO Multidisciplinary Analysis Optimization Conference*, Fort Worth, Texas, (2010)
- [83] Cui K, Hu SC. Shape design to minimize the peak heat-flux of blunt leading-edge. *AIAA 2013-0233*, 51st AIAA Aerospace Sciences Meeting including the New Horizons Forum and Aerospace Exposition, Grapevine, Dallas/Ft. Worth Region, Texas, (2013)
- [84] Naville AG, Candler GV. Computational-fluid-dynamics-based axisymmetric aeroshell shape optimization in hypersonic entry conditions, *Journal of Spacecraft and Rockets*, 52:76-88, (2014)
- [85] Huang G, Gardner S, Zishka E, Seager C, Agarwal RK. Shape optimization of a blunt body in hypersonic rarefied and reacting flow for reducing both drag and heat transfer. *AIAA 2016-2057*, 54th AIAA Aerospace Sciences Meeting, AIAA SciTech, San Diego, California, (2016)
- [86] Eyi S, Yumusak M. Aerothermodynamic shape optimisation of hypersonic blunt bodies, *Engineering Optimisation* 47:909-926, (2015)
- [87] Xia C, Tao Y, Jiang T, Chen W. Multiobjective shape optimization of a hypersonic lifting body using a correlation-based transition model, *Proceedings of the Institution of Mechanical Engineers, Part G: Journal of Aerospace Engineering*, 230:2220-2232, (2016)

- [88] Ogawa H, Boyce RR, Isaacs A, Ray T. Multi-objective design optimisation of inlet and combustor for axisymmetric scramjets, *The Open Thermodynamics Journal*, 4:86-91, (2010)
- [89] Thevenin D, Janiga G, Optimization and computational fluid dynamics, 1st edn. Springer-Verlag Berlin Heidelberg, (2008)
- [90] Koziel S, Leifsson L. Scaling properties of multi-fidelity shape optimization algorithms, *Proceedings of the International Conference on Computational Science*, 9:832-841, (2012)
- [91] Sahai A, John B, Natarajan G. The role of fineness ratio in the design of minimum drag axisymmetric forebodies in hypersonic flows, *Journal Spacecraft and Rockets*, 51:900-907, (2013)
- [92] Hinman WS, Schmitt S, Johansen CT. Computational Fluid Dynamics Study of Optimized Hypersonic Leading Edge Geometries, *AIAA 2015-3509*, 20th AIAA International Space Planes and Hypersonic Systems and Technologies Conference Glasgow, Scotland, (2015)
- [93] vanLeer B. Flux-vector splitting for the Euler equations. In *Eighth international conference on numerical methods in fluid dynamics*, Springer (1982)
- [94] Liou NS, Steffen Jr CJ. A new flux splitting scheme. *Journal of computational physics*, 107:23–39, (1993)
- [95] Bibin J. Numerical investigation of shock wave boundary layer interactions in laminar hypersonic flows. *Ph. D Thesis*, Department of Mechanical Engineering, Indian Institute of Technology Guwahati, (2014)
- [96] Godunov SK. A finite difference method for the numerical computation and discontinuous solutions of fluid dynamics. *Matematicheskii Sbornik*, 47:271-306, (1959)
- [97] Blazek J. *Computational fluid dynamics: principles and applications*, Elsevier, Amsterdam, (2001)
- [98] Deka M, Brahmachary S, Ramakrishnan T, Dalal A, Natarajan G. A new Green-Gauss reconstruction on unstructured meshes, Part I: Gradient reconstruction. *Journal of Computational Physics* (in-press), (2018)
- [99] Deka M. A well balanced finite volume solver for incompressible flows. *M-Tech Thesis*, Department of Mechanical Engineering, Indian Institute of Technology Guwahati, (2017)

- [100] Perot B. Conservation properties of unstructured staggered mesh schemes. *Journal of Computational Physics* 159:58–89, (2000)
- [101] Perot JB, Vidovic D, Wesseling P. Mimetic reconstruction of vectors. *IMA Volumes in Mathematics and Its Applications, Compatible Spatial Discretizations*, Springer, New York, (2006)
- [102] Subramanian V, Perot JB. Higher-order mimetic methods for unstructured meshes. *Journal of Computational Physics*, 219:68–85, (2006)
- [103] Basumatary M, Natarajan G, Mishra SC. Defect correction based velocity reconstruction for physically consistent simulations of non-Newtonian flows on unstructured grids. *Journal of Computational Physics* 272:227–244, (2014)
- [104] Jasak H. Error Analysis and Estimation for the Finite Volume Method with Applications to Fluid Flows, *PhD Thesis*, Department of Mechanical Engineering, Imperial College of Science, Technology and Medicine, London, (1996)
- [105] P. Zwart, The integrated space-time finite volume method, *PhD thesis*, University of Waterloo, Waterloo, OAT, Canada, (1999)
- [106] Bibin J, Sarath G, Vinayak K, Natarajan G. Performance comparison of flux schemes for numerical simulation of high-speed inviscid flows. *Progress in Computational Fluid Dynamics*, 14:83–96, (2014)
- [107] Aftosmis M, Gaitonde D, Tavares TS. The behavior of linear reconstruction techniques on unstructured meshes. *AIAA Journal* 1995; **33**:2038–2049.
- [108] Zhang S, Shu CW. Convergence towards steady state solutions of the Euler equations with WENO schemes, Technical Report, *Scientific Computing Group, Brown University*, Providence, RI, USA, (2006)
- [109] Holden MS. A study of flow separation in regions of shock wave-boundary layer interaction in hypersonic flow. *AIAA 1978-1169*, AIAA 11th Fluid and Plasma Dynamics Conference, Seattle, Washington, (1978)
- [110] Mo H, Lien FS, Zhang F, Cornin DS. A sharp interface immersed boundary method for solving flow with arbitrarily irregular and changing geometry. *Physics Fluid Dynamics*, eprint arXiv:1602.06830, (2016)

- [111] Mizuno Y, Takahashi S, Nonomura T, Nagata T, Fukuda K. A simple immersed boundary method for compressible flow simulation around a stationary and moving sphere. *Mathematical Problems in Engineering*, 2015:1–17, (2015)
- [112] Peskin CS, Printz BF. Improved volume conservation in the computation of flows with immersed elastic boundaries. *Journal of Computational Physics*, 105:33–46, (1993)
- [113] Ni RH. A multiple-grid scheme for solving the Euler equations. *AIAA Journal*, 20:1565–1571, (1982)
- [114] Luo H, Baum JD, Lohner R. A hybrid Cartesian grid and gridless method for compressible flows. *Journal of Computational Physics*, 214:618–632, (2005)
- [115] Sridar D, Balakrishnan N. An upwind finite difference scheme for meshless solvers. *Journal of Computational Physics*, 189:1–29, (2003)
- [116] MacColl JW. The conical shock wave formed by a cone moving at a high speed. *Proceedings of the Royal Society of Aeronautics*, 159: 459–472, (1937)
- [117] Machell RM. An experimental investigation of hypersonic flow over blunt nosed cones at a Mach number of 5.8. *Engineer's thesis*, California Institute of Technology, CA, (1956)
- [118] Anderson Jr JD. Hypersonic and high temperature gas dynamics, Second Edition. *American Institute of Aeronautics and Astronautics, Inc. Reston, Virginia*, (2006)
- [119] Gustaffson B, Enander EP, Sjogreen B. Solving flow equations for high Mach numbers on overlapping grids. *Hypersonic flows for reentry problems*, Springer-Verlag, (1991)
- [120] Praveen C, Deshpande SM. Kinetic meshless method for compressible flows. *International Journal of Numerical Methods in Fluids*, 55:1059–1089, (2007)
- [121] Shyue KM. A moving-boundary tracking algorithm for inviscid compressible flow. *Hyperbolic Problems: Theory, Numerics, Applications*, Springer-Verlag, 989–996, (2008)

- [122] Puscas MA, Monasse L. A three-dimensional conservative coupling method between an inviscid compressible flow and a moving rigid solid. *SIAM Journal of Scientific Computing*, 37:884-909, (2015)
- [123] Lee J, Kim J, Choi H, Yang KS. Sources of spurious force oscillations from an immersed boundary method for moving-body problems. *Journal of Computational Physics*, 230:2677-2695, (2011)
- [124] Sahai A, John B, Natarajan G. Effect of fineness ratio on minimum-drag shapes in hypersonic flows. *Journal of Spacecraft and Rockets*, 51: 900–907, (2014)
- [125] Mason WH, and Lee J. Minimum-drag bodies axisymmetric in the supersonic/hypersonic flow regimes, *Journal of Spacecraft and Rockets*, 31:406-413, (1994)
- [126] Hu P, Zhao H, Kamakoti R, Dittakavi N, Xue L, Ni K, Mao S, Marshall DD, Aftosmis M. Towards efficient viscous modeling based on Cartesian methods for automated flow simulation. *AIAA 2010-1472*, 48th AIAA Aerospace Sciences Meeting Including the New Horizons Forum and Aerospace Exposition, Orlando, Florida, (2010)
- [127] Sun Y, Wang ZJ, Liu Y. Spectral (finite) volume method for conservation laws on unstructured grids VI: Extension to viscous flow. *Journal of Computational Physics*, 215:41-58, (2006)
- [128] Swanson RC, Langer S. Comparison of NACA 0012 Laminar Flow Solutions: Structured and Unstructured Grid Methods. *NASA/TM-2016-219003*, (2016)
- [129] Jawahar P, Kamath H. A High-Resolution Procedure for Euler and Navier–Stokes Computations on Unstructured Grids. *Journal of Computational Physics*, 164:165-203, (2000)
- [130] Qiu YL, Shu C, Wu J, Sun Y, Yang LM, Guo TQ. A boundary condition-enforced immersed boundary method for compressible viscous flows. *Computers and Fluids*, 136: 104–113, (2016)
- [131] Parthasarathy V, Kallinderis Y. Directional viscous multigrid using adaptive prismatic meshes. *AIAA*, 33:69-78, (1995).

- [132] Marshall DD, Ruffin SM. An Embedded Boundary Cartesian Grid Scheme for Viscous Flows using a New Viscous Wall Boundary Condition Treatment. *AIAA 2004-581*, 42nd AIAA Aerospace Sciences Meeting and Exhibit, Reno, Nevada, (2004)
- [133] Lillard R, Dries K. Laminar heating validation of the overflow code. 43rd AIAA Aerospace Sciences Meeting and Exhibit, p-689. (2005)
- [134] Wieting A.R. Experimental study of shock wave interface heating on a cylindrical leading edge. *NASA TM-100484*, (1987)
- [135] Kitamura K, Shima E. Towards shock-stable and accurate hypersonic heating computations: A new pressure flux for AUSM-family schemes. *Journal of Computational Physics*, 245:62-83, (2013)
- [136] Satheesh K. The effect of energy deposition in hypersonic blunt body flow field. *PhD Thesis*, Indian Institute of Science, Bangalore, (2007)
- [137] Truitt WR. Hypersonic aerodynamics, *The Ronald press company*, (1959)
- [138] Fay JA, Riddell FR. Theory of stagnation point heat transfer in dissociated air, *Journal of Aeronautical Sciences*, 25:73-101, (2005)
- [139] Seo JH, Mittal R. A sharp-interface immersed boundary method with improved mass conservation and reduced spurious pressure oscillations. *Journal of Computational Physics*, 230:7347-7363, (2011)
- [140] Bruno D, Palma PD, de Tullio MD. Simulation of hypersonic rarefied flows with the immersed-boundary method. *27th International Symposium on Rarefied Gas Dynamics*, 1333:1283-1288, (2010)
- [141] Sun Q, Zhu H, Wang G, Fan J. Effects of mesh resolution on hypersonic heating prediction. *Theoretical & Applied Mechanics Letters*, (2011)
- [142] Péron S, Benoit C, Gleize V, Mary I, Terracol M. A mixed overset grid/immersed boundary approach for CFD simulations of complex geometries. *AIAA 2016-2055*, 54th AIAA Aerospace Sciences Meeting, AIAA SciTech Forum, San Diego, California, (2016)
- [143] Capizzano F. Coupling a wall diffusion-model with an immersed boundary technique. *AIAA*, 54:728-734, (2013)

- [144] Damljanovic D, Rasuo B, Mandic S, Vukovic D, Isakovic J. Usability of comparative experimental - numerical supersonic test cases with the HB reference model. *29th Congress of the International Council of the Aeronautical Sciences*, St. Petersberg, Russia, (2014)
- [145] Knight D. RTO WG 10: Test Cases for CFD validation of hypersonic flight. *40th AIAA Aerospace Sciences Meeting & Exhibit*, Reno, Nevada, (2002)
- [146] Berman RJ. Ballistic coefficients for power-law bodies. *AIAA Journal*, 5:166-167, (1967)
- [147] Heideman JC. Blunt-Nosed Missile Shapes of Minimum Ballistic Factor. *Journal of Optimization Theory and Application*, 1:242-252, (1967)
- [148] Fink MR. Comment on Ballistic Coefficients for Power Law Bodies, *AIAA*, 5:1535-1536, (1967)
- [149] ANSYS FLUENT, Software Package, Ver. 14.5, ANSYS, Inc., Canonsburg, PA, 2012.
- [150] ANSYS ICEM CFD, Software Package, Ver. 14.5, ANSYS, Inc., Canonsburg, PA, 2012.
- [151] Shanbhag VV. An empirical expression for maximum cone angle for attached shock at supersonic Mach numbers, *Journal of Aircraft*, 7:191-191, (1970)
- [152] Raj NOP, Venkatasubbaiah V. A new approach for the design of hypersonic scramjet inlets. *Physics of Fluids*, 24:1-16, (2012)
- [153] Smart MK. Optimisation of two-dimensional scramjet inlets. *Journal of Aircraft*, 36:430-433, (1999)
- [154] Gounko YP, Mazhul II. Gasdynamic design of a two-dimensional supersonic inlet with the increased flow rate factor, *Thermophysics and Aeromechanics*, 19:363-379, (2012)
- [155] Korte JJ, Singh DJ, Kumar A, Auslender AH. Numerical Study of the Performance of Swept, Curved Compression Surface Scramjet Inlets. *Journal of Propulsion and Power*, 10:841-847, (1994)
- [156] Veillard X, Tahir R, Timofeev E, Molder S. Limiting contractions for starting simple ramp-type scramjet intakes with overboard spillage. *Journal of Propulsion and Power*, 24:1042-1049, (2008)

- [157] Posa A. Balaras E. Model-based near-wall reconstructions for immersed-boundary methods. *Theoretical and Computational Fluid Dynamics*, 28:473-483, (2014)